University of Cambridge
Department of Chemical Engineering

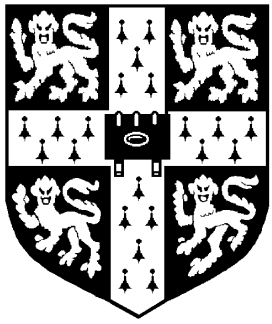

Mechanics of Paste Flow in Radial Screen Extruders

by

Peter James Martin
St John's College, Cambridge

A dissertation submitted for the degree of Doctor of Philosophy
at the University of Cambridge

June 2002

Preface

The work in this dissertation was undertaken in the Department of Chemical Engineering at the University of Cambridge, between October 1998 and June 2002. It is the original work of the author, except where specifically acknowledged in the text, and includes nothing that is the outcome of work done in collaboration. No part of the dissertation has been submitted for a degree to any other University.

This dissertation is approximately 65000 words in length, including appendices, references, tables and equations, and contains precisely 110 figures.

Peter Martin

Acknowledgements

A number of people have helped me with this project over the last few years, and I would like to take this opportunity to thank them.

I thank my supervisor, Ian Wilson, for his support and guidance over the course of my work. I am grateful for the help from my various industrial supervisors from the company that is now Syngenta. Paul Bonnett and Kay Challis have given me practical help with the running of the project, and I thank Peter Justen especially for his help in initiating the project.

I would not have been able to complete this work without the support of many different people from around the department. Paul Brittain and his group in the workshop have consistently provided invaluable assistance and good advice. I also note my debt to Jim Thompson and his computing section, as well as Wei-Yao Ma and the others in electronics. There were also many occasions when my work would have ground to a halt had Jim Young not always had just the right part in stores.

My research group and our technician, Zlatko Saracevic, have helped made my time in Cambridge greatly enjoyable, so I would like to give my final thanks to all of them.

Financial support from the Engineering and Physical Sciences Research Council, Syngenta, ICI and St. John's College, Cambridge, is gratefully acknowledged.

Other work which has been conducted during this project, which is not reported on in this dissertation, is published in the following two papers;

Martin, P. J., Wilson, D. I. and Challis, K. (2001) Extrusion of paste through non-axisymmetric systems. *6th World Congress of Chemical Engineering, Melbourne, Australia, 2001*.

Chou, S., Sydow, K., Martin, P. J., Bridgwater, J. and Wilson, D. I. (2002) Stress relaxation in the extrusion of pastes. *Journal of the European Ceramic Society*, forthcoming.

Summary

Mechanics of Paste Flow in Radial Screen Extruders

by

Peter James Martin

The extrusion of pastes has long been used as a means of achieving the desired shape of many different products. Whilst extrusion is basically a simple operation, the manufacture of more sophisticated products, the use of more complicated feed materials, the need to improve product quality, and the need to increase extruder performance have prompted the detailed study of extrusion flows. The radial screen extruder is one particular design of extruder commonly used to produce small, water-dispersible granules in the pharmaceutical and agrochemical industries. This project is the first rigorous attempt to understand the operation of this type of extruder.

Previous studies of pastes undergoing axisymmetric ram extrusion have led to the development of a simple modelling approach to describe the flow[†]. This model treats the paste as a yield stress material, and a relatively crude approximation is used to determine the pressure drop resulting from the complex flow in the die entry region.

A review of the sparse body of literature on radial screen extrusion revealed little understanding of these extrusional flows. In this work, the principles of the Benbow-Bridgwater approach have been applied to the case of radial screen extrusion, and a conceptualisation of the flow developed. From this, a quantitative model of the flow within radial screen extruders has been developed. Furthermore, two laboratory scale extruder modules have been designed and commissioned which facilitate the detailed study of key aspects of paste flow in radial screen extruders.

A model paste material, based on an industrially used paste, has been characterized according to the Benbow-Bridgwater approach. The material parameters obtained have been used with the new model to predict the flow patterns and stress states within both industrial radial screen extruders and laboratory extruder modules. Comparison with the experimental data indicates that the flow model correctly predicts the observed trends, but is of limited accuracy. Whether this is due to shortcomings of the model, or the limitations of the material characterization, remains open for discussion. The model paste exhibited noteworthy variability and proved difficult to characterise using a number of rheological approaches.

The proposed model offers new insight into the behaviour of radial screen extruders, and opens up the possibility of improving the performance of many industrial granulation devices.

[†] Benbow, J. and Bridgwater, J. (1993) *Paste Flow and Extrusion*. Clarendon Press, Oxford, U.K.

Contents

Notation

Roman

A	*(i)* current or final cross-sectional area
	(ii) total die land cross-sectional area
A_0	initial cross-sectional area
c	Coulombic cohesion
c_w	Coulombic wall adhesion
D	die land diameter
$\underline{D}$	*(i)* rate of energy dissipation per unit volume
	(ii) rate of work done
D_0	*(i)* barrel diameter
	(ii) core diameter at inlet
D_{hole}	screen hole diameter
D_s	diameter of screen
$D_{min.}$	fully plastic collapse screen diameter limit
F_{core}	axial force on extruder core
F_{screen}	axial force on extruder screen
$\boldsymbol{h}$	general channel height co-ordinate
$h_{channel}$	channel height at $\boldsymbol{w} = 0$
h_0	channel height at $\boldsymbol{w} = 0$ at channel inlet
l	*(i)* current or final length in homogeneous extension
	(ii) length of extruder channel
$\boldsymbol{l}$	general channel length co-ordinate
l_0	initial length in homogeneous extension
L	die land length
L_{blade}	length of blade tip in $\boldsymbol{w}$-direction
L_{blade}'	length of blade tip in $\boldsymbol{y}$-direction

L_{core} length of extruder core

L_{dam} length of dam at extruder exit

L_{hole} screen hole length

L_{screen}' length of pseudo screen die slot

m *(i)* Benbow-Bridgwater extrusion parameter: die entry velocity index

(ii) Tresca coefficient of wall friction

n *(i)* Benbow-Bridgwater extrusion parameter: die land velocity index

(ii) Power law wall shear stress slip velocity index

(iii) number of die holes in a screen

n_{blade} number of blades or flights on extruder core

n_{row} number of screen rows in front of blade through which paste flows

p *(i)* pitch of blade or flight on core

(ii) paste pressure

p_l paste pressure due to longitudinal flow

p_w paste pressure due to cross-sectional flow

p_{hole} screen hole pitch

P extrusion pressure

P_1 component of extrusion pressure associated with die entry

P_2 component of extrusion pressure associated with die land

P_{max} screen fully plastic collapse limit

Q volumetric flow rate

Q_{blade} volumetric flow rate per length through gap between screen and blade tip

Q_l volumetric flow rate along channel length

Q_{screen} volumetric flow rate per length through screen

Q_w volumetric flow rate per length across channel width

r general radial co-ordinate in cylindrical polars

r^2 coefficient of correlation

Ra average surface roughness

S rotational speed of extruder

t time

T torque

u *(i)* velocity along a streamline

(ii) pore pressure

v paste velocity

V *(i)* mean extrudate velocity

(ii) volume

V_p piston velocity

V_{shear} contribution to velocity by shear

V_{slip} *(i)* relative velocity between two bodies in contact

(ii) contribution to velocity by wall slip

w width of extruder channel

$\boldsymbol{w}$ general Cartesian co-ordinate

W work input

W_{blade} width of gap between blade tip and screen

W_{dam} gap between dam at the extruder exit and screen

W_{screen}' width of pseudo screen die slot

$\boldsymbol{x}$ general Cartesian co-ordinate

$\boldsymbol{y}$ general Cartesian co-ordinate

z *(i)* general Cartesian co-ordinate

(ii) general axial co-ordinate in cylindrical polars

Greek

α Benbow-Bridgwater extrusion parameter: die entry velocity factor

β *(i)* Benbow-Bridgwater extrusion parameter: die land velocity factor

(ii) power law and Jastrzebski coefficient of wall shear stress

$\dot{\gamma}$ shear strain rate

$\dot{\gamma}_A$ apparent shear strain rate

ε fraction of cross-sectional flow which passes through screen

$\dot{\varepsilon}$ direct strain rate

ϕ half-angle of extruder core

λ *(i)* power law or Herschel-Bulkley shear rate index

(ii) screen contact area factor

μ *(i)* Newtonian or apparent viscosity

(ii) power law, Bingham and Herschel-Bulkley plastic viscosity

(iii) Coulombic coefficient of friction

μ_w Coulombic coefficient of wall friction

μ_∞ Casson viscosity at high shear rate

ξ natural logarithm of ratio of barrel to die land diameter, $ln(D_0/D)$

ρ density

θ angle of nip between screen and blade in $\boldsymbol{w}$-$\boldsymbol{h}$ plane

θ' angle of nip between screen and blade in $\boldsymbol{y}$-$\boldsymbol{h}$ plane

σ normal stress

σ' effective stress

σ_0 Benbow-Bridgwater extrusion parameter: die entry yield stress

σ_y Benbow-Bridgwater extrusion uniaxial yielding stress, $\sigma_0+\alpha V^m$

σ_Y uniaxial yield stress

τ shear stress

τ_0 *(i)* perfect plastic, Bingham, Herschel-Bulkley and Casson shear yield stress
(ii) Benbow-Bridgwater extrusion parameter: die land wall yield stress
(iii) wall shear stress at zero slip velocity

τ_w general wall shear stress

χ inclination of channel core surface in ***l***-direction

ψ inclination of channel core surface in ***w***-direction

ζ helix angle of blade or flight on core

Subscripts

0 *(i)* at entry point
(ii) at zero velocity, or velocity extrapolated to zero
(iii) at yield point

1 *(i)* at exit point
(ii) associated with the die entry

2 associated with the die land

∞ at infinity

blade associated with the blade

channel associated with the extruder channel

dam associated with the extruder dam

feed associated with the feed screw

h associated with the ***h***-direction

l associated with the ***l***-direction

max. associated with a maximum

min. associated with a minimum

p associated with the piston

r associated with the ***r***-direction

s associated with the screen

screen associated with the screen

slip relative motion between two bodies in contact

w *(i)* at a wall or boundary between two bodies in contact
(ii) associated with the ***w***-direction

x associated with the ***x***-direction

y *(i)* associated with the ***y***-direction
(ii) at yield point

z associated with the ***z***-direction

Prefixes

d infinitesimal change

δ finite change

Figures

Tables

1 Introduction

This dissertation presents the results of a research project into the flow mechanics of pastes in twin-screw radial screen extruders. The project was initiated and sponsored by Syngenta, a multi-national agrochemicals business, for whom the twin-screw radial screen extrusion of pastes is an important process. The initial remit of the project was set by the sponsoring company, the direction of the project from that remit was selected by the author.

In this introduction we outline the problem presented by the sponsoring company. The extrusion operation is an integral part of the production process, and to understand what is required of the operation we must have some understanding of the whole process. We begin, in Section 1.1, with an overview of the final product's desirable properties. This is followed, in Section 1.2, with a summary of the different production techniques available which can achieve some of these product properties, and we describe the process used by the sponsoring company. The nature of the extruded paste material is discussed in Section 1.3. Finally, in Section 1.4, some difficulties experienced with radial screen extrusion are discussed; we state the aims of this project and an outline of the remainder of the dissertation is given.

1.1 Product form requirements

Many chemical products require a carefully designed product form in order to successfully deliver the right chemicals to the right place. Usually there are a number of different possible product forms, each with their own advantages and disadvantages. In this Section we consider the industrial needs which have driven this project.

The company which has sponsored this project, Syngenta (formerly Zeneca, then AstraZeneca), is a major manufacturer of chemicals for agricultural use (agrochemicals) supplying the global market. One of Syngenta's main businesses is the production of chemicals to protect crop yields and improve crop quality, be it; reducing competitive plant growth (herbicides), controlling damage by insect pests (insecticides), or reducing fungal plant diseases (fungicides). Generally, these products are applied either to the plant or soil by spraying a suspension or solution.

The product form must be designed to meet three main needs, namely;

- Basic properties: The chemical constituents which act on the crop (active ingredients) must be stored and transported before use safely and conveniently, also ensuring chemical stability of the active ingredients. At the time of use, the product form must allow the safe and convenient preparation of a solution/suspension for spraying.
- Marketing properties: The product must compete in the targeted market by meeting and exceeding customer needs and expectations, as well as meeting regulatory standards. In particular, this means designing the product form to maximise the inherent safety of the product, to maximise the product utility and to maximise the product's ease of use.
- Economic properties: The product form must be economically viable. This requires a form which enables efficient manufacture and thus competitive pricing, whilst being profitable for the manufacturer.

Where active ingredient application is by spraying, a number of agrochemical product forms are commonly used, namely; water dispersible granules (WDGs), wettable powders, suspension concentrates and emulsion concentrates. All of these forms include materials additional to the active ingredients, the bulk of which give the physical form of the product and carry the active ingredient (carriers). Economic factors have traditionally made concentrates and wettable powders the preferred forms. In more recent years, competition and occupational safety concerns have made WDGs, first developed in the 1960s, an important alternative product form (Bell (1989)). Some of the advantages and disadvantages of WDGs are listed in Table 1.1 overleaf. This project is concerned with increasing the efficiency of WDG production, and improving the control of WDG quality.

Table 1.1 Advantages and disadvantages of the WDG product form

Advantages	Disadvantages
spillages are easily dealt with	carriers are relatively expensive
no splashes	high proportion of carrier to active ingredient
low dermal toxicity	some active ingredients may decompose on carrier
non-dusty	
easy to pour and measure	
no long-term stability problems	
protection against frost not necessary	
little residue left in packaging	
packaging can be simple and cheap	
attractive uniform presentation	

(Bell (1989), and Zeneca Formulation Appreciation Course)

1.2 Production of Water Dispersible Granules

The active ingredient carried within a WDG is usually present in low fractions and has little effect on the production process. This Section outlines the important factors which do affect the production process. The challenge is to produce granules which retain integrity throughout transport, storage and handling, but which also readily disperse when put in contact with water – and to do this cheaply. The dispersibility feature must be stressed; these products may supply the whole market ranging from Third World to developed countries, and must perform reliably over the whole range of farming practices. Important physical properties of WDGs include; dispersion, size, friability (the degree to which the granules crumble), dry and wet density.

To achieve the desired physical properties, the whole granule production process must be considered. The key features of this process are shown in Figure 1.1 overleaf. Initially the granule must be formulated – consideration must be given not only to which materials might produce the desired granule, but also to the feasibility of using these materials in the process. The formulation is then realised by mixing together ingredients, shearing the mixture to create the desired microstructure, forming the desired granule shape and then drying the granule to produce the finished product. The final granule properties can then be assessed, and adjustments made to the formulation and processing stages. Generalised scientific codifications of this process are difficult to express; some aspects of it have been covered by Lyne and Johnston (1981) and Leuenberger (1984).

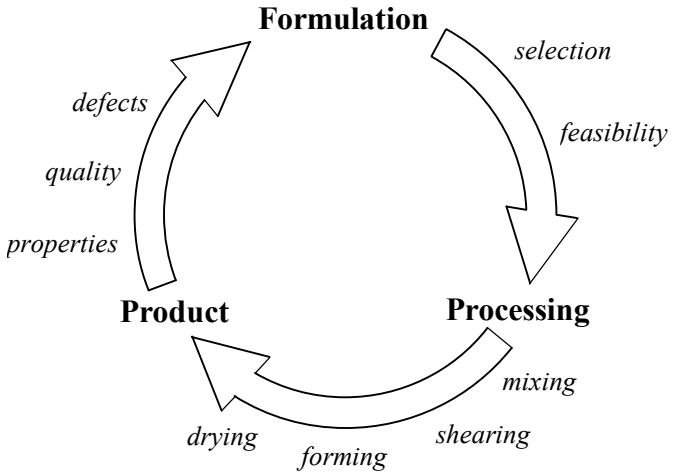

Figure 1.1 Locating the WDG product form requirements in the total product design process

A variety of industrial WDG processing routes have been developed. The specific route used by a particular industry is usually based on technology which has been proven in-house over years of trial and error, with a degree of scientific enquiry along the way. One route used by the sponsoring company features mixing dry powder ingredients together, before mixing with water and kneading to make a crumbly paste-like material. The product shape is formed from the paste crumble using commercially available twin-screw radial screen extruders. The product is then finished by drying, by which point it has broken into suitable lengths, and packaged. A schematic of this process is presented below in Figure 1.2. This project is specifically concerned with understanding the paste material flow within the extruder. The project has two particular aims; extending extruder efficiency/lifetime, and relating extruder design and operation to granule properties.

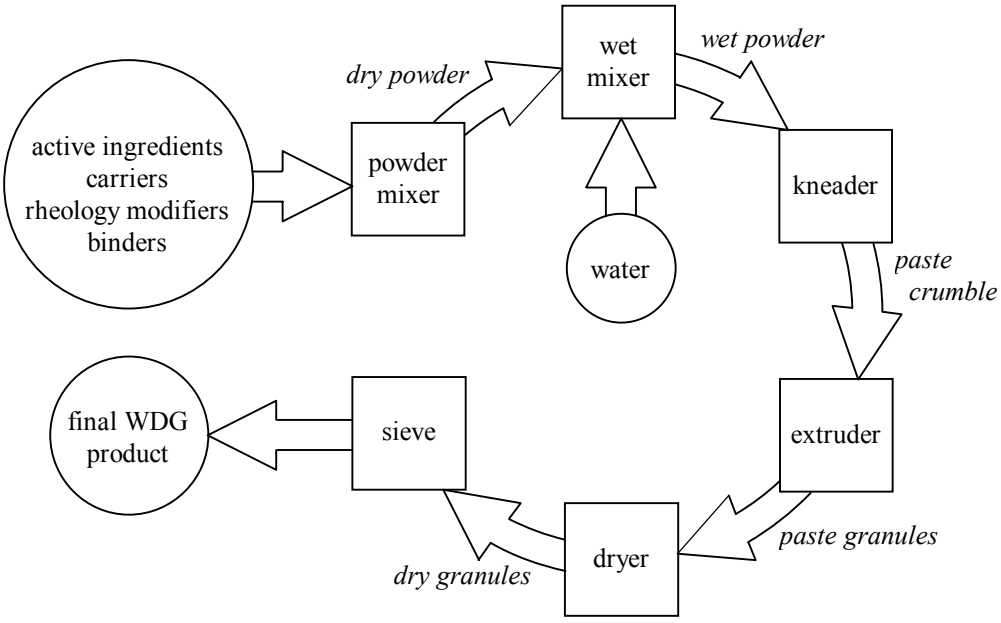

Figure 1.2 Schematic of Syngenta WDG production process

1.2.1 The twin-screw radial screen extruder

The sponsoring company has found that producing granules in the diameter range 0.6-1.2 mm with 'low pressure' extruders can satisfy the various product requirements discussed in the previous Section. The twin-screw radial screen extruder is one of the extruder types used by the sponsoring company, and this design of extruder is the principal subject of this dissertation. In Section 1.4, we consider some of the limitations of this extruder design which prompted the project. Here, we summarise the basic types of granulating, 'low pressure', extruders and then consider the twin-screw radial screen extruder in more detail.

'Low pressure' extruders have applications in many industries, especially the pharmaceutical industry. The sponsoring company uses extruders from the range produced by the Fuji Paudal Co. Ltd., Osaka, Japan. The extruder range is based on three basic types (summarised from Van doorslaer Tom (1997)). Figure 1.3 shows a variety of granules produced with Fuji Paudal extruders.

Figure 1.3 Selection of granules produced with Fuji Paudal extruders
Reproduced from Fuji Paudal promotional brochure. No scale was given.

Frontal extruders

Frontal extruders consist of a flat screen at the end of a double-barrel. Twin-screws feed paste along the length of the barrel to flat blades rotating against the screen, as detailed overleaf in Figure 1.4. The pressures necessary to extrude are higher than the other extruders, resulting in relatively hard and dense granules. Temperature increases of up to 75 °C are not uncommon for this type of extruder. Flow rates between 50-800 kg/hr are possible. The minimum screen opening is 1.5 mm, which is generally too large for the production of WDGs.

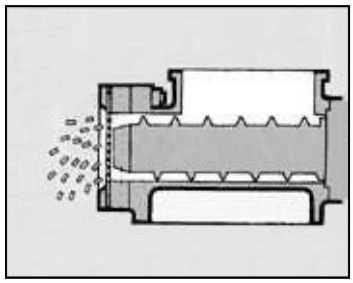

(a) Cross-sectional drawing

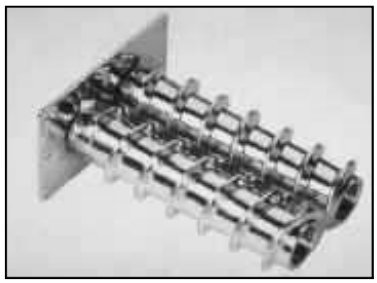

(b) Disassembled extruder

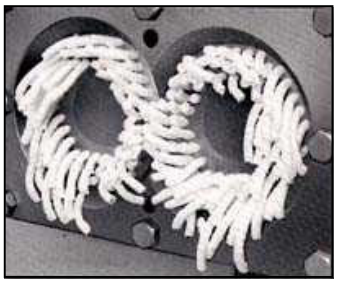

(c) Front view of extruder in operation

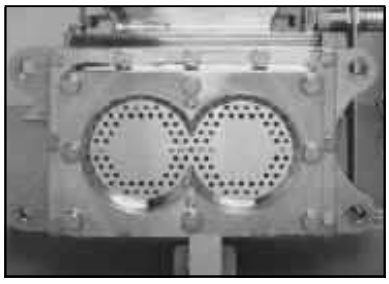

(d) Front view of extruder

Figure 1.4 Images of a Fuji Paudal frontal extruder
Reproduced from Fuji Paudal promotional brochures.

Radial extruders

Radial extruders consist of two semi-cylindrical screens along each side of two counter rotating extruder heads. Each head is a truncated cone in shape (a frustum) and has three longitudinal blades attached to it. Twin-screws within a double-barrel feed paste into the space between the extruder heads and the screens, as detailed overleaf in Figure 1.5. The relative motion between the screen and the blade causes the paste to be extruded through the screen in the vicinity of the blade. These extruders typically have 'overflow', where a small amount of material passes the extrusion area without being extruded and exits at the front, from where it can be recycled.

Compared to the other extruder technologies, radial extruders produce granules with a medium density and hardness. Temperature rises of up to 60 °C are normal and the screen openings range from 0.7 to 2.0 mm. Flow rates between 50-1000 kg/hr are possible. These extruders are generally suitable for WDG production.

Dome extruders

The dome extruder uses a dome-shaped screen in combination with dome shaped extrusion heads. As with the other designs, paste is fed to the extruder heads with a twin-screw in a double-barrel, as detailed overleaf in Figure 1.6. The dome extruder produces granules with the lowest density and hardness. The temperature rise is also the lowest of

the three extruder designs. The manufacturer links this efficiency increase with the dome shape design (Fujimoto *et al.* (1993)), but do not offer a detailed physical explanation. Screen openings range from 0.3 mm to 2.0 mm. Flow rates between 150-6000 kg/hr are possible. Again, these extruders are generally suitable for WDG production.

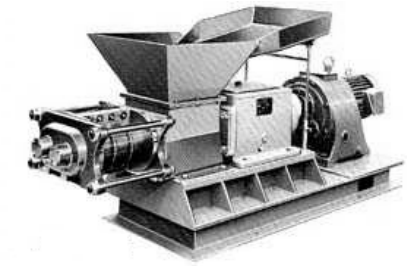

(a) Extruder unit

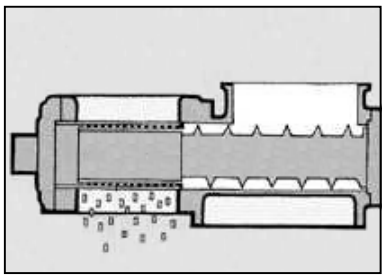

(b) Cross-sectional drawing

(c) Disassembled extruder

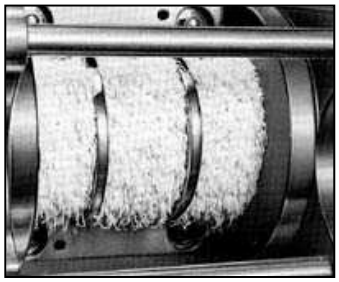

(d) Side view of extruder in operation

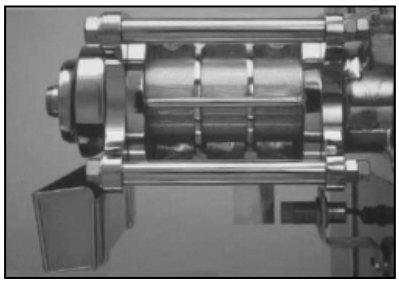

(e) Side view of extruder

Figure 1.5 Images of a Fuji Paudal radial extruder
Reproduced from Fuji Paudal promotional brochures.

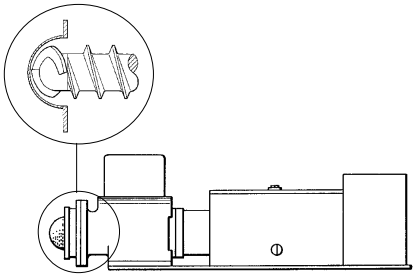

(a) Side drawing extruder

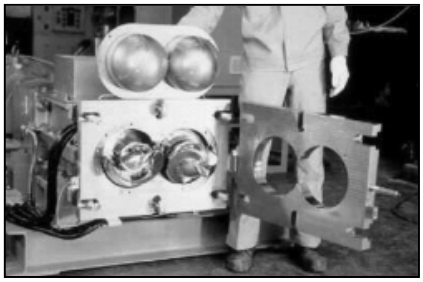

(b) Front view of extruder with screens removed

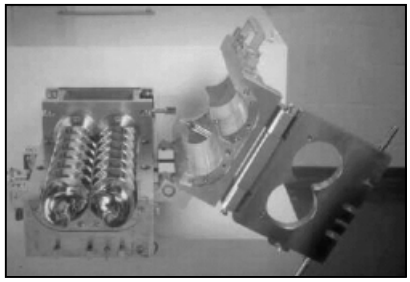

(c) Disassembled

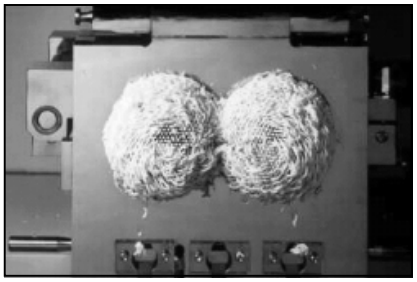

(d) Front view of extruder in operation

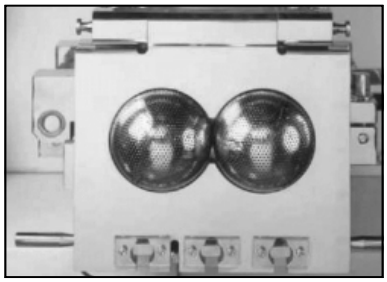

(e) Front view of extruder

Figure 1.6 Images of a Fuji Paudal dome extruder
Reproduced from Fuji Paudal promotional brochures.

Detailed description of the twin-screw radial screen extruder

Four key features of the operation of a radial screen extruder are indicated on the exploded view of one half of the extruder shown in Figure 1.7. Some more detailed engineering drawings of the frustum core/blades and feed screw of a Fuji Paudal extruder are reproduced in Appendix A.

① Paste crumble drops from a hopper onto the two counter rotating screws (also see Figure 1.5 *(a)* and *(b)*).

② The frictional forces between the paste, the single flighted screw and the barrel makes the paste move along the length of the barrel. Since paste is flowing into a constricted space, the stresses on the paste increase as it moves along the barrel, and the paste becomes compressed with air being expelled.

③ The screw forces the paste to flow into and along the region between the screen and the frustum core/blades (the extruder head), aided to some extent by the core blades.

④ In the extruder head the frictional forces between the paste, the core/blades and the screen make the paste flow out of the screen openings in a wave as the blades pass by (also see Figure 1.5 *(d)*). The extruded paste breaks off from the screen under gravity, and is removed for further processing.

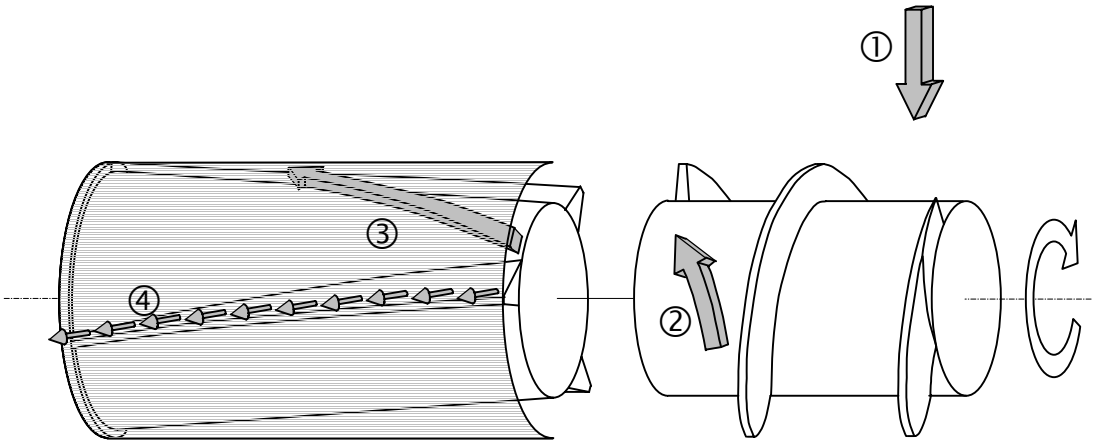

Figure 1.7 Exploded drawing of one half of a twin-screw radial screen extruder

A wide range of flow rates and flow patterns are experienced in the extruder; the dominant contributions are identified as part of the analysis in Chapter 6. Based on the operating conditions of one of the sponsoring company's extruders, detailed in Appendix A, approximate ranges for flow rate and area reduction have been calculated.

The typical paste velocity in the axial direction at entrance to the extruder might be 0.003 m/s, whereas a typical extrudate velocity through the screen perforations might be 0.3 m/s – two orders of magnitude larger. Over the length of the frustum, the ratio of inlet area to outlet area is around 3, and for the flow through the screen the ratio of inlet area to outlet area is around 5. The length to diameter ratio of a screen hole is approximately 1.

1.3 Pastes

Solid-liquid mixtures

The material from which the granule product is formed is generally comprised of dry powders mixed with water. A granule produced by compacting only the dry ingredients would posses poor dispersibility, since to maintain physical cohesion the granule would have to be highly compacted. By mixing the powders with water, a solid material is created which is soft enough to deform by hand and will keep its shape once deformed. Such pastes, featuring a solid but easily deformable nature, make possible the forming of relatively loosely consolidated granules which will subsequently disperse well in water. The project aim was to develop the understanding of the extruder operation, but this must be performed in conjunction with understanding the nature of the material flowing through the extruder. The nature of paste materials is introduced in this Section.

Pastes belong to the general type of materials called suspensions, which are comprised of mixtures of solid particles and a liquid-phase (and possibly also a gas-phase), and more specifically a type of materials called soft solids. There is tremendous scope for variation in the material's properties as the relative amounts and type of each phase are varied. Suspensions high in solids fraction are often used as a medium for transporting solids or as a medium through which the solids can be arranged into a particular shape, which is the case with paste extrusion. In these applications there is usually the desire to maximise the solids fraction in the suspension, with the limitation of maintaining the desired flow properties.

Examples of low solids fraction feed materials are river water or crude oil, the solids volume fraction of sand in a typical North Sea oil flowline being of the order 10^{-4} (Stevenson and Thorpe (1999)). An extensive list of solid volume fractions in aqueous waste flows is given by Perry and Green (1997b). For example, potato-processing waste features a solids volume fraction in the range 0.003-0.005, and flue-gas desulphurization sludge has a solids volume fraction in the range 0.03-0.12. One industrial application of using a liquid-phase to help transport a solid is that of coal slurries, which can feature solids volume fractions up to 0.4. These allow coal to be transported in a pipeline over hundreds of miles from a mine to a customer (Wasp (1977)). A high solids volume fraction might, again, be encountered when working with natural materials, *e.g.* a typical clay soil might have a solids volume fraction of the order 0.6 (Capper and Cassie (1969)). Solids volume fractions much higher than this are difficult to achieve due to the limitations of packing, as discussed in the following Section. On this solids volume fraction scale, pastes usually lie between slurries and soil-like materials.

Soft solids

E. C. Bingham, in *Fluidity and Plasticity* (Bingham (1922)) suggests the following way to distinguish between a liquid (more generally a fluid) and a solid:

> *"If a body is continuously deformed by a very small shearing stress, it is a liquid; whereas if the deformation stops increasing after a time, the substance is a solid."*

We can restate this as "solids are those materials that possess a yield stress" (although the existence of a true yield stress has been questioned, see Section 2.3.2). Substances that deform above the yield point without fracture are said to be plastic, and if the deformation is such that the stress increases with increasing strain rate, the substance is visco-plastic. A paste is often described as being a 'soft' solid. The solids volume fraction is high enough for the material to have an apparent yield stress – and thus can retain its shape once deformed – but is low enough for the material to be easily shaped say, by hand. Typically, a soft solid would have a yield stress of the order of a few hundred kPa. Most materials which may be described as soft solids are multi-phase systems, but do not necessarily include a solid-phase. The examples overleaf illustrate what might be considered to fall within the definition of a soft solid.

- Margarine

  Margarine is an emulsion, in which the dispersed phase is water and the continuous phase is a mixture of vegetable oils. At room temperature the oily-phase is semi-solid, in the sense that the temperature lies within the melting range of the mixture.

- Soap

  Amarasinghe (1998b) reported on the extrusion behaviour of soap. The soap investigated contained beef tallow as the major component and vegetable oil as the minor component. This is essentially a homogeneous material, and at room temperature the mixture is below its melting range.

- Ceramic pastes

  Ceramic pastes are used in the manufacture of a wide variety of products, ranging from the low-tech (bricks, tiles and pottery) to the high-tech (engine parts and electrical components). Another application is in the production of catalyst support materials, and this has been of particular interest in the development of paste extrusion models (Benbow and Bridgwater (1993a)).

- Chocolate

  Solid chocolate is another paste material. Plain chocolate, for example, consists of particles of sugar and cocoa solids embedded in a cocoa butter matrix, which is solid or semi-solid at room temperature. The extrusion of solid chocolate at room temperature has been the subject of research since it was patented almost a decade ago (Mackley (1992)).

1.3.1 Microstructure of a solid-liquid paste

We saw in Figure 1.2 that the paste is prepared by adding water to a mixture of dry powders. As more water is added to the powder, the soluble powders will enter the aqueous-phase and the mixture will pass through the following stages, as described by Newitt and Conway-Jones (1958).

With no liquid present, the dry powder behaves as a frictional material with the shear stresses and normal stresses being interrelated, sometimes in a linear manner. The first liquid added will be adsorbed onto the surface of the particles to form a thin coating around them. Further liquid will then start bridging between the films at points of contact between the solid particles (known as the pendular state). This liquid bridging will provide the first cohesive forces which allow the mixture to retain its shape under a shearing stress.

The next stage is the filling of the voids between the particles with liquid (known as the funicular state). Once these voids are full (known as the capillary state), additional liquid causes progressive separation of the particles. With only a slight excess liquid, the mixture is still able to retain its shape under low shearing stresses. Larger amounts of excess water produce a thick cream which readily flows under low stresses. With increasing water addition the suspension properties tend towards those of the pure liquid-phase. In practice the liquid-phase rarely fills the voids completely due to the presence of entrapped air, making most pastes three-phase mixtures. Where it is necessary to remove all air from the paste, a vacuum is applied during (or after) liquid addition and wet mixing.

It is apparent that some of the main factors affecting the nature of a paste are: the rheological behaviour of the liquid-phase, the surface chemistry of the liquid- and solid-phases (which affect the adsorption of the liquid onto the solid surface), the shape, size, and distribution of the solid particles, the constitution of the particulate-phase (which may be porous, agglomerated or deformable), and finally the processing history of the mixture (which will determine the degree of mixing, whether particle agglomerates are broken down, and the degree to which entrapped air has been expelled).

When the solid-phase particle size and shape distributions are well known, a packing arrangement might be predicted, and the expected voidage calculated. Based on the amount of liquid-phase added a judgement on the saturation of the voids can be made. For example, consider a paste made from mono-sized spheres with a solid-phase to liquid-phase volume ratio of 4:1. During preparation the paste is compacted to the limit where the mono-sized spheres develop, say the optimal close packed arrangement, which has a voidage of 0.26. Thus it may be calculated that 71 per cent of the void space is filled with liquid.

In practice this minimum voidage cannot be achieved. The packing behaviour of particles is of importance in many applications, and much research has been conducted into it. One example is the work of Scott and Kilgour (1969) who studied packing of one eighth inch diameter steel balls in cylinders of varying diameter. They reported that the minimum voidage of these balls when randomly packed was 0.37. When ‘loosely’ packed the voidage was 0.40. Voidages can be decreased by mixing together particles of different sizes such that smaller particles fill the voids between the larger particles. The first mathematical modelling of this was presented by Furnas in 1933.

This consideration of a solid-liquid paste's microstructure indicates the numerous, complex, and often unobtainable factors which will contribute to determine the bulk properties. This is the reason for the more general soft solid conceptualisation of pastes, where the many factors contributing to the material properties are averaged out and described as a yield stress.

1.4 Project aims

1.4.1 Problems associated with the twin-screw radial screen extrusion of pastes

Twin-screw radial screen extrusion is an industrially proven method of producing WDGs, and can be carried out profitably. However, little knowledge exists on how the extruder operates, and this manifests itself in the following two important ways (A more complete presentation of the research conducted into radial screen extrusion is presented later in Chapter 4).

Costs

It is thought that extruder lifetime, and possibly power consumption, could be improved. At present the extruder frustum core/blades and the screen are subject to significant attrition, with a typical screen lifetime being only ninety hours. The attrition is thought to be caused by one of the carriers in the paste, a hard material in the form of sharp particles. This component is considered necessary to achieve the desired granule dispersion, but it is not known how changes in extruder design or operation might affect the lifetime.

Product quality

Satisfactory operation of the extruders has been achieved over the years predominantly on a trial and error basis. For example, in an internal Syngenta report, Harris (1998), described the type of extrusion optimisation procedure used:

(a) *"A feed rate should be determined that is applicable to the milling and drying rate. This should be higher than the normal and reduced feed rates should be avoided."*
(b) *"The screen area should be reduced to optimise the granule form."*
(c) *"The correct water level must be determined. This should be as high as possible without causing agglomeration of granules during conveying or drying."*
(d) *At production scale, "the key to a good granulation is to keep the extrusion water level at the optimum, use a screen with the first third blanked off and keep the extrusion rate high".*

These guidelines display a limited, and sometimes confused, understanding of how the extruder operates.

1.4.2 Project aims

It has been the aim of this project to develop an understanding of how to design and operate twin-screw radial screen extruders by considering how the paste material flows through the extruder. In particular, the breakdown of required understanding can be listed as;

(a) Identifying the important features of the extruder, thus singling out the important operation and design parameters.

(b) Developing and verifying a model of the flow based on these parameters.

(c) Identifying the important trends in, and modes of, flow behaviour over the range of parameters.

(d) Relating these trends to extruder lifetime, operating costs and product quality.

1.5 Outline

The remainder of this dissertation is divided into seven Chapters. In Chapter 2 we outline the scope of the literature relating to pastes and soft solids. The various approaches to representing these materials are considered, and the approach of Benbow and Bridgwater (1993a) is presented in some detail. In Chapter 3 we describe a model paste material which has been used throughout the experimental work of this project. The paste constituents are investigated and related to the experimentally determined Benbow-Bridgwater material parameters.

Chapter 4 presents the literature relating to twin-screw radial screen extruders. Using the available knowledge possible extruder flow patterns are justified. Two laboratory scale extruder modules have been designed and commissioned to investigate the identified flows; these are described in Chapter 5. An extruder flow model is developed in Chapter 6, taking one of the proposed flow patterns and the Benbow-Bridgwater theory of paste flow outlined in Chapter 2 as its starting point. This model is capable of predicting the paste flow pattern within the extruder, the stress state of the paste throughout the extruder, torques and forces acting on the extruder, and the extruder work rate. Model predictions based on the geometry and operating conditions of an industrial extruder are considered over a range of parameters.

The model predictions are then compared against a wide range of experimental data obtained from the extruder modules in Chapter 7. The performance of the model is assessed and its future potential and its limitations discussed. Finally, in Chapter 8 the work presented in the dissertation is discussed as a whole. The project aims are reconsidered, conclusions drawn and consideration is given to the opportunities which might be exploited by any future work following on from this project.

2 Paste flow and extrusion

2.1 Introduction

In this Chapter we shall outline a number of approaches that are available for understanding and modelling pastes, particularly with respect to extrusion. The multi-phase nature of pastes has resulted in a wide variety of possible approaches. The range of possibilities varies in detail, complexity and accuracy. The selection of a modelling approach was based on how well the approach met the specific requirements of our situation. We describe two alternative types of approach in Section 2.2, and then in Section 2.3 describe in some detail the approach used for the remainder of this dissertation. Section 2.4 outlines how the selected approach has previously been utilised with success by the *Paste and Powder Processing Group* at Cambridge. Section 2.5 presents the work of some other groups which share a similar approach. Finally, in Section 2.6 the implications are considered of the selected approach to modelling on the analysis of stress states.

The aim of this Chapter is two-fold. Firstly, it is to convey the broad range of possible conceptual and theoretical approaches which have previously been used to understand paste like materials. The second aim is to justify the choice of the single approach which has been tested extensively during the course of this project. The chosen approach is then described and assessed in detail.

2.2 Approaches to modelling pastes and soft solids

We discussed in Section 1.3 the extent to which pastes can be thought of as a general class of materials, and offered a broad range of examples of materials which might be

included under this description. In this Section we seek to describe the range of approaches that have been employed to model the behaviour of these materials. The different approaches could be classified according to the level of detail in the model. For example, models in which the solid particles are individually represented, and equations of motion solved for each, can be described as microscopic models. On the other hand, macroscopic models deal with continuous phases that occupy the entire volume, although there may be more than one such phase, and so the material is not necessarily treated as a single-phase substance. The simplest approach is to model the material as if were a single phase, which is considered under Section 2.3.

2.2.1 Microscopic models

Advances in computing power have made it possible, in recent years, to carry out highly detailed analyses of multi-phase flows. Amongst the most detailed treatments for solid-liquid mixtures are those in which suitable flow equations (*e.g.* the Navier-Stokes equations) are solved for the liquid-phase between the particles, and the motion of each individual particle is calculated from Newton's laws using the Discrete Element Method (DEM). Yuan *et al.* (2001) give a concise summary of the scope of micro scale models.

These models are believed to be able to provide deep insight into the behaviour of suspensions. This insight could give some guidance in understanding how dense suspensions behave in processing equipment. Microscopic models could also be used to determine the constitutive behaviour of a suspension by examining a small volume undergoing a simple shear deformation. There are, however, some intrinsic limitations in applying them. One of the obstacles lies in the fact that particle-particle interactions are very complex and difficult to describe precisely. The interaction laws applied in the models are often theoretically debated, and sometimes include empirical factors. Another restriction of these models is the modelling scales, quite simply because the computing costs for realistic simulations are presently unacceptable to permit routine simulation. Typically, DEM models are restricted to 10^4-10^5 particles, which are many orders of magnitude lower than the number of particles in a typical industrial process. Simulated time scales, typically of the order of several seconds, are often not comparable to those characteristic of the real process. However, the advantages of explicitly modelling at the particle scale are considerable. For example, the microstructural behaviour of the suspensions may be difficult or impossible to measure experimentally or model on a continuum basis, but can be calculated from DEM simulations.

2.2.2 Macroscopic models

Macroscopic models deal with continuous phases that occupy the entire volume, although there may be more than one such phase, and so the material may not necessarily be treated as a single-phase substance. In these models, complex constitutive relationships have to be proposed for each phase, and it is found to be especially difficult to provide representative solid matrix constitutive laws.

An alternative approach has been to borrow concepts from a related analysis. Soil and pastes are similar materials, and concepts from soil mechanics have been introduced by Burbidge *et al.* (1995) and Poitou *et al.* (1997). The model splits the mixture into solid and liquid-phases and forces them into a dynamic equilibrium by means of a self diffusion equation based on Darcy's law for the fluid phase and Newton's law of motion for the solid-phase. Amongst the most recent work that has been reported, Yuan *et al.* (2001) have developed a numerical technique that combines a DEM and a Finite Element Method which can solve these equations. They report that this technique has reproduced some of the qualitative behaviour of the piston-driven extrusion process. The technique also yields extensive information regarding the pressure, velocity, density and permeability fields during an extrusion process.

2.3 Constitutive behaviour

Paste flow is related to many other disciplines due to the contributions of particle interactions and fluid mechanics. We have just considered one other discipline, soil mechanics, but there are also others, such as granular materials and polymer and suspension rheology. To date the field of rheology continues to be dominated by the description of concentrated suspensions in terms of effective single-phase continuum properties by invoking recognised non-Newtonian characteristics, and we shall follow this course below. Kytömaa (1993) made a rare effort to bridge the understanding of concentrated suspensions as a single-phase continuum with the understanding of soil mechanics and granular materials in the time before the development of computer processor speeds and memory capabilities which have made approaches such as Yuan *et al.* (2001) possible.

2.3.1 Suspension rheology

The viscosity of a solid-liquid mixture is always greater than that of the liquid phase alone, at a given temperature. Addition of particles to a Newtonian liquid results in a

mixture that exhibits non-Newtonian behaviour. The general form of the shear viscosity – shear rate curve for a concentrated suspension is discussed by Barnes (1989) from which Figure 2.1 is taken.

At low shear rates there is a Newtonian plateau, A, which is followed by a shear-thinning region B that culminates in a second Newtonian plateau, C. The shear-thinning behaviour is associated with the development of a structure within the flow (specifically, a two-dimensional layering) that facilitates the shearing. This structure is unstable, and at higher shear rates it breaks down into a random three-dimensional arrangement and an abrupt shear thickening (sometimes known as rheological dilatancy) is observed at D. This quite sudden shear-thickening phenomenon has received considerable attention, a summary of which has been presented by Barnes (1989). Shear-thickening of a paste has been observed by Yilmazer and Kalyon (1991), and was said to explain the unusual observation of plug flow occurring in a capillary *above* a certain wall shear stress.

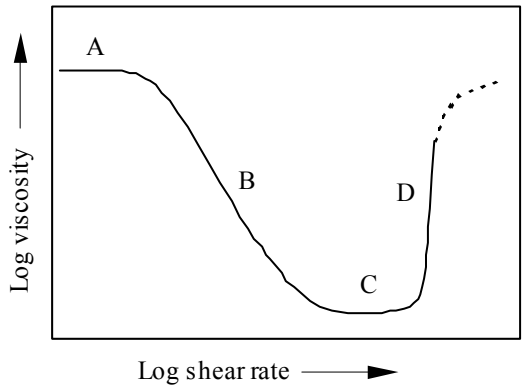

Figure 2.1 Schematic representation of viscosity against shear rate for a concentrated suspension Reproduced from Barnes (1989)

The effect of concentration is to accentuate all of the features seen in Figure 2.1. With sufficiently dense suspensions, the viscosity at the first Newtonian plateau can become very large, and the mixture exhibits a so-called yield stress. If the viscosity is truly infinite, the mixture will have a yield stress, but the existence of suspensions displaying this behaviour has been questioned (*e.g.* Barnes and Walters (1985)).

Husband *et al.* (1993) explain that there are essentially three different types of yield stress for a paste; the *elastic-limit yield stress* (the stress above which the material exhibits a permanent strain), the *static yield stress* (the minimum stress necessary to bring about unbounded strain), and the *dynamic yield stress* (the plateau stress for large strains). For a given material, the value of each yield stress may be different. It may even possess one type of yield stress, but not another. In the field of paste flow it is customary to accept

that a material exhibits a yield stress if a plot of deforming load against deformation rate does not extrapolate to zero. This is essentially a *dynamic yield stress*, although the deformation rates at which the material is tested may not reach a value low enough to distinguish between a true yield stress and very shear-thinning behaviour at low deformation rates.

2.3.2 Simple constitutive equations

Considering the material as a single-phase continuum enables its properties to be described by a single relationship between shear stress and shear rate. Pastes often exhibit wall slip, and so consideration has to be given to both the bulk properties of the material and interfacial properties of the material and the equipment. The study of these interfacial properties for pastes is not as developed as the study of the bulk properties. The only attempt to overview the whole range of approaches used known to the author was presented by Adams *et al.* (1991). This Section features a selection of some of the bulk and interfacial relationships which have been employed by different researchers (presented in one-dimensional form). The interfacial relationships have been classified into two types, distinguished by whether or not particle contact at the interface plays an important role.

Bulk behaviour

The bulk constitutive equations presented here are not complete yield criteria, but indicate the behaviour of the shear stress on a slip plane. Below the yield point, when the shear stress τ is less than the shear yield stress τ_0, the material is assumed to be perfectly rigid. The shear rate, $\dot{\gamma}$, is then zero when $\tau < \tau_0$. When $\tau > \tau_0$ the material deforms. The range of behaviours described are illustrated in Figure 2.2.

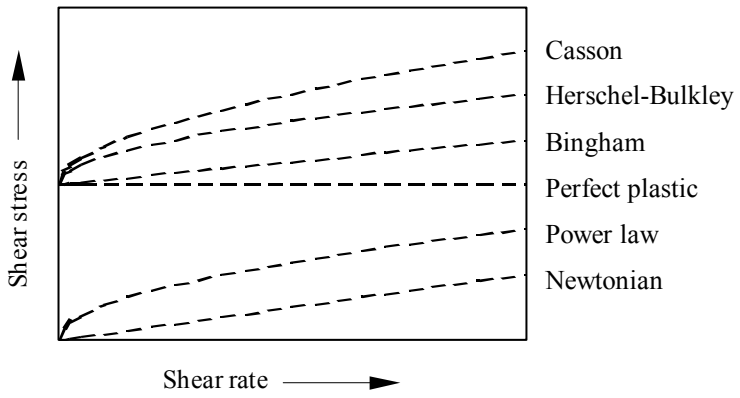

Figure 2.2 Shear stress against shear rate for various types of material

(i) Newtonian

$$\tau = \mu\dot{\gamma} \tag{2.1}$$

Newton's famous hypothesis about the response of fluids to a steady shearing motion was published in the *Principia* in 1687. This type of fluid is frequently considered as an 'ideal' fluid.

(ii) Power law

$$\tau = \mu\dot{\gamma}^{\lambda} \tag{2.2}$$

Many liquids do not follow ideal Newtonian behaviour and as interest in fluid rheology increased, there came a need to describe non-linear fluids in an appropriate manner. This was essentially a curve-fitting exercise, and, to be attractive, the models had to contain as few constraints as possible. The power law model, proposed in the early 1920s, has been successfully used to describe a wide range of fluids. It is also widely used in computational fluid dynamics (*e.g.* Zheng *et al.* (1992))

(iii) Perfect plastic

$$\tau = \tau_0 \tag{2.3}$$

Of materials which display a yield stress, the perfect plastic is the most simple, with no rate dependence, and thus can be considered to be an ideal case of yield behaviour. Metals are perhaps the best known examples of ideally behaved plastic materials. The perfect plastic model has been used extensively because of its relative simplicity in completely solving the equations of motion for a given flow, and deriving the complete stress and velocity fields. For the plane strain case, analytical solutions can be found using slipline field analysis (*e.g.* Hill (1950)). More complex cases can now be solved using the Finite Element Method (FEM). An extensive investigation into the use of the perfect plastic model and the FEM for understanding paste extrusion was conducted by Horrobin (1999).

(iv) Bingham plastic

$$\tau = \tau_0 + \mu\dot{\gamma} \tag{2.4}$$

Bingham studied the flow behaviour of many different materials in capillaries, and his findings regarding plastic solids, notably clay suspensions and paints, were summarised in *Fluidity and Plasticity* in 1922. He proposed an empirical relationship for such materials that contains two material parameters, equivalent to a yield stress and a viscosity.

(v) Herschel-Bulkley

$$\tau = \tau_0 + \mu\dot{\gamma}^{\lambda} \tag{2.5}$$

Herschel and Bulkley, in 1926, studied rubber-benzene solutions and encountered non-linear behaviour, which they accounted for by proposing an empirical relationship that contained three material parameters, equivalent to a yield stress and a power law relationship. Equation (2.5) is often considered to be the most general simple relationship for describing soft solid materials.

(vi) Casson

$$\sqrt{\tau} = \sqrt{\tau_0} + \sqrt{\mu_\infty \dot{\gamma}} \tag{2.6}$$

Casson, working in 1959 with printing inks, also encountered non-linear behaviour and proposed another semi-empirical shear stress – shear rate relationship, but containing only two parameters, where μ_∞ is the high shear rate viscosity. If the shear rate does not vary by more than a factor of ten, Casson's equation can be made to fit data points belonging to the Herschel-Bulkley relationship with almost equal effectiveness, but with the advantage of using only two parameters. Casson's model has not found widespread application in describing soft solids.

(vii) Coulombic

$$\tau = \mu\sigma + c \tag{2.7}$$

The Coulombic yield criterion represents another deviation from the ideal perfect plastic. It is used extensively to describe the bulk behaviour of granular materials. Particle-particle contact gives rise to the coefficient of friction, μ, which linearly relates the shear stress on a plane to the normal stress. Dampness, or other conditions, give rise to the cohesion, c. The high liquid-phase contents in pastes tend to create lubrication between particles, effectively making the coefficient of friction negligible and introducing a rate dependence. Thus the Coulombic yield criterion has not been found to be useful for describing paste materials.

(viii) Benbow-Bridgwater

$$\sigma = \sigma_0 + \alpha V^m \tag{2.8}$$

The Benbow-Bridgwater approach is discussed in detail later in Section 2.4.2. Equation (2.8) does not relate yield or shear stresses in three-dimensional space. It is an *ad hoc* relationship between the mean normal stress in the direction of the extrusional flow, σ, and terms representing the initial yield stress, σ_0, and the extrudate velocity, V. The extrudate velocity is used as an indicator of the dominant

shear rates. This approach assumes a yield-stress type of behaviour modified by shear rate, as in the Herschel-Bulkley model, and is often used when exact stress states and shear rates cannot be determined.

Interface behaviour (boundary conditions) – particle contact with the wall

(i) Coulombic

$$\tau_w = c_w + \mu_w \sigma_w \tag{2.9}$$

The Coulombic wall yield criterion is an extension of the bulk yield criterion. In this case μ_w is the coefficient of wall friction and c_w is known as the adhesion, but could be viewed as a wall shear yield stress. Like the Coulombic bulk yield criterion, the wall criterion is often used with granular materials, but it is also sometimes found useful for describing polymer and paste flows. Hatzikiriakos and Dealy (1992) used this criterion with no cohesive component for their capillary analysis of polymer flow. They had to use an assumed stress state at the wall in order to obtain the normal stress from the axial stress; it is not known whether there is any validity in using the same assumptions for pastes.

Paste wall shear stress has been reported to be dependent on pressure by a number of authors. Benbow and Bridgwater (1987c) measured the wall shear stress between two types of alumina paste and a metal surface for paste in a cylindrical pipe and paste in an annular shear cell. In these arrangements the normal stress on the wall could be varied at a controlled slip velocity. Wall shear stresses were found to increase by up to a factor of four as the normal stress on the wall was increased from around 0.1 to 1 MPa. Oliver and Whiskens (1996) conducted further experiments with a number of generally similar pastes for flow in a metal cylinder containing a baffle, and reported similar findings.

However, Benbow and Bridgwater noted that this dependence on normal stress is not usually apparent in die lands, where the measured stress gradient along the length of the die land is constant. Had the wall shear stress been varying with normal stress, the gradient would be expected to decrease along the die land length. They suggested that this might be due to the increased amount of liquid-phase migration to the wall which occurs in an extrusion process, compared to the shear cell or cylinder flow experiments. In some experiments solid particles might be in contact with the walls, thus, as with granular materials, a dependence of shear stress with normal stress would be expected. When liquid-phase migration occurs, a

boundary layer of rarefied suspension develops next to the wall and direct particle contact is significantly reduced.

Only one attempt is known, by Huzzard and Blackburn (1998), to use the Coulombic approach to model the flow of an alumina paste. It is not clear whether their work was valid since their gradient of axial stress along the die land appeared to be constant.

(ii) Tresca

$$\tau_w = m\tau_0 \tag{2.10}$$

The Tresca boundary condition defines the wall traction as being some fraction of the bulk shear yield stress τ_0. Adams *et al.* (1991) state that this criterion is of doubtful physical significance, at least in the case of metals, and was arguably introduced as a mathematical convenience, particularly for upper bound plasticity methods where Coulombic boundary conditions cannot be applied.

Interface behaviour (boundary conditions) – no particle contact with wall

The assumption of a predominantly liquid-phase boundary layer between the bulk paste and the wall is a dominant feature of paste flow analyses. However, estimates of the boundary layer thickness (*e.g.* Yilmazer and Kalyon (1991)) have shown that it is likely to be of the same order of magnitude as the paste particle diameter, and this small scale has made the measurement of any boundary layer properties difficult. Some increase in liquid fraction next to the wall might be expected due to boundary interruption of the particle packing, but a theory of shear-induced particle migration was not presented until the work of Leighton and Acrivos (1987).

Attempts to see a boundary layer using particles large enough to be conventionally photographed have been unsuccessful (*e.g.* Lukner and Bonnecaze (1999), who used 0.5 and 1.4 mm diameter glass spheres). Some attempts using Magnetic Resonance Imaging have been made, one of the most recent being the work of Modigell *et al.* (2000). These workers were able to detect an increase in liquid-phase next to the wall for a 50 per cent (by volume) suspension of 210-310 μm diameter PMMA spheres in a density matched aqueous saccharose solution. However, the imaging resolution was not sufficient to obtain any detailed information about the concentration gradient next to the wall. Promising work has been started using infrared spectroscopy, where initial results show an apparent decrease in concentration next to the wall for a system of ethylcellulose particles in aqueous solution (Tuchinda *et al.* (2001)). This method seems to promise the ability to

accurately measure the liquid-phase fraction as a function of distance from the wall, but requires an interface that is transparent to infrared radiation.

If we accept that there is a boundary layer of rarefied suspension between the wall and the bulk paste, then the information that would be needed to qualitatively describe the system would include,

(a) the rheology of the boundary layer material (in the simplest case the rheology would be constant over the boundary layer, in reality would probably vary),
(b) the thickness of the boundary layer,
(c) the slip velocity across the boundary layer,
(d) the surface roughness of the wall.

Together, these factors represent a complex system which would be difficult to investigate in detail. Consequently, the following boundary constitutive equations are based on only the slip velocity and the boundary layer rheology. The relationships all implicitly assume that the boundary layer thickness is constant, that the rheology does not vary through the boundary layer, and that the surface roughness is not a significant factor.

The author is not aware of any significant work in the paste literature which addresses these assumptions. A simple consideration of the boundary layer might suppose that its thickness would depend on the amount of liquid-phase migration, which would be dependent on time and liquid-phase pressure. The mechanism of suspension rarefication in the boundary layer is not well understood, the possibility of a concentration gradient may be assumed.

An initial study into the effect of surface roughness on wall shear stresses was made by Benbow and Bridgwater (1993e). Four dies were constructed with the same nominal diameter but different surface profiles, as shown in Figure 2.3 *(a)* overleaf. An alumina paste, with the particle size distribution and formulation given in Figure 2.3 *(b)*, was extruded through each of the dies over a range of velocities. The resulting pressures required to drive the flow (extrusion pressures) are shown in Figure 2.3 *(c)*. There was no systematic increase in extrusion pressure with die land surface roughness, but there does appear to be a significantly higher extrusion pressure for the roughest case, RI (roughness height/die land diameter = 0.14). The increase in extrusion pressure over the smooth case, S, for the other two cases, RII and RIII (both with roughness height/die land diameter = 0.046), was small on an absolute comparison. Benbow and Bridgwater concluded that whilst a smooth surface is desirable, mirror finishes are not required.

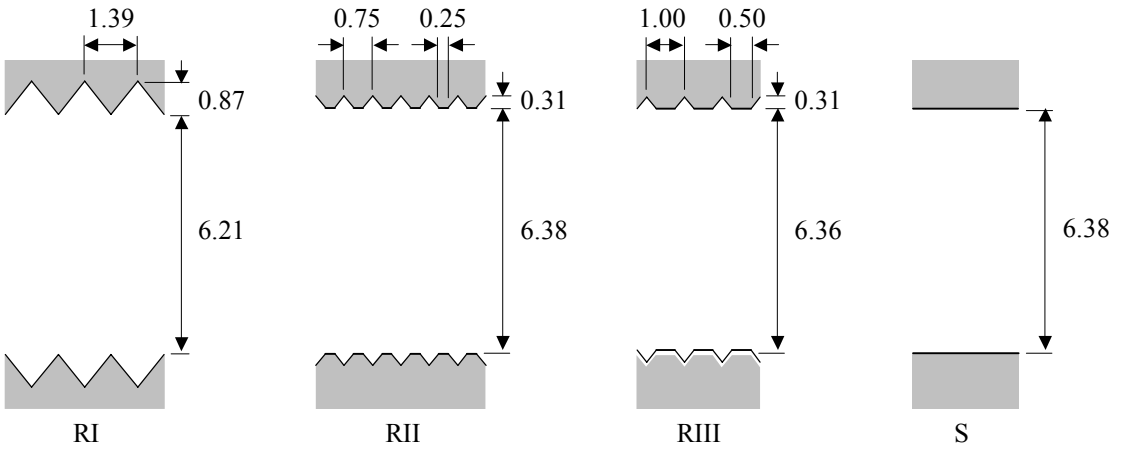

(a) Die roughness profiles

Dimensions are shown in mm.
Die length = 25.4 mm, Barrel diameter = 25.4 mm.

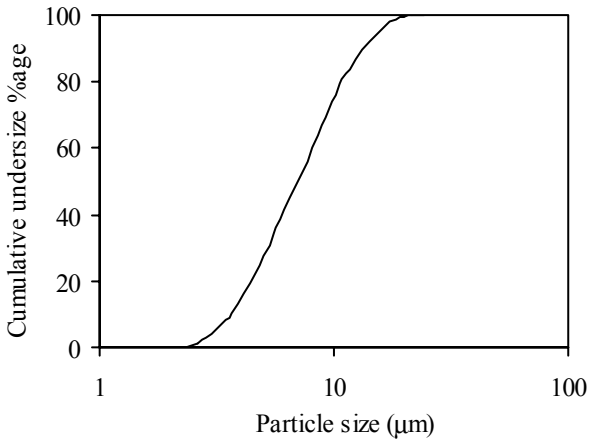

(b) α-alumina particle size distribution

Paste composition: a-alumina, 1000 g.
Bentonite clay 52 g, starch 52 g, water 280 g.

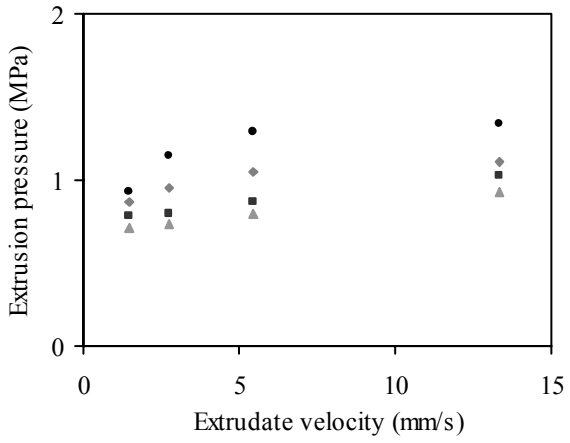

(c) Extrusion pressure against extrudate velocity

● *RI* ■ *RII* ◆ *RIII* ▲ *S*

Figure 2.3 The influence of die land surface roughness of extrusion pressure (Benbow and Bridgwater (1993e))

Benbow and Bridgwater's conclusion is probably valid for short die land configurations. The differences in extrusion pressures with surface roughness evident in Figure 2.3 *(c)* are actually very significant. It must be remembered that the extrusion pressure reported is a measure of the total work supplied to the paste, and includes a component to cover the deformation work on entry to the die land. Estimates indicate that the die land work in the smooth case (S) is ~ 10-20 per cent of the total work, so the increases shown on the figure are significant.

Surface roughness has been noticed to have an impact on results during the course of this project. Section 2.4 will describe the general types of ram extrusion experiments

which have been conducted, and typical apparatus is shown in Figure 2.6. During the course of the ram extrusion experiments it was noticed that the profile of piston force over time for nominally identical experiments systematically varied depending on the barrel used. Figure 2.4 below shows the piston force profiles for two such experimental ram extrusion runs carried out consecutively, using the same batch of model paste (described in Chapter 3).

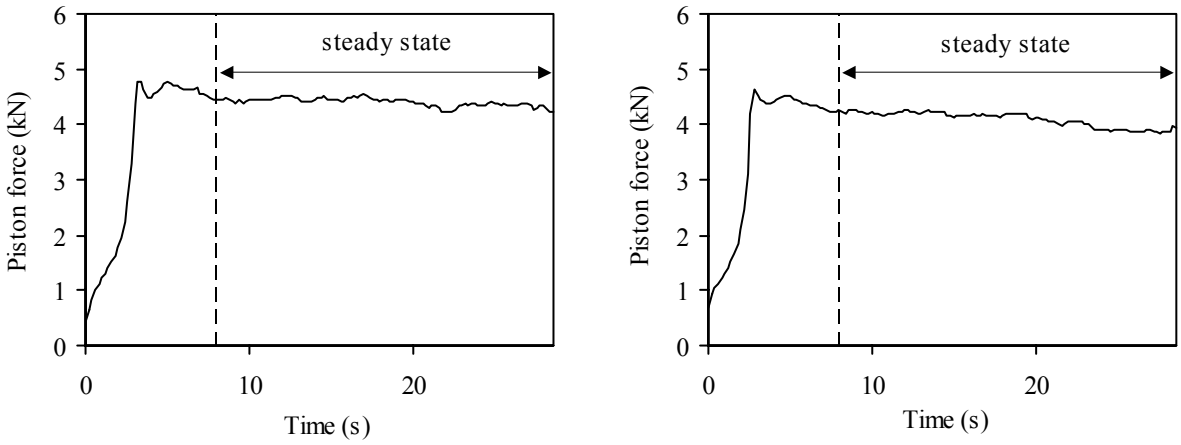

(a) Barrel I

Gradient = -0.0087 kN/s.

(b) Barrel II

Gradient = -0.021 kN/s.

Figure 2.4 Piston force against time for two different barrels

Piston velocity = 3.5 mm/s, D = 3 mm, L/D = 8.
Gradients found by linear regression over steady state period.

Both runs started with an initial transient region where the piston force increased as the paste was compacted. Shortly after flow commenced, approximately eight seconds, steady flow developed and the piston force gradually decreased as the piston passed along the length of the barrel.

This decrease in piston force might be understood by considering a force balance over the plug of paste in the barrel. As the piston progressed along the barrel length the length of paste plug decreased. If the material properties are constant, the wall shear stress on the surface of the paste plug due to friction with the wall would be constant. As the length of the plug decreases, the force on the plug due to wall friction would decrease at the same rate. Thus for extrusion at a constant piston velocity, the piston force would decrease linearly throughout the experiment. Aside from some fluctuations, which are thought to be due to paste inhomogeneity, the piston force followed this trend.

Comparing the piston force profiles for the two barrels in Figure 2.4 *(a)* and *(b)*, we see that the gradient is more than twice as steep for Barrel II than for Barrel I. Since these

runs were nominally identical, except for the barrel, we might presume that the difference in gradient is due to the occurrence of a higher wall shear stress with Barrel II than Barrel I.

Measurements of the surface profile of the two barrels, shown in Figure 2.5, indicate that the surface of Barrel II appears to be rougher than that of Barrel I, which is consistent with the apparently greater wall shear stress associated with Barrel II. The surface profiles of a selection of other extrusion equipment used in this project, detailed in later Sections, are also shown in Figure 2.5 for comparison. The average surface roughness, *Ra*, (the average absolute deviation of the profile from the mean line) is indicated for each surface. The average surface roughness of Barrel II is almost a factor of three greater than that of Barrel I.

It was beyond the scope of this project to develop a full model of boundary layer behaviour. The boundary constitutive equations proposed by previous researchers (detailed next), which are based on the slip velocity only, were followed. It was hoped that the variation in the paste-wall interface properties is small enough over the conditions used in this project for a model based on the slip velocity alone to be sufficiently accurate.

(iii) Power law

$$\tau_w = \beta V_{slip}^n \tag{2.11}$$

A power law relationship between the wall shear stress and the slip velocity has found extensive use in describing the boundary behaviour of pastes. For the case of a constant slip layer thickness of pure liquid-phase, this criterion would directly relate to a power law description of the liquid-phase. Likewise, for the special case where $n = 1$, the criterion relates to a Newtonian description of the liquid-phase and this case is sometimes called the Navier boundary condition.

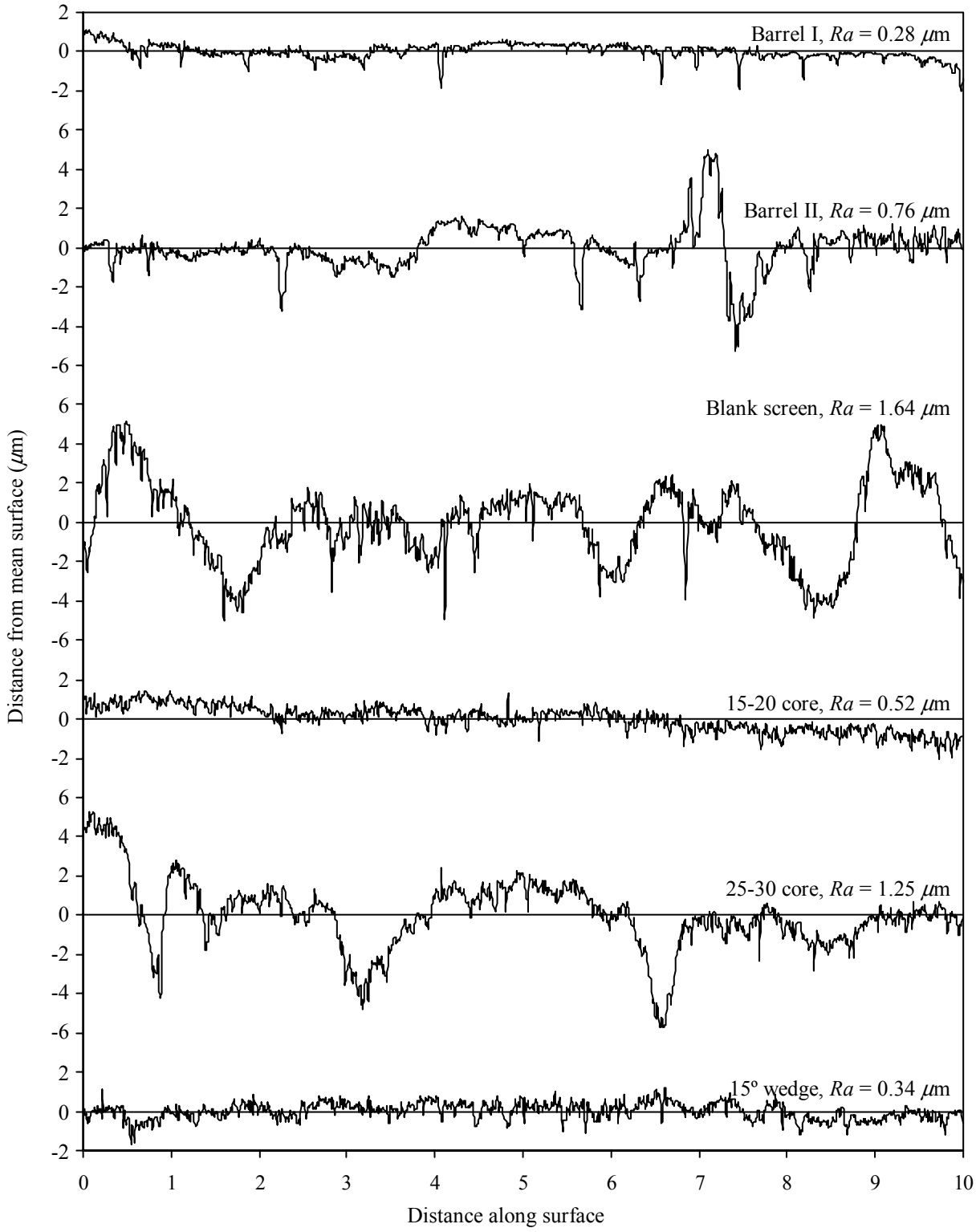

Figure 2.5 Surface profiles of extrusion apparatus

Acquired with Talysurf 6 stylus profilometer, Rank Taylor Hobson Ltd., Leicester, U.K.

Barrel I – see Chapter 3, Barrel II – Martin et al. (2001).
Blank screen – see Chapter 5, 15-20 core – see Chapter 5.
25-30 core – see Chapter 5, 15° wedge – see Chapter 5.

(iv) Benbow-Bridgwater

$$\tau_w = \tau_0 + \beta V_{slip}^n \tag{2.12}$$

Addition of special ingredients into the liquid-phase, often to limit phase migration or to act as binders after drying, can lead to the wall shear stress exhibiting an apparent shear yield stress. This approach to modelling the boundary layers in paste flow has become fairly common. First proposed without the power index in the English literature by Oveston and Benbow (1968), the power index added later by Benbow and Bridgwater (1993a).

(v) Jastrzebski

$$\tau_w = \beta V_{slip} D \tag{2.13}$$

It has been noted by a number of authors that the wall shear stress due to slip is not solely a function of slip velocity (manifested by physically impossible Mooney plots, see Section 2.4.1). Jastrzebski (1967) noticed this in his work on kaolinite pastes. He empirically found that wall shear stress against wall slip velocity data over a range of capillary diameters aligned on the same curve when the wall slip velocity was divided by the capillary diameter, D, but offered no physical justification for why this might be the case. The gradient of this line gave the factor β, which he found to vary with the wall shear stress, and suggested was dependent on the suspension microstructure. Despite this being an empirical approach, rather than a physical model of the boundary layer, it has become common enough to be reported in some rheology text books (*e.g.* Steffe (1996)).

Two capillary flow analyses reported from the group at Imperial College have made use of this method. Adams *et al.* (1995) and Khan *et al.* (2001) studied a clay/oil paste and an alumina/aqueous solution paste respectively. Both studies found that the Mooney plots were problematic. Adams *et al.* reported Mooney plots suggesting slip velocities greater than the mean extrudate velocity; Khan *et al.* reported Mooney plots with negative ordinate axis intercepts. Application of modified Jastrzebski boundary conditions (the slip velocity and diameter were raised to a power) yielded apparently sensible results in both cases.

A range of bulk material and boundary layer constitutive equations have been described in this Section. Section 2.4 focuses on one set of equations which have been used with particular success by the *Paste and Powder Processing Group* at Cambridge.

2.4 Paste and Powder Processing Group approach

In this Section we describe the basic approach to understanding paste flow as developed in the *Paste and Powder Processing Group* in the Department of Chemical Engineering at Cambridge. The group's approach has been used with particular success to model paste flow in simple extruders and improve on industrial extruder performance over the past thirty years. Some of this work is compiled by Benbow and Bridgwater (1993a) to (1993e).

The *Paste and Powder Processing Group* approach was adopted as the basis for all of the material characterization and modelling work in this project. This approach is approximate and can be open to considerable uncertainty, as is discussed over this Section. However, it possess the advantage that it is readily applicable to industrial materials, and relatively simple to apply. More accurate and precise methods, for example the use of Finite Element Analysis, result in more rigorous and precise solutions (for example, the work of Horrobin (1999), which is discussed in Section 2.5), but their application is considerably more complex and time consuming.

Any analysis is only as accurate as the parameters on which it is based. Fundamental uncertainty over paste material parameters (some aspects of which were considered in Section 2.3) limits the accuracy of any analysis. This project is an attempt to extend the use of an existing and proven approximate analysis to a new type of extruder. The relative success or failure of this attempt will indicate to what extent the analysis is limited by its approximations. It may prove to be the case that alternative techniques for modelling flow and for measuring material parameters are required in order to achieve satisfactory results.

Firstly, we detail a brief history of the group's research which gives a background to the modelling approach which we shall use. Then a basic paste extrusion experiment is described, which is followed by a discussion of the theoretical approach which is used within the group to understand this basic case of paste flow.

Group research history

The current *Paste and Powder Processing Group*, part of the Department of Chemical Engineering at the University of Cambridge, has its roots in a research group at the University of Birmingham developed, principally under J. J. Benbow, since the early 1970s. The group at Birmingham divided in the early 1990s when J. Bridgwater moved to form a parallel group at Cambridge.

Central to the understanding of paste flow which has been developed by this group is the case of ram extrusion in a square entry axisymmetric system, as shown in Figure 2.6. The first major group publication was by Oveston and Benbow (1968) whose interest lay in the production of ceramic catalyst supports, and it was this paper which established the square entry axisymmetric system as a standard apparatus for characterizing paste materials. A number of other standard systems exist, as will be discussed in Section 2.5. However, like the square entry axisymmetric system, they all suffer from not being able to determine the exact shear rates of the paste. Given this problem, Oveston and Benbow (1968) defended their system from critics such as Stieß-Konstanz (1955) on the basis that it gave characterization parameters from well defined operating conditions which were useful for the industrial applications which drove the research.

This paper drew on the work of a number of previously disparate publications. Capriz (1963) and Krieger and Maron (1952) studied the flow of Bingham bodies through capillaries. Berghaus (1957) found that once a critical wall shear stress had been exceeded, slip at the wall and plug flow of the bulk occurred. The wall shear stress then increased with extrudate velocity until the internal yield value of the material was reached and internal shear then occurred in addition to slip at the die walls. He extended the method of Krieger and Maron (1952) to incorporate the possibility of both slip at the die wall and internal deformation occurring simultaneously, and by measuring the pressure relationships for different die radii was able to determine the precise nature of flow behaviour. Berghaus also found that the principal term in an expression describing the work done in the metal wire drawing process adequately accounted for the flow of clays through orifices. Pels Leusden (1962) made the development of defining an extrusion pressure, and finding it by summing two terms; the first due to the change in cross-section undergone by the material, the second due to the frictional resistance to be overcome in the die.

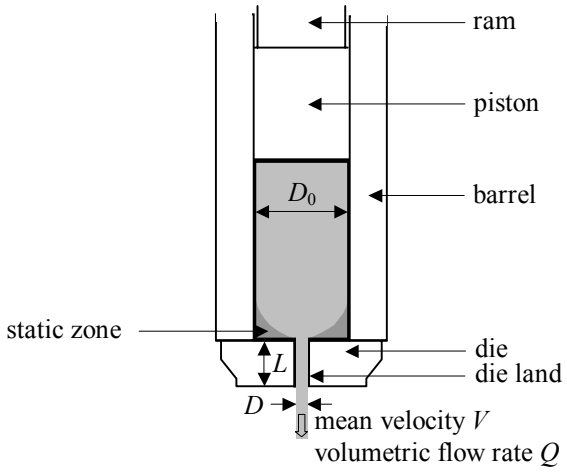

Figure 2.6 Cross-section of ram extruder with a square entry die

From the basic principles outlined in this first paper, the group's work has grown to cover an increasing variety of paste extrusion problems. Chronologically, the scope of the group's work has developed as follows; development of improved rate dependence model (Benbow (1971)) relating paste formulation to paste properties (Benbow and Bridgwater (1987a)), extending theory to dies of complex geometry (Benbow *et al.* (1991)), studying extrudate defects (Benbow *et al.* (1992)), extending theory to screw extruders (Burbidge and Bridgwater (1992)), investigating liquid-phase migration (Burbidge *et al.* (1995)) and developing on-line control systems (Amarasinghe and Wilson (1997)).

Basic experimental method

We now move on from this general discussion to consider a specific case of experimental ram extrusion. Full details of the experimental technique are presented, as this Section serves as a reference for future experimental methods throughout the dissertation.

Extrusion experiments have been carried out with apparatus shown in Figure 2.6. The barrel was loaded with a known amount of paste (weighed on a LC 62105 or BA 6100 Sartorius balance, Sartorius Ltd., Edgewood, New York, USA) for each extrusion, compacting manually with a rod to enable all of the paste to fit in the barrel. A screw action strain frame (SA100 Loading Frame, Dartec Ltd., Stourbridge, UK) was used to drive the ram though a displacement of 100 mm. A piston attached to the ram forces the paste in the barrel to flow through the die. A PC running the software Dartec Workshop 95 is used to program a controller (Modular 9500 Digital Control System, Dartec Ltd., Stourbridge, UK) which regulates the strain frame's load, position or velocity. The controller records data from transducers in the strain frame which measure the force on the

frame cross member and the cross member displacement against time. At least 220 force, displacement and time readings were recorded during each extrusion.

The Benbow-Bridgwater equation (2.29) models the mean pressure required to extrude a paste by considering an energy balance of the work done by the piston and the work done in deforming the paste and overcoming friction in the die land. Thus it was the mean axial stress on the piston due to deformation and friction in the die land during characterization which was of interest. The piston will in addition have to do work against any wall friction in the barrel. For a perfectly smooth barrel, the mean axial stress on the piston will be constant as the piston approaches the die until the point where the flow pattern near the die starts to change. Over all seventy five characterization runs where initial and final piston velocities were the same, as detailed later in Section 3.4, the mean decrease of the mean axial stress on the piston from the first to last velocity period was 8.4 per cent. Other approaches to measuring the extrusion pressure are either prohibitively complex or time consuming, thus the mean axial stress on the piston (with its associated error) was accepted as the extrusion pressure.

To illustrate a typical extrusion pressure profile for a basic extrusion experiment, the data previously displayed in Figure 2.4 *(a)* are represented in Figure 2.7 overleaf as extrusion pressure against time. The profile can be divided into three flow regions; compaction, transient and steady state. Over the compaction region air entrained in the paste is expelled. As the paste is much less elastic than air, the extrusion pressure starts to rise very rapidly until it reaches a peak, at which point flow commences. Immediately after flow has commenced there is a transient region, where the flow pattern and extrusion pressure are unsteady. After a short time some optimal flow pattern is reached and the rest of the extrusion run proceeds under nominally steady state conditions. We have already discussed in Section 2.3.2 how the extrusion pressure tends to decrease over time due to friction between paste and the barrel. Other factors will also prevent this period being truly steady state. If sufficient migration of the liquid-phase occurs the paste in the barrel can dry out over the course of a run. In such cases, since the drier paste offers more resistance to being extruded, the extrusion pressure would tend to increase over time. Inhomogeneity in the paste (*e.g.* air bubbles or agglomerates) can lead to fluctuations and spikes in the steady state extrusion pressure.

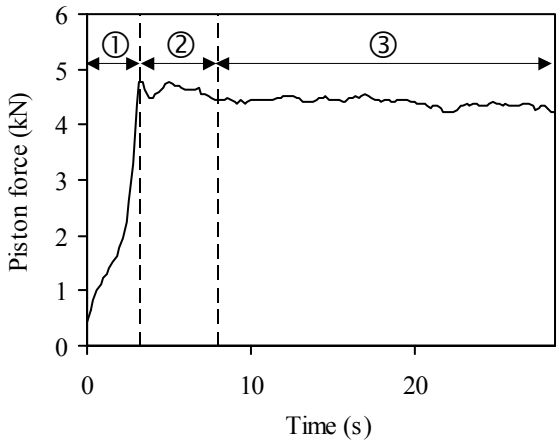

Figure 2.7 Extrusion pressure against time for a basic extrusion experiment

Piston velocity = 3.5 mm/s, D = 3 mm, L/D = 8.
① compaction ② transient ③ steady state

2.4.1 Capillary flow analysis

This Section begins to deal with the interpretation of data obtained from ram extrusion experiments. Ram extrusion, as previously described, is a crude form of capillary flow experiment. Here we consider the theory which has been developed for capillary flow. The following Section considers how this theory has been adapted for the specific case of ram extrusion of paste.

The flow of Newtonian liquids in capillaries was first studied in the mid-nineteenth century, independently by Jean Léonard Marie Poiseuille (Poiseuille (1835)), a physician, and G. Hagen (Hagen (1839)), a civil engineer. These analyses underpin one of the fundamental methods of liquid rheology. The important feature of flow in a capillary was the use of very small capillary diameters, small enough such that flow was laminar throughout with no turbulent core. With this knowledge the liquid viscosity could be used to either predict the flow properties for a material with a given viscosity, or, importantly, to find the viscosity from experimental measurements of a flowing liquid.

Since the start of mass polymer production, the types of material which require understanding has increased greatly. Some are described by the more complex constitutive equations of Section 2.3.2. Capillary flow analysis has been extended to allow the rheological properties of many of these materials to be found. The extension for power law fluids is attributed to Karl Weissenberg, and is sometimes know as the Weissenberg-Rabinowitsch equation (Rabinowitsch (1929)). Here we also describe advancements made

by Mooney (1931) on the inclusion of wall slip. There are three important considerations when performing a capillary analysis of pastes, as listed below;

(a) It might be that the pressure, or specifically the axial stress, will be a function of radial position on a plane normal to the capillary axis. This could be a consequence of either yield or non-isotropic properties.

(b) The high apparent viscosity typical of pastes makes turbulence unlikely, thus larger diameters can be used (strictly speaking, they are no longer capillaries).

(c) Significant wall slip is often observed. The flowing material may slip against the capillary wall. More commonly, in paste flow, there is a region of highly sheared material next to the wall, possibly caused by liquid-phase migration to the wall, which gives rise to apparent wall slip.

To the author's knowledge, the first of these points has not been recognised in any other study; its significance has not been assessed and no suitable analysis is known which accounts for it. Pressure has always been implicitly assumed to be constant over the cross-section in all analyses. We present an analysis of the steady state flow of an Herschel-Bulkley material, the most general type considered in Section 2.3.2, which is experiencing apparent wall slip and a central region of plug flow, and which is assumed not to have a radial pressure dependence. A schematic of this flow pattern is shown in Figure 2.8 below.

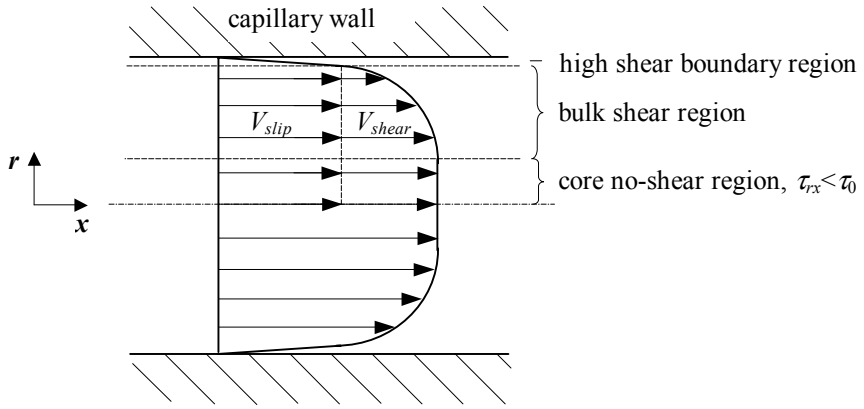

Figure 2.8 Generalised capillary flow pattern

Force balance over a central element of material

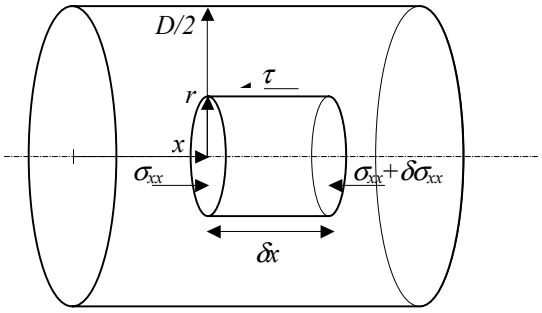

Figure 2.9 Force balance over a central element of material

A force balance over the parallel sided, axisymmetric element of material flowing in steady state as shown in Figure 2.9 above yields,

$$-\frac{\mathrm{d}\sigma_{xx}}{\mathrm{d}x}=\frac{2\tau_{rx}}{r}=\frac{4\tau_{rx,w}}{D} \tag{2.14}$$

where the ***x***-axis is the axis of symmetry, σ_{xx} is the normal stress in the axial direction acting on the ends of the element, τ_{rx} is the shear stress in the axial direction acting on the sides of the element, $\tau_{rx,w}$ is the shear stress in the axial direction acting on the sides of the element next to the capillary wall, r is the element radius and D is the capillary diameter. For simplicity, from this point onward shear stresses and rates of shear shall be assumed to be in the axial direction and acting on a plane normal to the radial direction unless otherwise stated; thus τ and $\dot{\gamma}$ are τ_{rx} and $\dot{\gamma}_{rx}$.

Continuity of flow

Integrating the flow through an annulus over the capillary cross-section gives the volumetric flow rate, Q,

$$Q=2\pi\int_0^{D/2}Vr\mathrm{d}r \tag{2.15}$$

which can be separated into the slip and shear components of velocity,

$$Q=\frac{\pi D^2}{4}V_{slip}+2\pi\int_0^{D/2}V_{shear}r\mathrm{d}r \tag{2.16}$$

and integrating by parts gives,

$$Q=\frac{\pi D^2}{4}V_{slip}-\pi\int_0^{D/2}\frac{\mathrm{d}V_{shear}}{\mathrm{d}r}r^2\mathrm{d}r \tag{2.17}$$

The Herschel-Bulkley constitutive equation (2.5) can be used to substitute for the shear rate $\mathrm{d}V_{shear}/\mathrm{d}r$, and substituting with the force balance (2.14), gives an integral which is a function of the yield and wall shear stresses only,

$$Q = \frac{\pi D^2}{4} V_{slip} + \frac{\pi D^3}{8\tau_w^3} \int_{\tau_0}^{\tau_w} \left(\frac{\tau - \tau_0}{\mu} \right)^{1/\lambda} \tau^2 \mathrm{d}\tau \tag{2.18}$$

which is often expressed as

$$\frac{32Q}{\pi D^3} = \frac{8}{D} V_{slip} + \frac{4}{\tau_w^3} \int_{\tau_0}^{\tau_w} \left(\frac{\tau - \tau_0}{\mu} \right)^{1/\lambda} \tau^2 \mathrm{d}\tau \tag{2.19}$$

For a Newtonian fluid (constitutive equation (2.1)) which experiences no wall slip, the right hand side of this expression reduces to the wall shear stress τ_w; correspondingly the left hand term, $32Q/\pi D^3$, is sometimes called the apparent shear rate, $\dot{\gamma}_A$.

Given the flow rates, for constant wall shear stress, in a set of capillaries with a range of diameters (assuming the slip velocity is exclusively a function of the wall shear stress, such as equations (2.11) and (2.12)), a plot of $\dot{\gamma}_A$ against $8/D$ can be constructed. The gradient would be equal to the slip velocity V_{slip}, and the intercept on the ordinate axis would be related to the wall shear stress and the material parameters τ_0, μ and λ. Given these data over a range of wall shear stresses, the relationship of the wall slip velocity to wall shear stress, and values of the material parameters can be found. This method of finding the wall slip velocity was first presented by Mooney in 1931 and the construction is sometimes called the Mooney plot. For a slip velocity which is related to the wall shear stress and capillary diameter, as in equation (2.13), a plot of $\dot{\gamma}_A$ against $8/D^2$ would give a gradient equal to the product of the capillary diameter and the slip velocity, and an ordinate axis intercept as before.

Capillary flow experiments usually utilise a reservoir of material, connected to the capillary (respectively the barrel and die land in Figure 2.6), which is reduced in volume at a known rate and pressure to force the material to flow in the capillary. The pressure contains contributions from both the wall shear stress and the entry effect. Thus it is difficult to directly control the wall shear stress experimentally.

In practice a series of experiments are conducted with a constant flow rate and capillary diameter with a variety of capillary length to diameter ratios. We assume that the entry effect is not dependent on the absolute pressure, so if the flow rate was unaltered the

entry effect will be constant over the series. If the wall shear stress is constant along the length of the capillary, equation (2.14) can be expressed as,

$$\sigma_{xx} = \text{entry term} + 4\frac{L}{D}\tau_w \tag{2.20}$$

A plot of pressure against capillary length to diameter ratio (L/D) will have a gradient equal to four times the wall shear stress and an ordinate axis intercept related to the entry effect. This approach was first proposed by Bagley (1957) and the construction is sometimes called the Bagley plot.

Repeating this approach over a range of flow rates and capillary diameters provides wall shear stress vs. flow rate data which can be presented as in Figure 2.10 below. Values of flow rate at constant wall shear stress can then be read off for each diameter used, and with these the Mooney plot can be compiled. It was noted in Section 2.3.2 that some researchers have experienced difficulty constructing physically realistic Mooney plots. However, this has not been the case in all studies. For example, Amarasinghe (1998b) successfully constructed Mooney plots for an alumina paste and a soap material, both of which exhibited plug flow over the whole flow rate range investigated. Yilmazer and Kalyon (1991) working with an ammonium sulphate/polymeric liquid paste, present a good example of finding the fraction of flow due to wall slip using Mooney plots. In their work they were able to directly record the transition from flow due to wall slip and internal shearing to wall slip only (plug flow).

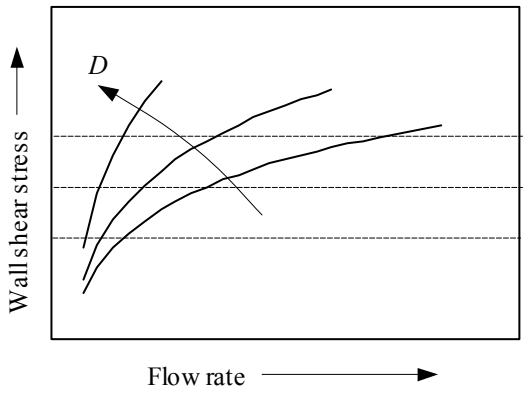

Figure 2.10 Flow curves of capillary wall shear stress against flow rate

The ram extrusion experiments described are a form of capillary rheometry. The analyses described here may be used to obtain plane strain (shearing) rheology parameters, although this is dependent on being able to construct physically realistic Mooney plots. At the very least some sort of relationship between the capillary wall shear stress and the

mean material velocity in the capillary can be drawn. However, the die land entry contributions (extensional) are not considered – these are the subject of the next Section.

2.4.2 Benbow-Bridgwater model

Many studies have found that paste materials often exhibit a substantial yield stress such that there is little bulk shearing of the material when flowing in a capillary, *i.e.* plug flow. In such cases we can use extrudate velocity, V, as a measure of volumetric flow rate. In these cases, capillary flow analysis can provide boundary properties of the material, but no information about the bulk yielding properties of the material. It has become common place to use the entry term, where bulk shearing is forced on the material, as a means of finding a material's bulk yield properties. Other approaches to shearing the material are available, and some are listed in Section 2.5. The capillary entry term is often preferred since it is directly relevant to other ram extrusion applications.

Benbow and Bridgwater (1993a) describe a simple model for the flow of pastes in a ram extruder as was shown in Figure 2.6. If the material is thought to behave as a perfect plastic in the bulk, the work done in the die entry region can be considered as identical to that for homogeneous compression.

In homogeneous compression, an element in the undeformed specimen, with sides parallel to the principal directions of stress and strain, retains a similar shape in the deformed state. In this case, all the energy supplied via the platens results in a change in the height of the specimen, and the work done is a minimum and is termed the *ideal work*. During extrusion, the deformation in the die entry region is not homogeneous, additional work goes into shearing material elements without causing a reduction in the overall diameter. The actual die entry pressure drop is greater than that predicted by this model.

Consider the element shown in Figure 2.11 overleaf, where an element of cross-sectional area A_0 and length l_0 is extended by applying a tensile stress to each end. Considering the material as a perfect plastic (described in Section 2.3.2), the tensile stress is the material's uniaxial yield stress, σ_Y, and is constant. If the element has a constant volume then,

$$A_0 l_0 = Al \tag{2.21}$$

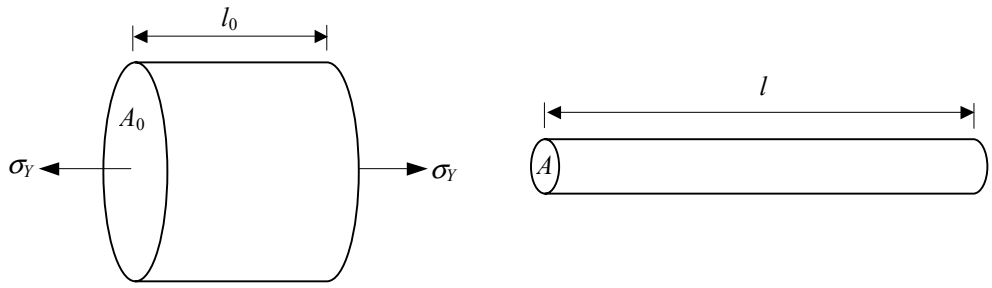

(a) Pre-deformation *(b) Post-deformation*

Figure 2.11 Ideal deformation of an element of material

Differentiating the constant volume expression gives,

$$l\mathrm{d}A + A\mathrm{d}l = 0 \tag{2.22}$$

or,

$$A\mathrm{d}l = -\frac{A_0 l_0 \mathrm{d}A}{A} \tag{2.23}$$

which can be used to find the work done over the extrusion from area A_0 to area A,

$$\int_{A_0}^{A} \sigma_Y A\mathrm{d}l = -\int_{A_0}^{A} \sigma_Y \frac{A_0 l_0}{\mathrm{A}} \mathrm{d}l = \sigma_Y A_0 l_0 \ln\left(\frac{A_0}{A}\right) \tag{2.24}$$

To extrude this whole element, the work done by the die entry extrusion pressure P_1 must be equal to $P_1 A_0 l_0$, thus equating the two amounts of work gives,

$$P_1 = \sigma_Y \ln\left(\frac{A_0}{A}\right) \tag{2.25}$$

which for the axisymmetrical geometry of Figure 2.6 gives the die entry pressure drop as,

$$P_1 = 2\sigma_Y \ln\left(\frac{D_0}{D}\right) \tag{2.26}$$

where D_0 is the barrel diameter, and D is the die land diameter. Oveston and Benbow (1968) and Benbow (1971) present experimental results for the extrusion of ceramic pastes through square and conical entry dies, and argue that the effect of geometry on the die entry pressure drop is consistent with equation (2.26).

It is often found experimentally that materials are not perfect plastics and that P_1 exhibits some rate dependence, and equation (2.26) was modified by Benbow and Bridgwater (1993a) as follows

$$P_1 = 2\left(\sigma_0 + \alpha V^m\right)\ln\left(\frac{D_0}{D}\right) \tag{2.27}$$

where V is the velocity of the paste in the die land, σ_0 is an initial yield stress, and α and m, are parameters characterizing the effect of velocity on the die entry. All three parameters

σ_0, α and m are regarded as material constants characterizing the material's resistance to change in cross-sectional area in the die entry, and are assumed to be independent of die geometry and extrusion rate. This key assumption is open to some doubt and is considered in more detail later in this Section.

Benbow and Bridgwater calculated the pressure drop over the die land, P_2, by considering a force balance and obtained the result equivalent to that presented in equation (2.20),

$$P_2 = 4\left(\tau_0 + \beta V^n\right)\frac{L}{D} \tag{2.28}$$

where they chose to model the wall boundary layer shear stress with the material constants τ_0, β and n. This analysis assumes that any transition effects are negligible.

Adding the pressure drops (2.27) and (2.28) together leads to the six-parameter model for the overall pressure drop, sometimes known as the Benbow-Bridgwater equation.

$$P = 2\left(\sigma_0 + aV^m\right)\ln\left(\frac{D_0}{D}\right) + 4\left(\tau_0 + \beta V^n\right)\frac{L}{D} \tag{2.29}$$

The Benbow-Bridgwater equation has provided a good first order model for axisymmetric extrusion and provides reasonable industrial design information, although the assumptions involved in the analysis make its precision low. The model is sometimes used to ascertain material constants for more general use. In this case the material constant σ_0 is often treated as being equal to the uniaxial yield stress of the material. Horrobin and Nedderman (1998) performed finite element analysis of axially symmetric extrusion of perfect plastics. Writing ξ for $ln(D_0/D)$ they found that the die entry pressure drop for the case of perfectly smooth walls can be well approximated by the following best fit parabola and straight line,

$$P_1 = 0.700\left(\sqrt{26.8\xi + 1} - 1\right)\sigma_Y$$

$$D_0/D < 2.5,\ \xi < 0.92 \tag{2.30}$$

$$P_1 = \left(1.92\xi + 1.08\right)\sigma_Y$$

$$D_0/D \geq 2.5,\ \xi \geq 0.92. \tag{2.31}$$

The straight line for large reductions has a slope that is slightly less than two, and thus approaches the ideal work line as the reduction increases. Hence for large diameter reductions with a barrel wall which approximates a perfectly smooth surface, the material constant σ_0 is an adequate (over-) estimation of the uniaxial yield stress σ_Y.

A critical assessment of the Benbow-Bridgwater model

As we discussed earlier, when the Benbow-Bridgwater model was first presented by Oveston and Benbow (1968) it was accepted to be an imperfect method of modelling flow. However, it successfully bridged the gap between difficult to obtain, but well defined, material parameters and easy to obtain and industrially relevant, but poorly defined, material parameters. Even if well defined material parameters are available, finding the extrusion pressure for a given set of conditions is a difficult problem (*e.g.* Horrobin (1999)). Parameters obtained by the Benbow-Bridgwater method can readily be used to find an extrusion pressure for a given set of conditions, although it may only be accurate for design purposes.

The Benbow-Bridgwater model is based around one particular type of extruder (axisymmetric, square entry), and this limits the general usefulness of the Benbow-Bridgwater material parameters. However, the Benbow-Bridgwater treatment of the yielding stress ($\sigma_0 + \alpha V^m$) rate dependence has been particularly seriously questioned – although this has not been picked up on by many researchers. Only twice has the deficiency been reported in the literature.

The first time was by Zheng *et al.* (1992) who were engaged in early numerical computer simulations of paste extrusion. Using a power law model for the bulk behaviour of the paste and a perfectly smooth (no wall friction) boundary condition they noticed that the extrusion pressure (P) was dependent on the ratio of extrudate velocity to die diameter (V/D) rather than just the extrudate velocity (V). However, they did not pursue a rigorous investigation of this.

Blackburn *et al.* (2000) also highlighted the problematic way in which rate dependence is dealt with in the Benbow-Bridgwater yielding stress term. In this expression the extrudate velocity term V is being used in some way to represent shear rate. However, this is dimensionally inconsistent; shear rate has dimensions $[\text{Time}]^{-1}$, whereas velocity has dimensions $[\text{Length}][\text{Time}]^{-1}$. Thus, in effect, a term representing the geometry of the extruder has been neglected. Simple analysis suggests that a suitable rate dependence might be based on the product of the extrudate velocity to die diameter ratio raised to some power ($(V/D)^x$, as suggested by Zheng *et al.*) and the barrel to die diameter ratio raised to some power $((D_0/D))^y$. Consequently, if a material is characterized on an

extruder of set dimensions, then it might be expected that those material parameters could only be used to predict material behaviour on extruders of similar dimensions.

It is surprising that this issue has not been considered further. It is not even commonplace, when characterizing a paste, to vary any of the extruder dimensions except the die length. Thus the validity of the characterization material parameters is not assessed over a range of dimensions. It is perhaps also surprising that on the few occasions where die diameter, or barrel diameter, have been varied over the set of characterization data the yield stress only appears to be a function of the extrudate velocity (*e.g.* Benbow *et al.* (1987)). To the author's knowledge, no clear reason for why this might be has been presented.

2.5 Other modelling and experimental approaches

2.5.1 Modelling approaches

The Benbow-Bridgwater model described previously in Section 2.4 is only one of a number of possible ways of modelling the flow in a axisymmetric square entry extruder. It is probably the most simple, although amongst the most approximate, which is probably why it has become used widely by researchers in this area. It was stated that this was the approach adopted for this project, and some justifications were given for this choice. However, some other principles will also be incorporated into our analysis in future Chapters. These are outlined in this Section as part of a general description of some other methods which have been used to model the flow of paste in an extruder.

For some material flow problems an exact solution for the flow pattern and stress distribution may be found, but this is not always possible or time-effective. Where the exact solution is not known, it is often possible to bound it by finding upper and lower bound solutions to the problem. These methods are presented by Hill (1951) and are not rigorously worked through here. Each of these approaches is discussed in turn, and finally Figure 2.15 is reproduced from Horrobin (1999) to compare some exact, upper, and lower bound solutions over a range of barrel-die diameter ratios.

Exact solutions

There are essentially two things which need to be known in order to have a complete solution to the problem; the velocity field, and the stress field. If we know these then both the velocity of the paste at every point in the system (velocity field) and the stress state of

the paste at every point in the system (stress field) will be known. If we know both of these fields, and they are compatible with each other, then it can be said that we have the exact solution to the problem.

We mentioned in Section 2.3.2 that for a perfect plastic under plane strain (that is, two-dimensional flow) exact solutions can be found analytically using slipline field theory. The exact solution for the axisymmetric problem cannot be found analytically, and recourse to numerical solutions through Finite Element Methods *etc*. has to be made. Horrobin (1999) made extensive developments to a commercial FEM code (ABAQUS, v. 5.5) to find exact solutions for the axisymmtric case with a variety of paste-barrel interface relationships. He made the interesting discovery that the extrusion pressure for plane strain extrusion is very close to that for axisymmetric extrusion when the area reduction ratios are the same. It is not known if this is a general result, or just restricted to the range of conditions he was using (a perfect plastic material extruded through perfectly smooth or perfectly rough square entry dies of up to 92 per cent area reduction).

To demonstrate the potential of this method we have reproduced results from Horrobin (1999); Figure 2.12 overleaf illustrates the effect of varying the flow rate when extruding a perfect plastic with a Navier boundary condition (the die land was perfectly smooth in all cases). The dimensionless piston velocity, V_0^+, is defined to be equal to unity when the wall shear stress of the paste in the barrel reaches the bulk shear yield stress of the material. Figure 2.13 illustrates some aspects of the total velocity and stress fields which have been calculated for a particular case. A scaled strain rate, $|\underline{\dot{\varepsilon}}|R/v'$, is used to highlight particular aspects of the pattern. We see in Figure 2.12 how the extrusion pressure rises from the perfectly smooth (no wall shear stress) to the perfectly rough (wall shear stress is equal to bulk yield stress of the material) values as the piston velocity is increased from 0 to 1. Figure 2.13 shows clearly the location of the high shear rate regions near the vicinity of the die entrance, and how the static zone for a partially rough barrel is smaller than for a perfectly rough barrel. Despite this progress, there are still no exact solutions available in the literature for rate dependent materials.

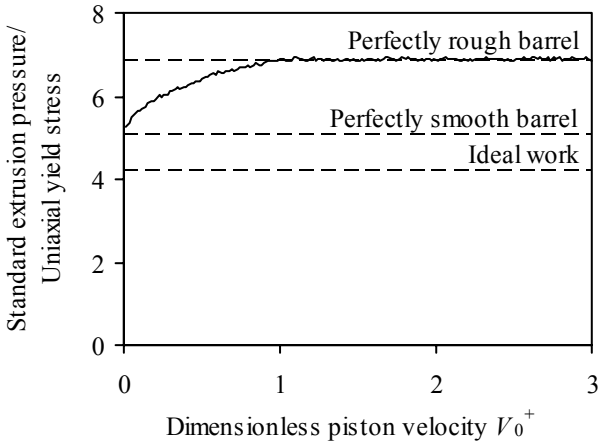

Figure 2.12 Exact solution extrusion pressure against piston velocity (Horrobin (1999))

Axisymmetric extrusion through a square entry die of 88% diameter reduction, for a perfect plastic with a Navier boundary condition.

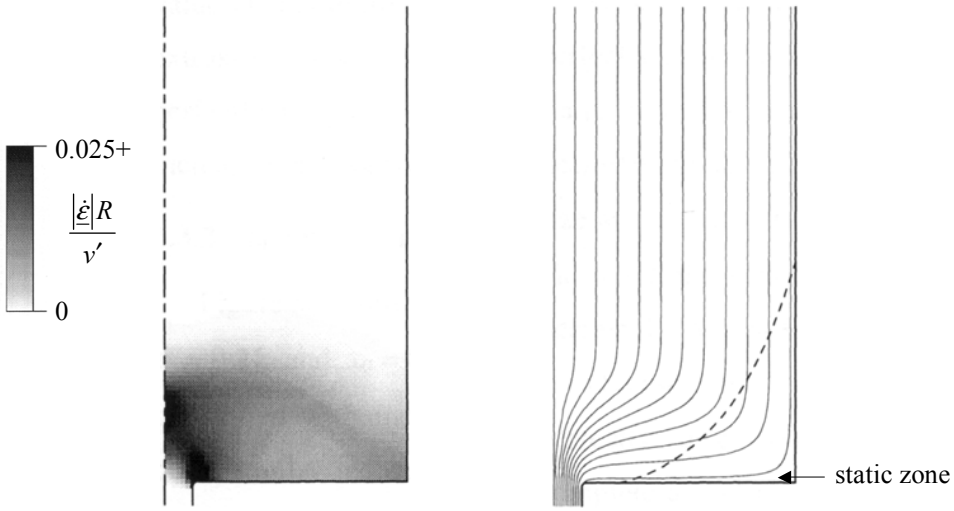

(a) Strain rate *(b) Streamlines*

Figure 2.13 Exact solution strain rate and streamline diagrams (Horrobin (1999))

Axisymmetric extrusion through a square entry die of 88% diameter reduction, for a perfect plastic with a Navier boundary condition and $V_0^+ = 0.1$.
- - - boundary of static zone for perfectly rough case

Upper bound solutions

An upper bound [to the rate of work by the forces over surface S_U] is to be obtained ... by means of any velocity distribution. (Hill (1951))

The exact solution will always be that which has the lowest work rate requirement. If the exact solution is unknown, we can find a value for which the work done by a force over a surface must be below (an upper bound) by selecting an assumed velocity field which satisfies the velocity boundary conditions of the problem. Unless we have

fortuitously picked the exact solution, the assumed velocity field will have a greater work rate than the exact solution.

Work may be done either within a deforming field, or at a velocity discontinuity. The rate at which work is done at a velocity discontinuity may be calculated simply as the product of the slip velocity and the shear stress. The rate at which work is done within a deforming field is more involved. A simple appreciation of how to calculate it is achieved by considering an element of dimensions δx, δy and δz subject to a normal stress σ_{xx} and velocity u at x and $u + \delta u$ at $x + \delta x$, as illustrated in Figure 2.14 below. The work done on the element (that is, on face EFGH) in unit time is $\sigma_{xx}\,\delta y \delta z(u + \delta u)$ and that done by the element (that is, by face ABCD) is $\sigma_{xx}\,\delta y \delta z u$. Thus the net rate of energy dissipation is $\sigma_{xx}\delta y \delta z \delta u$, and the rate of energy dissipation per unit volume $\underline{D}$ is,

$$\underline{D} = \sigma_{xx}\frac{\delta u_{xx}}{\delta x} = \sigma_{xx}\dot{\varepsilon}_{xx} \tag{2.32}$$

There will be similar terms for the ***y*** and ***z***-directions. Considering the same element being sheared in the ***x***-direction gives the dissipation per unit volume as $\tau_{xy}\dot{\gamma}_{xy}$, again with similar terms for the ***y*** and ***z***-directions. Summing all of these terms, the dissipation rate per unit volume can be written as,

$$\underline{D} = \sigma_{xx}\dot{\varepsilon}_{xx} + \sigma_{yy}\dot{\varepsilon}_{yy} + \sigma_{zz}\dot{\varepsilon}_{zz} + \tau_{xy}\frac{\dot{\gamma}_{xy}}{2} + \tau_{yx}\frac{\dot{\gamma}_{yx}}{2} + \tau_{yz}\frac{\dot{\gamma}_{yz}}{2} + \tau_{zy}\frac{\dot{\gamma}_{zy}}{2} + \tau_{xz}\frac{\dot{\gamma}_{xz}}{2} + \tau_{zx}\frac{\dot{\gamma}_{zx}}{2} \tag{2.33}$$

Similar expressions can be found for other co-ordinate systems.

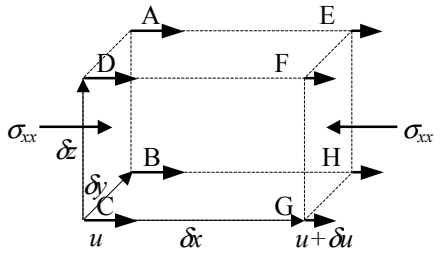

Figure 2.14 An element experiencing direct strain in one direction

Upper bound solutions to plane strain problems are straightforward to derive. Axisymmetric problems are more involved. Horrobin (1999) discusses in detail how various authors have developed assumed velocity fields for these problems and found an upper bound for perfect plastics. The author knows of no solutions in the literature for rate dependent materials. In any case, as we have already discussed in Section 2.3, finding the exact constitutive behaviour of a paste material is problematic, so the parameters

required to use the upper bound solution would not be available. For these reasons, upper bound solutions are not considered any further here.

Lower bound solutions

... a lower bound to the rate of work by the forces over [surface] S_U is to be obtained by selecting any equilibrium distribution of stress not violating the yield condition. (Hill (1951))

Any stress field can be selected which is in equilibrium and in accordance with prescribed boundary conditions – however, only one such stress field is compatible with flow. All stress fields with greater forces over a given surface than the exact solution (for example, the stress field associated with an upper bound assumed velocity field) would not be in mechanical equilibrium.

One lower bound solution to the axisymmetric extrusion of a perfect plastic was worked through in Section 2.4. This was the ideal case, where deformation was homogeneous and no smaller amount of work could have resulted in the material's change of shape.

Fewer lower bound solutions have been proposed for extrusion than upper bound solutions, due to the difficulty of constructing stress fields which satisfy both the equilibrium equations and the stress boundary conditions. One example is included in Figure 2.15 below. Once again, extending the stress field of a perfect plastic material to the rate dependent case would prove very difficult, and no attempts of this are known.

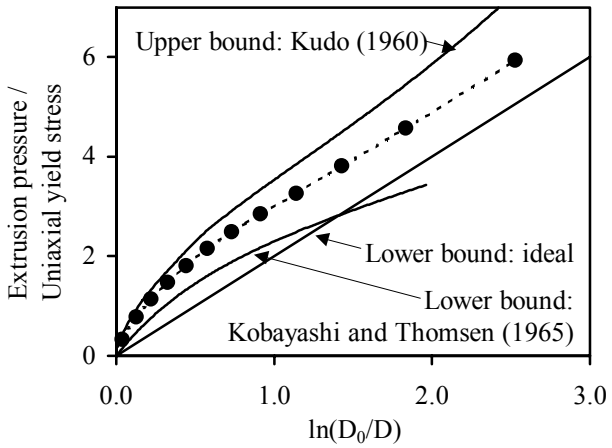

Figure 2.15 Extrusion pressure against natural logarithm of barrel-die diameter ratio (Horrobin (1999))

Axisymmetric extrusion of a perfect plastic through a perfectly smooth square entry die.
— boundary solution • exact solution

2.5.2 Experimental approaches

A small variety of techniques and materials has been used by the *Paste and Powder Processing Group*. Investigations have mainly been interested in ceramic pastes, but some other materials which have recently been studied include starch based food pastes (Cheyne *et al.* (2001)) and commercial washing detergent surfactant pastes (Liaw (2001)). Other experimental techniques which have been used include cone indentation tests (Benbow and Bridgwater (1987b)) and squeeze flow between parallel plates (Barnes (2001)). However, these tests have not yet successfully yielded material parameters which are of general use. Below we present summaries of the work of other research groups which have carried out more systematic investigations of paste flow using other materials and techniques.

Kalyon and co-workers

In 1989 the Highly Filled Materials Institute was established at Stevens Institute of Technology, New Jersey, to investigate both experimentally and theoretically the rheological behaviour, microstructure, processability and ultimate properties of highly filled materials, including suspensions and dispersions. Throughout this time Dilhan Kalyon has been the Institute's director and has published extensively in this field.

Much of the group's earliest work was experimental and concerned with a model material comprised of 60 per cent by volume solid ammonium sulphate particles in a matrix of Newtonian PBAN (*e.g.* Yilmazer and Kalyon (1989); Yilmazer and Kalyon (1991); and reviewed in Kalyon (1993)). In this work they made use of both capillary and parallel plate torsional techniques to investigate and model the behaviour of the material. Using the analysis of Mooney (1931) for the capillary flow data and Yoshimura and Prud'homme (1988) for the parallel plate flow data, slip velocities as a function of shear stress were obtained; the images reproduced from the parallel plate experiments show the effect of wall slip very clearly. The slip velocity – shear stress data from both approaches were consistent. The parallel plate approach was found to be more suitable for a lower range of shear stresses ($\tau_w < 6$ kPa) than the capillary flow approach ($\tau_w > 6$ kPa). The slip velocity – shear stress relationship was found to be linear, suggesting a Navier boundary condition, which might be considered consistent with the use of a Newtonian liquid-phase. Using these data they estimated the boundary layer thickness, which proved to be a small fraction of the mean particle size (about 5 to 15 per cent).

Other work by this group has included the study of simulant rocket fuels which contained 75.6 per cent by volume solids (Kalyon *et al.* (1993)), flow instabilities (Yaras et al (1994)) and viscous heating (Lawal and Kalyon (1997)).

Briscoe, Adams and co-workers

Brian Briscoe has been publishing papers on the behaviour of non-Newtonian materials for over twenty years, for much of that time in collaboration with Michael Adams from Unilever Research, Port Sunlight. They have formed the core of a research group based at Imperial College of Science, Technology and Medicine, London, which has published a considerable amount of theoretical and experimental work on the flow of soft solid materials.

One of the group's techniques has been the use of squeeze film rheometry, sometimes known as upsetting or parallel plate squeezing. In this method a flat sample of material is squeezed between two parallel plates moving towards each other. For over seventy years, this method has been widely used for assessing the rheological properties of materials which are too thick or which exhibit wall slip (from foods to metals), and thus are not suitable for traditional rheometers. However, the actual understanding of the flow has been poor, so it must be thought that the method was used in a more qualitative than quantitative way.

For the perfectly lubricated case of complete wall slip, it is straightforward to calculate the velocity and stress fields. However, the cases of no-slip or partial slip at the wall are more complicated. Covey and Stanmore summarised the understanding as it stood in 1981 (Covey and Stanmore (1981)). They reported that there was no satisfactory theory for the behaviour of material in the instrument, except for Newtonian and power law fluids. They proposed some methods for finding Bingham and Herschel-Bulkley material parameters from force – displacement – time data, but they did not provide a complete solution to the problem.

Since then the Imperial College group, amongst other researchers, have made considerable developments in understanding these flow patterns, thus making the squeeze flow technique more suitable for quantitative material characterization. Adams *et al.* (1994) improved the theory for the no-slip flow case, while Lawrence and Corfield (1998) seem to have improved it further. However, these methods are relatively complex and are expressed in tensor notation, which is probably not very accessible to the

many people who use squeeze flow equipment practically. The group has also extended the analysis to use FEM (*e.g.* Adams *et al.* (1997), (1998)).

Tied in with this work has been an interest in the wall – paste interface behaviour. The group has typically used a clay-oil based paste material for their experimental work, and this does not display the straightforward Navier boundary condition which Kalyon and co-workers reported. The work has predominantly used capillary flow techniques as in the papers by Adams *et al.* (1991) and Khan *et al.* (2001), although this work has not yet yielded any significant insight into the quantitative nature of complex boundaries. New work by Tuchinda *et al.* (2001) using infrared spectroscopy of the boundary layer promises to provide quantitative suspension concentration gradients in the boundary layer which would open up the possibility of a rigorous analysis.

2.6 Stress states

This Section is concerned with the practical reality of how the stress state of a paste material is best described. For each of the approaches outlined previously the stress state of the material is considered in different terms. For example, the microscopic modelling approach calculates the stress state of the interstitial fluid over the whole of its volume, as well as the interaction forces between all of the particles. When the material is considered as a single- or multi-phase continuum, the interstitial stress state and particle interaction forces are averaged to a greater or lesser extent. There has been little experimental consideration of paste stress states in the literature. For the cases of soil mechanics and granular materials, the stress states have been considered in much greater detail. The typical approaches for each of these are described briefly below, and then it is considered how practically these approaches might be extended to paste materials.

2.6.1 Soil mechanics

It was mentioned in Section 2.2.2 that one approach to modelling soils involves the use of a two-phase continuum. In practice the phases considered are a liquid-phase, characterized as having a pore pressure u, and a solid-phase, characterized as carrying an effective stress σ' (*e.g.* Atkinson (1993)). The total stress is the sum of the pore pressure and the effective stress. The stress state might then be illustrated by use of Mohr's circle.

A change in loading will give rise to a changed stress state. The nature of the change might depend on the freedom of the liquid-phase to flow, or the freedom of the solid-phase

to rearrange –time effects are also significant. Following an increase in total stress for a sample in which the liquid-phase is constrained, initially the pore pressure carries all of the additional stress, but over time this becomes redistributed over the solid matrix and is manifested as an increase in effective stress.

2.6.2 Granular materials

Granular materials are similarly described, except the interstitial fluid-phase (usually air) is considered to have negligible significance. Mohr's circles are used to analyse the stress state of the solid-phase, treated as a continuum. Despite the similarity in constitutive modelling, granular materials present alternative approaches to soil mechanics because of the importance of flow in granular material applications (*e.g.* Nedderman (1992)).

2.6.3 Pastes

The detail of stress state analysis achieved in soil mechanics and granular material flow has yet to be achieved for paste materials, although this is partly due to a lack of effort. One study in the Cambridge group by Stones (1999) attempted to measure the pore pressure of a paste material under different radial and axial loading conditions using conventional soil mechanics apparatus (a triaxial test cell). However, it was generally found that there was insufficient liquid-phase to create an unbroken path of liquid from the sample to the pressure transducer and reliable readings could not easily be obtained.

Where attempts have been made to compare the axial and radial stresses of a paste undergoing flow, for example in Amarasinghe (1998a), the values measured were very similar and the two could not be differentiated. Amarasinghe worked with alumina pastes and soap which had yield shear stresses of around 50 kPa but were flowing under stresses of 2 MPa, so perhaps it is not surprising that the radial and axial stresses could not be differentiated. Alternatively, the isotropic liquid-phase could have been carrying the greater part of the stress, thus tending to make the axial and radial stresses equal.

In conclusion, a rigorous description of the stress states within paste materials has proved elusive. Without such data, any detailed modelling of the stress state would be quite speculative. Thus, for the purposes of this project the precise stress state is not considered in any further detail. It is generally taken that the paste material can be approximated as isotropic, so that the radial and axial stresses are taken as being equal, as this greatly simplifies the flow modelling presented in later Chapters. However, it is noted

that this is an approximation dependent on the total stress being considerably greater than the material yield stress. Throughout this dissertation the terms stress and pressure are often used loosely, and sometimes interchangeably.

2.7 Summary

In this Chapter the range of conceptual and modelling approaches found in the literature has been summarised. It is clear that a single modelling approach has yet to be demonstrated as universally appropriate. The approximate model of Benbow-Bridgwater, based on the flow of a Herschel-Bulkley type material in a ram extruder, has been presented and critiqued. Despite the shortcomings of this approach, it is commonly used. In the absence of a more appropriate model, the Benbow-Bridgwater model has been employed as the central modelling technique in the Chapters which follow.

3 Characterization of materials

This Chapter is concerned with describing the general properties of the paste material used by the sponsoring company, and the specific properties of a model paste material which has been used throughout this project. In Section 3.1 a justification is given for the choice of materials used for the model paste. Our aim in characterizing this material is to obtain suitable parameters which describe how the model paste behaves when flowing, and to relate this to the individual properties of the model paste constituents. Section 3.2 describes some of the basic properties of the model paste constituents; in Section 3.3 we document how the constituents were combined to prepare the model paste. In later Chapters this knowledge is used to predict the flow of the model paste through some geometries which are of interest to us.

The investigation into the properties of the model paste are presented in Section 3.4 in three parts. Initially, we present in Section 3.4.1 some general investigations into density and compressibility. Section 3.4.2 details a capillary flow analysis and discusses the limitations of this method for paste flows. Finally, in Section 3.4.3, we present a Benbow-Bridgwater type analysis of the die entry pressure drops observed during the capillary flow experiments.

3.1 Model paste constituents

Two competing factors were balanced in the selection of materials. In order to maintain industrial significance, the materials studied had to be similar to those used in the industrial processes. However, the project was substantially experimental; thus the materials also had to be suitable for laboratory use. The sponsors supplied a material formulation and its constituents, which were deemed to satisfy these two demands.

The constituent types which make up an industrial paste were outlined in Chapter 1 as; active ingredients, solid bulk material, water, and special components which act as binders, rheology modifiers or dispersants. Most active ingredients are detrimental to human health and thus only used in experimental work when essential. Within the sponsoring company, it is thought that eliminating the active ingredients for experimental work on paste flow is an appropriate compromise, and this has been adopted in the work presented here. The sponsoring company has also identified a number of ingredients for a model paste, listed in Table 3.1 below, the inclusion of which would be key to producing a paste similar to that used industrially. The talc and harborlite constitute the solid-phases. The two surfactant constituents enter the water to form an aqueous solution (at the quantities used, it would be expected that the critical micelle concentration is exceeded). This solution binds the two solid constituents together to form the paste.

Rough and Saracevic (1997) evaluated the flow properties of a variety of different formulations based on these constituents. All of the paste formulations were found to be shear-thinning and yield dominated. The studies concluded that including harborlite as a constituent gave a paste which required excessively large forces for extrusion and caused significant amounts of attrition. Consequently it was decided necessary to exclude harborlite as a constituent for our model paste. The pastes used in the industrial processes of the sponsor are not degassed or prepared under a vacuum. This practice was followed in the experimental work for the sake of relevance and simplicity, although this did leave an uncertainty as to the degree and nature of air entrainment in the paste. The formulation used for the model paste is given in Table 3.2 overleaf.

Table 3.1 Key constituents for a model paste

Constituent	Description	Function
Micro-Talc AT Extra	Magnesium silicate	Soft bulk material – easily dispersible
Harborlite S200Z	Milled perlite - siliceous volcanic glass	Hard bulk material – easily dispersible
Morwet EFW	Anionic surfactant – formulation trade secret	Binder/rheology modifier/dispersant
Morwet D425	Surfactant – sodium naphthalene sulphonate-formaldehyde condensate	Binder/rheology modifier/dispersant
Water	Reverse osmosis water	Solvent/liquid-phase

Table 3.2 Model paste formulation

Constituent	Fraction (wt.)	Source
Micro-Talc AT Extra	0.708	Norwegian Talc (U.K.) Ltd.
Morwet EFW	0.0833	Petrochemicals Company Ltd., Ft. Worth, Texas, USA
Morwet D425	0.0417	Witco Corporation, Houston, Texas, USA
Reverse osmosis water	0.167	Elgastat Prima 4, Elga Ltd., High Wycombe, U.K.

3.2 Constituent properties

3.2.1 Micro-Talc AT Extra

A scanning electron microscope (SEM) image of a sample of the talc used is shown in Figure 3.1. The talc particles are soft platelets and this is evident in the image as we can see the particles to be flat and thin with worn edges. These properties make talc a well known lubricant. It has been difficult to obtain useful particle size distributions for platelets since all available methods contain some uncertainty. A particle size distribution obtained by laser diffraction is presented in Figure 3.2 and the available manufacturer's data are presented in Table 3.3. The 'diameter' parameter returned by laser diffraction is related to some average linear profile measurement of a particle cluster flowing through the laser. The flow past the laser is expected to be turbulent, thus the aspect of a particle presented to the sensor would be random. The manufacturers (Beckman Coulter, Inc.) suggested that under these circumstances, the particle size distribution returned by the sensor would be Gaussian. The measured distribution has some similarities to a Gaussian curve, with a peak at approximately 8 microns. The talc manufacturer's data suggests that the mean particle size is less than one micron, but given the subsequent size distribution curve one might suppose that the manufacturer's size may include thickness and so does not clearly relate to either the thickness, or diameter of the platelets. The SEM image seems to agree with this; the widths of the platelets are around 8 microns and the thickness of the platelets is well below one micron. Thus we shall not consider this material as being in the colloid range where particle diameters are typically less than one micron (*e.g.* Hamley (2000a)). Platelets of 8 microns diameter with the specific surface and density given in Table 3.3 would have a thickness of approximately 0.05 microns, which is plausible.

A very high voidage is possible when platelets are randomly orientated and not compacted, resulting in the order of magnitude difference between the actual particle

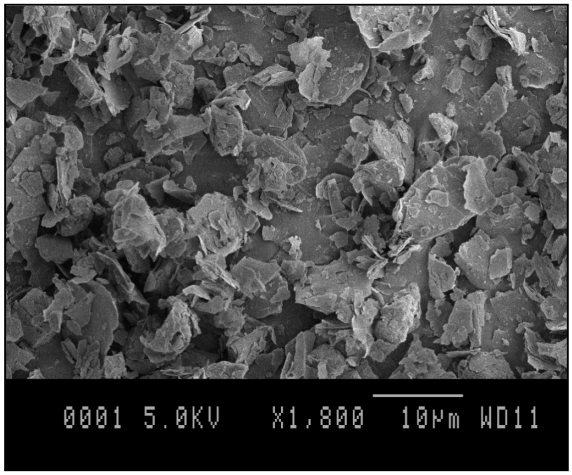

Figure 3.1 SEM image of Micro-Talc AT Extra

Acquired with JSM-820, JEOL (UK) Ltd., U.K.

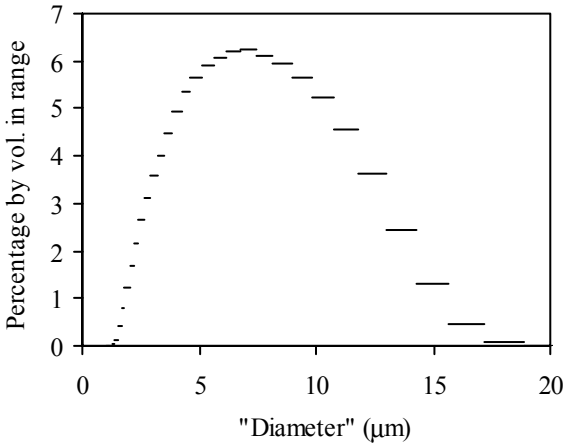

Figure 3.2 Laser diffraction particle size distribution for Micro-Talc AT Extra

Acquired with LS 200, Beckman Coulter, Inc., U.S.A.

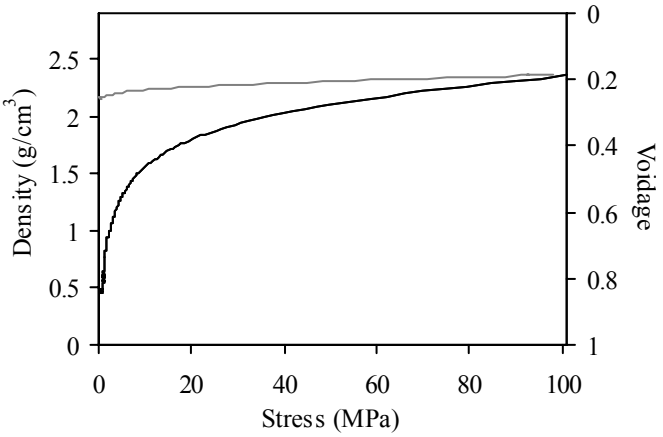

Figure 3.3 Density and voidage of Micro-Talc AT Extra against compaction stress

compaction curve *relaxation curve*

Table 3.3 Manufacturer's data on Micro-Talc AT Extra

Mean particle size, μm	0.85
Specific surface, N_2-ads., m^2/g	7.70
Density, g/cm^3	2.90
Tamped apparent density, g/cm^3	0.34

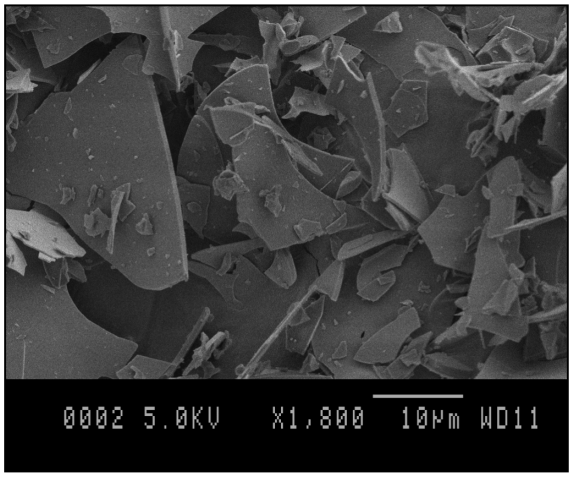

Figure 3.4 SEM image of Harborlite S200Z

Acquired with JSM-820, JEOL(UK)Ltd, U.K.

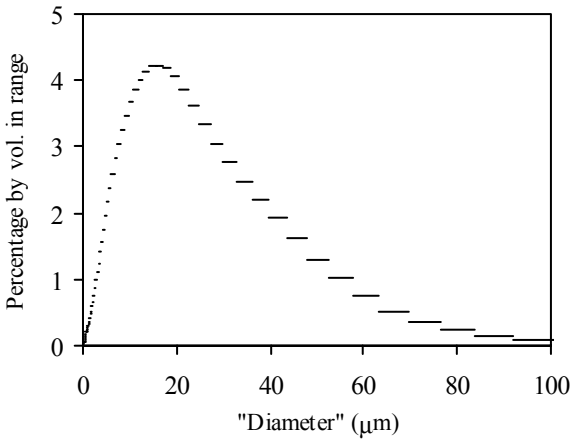

Figure 3.5 Laser diffraction particle size distribution for Harborlite S200Z

Acquired with LS 230, Beckman Coulter, Inc., U.S.A.

density and the tamped apparent density. A compaction experiment, using the apparatus described in Section 2.4, was conducted in order to study the variation in the dry material voidage with compaction stress. A sample of talc powder with a weighed mass of 22.71 g (± 0.01 g) was poured into a blanked barrel of 25.1 mm diameter, ~ 200 mm length and ~ 12 mm wall thickness. The piston was lowered into the barrel with care being taken to record the distance from the blanked end of the barrel to the piston. The piston was lowered to compact the sample at a velocity of 0.5 mm/s until the force on the piston had reached its safe maximum limit of 50 kN, corresponding to a mean axial stress on the piston of ~ 100 MPa. The piston was then raised at a velocity of 0.1 mm/s until the sample had fully relaxed. The force on the piston and the piston position were recorded throughout the experiment allowing the compaction and relaxation density to be plotted against the mean axial stress on the top surface of the sample. The voidage of the sample can be calculated using the talc particle density from Table 3.1. These voidages are shown in Figure 3.3 where we see that the density of the sample increases from below 0.5 g/cm^3 to above 2 g/cm^3; the limiting density is not yet reached. On relaxing the sample a small elastic response is apparent, but by far the majority of the compaction is irreversible; either due to particle rearrangement or breakage.

3.2.2 Harborlite S200Z

Some details of harborlite are discussed as it is an important constituent of the industrial paste, although it is not used in the model paste. A SEM image of the harborlite used is shown in Figure 3.4. Like the talc, the harborlite particles appear to be platelets, but have much sharper edges. Harborlite is a volcanic glass and is much harder than talc, thus the edges of the particles do not wear as easily. It is this hard and sharp edged nature of harborlite which made it problematic for repeated experimental use. The SEM image and the laser diffraction particle size distribution, presented in Figure 3.5, both show the platelets to be larger than the talc. The typical width is approximately 20 microns, but is distributed up to 100 microns. The manufacturer gives the density of harborlite as 2.3 g/cm^3.

3.2.3 Aqueous Morwet solution

Triplicate weighed samples of both Morwet powders were dried under a partial vacuum at 110 °C for a period of approximately three hours, until the weighed mass became constant. From this data the absorbed water mass fractions of Morwet EFW and

Morwet D425 were calculated as 0.097 and 0.059 respectively (calculated on a wet basis). These represent a significant fraction; where solution concentrations have been calculated the water absorbed in the powders has been included. Similar results for the talc powder indicated an absorbed water mass fraction of only a fraction of a per cent, which has been treated as negligible.

Both Morwet constituents are surface active agents (surfactants). In an aqueous solution, the Morwet molecules have an affinity for interfaces between the solution and other materials. Thus they will be adsorbed onto the interface and change its properties. Many surfactants lower the surface tension of a solution, enabling it to wet surfaces more easily. Hence they are often used in laundry detergents where good wetting of the fibres is essential. Surfactant molecules can exist separately from each other in solution, but above a critical concentration (the critical micelle concentration, CMC) they combine to form spherical colloidal groups of molecules (micelles); At higher concentrations further aggregate structures can form (for an introductory text, see Hamley (2000b)). A solution with the composition given in Table 3.2, at over 40 weight per cent surfactant, would be expected to be well above the CMC and the structure of the colloidal suspension will be complex. The precise mechanisms in which the Morwet constituents aid the production and properties of the water dispersible granule product are not known.

Simple investigations into the physical properties of aqueous Morwet solutions prepared with the Morwet EFW to D425 ratio given in Table 3.2 have been conducted from zero concentration to a Morwet powder mass fraction of 0.5, slightly higher than that used in the model paste formulation. Above this concentration solutions could not be successfully prepared. A concentric cylinder viscometer (LVDV–II +, Brookfield Engineering Laboratories, Inc., Stougton, MA, USA) was used with a low viscosity adapter to measure solution viscosities over the available range of shear rates at room temperature (recorded as 20.5 °C). An electronic balance and measuring cylinder were used to calculate the solution density. Viscosity measurements for a 0.275 mass fraction solution in water over the available range of shear rates are presented in Figure 3.6 *(a)*. The solution does not exhibit any significant shear rate dependence over the shear rate range considered, so it may be described as a Newtonian fluid, and hence a mean viscosity can be calculated. The volume against mass measurements for the same solution are presented in *(b)*, where the gradient found by linear regression is equal to the solution density.

We show in Figure 3.6 *(c)* that the solution viscosity increases rapidly with solution concentration for a Morwet mass fraction greater than 0.3. The Mowet mass fraction used in the model paste is 0.392; the viscosity at this value is 13.4 cP, but clearly the viscosity of the model paste liquid-phase is sensitive to the exact Morwet concentration. The variation of solution density with concentration, shown in *(d)*, appears to be linear – although no physical reason why this should be so is known to the author. The density at the Morwet mass fraction used in the model paste is 1160 kg/m^3.

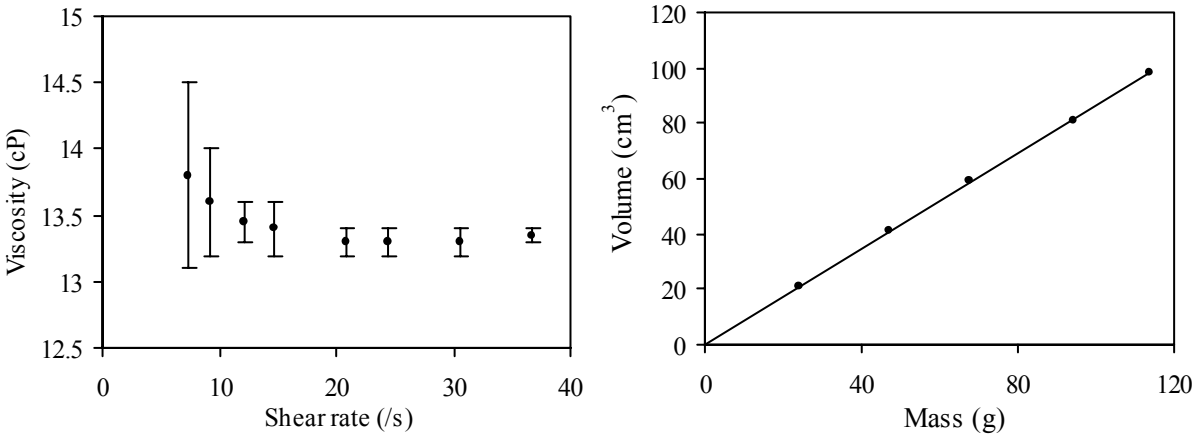

(a) Viscosity against shear rate
0.392 mass fraction Morwet solution.

(b) Volume against mass
0.392 mass fraction Morwet solution.
— least squares fit through origin

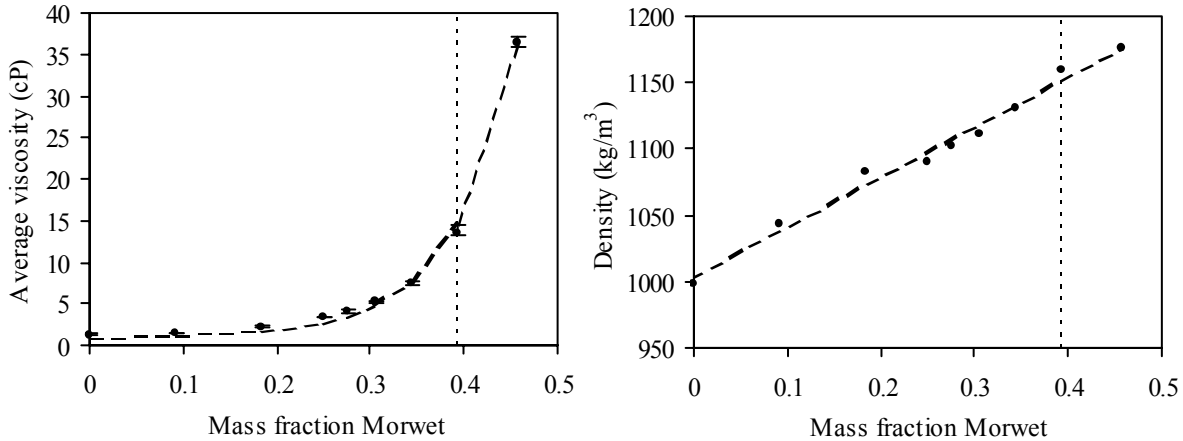

(c) Viscosity against concentration
– – fitted line, $\mu = 1 + 0.0412e^{14.7x}$

(d) Density against concentration
– – fitted line, $\rho = 1000 + 378x$

Figure 3.6 Morwet solution properties

3.3 Preparation of model paste

The model talc paste was prepared in batches ranging from 1.40 to 3.86 kg following the procedure outlined by Rough and Saracevic (1997). Materials were weighed out in appropriate amounts on an electronic balance (LC 62105 or BA 6100 Sartorius balance,

Sartorius Ltd., Edgewood, New York, USA). The dry talc and Morwet constituents were mixed in a planetary mixer (AE 200, Hobart Manufacturing Company Ltd., London, UK) for thirty minutes on speed setting one, stirring manually with a spatula every five minutes to displace any static zones. Over the period between the fifteenth and twentieth minute the water was gradually poured into the dry mix. The resulting wet powder was then twice pugged through the mixer's mincer attachment at speed setting two.

In the first fifteen minutes of mixing the materials were blended together and any large agglomerates were broken up. The second fifteen minutes allowed the water to be mixed in with the dry particles. As the water was distributed, it formed a solution with the Morwet and wetted the surface of the talc particles. The pugging operation acted as high shear local mixing, breaking down small agglomerates and compacting the powder into soft cylindrical pellets of length ~ 10 mm and diameter ~ 4 mm. The final paste was left to relax in a hermetically sealed polythene bag for at least two hours before use. Paste was always used on the same, or following, day as it was produced.

3.4 Model paste properties

First we describe the general character of the model paste material. A rigorous rheological characterization is then presented in two forms. A capillary flow analysis is presented in Section 3.4.2; from this study it was established that the paste is best understood as flowing through the capillary as a plug. Consequently only the interfacial slip could be characterized with these data. A Benbow-Bridgwater die entry pressure drop analysis is presented in Section 3.4.3 which provides a characterization of the bulk deformation of the model paste.

The material in a twin-screw radial screen extruder experiences a wide range of shear rates and deformation modes. It was essential that the scope of the characterization covered this range. Operational data are presented in Appendix A. In summary; the paste velocity will vary from approximately 0.002 m/s to 0.3 m/s and the ratio of outlet to inlet areas of deformation zones are typically between 2 and 5. The length to diameter ratio of a screen hole is approximately 1.

3.4.1 General properties

After the mixing operation the paste material had the consistency of a damp powder. A dramatic change in its consistency was apparent after the pugging operation. The model

paste then had a solid appearance and soft texture which was readily deformable by hand, although somewhat crumbly. An image of the model paste granules after pugging is shown in Figure 3.7.

The expected mass fraction of water in the paste, including the absorbed water in the Morwet, was calculated at 0.178 using the data from Table 3.2 and Section 3.2.1. The actual water content of triplicate samples from seven separate batches of paste made over the course of two months was found by drying samples under a partial vacuum at 60 °C until the mass was constant. These values ranged from 0.173 to 0.178, with a mean of 0.176. It may be the case that a little drying of the material occurred during preparation, but it seems reasonable to assume that the actual composition of the paste was within one or two per cent of the intended composition – although the sensitivity of the aqueous Morwet solution viscosity to concentration seen in Figure 3.6 *(c)* may still have made this variation significant.

The density of the model paste with no air entrainment can be predicted to be 2.02 g/cm^3 from the talc particle density given in Table 3.3 and the aqueous Morwet solution density from Section 3.2.1. Again with no air entrainment, the liquid-phase volume fraction is expected to be 0.507. This value is noticeably larger than the void fractions of regularly packed spheres (range 0.26 to 0.48) and values reported for pastes containing near-spherical particles (near 0.40), as was discussed in Section 1.3.1. However, unless well organised, the platelet nature of the talc particles will result in higher voidages than found with smooth, near-spherical particles.

A compaction experiment similar to that described for talc in Section 3.2.1 was conducted on a sample of the model paste. The compaction curves presented in Figure 3.8 show that the measured density and voidage of the paste appear to approach those values predicted above. No liquid-phase was observed to escape during the compaction, so it seems fair to assume that the increase in density was due to compression and expulsion of air entrained in the sample. The high liquid-phase volume fraction means that once the majority of the entrained air has been expelled, and after a little rearrangement of the talc particles, the voids in the paste are likely to be saturated. Thus less particle deformation and breakage will occur as stress is being transmitted in the liquid-phase rather than the solid matrix. The compaction behaviour evident with the talc powder in Figure 3.3, where compaction was still being observed at stresses up to 100 MPa, is not occurring here. Above a compressive stress of 5 MPa the model paste can reasonably be assumed to be

incompressible. A little elasticity of the sample is apparent; this may be due to compression of entrained air or particle elasticity. The bulk of the compression was irreversible, with the relaxed post-compression sample having a density of 1.9 g/cm^3. At these high liquid fractions, the treatment of the paste as a 'pseudo-fluid', as was proposed in Section 2.6.3, becomes more valid unless liquid-phase migration becomes a significant issue.

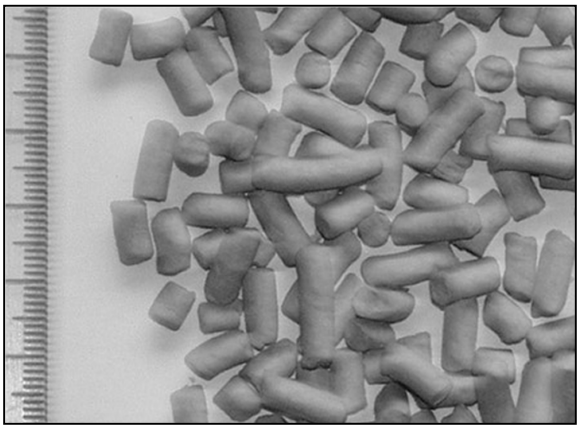

Figure 3.7 Granules of model paste after pugging

Scale gradations in mm.

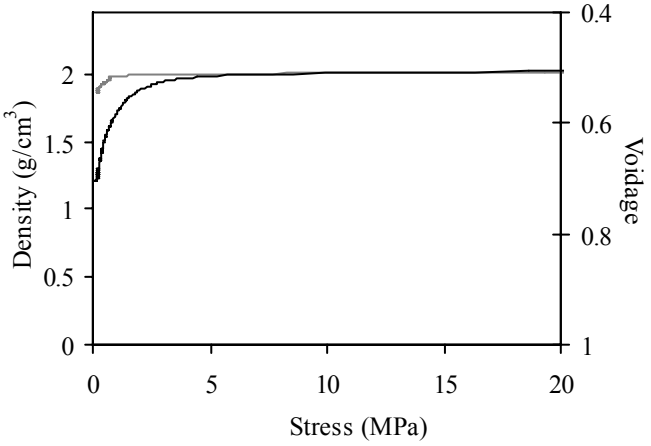

Figure 3.8 Density and voidage of model paste against compaction stress

Phase migration and dilation

The following Sections present a rheological characterization of the model paste which assumes that a single constitutive equation can be used to describe the bulk material. However, in practice, as a paste flows its structure will change. Two effects are often of particular importance; a pressure gradient in the paste may cause the liquid-phase to migrate, and a compacted material forced to flow will dilate as particles rearrange to move over one another. This project has not sought to develop a complete description of the microstructural changes of the flowing model paste, but a sample extrusion run was conducted to gain an impression of how significant these effects might be.

To maximise any phase migration a long die was chosen to increase the extrusion pressure, and a low piston velocity was chosen to allow the liquid-phase more time to migrate (*e.g.* Rough *et al.* (2000)). The barrel was loaded with 135 g of paste crumble and precompacted to 5 kN, which after a 100 mm extrusion run left a 50-60 mm plug of paste in the barrel. Samples of extrudate were collected over the course of the extrusion run and analysed for density (volume calculated by assuming diameter equal to die diameter and measuring the extrudate length; mass found by weighing on an electronic

balance) and water content (found by measuring mass loss after drying under a partial vacuum at 60°C until no further mass change was observed). Once the extrusion run was complete, the remaining plug of paste in the barrel was removed and sliced into 10 mm thick sections. These were also analysed for density and water content using the same methods. The results are presented in Figure 3.9.

We see in Figure 3.9 *(a)* overleaf that the extrusion pressure remains largely constant over the course of the extrusion run at approximately 7 MPa, albeit with quite significant fluctuations, which suggests that any physical change in the paste in the barrel over the course of the run was not significant enough to alter the extrusion pressure. This is consistent with the extrudate properties shown in Figure 3.9 *(b)* and *(d)*, where the density and water content do not appear to vary significantly over the course of the extrusion run. However, it is apparent that both dilatancy and liquid-phase migration have occurred through the course of the run.

We saw in Figure 3.8 that for a simple compaction experiment the paste was fully compacted once the axial stress on the piston had exceeded 5 MPa. Also, the measured density corresponded well with the calculated density for no air entrainment based on the constituent properties, and once the sample was relaxed the density decreased to 1.9 g/cm^3. In the present case the extrusion pressure is around 7 MPa (Figure 3.9 *(a)*), yet the measured density of the relaxed extrudate is below this value (Figure 3.9 *(b)*), suggesting that dilatancy may have occurred as the paste was sheared during extrusion. However, the density of the relaxed barrel plug is also below the expected value, as seen in Figure 3.9 *(c)*, which was not expected since most of the paste in the barrel flows as a plug without shearing. The reason for this discrepancy is not clear. Dilatancy would create pressure gradients within the liquid- and gaseous-phases, and consequently liquid-phase migration might also have been occurring.

Whereas air can be drawn into the system from the atmosphere, water cannot and so the total water content of the extrudate and barrel plug should to be equal to the original amount. This can be seen to be approximately true in Figure 3.9 *(d)* and *(e)* where we see that the water content of the extrudate is consistently greater than expected, and the water content of the barrel plug is lower. Dilation of material in the deformation zone would cause a pressure gradient drawing in liquid-phase from the surrounding region, which might account for the decrease in water content in the barrel plug towards the die face. This drier material is likely to be more resistant to flow, and may contribute towards

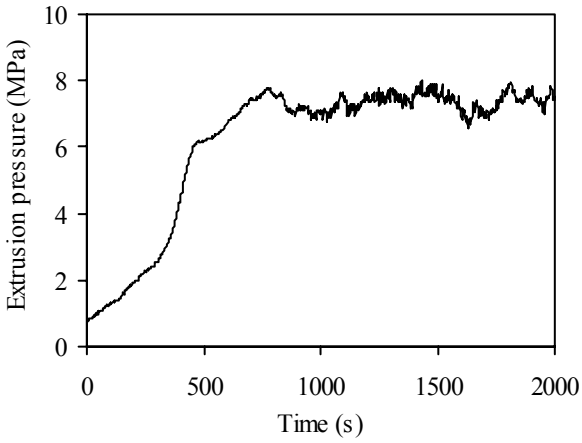

(a) Extrusion pressure against time

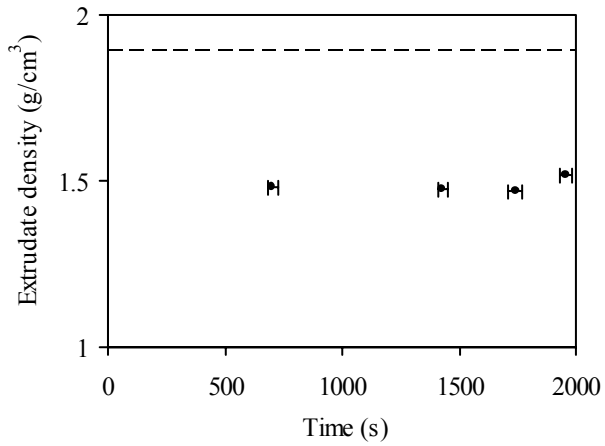

(b) Relaxed extrudate density against time

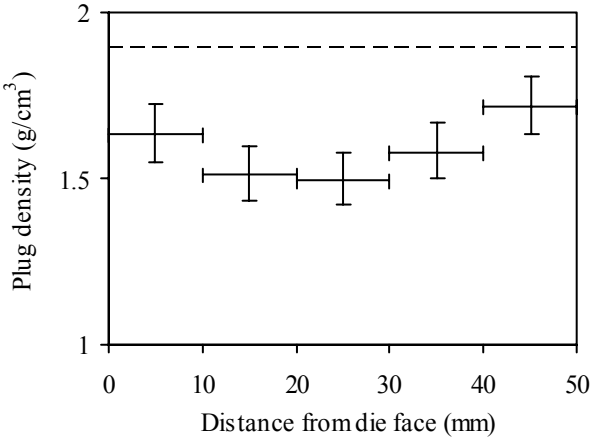

(c) Relaxed barrel plug density against position

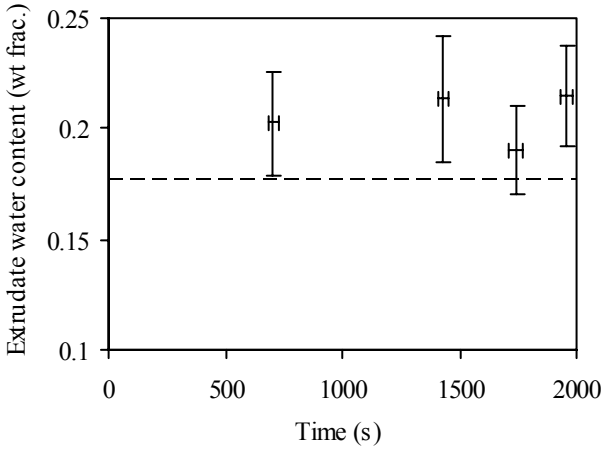

(d) Extrudate water content against time

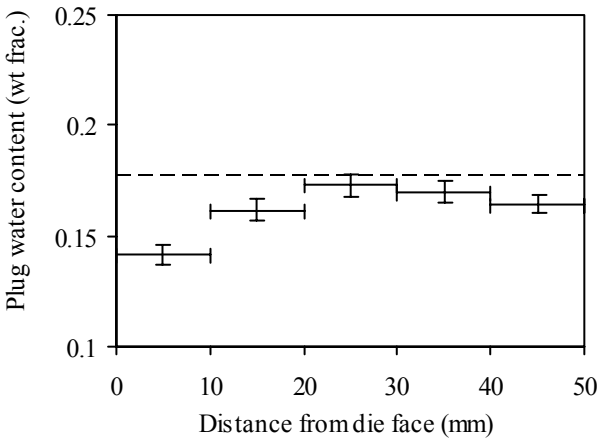

(e) Barrel plug water content against position

Figure 3.9 Density and water content variation over a sample ram extrusion run

Error bars bound regions of possible values.
D = 3 mm, L/D = 16, Piston velocity = 0.05 mm/s.
−− expected values based on paste composition

the development of the static zone around the die entry region noted in Section 2.4. The trends observed in this experiment match those observed by Rough *et al.* (2000) who studied liquid-phase migration in microcrystalline cellulose pastes much more extensively.

We have shown that liquid-phase migration and dilatancy occur at significant levels during the extrusion of the model paste. However, to incorporate these effects into any rheological characterization would pose considerable problems, and significantly add to the complexity of the model. The extrusion pressure and extrudate properties remained constant throughout the extrusion run – thus the run can still be thought of as steady state flow. If the plug of paste left in the barrel had not been so long then the effect of phase migration might have been more pronounced, and the extrudate may have become drier during through the run. In such a case the extrusion pressure might be expected to increase correspondingly, since the drier paste would be more difficult to extrude (as was experienced by Bayfield (1997) when extruding icing sugar pastes). These effects are not considered further here, with the hope that they will not excessively limit the applicability of our material flow models.

3.4.2 Capillary flow analysis

Flow through a capillary is one of the simplest arrangements which can be investigated, and can yield basic information from which more complex flows can be understood. The capillary flow analysis method presented in Section 2.4.1 was followed.

Experimental method

Sixty experimental runs as detailed in Table 3.4 were carried out in triplicate using the equipment outline detailed in Section 2.4. A single barrel of diameter 25.1 mm was used for all runs. To obtain useful capillary flow data it was necessary for the capillary length to diameter ratio to be sufficiently large for flow in the capillary to become fully developed and entry and exit effects to become negligible. In most cases capillary flow analysis requires small diameters to ensure laminar flows, but the high apparent viscosity of paste makes this requirement redundant. For reasons of practicality sufficiently high length to diameter ratios could only be achieved for capillary diameters of 3 mm or less. Three such diameters were used, being 1 mm, 2 mm and 3 mm. Larger diameters than these (8 mm, 15 mm and 20 mm) were used to provide die entry pressure drop data in the area reduction ratio range of 2-5 as required (see Section 1.2.1). The capillary flow data for these results are presented, but not commented upon. Flow rates covering a mean

extrudate velocity from 1.17 to 490 mm/s were studied, which covered the range of material velocities anticipated in the industrial extruder (see Section 1.2.1). The maximum mean extrudate velocities for the three largest capillary diameters were limited by machine constraints.

Usually a number of piston velocities were used during the course of a run. This practice allowed the number of mean extrudate velocities studied to be increased without making the number of runs required unmanageable. The quality of extrusion pressure data is compromised by this practice since the flow pattern and material changes occurring under one velocity may affect the flow pattern developed under the next, and enough time must be allowed for steady state conditions to occur at each velocity. It was thought that the sequences used were satisfactory (for example, see the text by Benbow and Bridgwater (1993b), who developed many of these techniques). Using the fastest velocity first subjected all of the paste in the barrel to the same maximum pressure, and thus kept the paste history as similar as possible for each velocity. Where possible, this velocity was then repeated at the end of the sequence. For all seventy five of the runs where this was done, the extrusion pressure for the final velocity was on average 8.4 per cent less than for the first velocity. The combined effects of friction between the paste and the barrel surface (causing a pressure decrease from start to finish, as was discussed in Section 2.4) and liquid-phase migration (causing a pressure increase from start to finish, as was discussed in the last Section) may have been responsible for much of this net pressure drop.

For each extrusion run a 140 g load of paste granules was weighed out and manually compacted into the barrel with a blank die at its end. The piston was then used to precompact the material with a force of 5 kN (a mean axial stress of 10 MPa) applied for five to ten seconds which was thought to be sufficient to expel any entrained air. A plug of compacted paste approximately 140 mm in length was left in the barrel. The blank die was then replaced with the appropriate characterization die. The piston was lowered to make contact with the paste plug with a force of 0.5 kN and the characterization run commenced.

Results

The extrusion pressure-time profiles such as those shown in Figure 3.10 show noticeable transients when the piston velocity is changed, presumably due to a combination of machine adjustment, elastic effects and changes in flow pattern. These transients are more significant for the runs with smaller area reduction, such as those shown in Figure 3.10 *(b)*. Presumably this is because the ratio of the volume of paste in the barrel and the volume of paste in the die land decreases as the area reduction is decreased for a constant barrel diameter. Thus the effective duration of the experiments is shortened, and the transients become more dominant. A steady state is reached so long as the extrusion period is sufficiently long, and the mean value of extrusion pressure in these steady regions is used for the analysis.

A total of forty five Bagley plots were constructed in order to find the wall shear stresses and die entry pressures for each of the six capillary diameters using all of the piston velocities (flow rates) used. Two sample plots are presented in Figure 3.11, which correspond to the lowest flow rates of Figure 3.10. Both plots appear to show a linear relationship between the extrusion pressure and L/D ratio which suggests that the wall shear stress is not a function of the normal stress on the wall (*i.e.*, not a Coulombic boundary condition) as was expected from Section 2.4.

It is clear that the reproducibility between independent runs is poor, with factors of up to 1.5 separating the data for the D = 15 mm case. This problem is most apparent with the larger capillaries, where the capillary diameter is approaching the barrel diameter. Longer periods for each piston velocity are required for steady state to be reached with these diameters. The compromise between the quality of the extrusion pressure data and the number of piston velocities may have been weighted too far towards maximising the number of piston velocities.

Table 3.4 Capillary analysis die geometries and flow rates

D_0, mm	D, mm (A_0/A)	L, mm (L/D)	{V_p sequence, mm/s: run 1}, { V_p sequence, mm/s: run 2}, … {Q sequence, mm^3/s: run 1}, { Q sequence, mm^3/s: run 2}, … {V sequence, mm/s: run 1}, { V sequence, mm/s: run 2}, …
25.1	1 (630)	2 (2)	{0.777, 0.389, 0.111, 0.0556, 0.0370, 0.0186, 0.00926, 0.00370, 0.00186, 0.777} {384, 192, 54.9, 28.0, 18.3, 9.20, 4.58, 1.83, 0.920, 384} {490, 245, 69.9, 35.0, 23.3, 11.7, 5.83, 2.33, 1.17, 490}
		4 (4)	
		8 (8)	
		12 (12)	
		16 (16)	
	2 (158)	2 (2)	{3.11, 1.56}, {0.370, 0.296, 0.222, 0.148, 0.0742, 0.037, 0.0148, 0.00742, 0.370} {1540, 772}, {183, 146, 110, 73.2, 36.7, 18.3, 7.32, 3.67, 183} {490, 246}, {58.3, 46.6, 35.0, 23.3, 11.7, 5.83, 2.33, 1.17, 58.3}
		4 (4)	
		8 (8)	
		12 (12)	
		16 (16)	
	3 (70.0)	6 (2)	{7}, {3.5}, {0.833, 0.667, 0.500, 0.333, 0.167, 0.0833, 0.0333, 0.0167, 0.833} {3460}, {1730}, {412, 330, 247, 165, 82.6, 41.2, 16.5, 8.26, 412} {490}, {245}, {58.3, 46.7, 35.0, 23.3, 11.7, 5.83, 2.33, 1.17, 58.3}
		12 (4)	
		24 (8)	
		36 (12)	
		48 (16)	
	8 (9.84)	6 (0.75)	{7, 3.5}, {2.3, 1.2, 0.6, 0.24, 0.119, 2.3} {3460, 1730}, {1140, 594, 297, 119, 58.9, 1140} {68.9, 34.5}, {22.6, 11.8, 5.91, 2.36, 1.17, 22.6}
		16 (1.5)	
		24 (3)	
		36 (4.5)	
		48 (6)	
	15 (2.80)	6 (0.4)	{7, 4}, {2, 0.83, 0.42, 2} {3460, 1980}, {990, 411, 208, 990} {19.6, 11.2}, {5.60, 2.32, 1.18, 5.60}
		16 (0.8)	
		24 (1.6)	
		36 (2.4)	
		48 (3.2)	
	20 (1.58)	6 (0.3)	{7, 1.5}, {3.7, 0.74} {3460, 742}, {1830, 366} {11.0, 2.36}, {5.83, 1.17}
		16 (0.6)	
		24 (1.2)	
		36 (1.8)	
		48 (2.4)	

Notes:

- D_0 *barrel diameter, ± 0.02 mm*
- D *die land (capillary) diameter, ± 0.02 mm*
- A_0 *cross-sectional area of barrel (cross-sectional area of deformation zone inlet)*
- A *cross-sectional area of die land (capillary) (cross-section area of deformation zone outlet)*
- A_0/A *ratio of inlet to outlet deformation zone cross-sectional area*
- L *die land (capillary) length, ± 0.02 mm*
- L/D *ratio of die land (capillary) length to diameter*
- V_p *piston velocity, error increased from 0.01 % at the highest velocities to 1 % at the lowest*
- Q *flow rate, assuming material is incompressible*
- V *mean extrudate velocity, assuming material is incompressible*

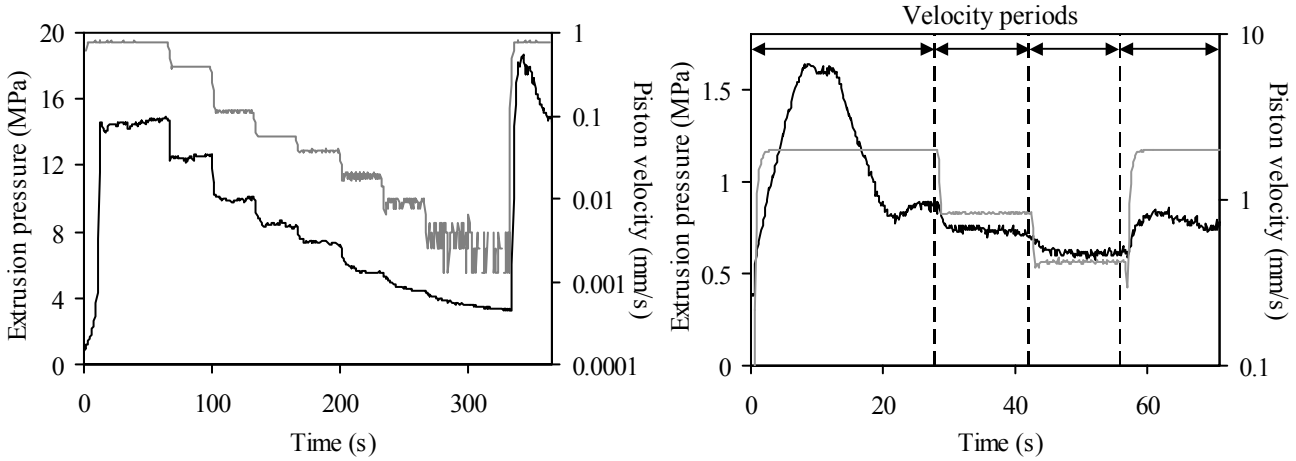

(a) D = 1 mm, L/D = 16 *(b) D = 15 mm, L/D = 3.2*

Figure 3.10 Extrusion pressure and piston velocity against time

extrusion pressure *piston velocity*

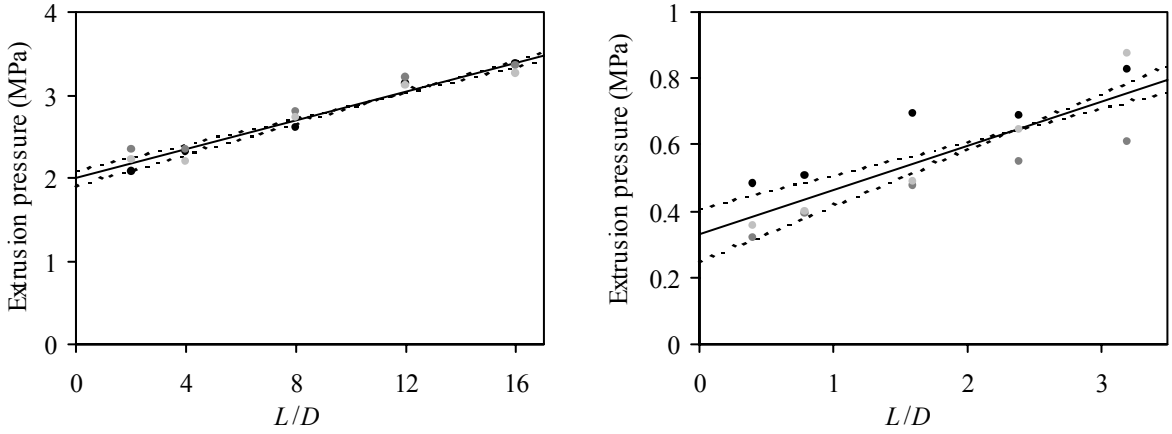

(a) D = 1 mm, V =0.00117 m/s ($\dot{\gamma}_A$ = 9.36 /s) *(b) D = 15 mm, V = 0.00118 m/s ($\dot{\gamma}_A$ = 0.629 /s)*

Figure 3.11 Bagley plots of extrusion pressure against capillary length to diameter ratio

independent sets of data

least squares fit *boundary least squares fit*

Linear regression of the data allowed wall shear stresses and die entry pressures to be calculated. From equation (2.20) we know the wall shear stress to be one quarter of the gradient, and the die entry pressure to be the ordinate intercept. Without further statistical information about the data, this was considered to be an appropriate method of finding the most probable values. The variation in reproducibility of the data was expressed by finding some boundaries to what the 'best' linear fit might be. If statistical information about the data were known, then exact probability distributions for the fit parameters might be calculated. Rather, a novel approach was used where the square of the coefficient of correlation (often known as r^2) was taken to be an indicator of the quality of the data. Regression parameters were then found which had a squared coefficient of correlation

equal to the original raised to the power 1.3. This index was chosen arbitrarily to give fits which appeared reasonable. The least squares and the boundary fits are shown on the charts of Figure 3.11, and it can be seen that the boundaries of the gradients and ordinate intercepts would seem to cover all linear fits which might be deemed reasonable by common sense. Most advanced mathematics textbooks include derivations and discussion of the statistical methods of fitting data to a straight line, such as that by Press *et al.* (1993).

The wall shear stress data obtained from the Bagley plots for each capillary diameter are presented in Figure 3.12 against the mean axial velocity, following Figure 2.10. Interpolations were read off these charts at the wall shear stresses indicated, and the Mooney diagrams of Figure 3.13 compiled. These results are disappointing; although a straight line could be fitted to these data with a gradient of the slip velocity, the line would intercept the ordinate axis at a negative value which, considering equation (2.19), is not consistent with the physical model presented. Thus no conclusions about the nature of the flow can be drawn from the Mooney plots.

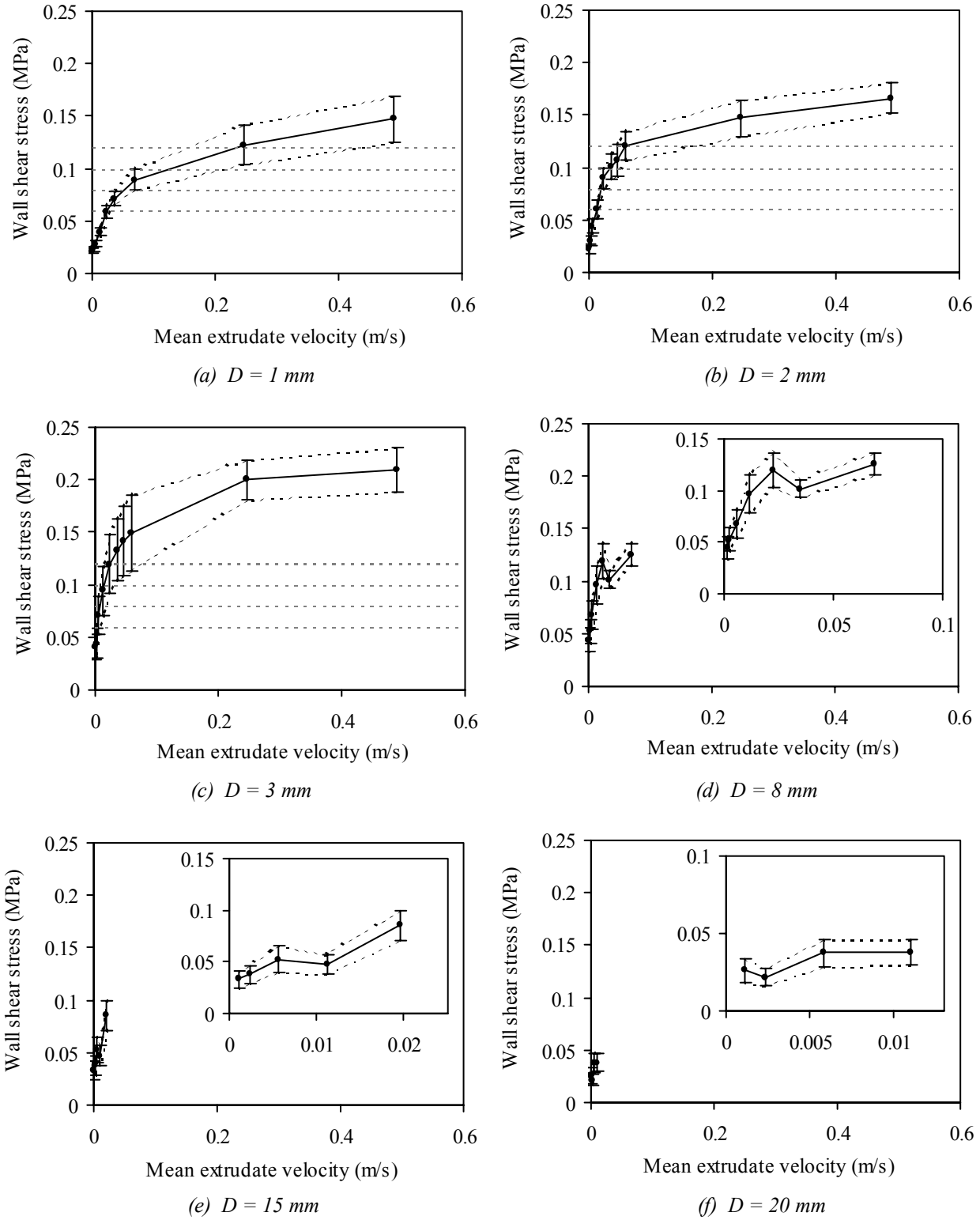

(a) D = 1 mm

(b) D = 2 mm

(c) D = 3 mm

(d) D = 8 mm

(e) D = 15 mm

(f) D = 20 mm

Figure 3.12 Wall shear stress against mean extrudate velocity

Error bars bound regions of possible values. Insets show enlarged regions.
—— interpolated most likely value - - - interpolated boundary value
- - - constant wall shear stress values

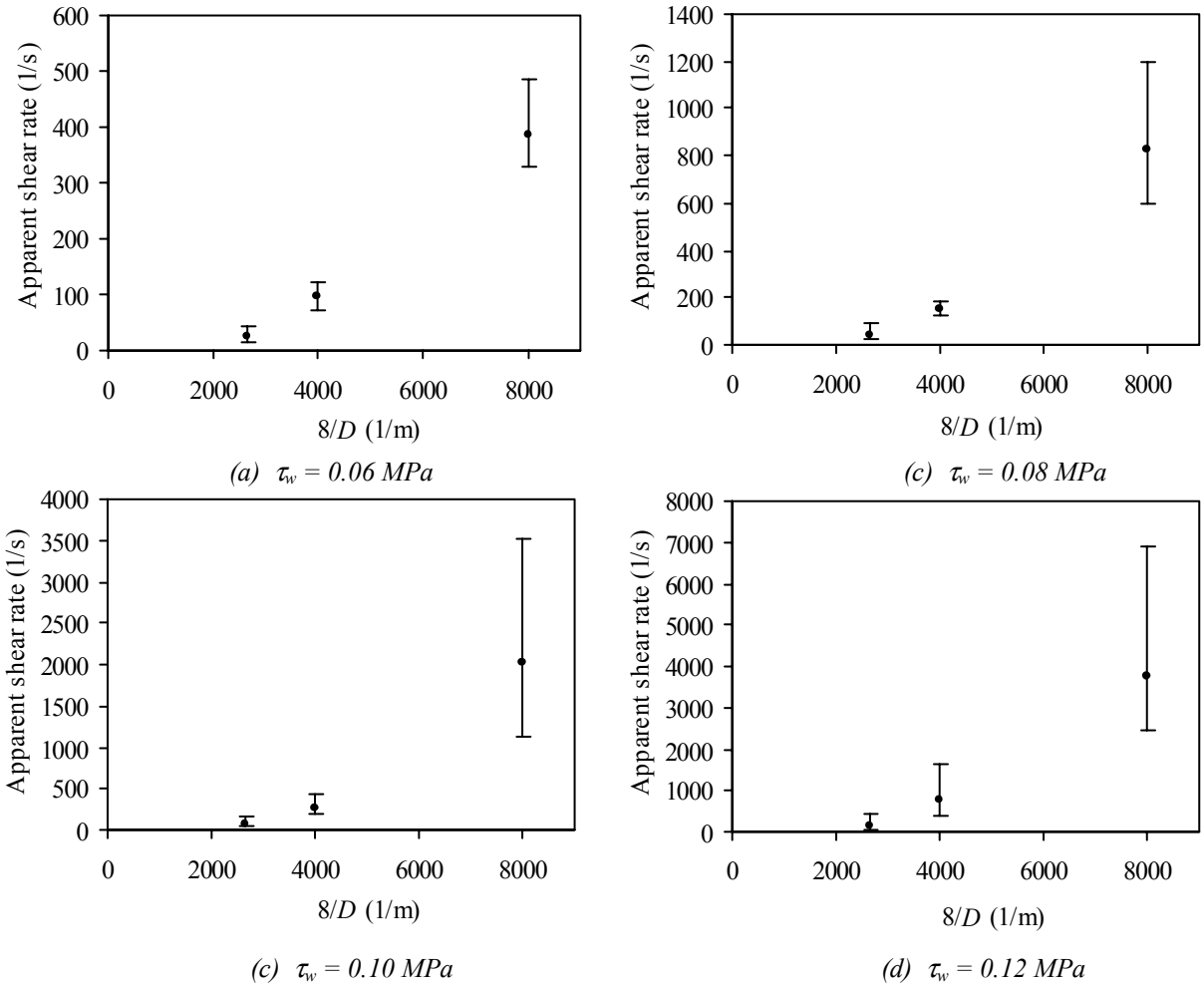

Figure 3.13 Mooney plots of apparent shear rate against 8/D
Error bars bound regions of possible values.

If the Jastrzebski boundary condition (detailed in Section 2.3.2) is used, the Mooney diagrams of Figure 3.14 can be compiled. Linear least squares fits, forced to pass through the origin, were applied to these data. The resulting lines pass through the regions of possible apparent shear rates, and look like plausible trends. These trends could be taken to suggest that there is plug flow in the capillary. However, since there is no physical basis for the Jastrzebski boundary condition, any such conclusion would be suspect. Figure 3.15 shows that the boundary condition β term decreases as the wall shear stress increases, possibly in a linear manner. By comparison, both Adams *et al.* (1995) and Jastrzebski (1967) reported that β increases with wall shear stress (linearly in the case of Adams *et al.*). However, little can be concluded from these trends. Also, without any physical model for this boundary condition, there is no indication of how it could be extended for flow in non-cylindrical ducts, as have been used in this project. Due to these shortcomings, no further use is made of this boundary condition.

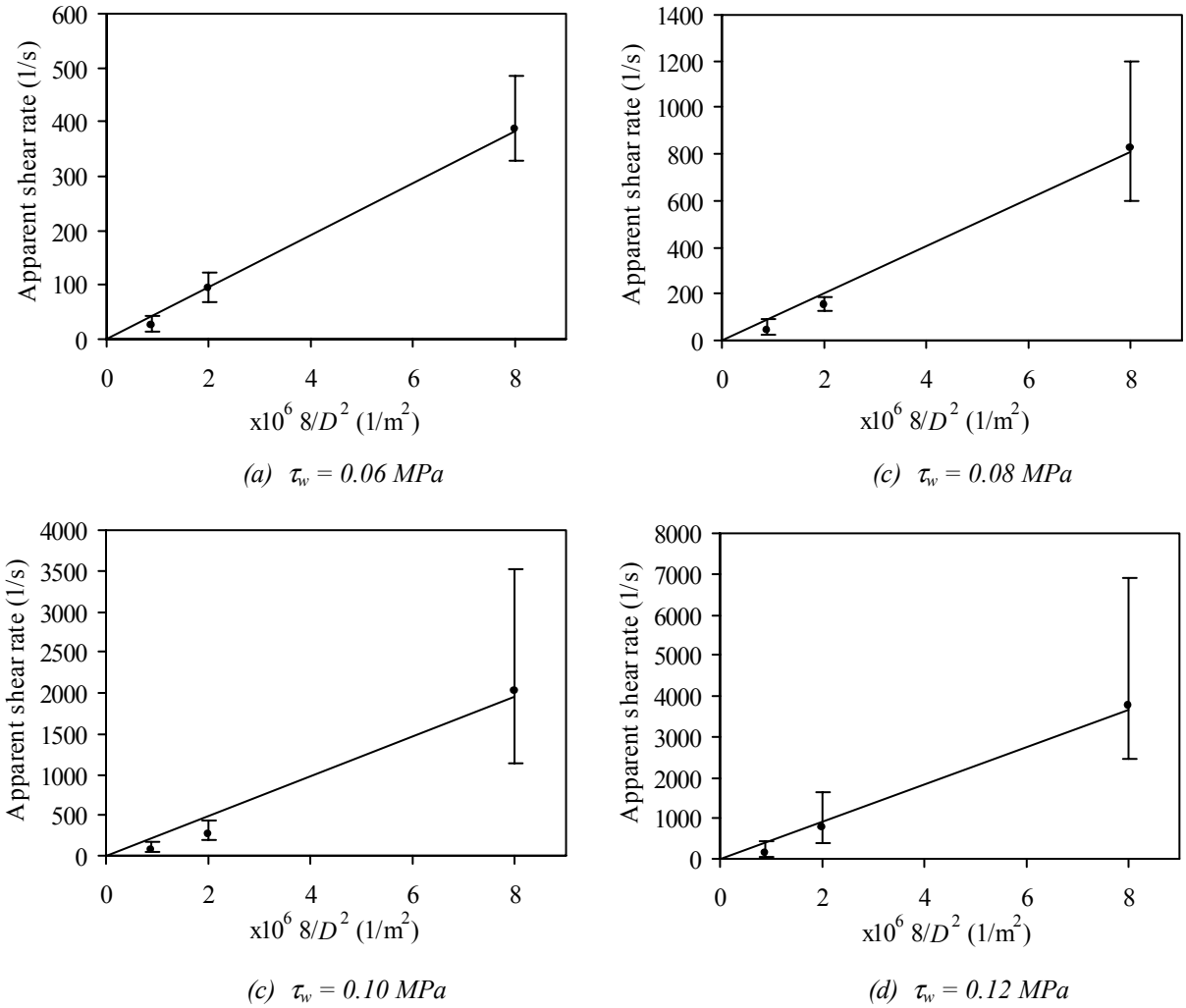

Figure 3.14 Mooney plots of apparent shear rate against $8/D^2$

Jastrzebski boundary condition. Error bars bound regions of possible apparent shear rate.
— linear least-squares fit; forced to pass through the origin

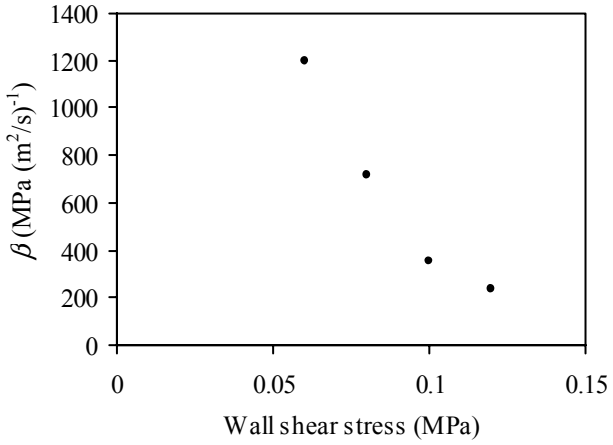

Figure 3.15 Jastrzebski boundary condition: variation of β against wall shear stress

From the Mooney plots which have been considered, it appears that both wall slip and shearing of the bulk material occur. Figure 3.16 indicates this further. The wall shear stress has been plotted against each factor; the apparent shear rate (plots *(a)* and *(b)*) and the extrudate velocity (plots *(c)* and *(d)*). If there were no slip, then the wall shear stress would be a function of the apparent shear rate only, and vice versa. The figure shows that the flow curves for each capillary diameter do not collapse onto a single curve on either plot – thus the flow is neither total wall slip (plug flow) nor no wall slip (total bulk shear).

It was noted in Section 2.4.1 that Amarasinghe (1998b) successfully constructed Mooney diagrams to separate the wall slip and bulk shear contributions to flow for an alumina paste and a soap material, as did Yilmazer and Kalyon (1991) for an ammonium sulphate/polymeric liquid paste. This type of material could be considered as 'well-behaved'. Materials which give unsuccessful Mooney diagrams, such as the model talc paste presented here, the Plasticine used by Adams *et al.* (1995), or the kaolinite paste used by Jastrzebski (1967), could be considered as *badly-behaved*. No physically based analysis is currently available which satisfactorily separates the contributions to flow from wall slip and bulk shear. It has been beyond the scope of this project to attempt to develop such a model, and from this point forward we shall assume that the model paste material undergoes plug flow with no shearing in the bulk and the mean extrudate velocity is referred to simply as the extrudate velocity, V. This assumption simplifies all future modelling work, and yields models valid for *well-behaved* pastes.

The wall shear stress shown in Figure 3.16 *(c)* possibly displays a power law dependence against slip velocity. Thus the interface behaviour was modelled using equation (2.12) which allows for a yield and power law relationship. Material boundary parameters were found by a least squares fit through all three diameter data sets. The spread of the data was taken into account by fitting lower and upper bounds to the parameters. The lower bound parameters were found by a least squares fit through the lower boundary data for the capillary of diameter 1 mm as shown in Figure 3.12 *(a)*. Upper bound parameters were found by a least squares fit through the upper boundary data for the capillary of diameter 3 mm as shown in Figure 3.12 *(c)*. These parameter fits are shown in Figure 3.16 *(c)* and *(d)*, and the parameters are listed in Table 3.5, where we see that the best fits are achieved with a simple Navier power law boundary condition (where $\tau_0 = 0$). This would apparently correspond to our early finding from Section 3.2.3 that the liquid-phase was approximately Newtonian.

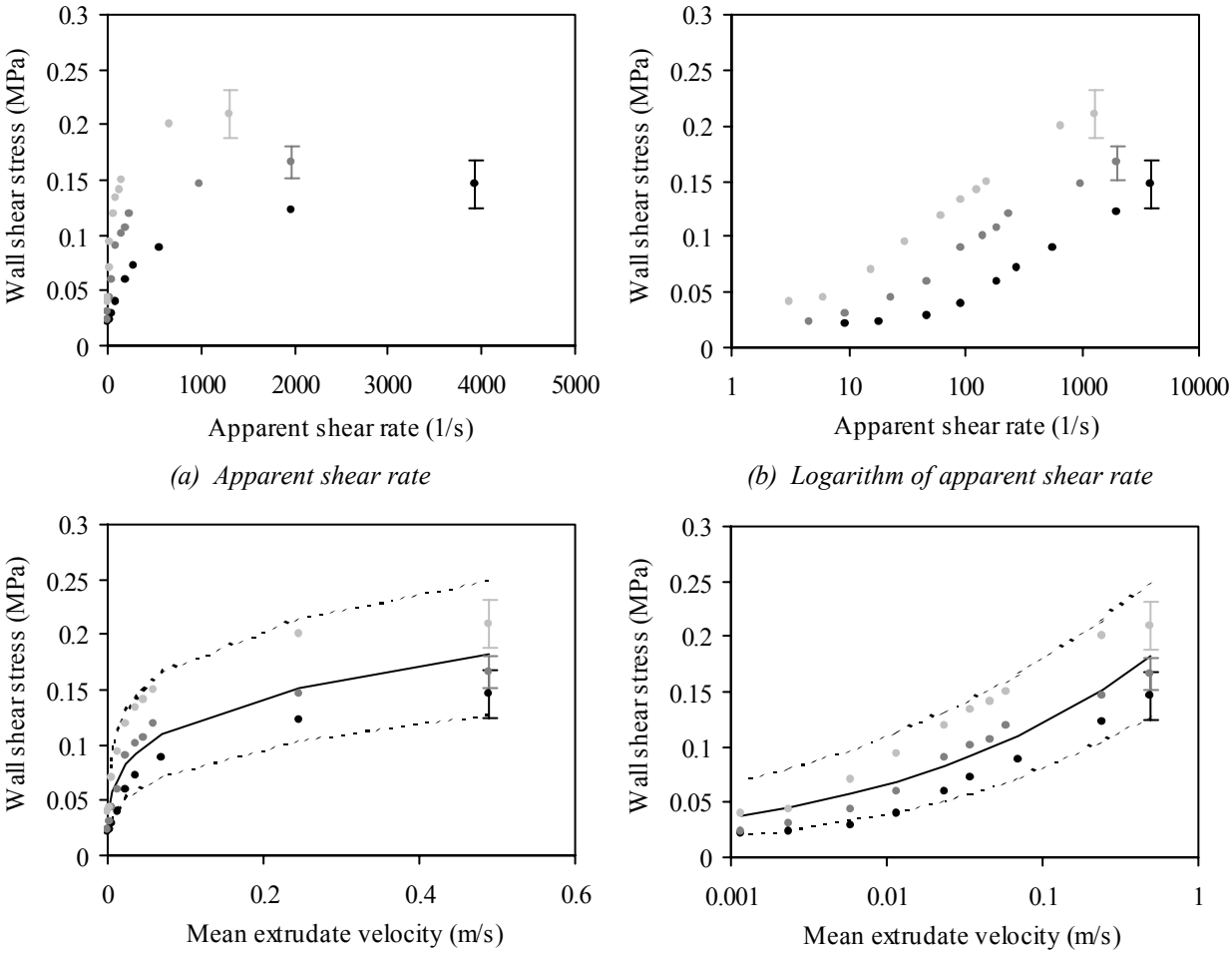

(a) Apparent shear rate *(b) Logarithm of apparent shear rate*

(c) Mean extrudate velocity *(d) Logarithm of mean extrudate velocity*

Figure 3.16 Wall shear stress against apparent shear rate and mean extrudate velocity

Selected error bars bound regions of possible values.
capillary diameter, D = 1, 2, 3 mm respectively
least squares fit *boundary least squares fit*

3.4.3 Benbow-Bridgwater die entry pressure drop analysis

The capillary flow analysis did not yield any results about the bulk shearing or extensional properties of the model paste. The die entry extrusion pressures found from Bagley plots such as those of Figure 3.11 have been analysed by the Benbow-Bridgwater method presented in Section 2.4.2. This analysis does not yield material parameters which are as specific as the parameters of the Herschel-Bulkley constitutive equation, but the die entry yielding stress which it provides is generally useful for extrusion models. The variation of the die entry yielding stress with extrudate velocity is shown in Figure 3.17 *(a)* and *(b)*. In this Section all of the capillary diameters are used in the analysis such that the characterization covers the conditions found in the industrial extruder.

The relationship between the die entry yielding stress and the extrudate velocity seems to follow a power law, possibly with a yield stress. The three parameter model proposed by Benbow and Bridgwater (1993a) was used. As with the wall boundary data, the data do not lie on a consistent curve. Again the approach of using best fit parameters and boundary parameters was used, found with the least squares method. The fitted parameters are shown in Table 3.5.

In Section 2.4.2 we discussed the validity of using the extrudate velocity as the rate term in the die entry yielding stress. One possible alternative which was considered was the ratio of extrudate velocity to capillary diameter, V/D (a form of the apparent shear rate). The yielding stress is shown plotted against V/D in Figure 3.19 *(c)* and *(d)*, but the data do not lie noticeably closer to one curve than when plotted against the extrudate velocity in *(a)* and *(b)*. Thus the extrudate velocity has been taken as an adequate rate term.

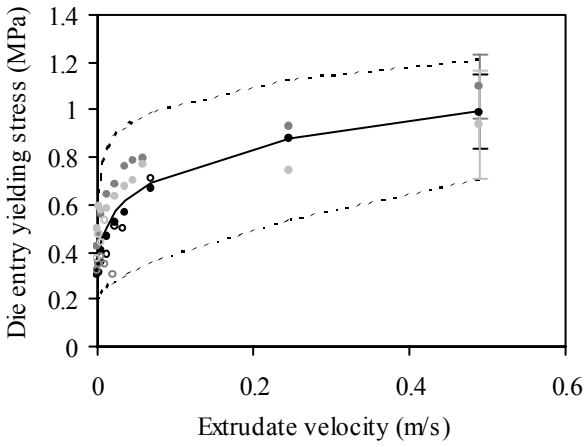

(a) Extrudate velocity

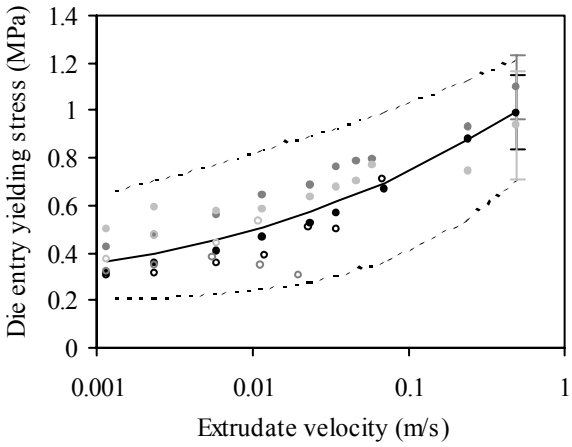

(b) Logarithm of extrudate velocity

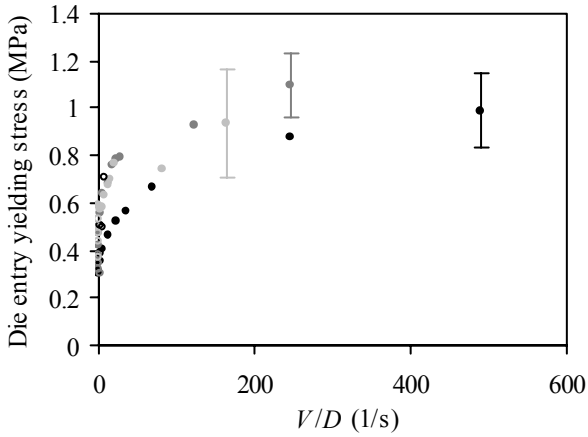

(c) Extrudate velocity to capillary diameter ratio

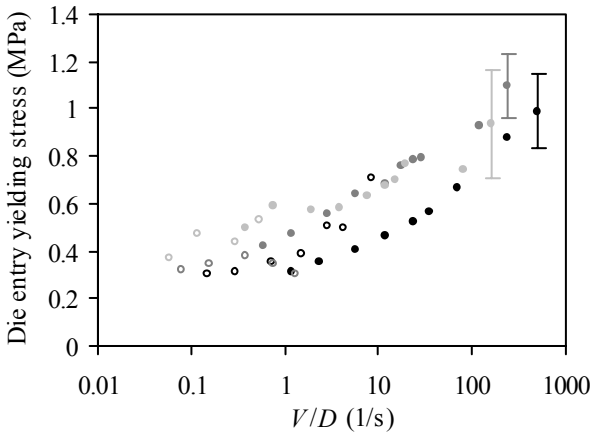

(d) Log extrudate velocity to capillary diameter ratio

Figure 3.17 Die entry yielding stress against extrudate velocity and velocity to diameter ratio

Selected error bars bound regions of possible values.
● ● ● capillary diameter D = 1, 2, 3 mm respectively
○ ○ ○ capillary diameter D = 8, 15, 20 mm respectively
—— least squares fit --- boundary least squares fit

Table 3.5 Model paste constitutive parameters

Parameter	Best fit	Lower bound	Upper bound
σ_0, MPa	0.15	0.19	(0)
α, MPa (m/s)$^{-m}$	1.0	0.78	1.3
m	0.23	0.57	0.10
τ_0, MPa	(0)	(0)	(0)
β, MPa (m/s)$^{-n}$	0.22	0.16	0.29
n	0.26	0.3	0.21

Note: Parameter fits were forced to be non-negative.
Parameters shown to 2 significant figures.

3.5 Summary

The model paste material provided by the sponsoring company has proven difficult to characterize rigorously. Experimental difficulties were found achieving reproducible extrusion pressures. Investigation of the model paste constituency suggested that little variation occurred between batches, although the viscosity of the Morwet solution was found to be very sensitive to concentration in the range used. Improvement of the extrusion pressure data might be achieved without increased experimental work by reducing the number of piston velocities used per run, and basing the characterization on fewer velocities.

A significant problem was found when using the Mooney analysis for finding the slip velocity in capillary flow. If the data were fitted to a straight line, it would pass through a (physically non-sensical) negative value on the ordinate axis. The reasons for this are unclear, but it is not the first time this has been reported, as was discussed in Section 2.3.2. The boundary model proposed by Jastrzebski (1967) which other researchers have found useful, was found to be valid and suggested that plug flow was occurring. However, the Jastrzebski boundary condition does not offer any insight into general slip conditions and lacks a physical basis. Consequently this result cannot be treated with much confidence.

It is not clear where the problem with the Mooney analysis lies. The nature of the boundary condition is certainly one problematic area, and this is where most researchers' attention has been directed. However, there is little physical insight directing this. No substantial explanation has been given to explain why the boundary layer should be related to the capillary diameter. It is thought that the surface nature of the wall does not affect the wall shear stress (at least for systems which are not dependent on the normal stress), but little investigation has been made into this.

A substantial problem which no researcher has addressed to date is the significance of the assumption of the axial stress being independent of radial position. This assumption might not be true for a paste material, but there is little to guide us in what the actual stress distribution might be. The likelihood of complex stress distributions is enhanced with materials such as the talc with its platelet nature. Such a material might rearrange at a microstructural level and form regions of varying flow properties.

Consequently our characterization of our model material is only approximate, based on a best fit with boundary limits. Figure 3.19 shows a comparison of the means of the

triplicate experimental extrusion pressures and the fitted six parameter material model, with selected error bars covering the range of the three extrusion pressures. The root-mean-square normalised error over all the data points for all die land diameters is calculated to be 0.22. The Benbow-Bridgwater characterization method provides a simple model of the material, but the accuracy of predicted experimental extrusion pressures in axisymmetric systems should not be expected to be any better than around twenty per cent.

If the material's resistance to cross-sectional change in the die entry $\sigma_0 + \alpha V^m$ is taken to be equal to the uniaxial yield stress of the material at the associated strain rate, then Tresca's yield criterion suggests that the maximum shear stress at this rate of strain, $\tau_{y,bulk}$, is $(\sigma_0 + \alpha V^m)/2$. Thus the shear yield stress of the bulk material $\tau_{0,bulk}$ could be taken as $\sigma_0/2$. Plug flow in the die land requires the wall shear stress τ_{wall} $(= \tau_0 + \beta V^n)$ to be less than the bulk shear yield stress of the material $\tau_{0,bulk}$. Figure 3.18 shows this is not observed above an extrudate velocity of around 0.01 m/s, but this was to be expected since our use of a plug flow model was known to be a poor assumption.

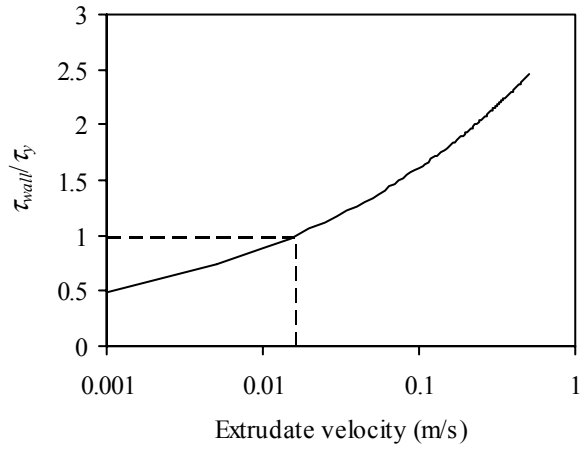

Figure 3.18 Ratio of wall shear stress to bulk shear yield stress

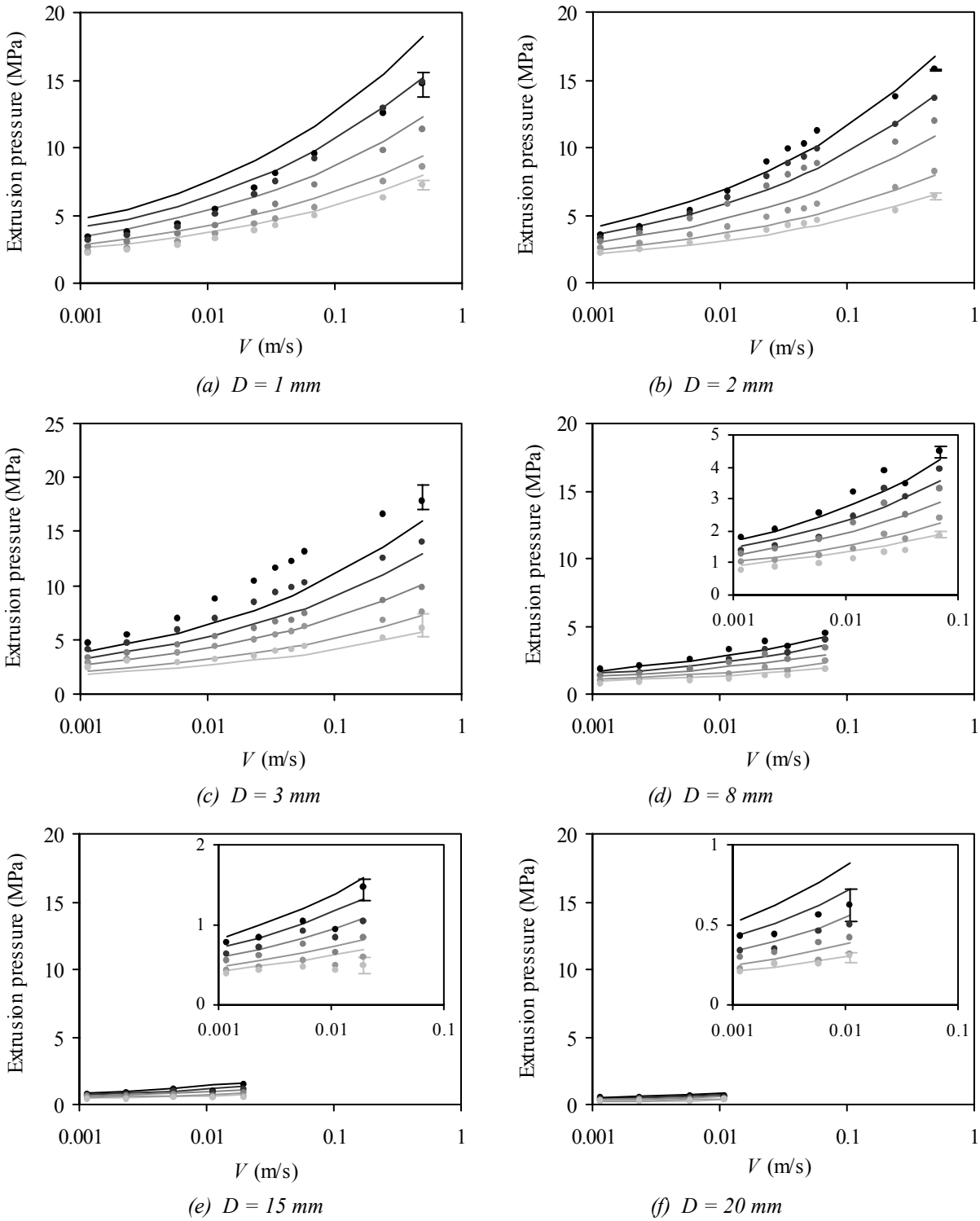

(a) D = 1 mm *(b) D = 2 mm*

(c) D = 3 mm *(d) D = 8 mm*

(e) D = 15 mm *(f) D = 20 mm*

Figure 3.19 Extrusion pressure against extrudate velocity

Selected error bars show range of triplicate extrusion pressures. Insets show enlarged regions.

• mean of triplicate extrusion pressures — material characterization model

— L/D = 16, 16, 16, 6, 3.2, 2.4 for D = 1, 2, 3, 8, 15, 20 mm

— L/D = 12, 12, 12, 4.5, 2.4, 1.8 for D = 1, 2, 3, 8, 15, 20 mm

— L/D = 8, 8, 8, 3, 1.6, 1.2 for D = 1, 2, 3, 8, 15, 20 mm

— L/D = 4, 4, 4, 1.5, 0.8, 0.6 for D = 1, 2, 3, 8, 15, 20 mm

— L/D = 2, 2, 2, 0.75, 0.4, 0.3 for D = 1, 2, 3, 8, 15, 20 mm

4 The twin-screw radial screen extruder

In Chapter 1 we introduced the twin-screw radial screen extruder as a viable piece of equipment for the production of water dispersible granules. Further, we noted some of the areas where it was hoped that improvements to the extruder's operation and design could be made. This Chapter is in two parts; the first part, Section 4.1, reviews the previous research into and the current understanding of twin-screw radial screen extruders. The second part, Section 4.2, outlines the approach which has been adopted for this work to develop an understanding of paste flow in these extruders.

4.1 Previous research

In Section 1.2.1 we separated the twin-screw radial screen extruder into four different flow regions (Figure 1.7). The first of these regions, where paste crumble drops from a hopper onto the counter rotating screws, is essentially a granular flow and compaction stage. This region is not thought to have any significant impact on the overall operation of the extruder (so long as the extruder is operated properly), and so we do not consider it any further here. The second region, where paste flows along the length of the screws, has received quite comprehensive coverage in the literature. A summary of this literature is presented here. The third and fourth flow regions, where paste flows along the length of the extruder and is then extruded through the screen by the interaction of the blade and screen, have received relatively little attention in the literature. The published research relating to these flows is discussed in detail.

4.1.1 Single and twin-screw extrusion of pastes

Single-screw

Screw extruders were developed over the latter part of the nineteenth century to meet the need for a non-intermittent process for cable covering. The earliest known concept of single-screw extrusion is found in an 1873 drawing, and the first known twin-screw extruder was developed in 1869 for sausage manufacture (Janssen (1978a)). With the development of the synthetic polymer industry around the middle of the twentieth century these extruders became increasingly popular, this has prompted extensive research into their behaviour.

Carley and Strub (1953) summarised the understanding of single-screw extrusion which slowly developed up until the 1950s. Three components of flow can be identified in a fully filled single screw extruder; a drag flow, caused by contact effects between the material and the barrel and screw surfaces; a pressure flow, due to the pressure that is built up at the end die of the extruder (the direction of this flow is opposite to that of the drag flow); and a leakage flow through the gap between the barrel and the flight of the screw (this flow is normally very small and is usually neglected in analytical treatments). The first solutions for the flow pattern of a fluid in a single screw extruder were for a isothermal Newtonian fluid, presented by Rowell and Finlayson (1922). This work contained the important conceptual step of flattening a single channel out and analysing it using rectilinear co-ordinates. A further, simplified model was presented by Carley *et al.* (1953). Since then, the scope of these models has been broadened to cover other aspects of real flow, such as complex fluids (*e.g.* Bingham fluids by Capriz and Laratta (1965)) and non-isothermal extrusion (*e.g.* Lawal and Kalyon (1999)).

Darnell and Mol (1956) were interested in the screw extrusion of solid polymer particles, and found that they were able use a similar analysis to Carley *et al.,* but with the simplifying assumption of plug flow with wall slip. This model became a standard model for the flow of powders in screw extruders. It has recently been advanced by Weert *et al.* (2001) to incorporate such factors as powder compaction.

The first coherent analysis of single screw paste extrusion was proposed by Burbidge and Bridgwater (1995). They summarised the previous work, concluding that most of it was concerned with machine-specific correlations. Previous attempts to model the paste flow had not properly considered the nature of the paste-screw/barrel interface. Burbidge and Bridgwater took the plug flow model of Darnell and Mol and introduced those

boundary conditions suitable for pastes presented by Benbow and Bridgwater (1993a). Engländer *et al.* (2000) compared this analysis to experimental work conducted with two clay-like materials. The analysis seemed able to predict the major differences in flow, although the absolute values of the predicted pressures were subject to considerable error.

Twin-screw

Much work has been published on twin or multiple-screw extruders. Janssen (1978b) provides a useful summary of some of this material. In a twin-screw extruder, two parallel screws are placed in a figure-of-eight shaped barrel. The original objective of this was to overcome the effects of slip at the wall, which was limiting screw extrusion.

Screws can generally be divided into the two major categories of intermeshing and non-intermeshing screws. In non-intermeshing extruders the separation between the screw axes is at least equal to the screw outer diameter. This configuration can be regarded approximately as two single screw extruders which influence each other. When the screws are intermeshing the separation between the screw axes is somewhat less than the outer screw diameter; in the limit the screw surfaces can be in mutual contact. Intermeshing screws imply that more or less C-shaped chambers are present that positively convey process material to the die end of the extruder. Thus slip at the wall becomes irrelevant, since the intermeshing part of one screw prevents the material in the other screw rotating freely.

Summary

Industrial twin-screw radial screen extruders are available in both intermeshing and non-intermeshing, counter and co-rotating varieties. It is apparent that the flow behaviour in each type will be quite different. However, it has been suggested that the flow in non-intermeshing twin-screw extruders will be similar to the flow in single-screw extruders (the sponsoring company uses a non-intermeshing extruder).

This area of research has been reasonably well developed. For the purposes of this project it was decided to concentrate on the less well understood paste flow in the extruder head.

4.1.2 Paste flow in the extruder head

Little work has been published which considers the flow of paste in the head of a twin-screw radial screen extruder. A more extensive literature exists concerning the use of screen extruders as part of the extrusion-spheronization process, which is popular in the

pharmaceutical industry as part of a process for manufacturing drug tablets. A small amount of information is available from manufacturers, where extruder designs have been patented. The available information from each of these sources is discussed below.

Work done within Syngenta

Twin-screw radial screen extrusion has been one of the technologies used by Syngenta for granule production, using machines supplied by Fuji Paudal. The company has experienced significant difficulties in producing consistently good quality granules. The only successful extrusion technique developed between Syngenta and Fuji Paudal has been to vary the open screen area by blanking sections off (often the first third of the extruder, or alternative segments of the twin-extruder head) and varying the water content of the paste, generally adding more water if extrusion is not satisfactory. Although this approach has led to adequate (although non-optimal) operating procedures, it results in significant problems when new products are to be manufactured by the extrusion route.

Some work has been performed to identify links between the paste constituents, consistency and extrudability, since this would enable new products to be designed for satisfactory extrudability before they are officially registered and produced in bulk. This work has focused on pilot plant studies (based on the assumption that if it extrudes well on the pilot plant, it will extrude well on the production plant) and attempts to understand the conditions of flow in the extruder. The pilot plant work has given little insight into the actual nature of the paste flow. The work specifically concerned with the paste flow has not been fully developed. Two interesting internal company reports stand out.

Formstone (1997) described an attempt to find some indication of the stress state of the paste next to the screen in the extruder. However, the scale of the pressure transducer being used was considerably larger than the screen hole dimensions. The device was mounted outside of the screen, as shown in Figure 4.1 overleaf. Unfortunately, this arrangement only allows some sort of post extrusion stress to be measured – there will inevitably be a pressure drop as the paste flows through the dies. In order to measure the paste stress state prior to being extruded, the transducer must be on the other side of the screen. The report noted that Fuji Paudal's distributors, Russel-Finex Ltd. (Feltham, Middlesex, U.K.), did not offer any pressure measuring facilities for their equipment.

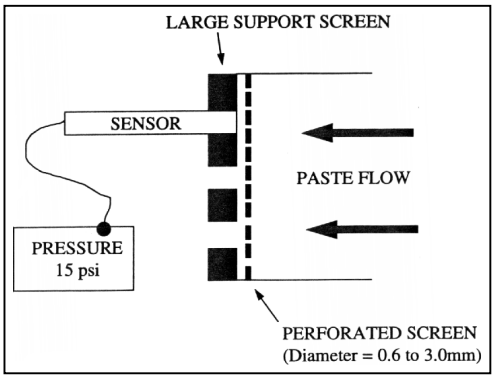

Figure 4.1 Schematic of pressure transducer mounting (Formstone (1997))

Other interesting work using scanning electron microscopy (SEM) was reported by Formstone (1995). SEM imaging of talc-based pastes showed that the talc platelets in the extrudate featured different orientation patterns depending on how it was extruded. Experiments were performed with two configurations of extruder. The extruder consisted of a single screw which fed paste down a rifled barrel to a frontal perforated stainless-steel mesh, with 1.2 mm diameter holes. The other extruder configuration used a chopper blade in the region just behind the mesh. The chopper blade sweeps across the mesh with a very close tolerance and assists in the passage of the paste through the dies. The images are reproduced in Figure 4.2 below.

This study found that extrusion in the absence of chopper blades resulted in the talc platelets being aligned in the direction of motion. Two regions of alignment were seen when the chopper blade was present. In the extrudate core, the platelets were found to be orientated normally to the flow direction. In the annular zone surrounding the core, *i.e.* in the shear zone in which particles interact strongly with the die walls, the platelets were aligned in the same direction as the flow. This shear zone was approximately 30 μm thick; the extrudate diameter was 1200 μm.

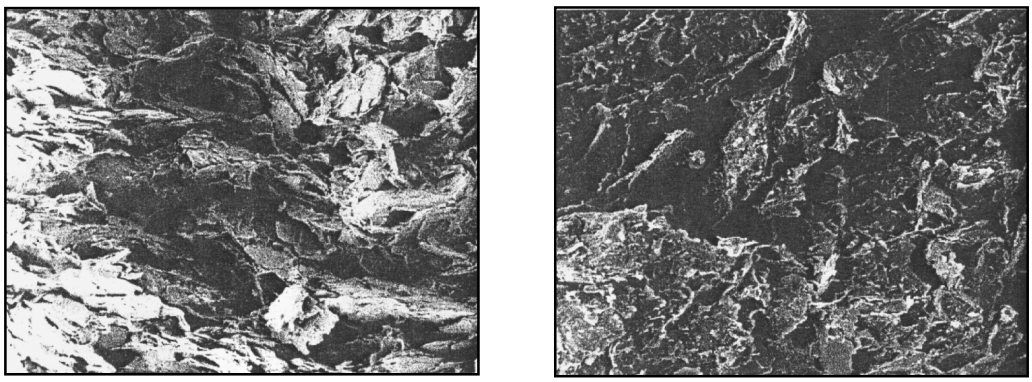

(a) No chopper blade *(b) Chopper blade*

Figure 4.2 SEM images of talc paste extrudate (Formstone (1995))

Extrusion-spheronization

A variety of screen extrusion techniques are used as the first forming stage of the extrusion-spheronization process; radial screen extrusion is one of them. The objective of this process it to convert a dry powder (mainly a mixture of active drug ingredients and filler materials – often microcrystalline cellulose, calcium carbonate or lactose) into small spheres (maybe 1 mm in diameter) which possess structural integrity. This is achieved in four stages; mixing the powder with a liquid to form a paste; extruding the paste through a screen to create small granules; rolling these granules in a drum (a spheronizer) to form spheres; finally, drying. These spheres can then be coated to form controlled drug delivery systems. A general summary of the literature relating to extrusion-spheronization is presented by Vervaet *et al.* (1995).

Although the literature on extrusion-spheronization is quite extensive, the extrusion stage only makes up a relatively small part of the process. The extruder is often treated as a black box where only the nature of the feed material is controlled and the properties of the extrudate coming out examined. The group at the London School of Pharmacy (Michael Newton and co-workers) have led the work on extruder conditions: their studies have illustrated the difficulty of measuring and understanding the flow inside a screen extruder and have investigated two approaches to the problem.

One approach has been to follow the method of Oveston and Benbow (1968) and use a ram extruder, where the flow pattern is relatively well known and only small amounts of material are needed, as a substitute for the screen extruder. This method has been found useful for characterizing some of the properties of pharmaceutical pastes, but it has only been of limited success in predicting how a paste is likely to perform in a screen extruder. For example, Fielden *et al.* (1992) compared the extrusion of the same pastes through both a ram and a screen extruder. For the ram extruder they found that, the higher extrusion pressures (a consequence of the percentage open area of the die being much lower than that of the screen) and the longer compaction period (in a screen extruder paste is only compacted in the extrusion nip between the blade and screen for a brief period, in a ram extruder paste is compacted in the barrel for the duration of the extrusion run) led to increased phase migration. This phase migration resulted in a film of liquid on the extrudate surface which caused agglomeration during the spheronization stage, whereas no agglomeration was seen with the screen extruder.

The second approach has been to attempt to instrument screen extruders to give some measure of the paste flow conditions. The first, and simplest, attempts at instrumentation focused on measuring extruder power consumption (Baert *et al.* (1993) and Vervaet *et al.* (1994)). The extruders were operated at constant speed, so that the power consumption is a measure of the torque on the rotating core. This provided a useful measure for comparing the relative ease of extrusion for different paste formulations and different types of extruder. It was generally found that increasing the water content decreased the power consumption. However, this method does not provide any insight into the flow conditions inside the extruder.

The author is aware of two attempts to measure the actual stress state inside the extruder head as the paste is extruded. Both rely on fixing a strain gauge to a point on the screen, and using the local screen deformation as an indication of the local stress on the screen. Baert and Down (1994) used this approach in conjunction with measuring power consumption. They attempted to calibrate the strain gauge output to a notional extrusional force by hanging weights from the screen. The strain gauge output was found to be proportional to the weight over the range used. The strain gauge amplifier voltage was taken as the nominal extrusion force as the authors noted that their method could not give a quantitative measure of pressure. All experiments were conducted at the same extrusion speed and the ratio of extruder force to power consumption was found to be constant over the range of paste formulations used, to within approximately ±10 per cent.

Shah *et al.* (1994) used a strain gauge load cell positioned tangentially against a supported area of screen, as illustrated in Figure 4.3. They reasoned that, since the screen was relatively unsupported at the point of contact, any radial deformation of the screen would be directly related to the local normal stress exerted on the inside of the screen by the paste. The strain gauge measures the strain of the screen, and thus the stress imposed on it. A large, snug fitting, rubber bung was fitted into one hemisphere of the screen holder with the flat surface blanked and a measured pressure applied on the end surfaces. The normal stress applied to the bung was taken to be equal to the normal stress on the screen. The strain gauge reading was found to increase linearly with the notional screen normal stress, and a calibration line was fitted. This approach yielded the first, and as yet only, results relating the screen extrusion extrudate properties and screen extrusion pressure to the feed material properties and the extruder screen design. The significance of these results merits a thorough review.

Shah *et al.* (1994) performed a variety of experiments using a 50/50 lactose/microcrystalline cellulose paste with a range of water contents. These pastes were fed to the extruder operating at a speed of 19 rpm and with 1 mm diameter die holes – die hole length was unreported; screen temperature and pressure were recorded over the steady state extrusion period. The extrudate was spheronized and the resulting spheres dried. The dried product was sieved into size fractions, and the desired size fraction was taken to be the yield of the 18/25 (1000 to 710 μm) mesh cut sieve. Both the yield and the tamped density of the desired size were measured. Further experiments were conducted (with just a single paste type) investigating the variation of screen pressure with percentage of screen open area by varying the die hole diameter (we must presume that the same load cell calibration was used for all of the screens, which may not be a valid assumption). The results of all of these investigations are presented in Figure 4.4.

The response of the strain gauge over a period of an extrusion run is shown in Figure 4.4 *(a)*. A repeated cycle of three peaks is evident. Each of these peaks is distinctively different, and they are evenly spaced. The period of the cycle is 3.2 seconds, which corresponds to a rotational speed of 19 rpm. A reasonable conclusion appears to be that each peak is the result of one of the three extruder blades passing the strain gauge location. This clearly shows that there is a local pressure increase in the vicinity of each blade, and that the differences between each blade result in slightly different pressures. When the screen force is converted into screen pressure using the given calibration we see that the peak pressure is around 6 MPa, which would seem to be a reasonable extrusion pressure. The minimum pressure is calculated as around -1 MPa. It is unlikely that the radial stress on the screen is negative, since that would suggest that the paste is pulling on the screen rather than pushing against it. Presumably this value is a consequence of the general deformation of the screen during an extrusion. This suggests that the screen pressures obtained cannot be taken as a very accurate measure of the stress on the screen, but should be treated as approximate values. For further results the screen pressure was taken to be the mean value of the peaks.

In Figure 4.4 *(b)* we see that the screen pressure increases linearly as the paste becomes drier, and that the screen temperature has the same increasing trend as the screen pressure. These are the first ever reported results which link the paste formulation to quantitative extrusion conditions in a screen extruder.

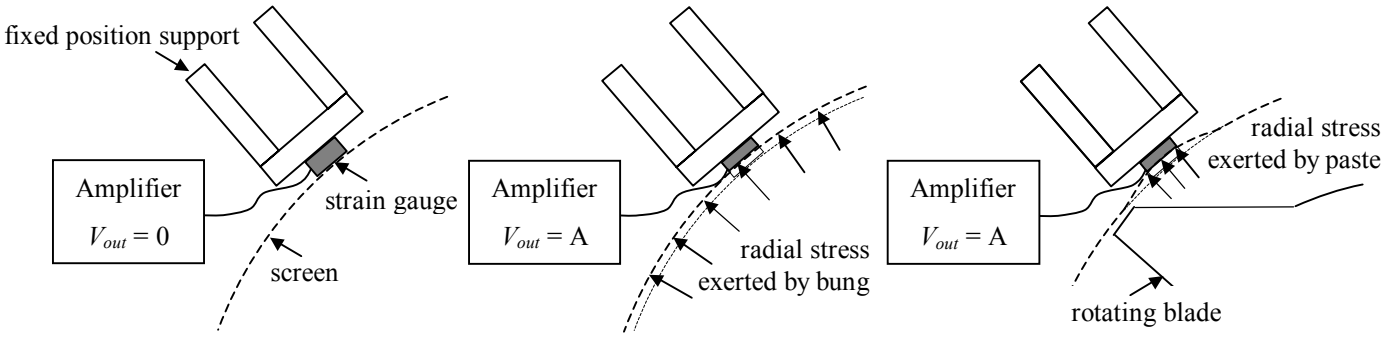

(a) Load cell on unstrained screen *(b) Screen strained by bung* *(c) Screen strained by paste*

Figure 4.3 Load cell arrangement used by Shah et al. (1994)

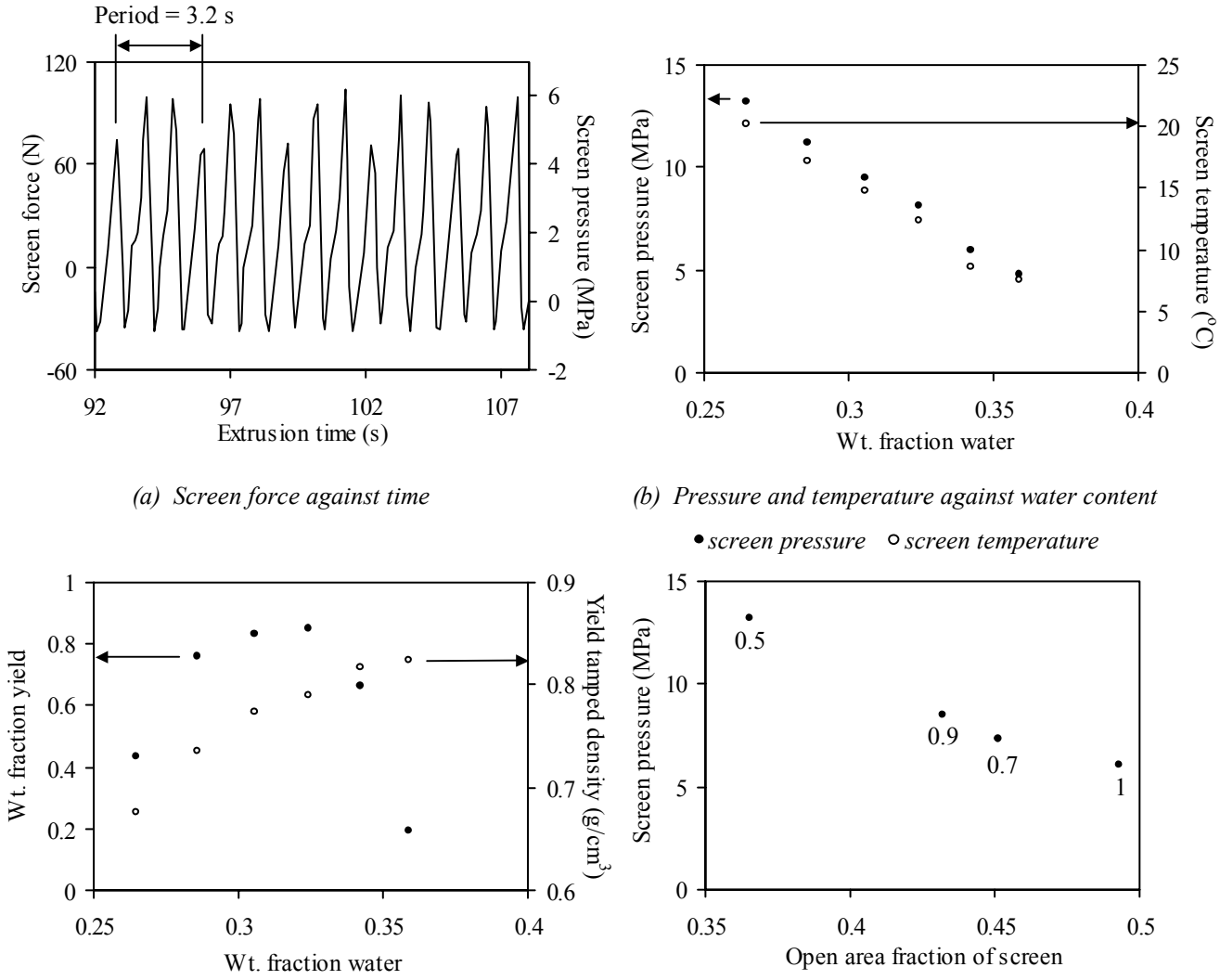

(a) Screen force against time

(b) Pressure and temperature against water content
• screen pressure ○ screen temperature

(c) Yield wt. frac. and density against wt. frac. water
• wt. frac. yield ○ tamped density of yield

(d) Screen pressure against open area of screen
Die hole diameters are shown in mm.

Figure 4.4 Instrumented radial screen extruder results (Shah et al. (1994))

Luwa EXDS-60 twin screen extruder with three blades.
Rotational speed = 19 rpm. Die hole diameter = 1 mm, or as stated.

In Figure 4.4 *(c)* we see that the fraction of the spheronized product which is within the desired size range (the yield) exhibits a maximum as the paste water content is varied. The tamped density of the spheres shown in this figure increases towards the density of water (1 g/cm^3) as the water content increases, which corresponds to a reduced screen pressure. It might be anticipated that wetter spheres produced at lower pressures would have relatively large pores and thus a relatively low density. These results remain unexplained, but are still the first recorded link between extrudate quality and quantitative conditions in a screen extruder.

Finally, we see in Figure 4.4 *(d)* that the screen pressure decreases as the fraction of open area in the screen increases. This decrease is expected due to both the decrease in area reduction and the increase in die diameter.

Manufacturer's information

Very little information has been available directly from any screen extruder manufacturers. The standard manufacturer's literature, for example the Fuji Paudal document by Van doorslaer Tom (1997) only categorises different extruder designs as 'low' or 'high' pressure extruders, with no indication of what the stresses developed might be. A better indication of the understanding possessed by the manufacturers can be gained from patents. Below we discuss two patents which are of particular interest.

Since 1992, when Fuji Paudal introduced the twin-screw dome extruder (as described in Section 1.2.1) to the market, the company has taken out quite extensive patents on the extruder design. One such patent by Fujimoto *et al.* (1993) details quite extensively the development of granulating extruder technology from frontal extruders, through radial screen extruders, to dome extruders. All three designs have essentially the same twin-screw feed system, which is considered in a little detail for the case of the frontal extruder. The profile of the internal extrusion pressure (which is not defined) over the length of the extruder is reproduced in Figure 4.5 overleaf. We can see that in region A, representing the region of the screw chamber [27] communicating with the feed hopper [22], the pressure is at a minimum, but rises rapidly as the material is conveyed beyond the feed hopper [22] to the front end of the screw [26], represented by the regions B and C. As the paste is conveyed to the extrusion blade [28] in the region D, maximum pressure is reached as the material is forced into the openings of the die. As the paste passes through the die openings, the pressure drops from the maximum pressure level at the entrance end

of the openings to ambient atmospheric pressure at the exit end of the openings, as represented by region E.

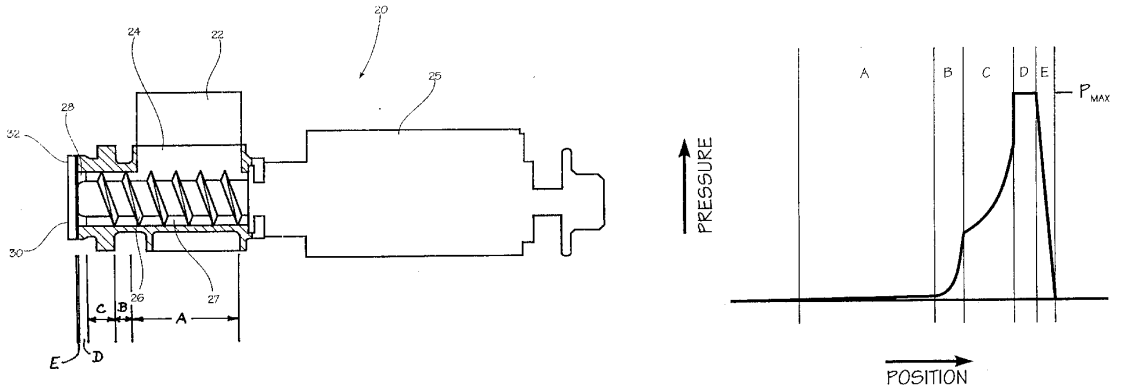

(a) Schematic of extruder *(b) Internal extrusion pressure within extrusion housing*

Figure 4.5 Internal extrusion pressure within a Fuji Paudal frontal extruder (Fujimoto et al. (1993))

The authors noted that the die sheet must be designed to withstand the maximum extruding pressure. Typically, conventional frontal extruders with a die thickness great enough to withstand this pressure, perhaps 5-8 mm, can only operate at very small production rates, far below acceptable industrial levels, when the die hole diameter is below 1.5 mm. Reducing the die thickness to be approximately equal to the die hole diameter led to a substantial increase in production capacity, but the die rapidly ruptured. The explanation given by the author, with reference to Figure 4.6, reads,

> *"The extruding force F applied to the moistened raw materials 34 at the die 30 should be greater than the drag force R created by the friction imposed on the material to be extruded moving along the die hole wall 35. Generally, at a constant die hole diameter d, the drag force R is proportional to the die hole length L, i.e. the thickness of the die 30. Therefore reducing the diameter d of the die opening while maintaining sufficient thickness L to resist [the maximum extruding pressure] results in increasing the attendant drag force R which ultimately results in a lowered production capacity or even clogging of the die openings 31."*

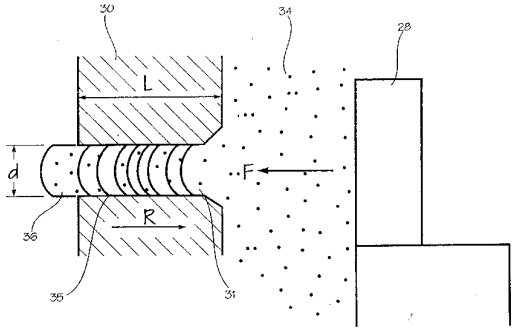

Figure 4.6 Representation of the extrusion operation (Fujimoto et al. (1993))

This explanation is not complete, and suggests a limited understanding of the extrusion process. We know from Section 2.4 that what we might call the extrusion pressure,

described here as the extruding force, must be sufficient to overcome the wall shear stress, described here as the drag force, but it must also be sufficient to deform the material such that it can flow out of the die. This aspect of flow has not been considered in the patent. Also, whilst it is true that if the die diameter is constant, the extrusion pressure is proportional to the die length, this does not explain why there is a limit to the minimum practical die diameter, as claimed in the patent.

Using the extrusion theory detailed in Section 2.4.2, a more rigorous explanation of this problem can be presented. Combining the previously derived expressions for extrusion pressure due to deformation, equation (2.25), and for extrusion pressure due to wall friction in the die, equation (2.28), gives the total extrusion pressure, P, as,

$$P = \sigma_y \ln(A_0/A) + 4\tau_w L/D \tag{4.1}$$

where σ_y is the yielding stress of the material (for simplicity, treated as a perfect plastic here), A_0 is the barrel area, A is the total die land area, τ_w is the wall shear stress (for simplicity, assumed constant here), L is the die length and D is the diameter of each die.

For extrusion through a screen, it has previously been suggested by Benbow and Bridgwater (1993d), that this equation can be modified to give the total extrusion pressure as,

$$P = 2\sigma_y \ln\left(D_0/\left(\sqrt{n}D\right)\right) + 4\tau_w L/D \tag{4.2}$$

where D_0 is the barrel diameter and n is the number of die holes in the screen. This simply takes the axisymmetric case discussed in Section 2.4.2 and treats die holes in the screen as equivalent to a single die hole of an area equal to the sum of the areas of all the dies holes in the screen. It might be expected that an industrial extruder would be run at its optimal or maximum power output, which is taken to be a constant value. The power output is equal to the product of material flow rate, Q, and the extrusion pressure, P. Thus the flow rate is inversely proportional to the extrusion pressure, giving,

$$Q \propto 1/P \tag{4.3}$$

Now we can see that, all else being equal, as the die diameter, D, is reduced the extrusion pressure, P, will increase and thus the flow rate, Q, will decrease, as reported in the patent. Further, we can roughly estimate the screen fully plastic collapse limit pressure, $P_{max.}$, as (Stronge (1998)),

$$P_{\max.} = \frac{12\sigma_Y L^2}{D_0^{\,2}} \tag{4.4}$$

where σ_Y is the uniaxial yield stress of the screen metal. This expression takes no account of the die holes in the screen. We can now illustrate the approximate relationship between the extrusion pressure, P, and the screen limit pressure, P_{max}, as a function of the die hole diameter (for constant barrel diameter, number of die holes and screen thickness/die land length) in Figure 4.7. As we noted before, the extrusion pressure increases as the die diameter is reduced and thus the flow rate decreases for constant energy input. We can now see that increasing the screen thickness (or die length) as a measure to allow smaller diameter granules to be produced without rupturing the screen might significantly increase the strength of the screen, but the increase in extrusion pressure due to the longer dies further reduces the flow rate. It might be thought that increasing the number of die holes, n, in equation (4.2) would enable the extrusion pressure to be reduced for small diameter granules. This might be true to an extent, but beyond a certain point the decrease in the screen limit pressure would outweigh the decrease in extrusion pressure. Thus we have provided an approximate, but physically grounded explanation of the results presented in the patent.

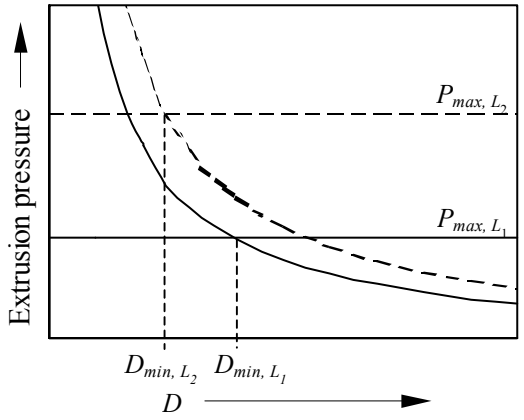

Figure 4.7 Schematic of extrusion pressure against die diameter for a frontal extruder

Screen diameter and number of holes held constant. $L_2 > L_1$

—— L_1 - - - L_2

The authors of the patent go on further to describe the twin-screw radial screen extruder as an improved design which enables the desired larger flow rates of small diameter granules. The way in which this is achieved in the radial screen extruder is not discussed. Presumably the screen design in this case, by virtue of being cylindrical rather than flat, enables many more die holes per unit area of screen to be used, relative to the frontal screen case, without violating the screen limit pressure condition. With more die holes the extrusion pressure will be reduced (hence this is known as 'low' pressure

extrusion as opposed to the frontal extruder, which is known as 'high' pressure extrusion) and satisfactory flow rates can be maintained. The authors state that,

> *"a problem with this [cylindrical screen] arrangement is that internal pressure generated by the conveying screw within the housing cannot be fully employed for the extrusion of the raw material through the die because the raw material is forced to change direction from a generally axial flow to a movement directed radially outwardly from the extracting screw, thus resulting in energy loss and inefficient production of granulate. Accordingly, the production capacity of this radial type extrusion granulator is far smaller than that of the front-type extrusion granulator."*

This statement is a recognition that the radial screen extruder is of limited effectiveness. However, it seems unlikely that this is due to the change in direction of flow. A typical twin-screw extruder might be powered by a 20 kW motor, extruding 1000 kg/hr of material. In Appendix A, the extrudate radial velocity is estimated as ~ 0.3 m/s – thus to accelerate 1000 kg of material to a velocity of 0.3 m/s over one hour would require approximately 0.01 W. Thus the energy loss due to change of flow direction seems to be an unlikely cause of this extruder's limitations. However, it is wholly possible that the flow patterns developed in this extruder are not the most efficient for producing extrusion.

The patent then goes on to claim that the twin-screw dome extruder provides a design which, like the radial screen extruder, does not suffer from screen rupture but improves upon the radial screen extruder's flow rate for equivalent power input. For the same power output and increased flow rate, either the extrusion pressure or the amount of wasted energy in this extruder will be less than for the radial screen extruder. It is thought that there might be a contribution from both factors.

We speculated that the improved performance of the radial screen extruder over the frontal screen extruder was in part due to the increased strength of the semi-cylindrical screen over the flat screen. This is recognised in the patent for the dome screen, which is reported to be able to withstand an internal extrusion pressure up to twelve times greater than a flat screen of the same thickness. The patent also claims that the dome extruder operates more effectively because the pressure of the material against the screen is more evenly spread than with the radial screen extruder. Thus extrusion can occur over the whole screen surface continuously, whereas on a radial screen extruder extrusion only occurs in the region immediately leading the blade.

For the purposes of comparison, the authors carried out like-for-like tests on each of the three types of extruder. The frontal extrusion granulator utilised in the tests was a

Model EXDF-100 manufactured by Fuji Paudal, while the radial extrusion granulator was a model EXD-100, also manufactured by Fuji Paudal. In each case the granulator was equipped with a conveying screw having a 100 mm diameter. The material processed in each case was a mixture of 70 per cent talc powder and 30 per cent bentonite powder, by weight, with 17 per cent quantity of water based upon the dry weight of the materials. The holes in all of the screens were uniformly spaced. The results are summarised in Table 4.1.

It is clear that the frontal extruder screen is not strong enough to support the pressures necessary for extrusion at satisfactory flow rates. The radial screen extruder can be seen to be an adequate alternative in many cases, but the dome extruder does appear to out-perform the radial screen extruder quite comprehensively. The only reported advantage of using a radial screen extruder over a dome extruder is that the extrusion pressure is greater in the radial screen case, thus giving a denser product which is sometimes desirable. However, presumably by suitable designing (for example, reducing the open screen area) a dome extruder could be operated at a higher pressure.

Table 4.1 Like for like comparison of frontal, radial and dome screen extruders (Fujimoto et al. (1993))

Extruder type	Motor max. power (kW)	Operating current (A)	D (mm)	L (mm)	% age screen open area	Flow rate (kg/hr)	Notes
frontal	3.7	15-18	1	5	22.4	150	Unstable with clogging of dies.
frontal	3.7	15	1	1	22.4	1 200	Deformation and breakage of screen shortly into run.
radial	3.7	15	1	1	22.4	520	Stable and no die deformation, although pulsing of extrudate.
dome	3.7	15	1	1	22.4	1 950	Stable with no die deformation or pulsation.
frontal	5.5	N/A	0.3	0.4	13	0	No acceptable production, screen failure very shortly into run.
radial	5.5	N/A	0.3	0.4	13	80	Die deformation caused operational failure after ~10 mins.
dome	5.5	N/A	0.3	0.4	13	400	Smooth with no operational problems.

The second patent of interest takes a different approach to improving the screen strength. Typically a screen is produced by punching or etching holes in a flat sheet which is then formed into the screen shape, possibly with some finishing of the die holes (*e.g.* Koga (1994)). Iwata and Inoue (2001) described a novel die design and production method which, although perhaps more costly to produce, results in screens with much improved life expectances.

Figure 4.8 illustrates their novel design. The screen strength limitation is overcome by, in effect, thickening the screen in the areas between the die holes. The screen is produced by drilling two holes, the smaller passing all the way through the screen and the second only extending part way through the screen. The inventors describe the advantage of this design as follows,

> *"The invention ... communicates the inner die hole 3 with the outer relief hole 5 having the diameter larger than that of the inner die hole 3 concentrically through the stepped portion 4 and sets the thickness (T) of the screen larger than the diameter (d1) of the inner die hole 3. Therefore, even if the scraper exerts a strong pushing force to the screen when effecting the extrusion granulating, the screen augments its compressive strength which resists the strong pushing force, much more than the conventional one. This results in extending the durable term of the screen to greatly reduce the running cost of the extrusion granulating device."*

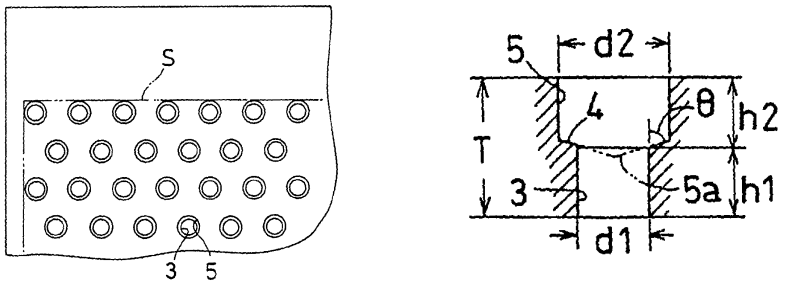

(a) Plan view of screen *(b) Cross-sectional view of die hole*

Figure 4.8 Increased strength screen die hole design (Iwata and Inoue (2001))

We might also note that this design not only improves the durability of screens with existing die hole arrangements, but might also allow screens to be designed with a larger percentage of die hole open area. As we discussed earlier, this would reduce extrusion pressure and increase flow rate, and with the new screen design the screen would be sufficiently strong, even with the increased open area.

Other work

There appears to be little else in the literature, which relates to paste flow in the extruder head. However, there are occasional publications which have a more tangential

bearing, but these are generally of limited use. For example, Richardson *et al.* (2000), published a paper concerning the mixing of high loads of titanium dioxide pigments (> 70 per cent by weight) with polymers. The mixing process used the Banbury type mixer (Farrel Corporation, Ansonia, Connecticut, U.S.A.), a high-energy batch mixer with two contra-rotating rotors within a dumb-bell shaped chamber, as illustrated in Figure 4.9 *(a)* below. The clearance between the rotors and the walls is extremely small, and it is here that the mixing takes place.

The nip developed between the rotor and the wall is superficially similar to the nip developed between the blade and screen in a screen extruder. Richardson *et al.* (2000) present a model for the behaviour of material in the nip between the rotor and wall. They choose to use a compression analysis for the material as it is deformed from height h_1 to h_2 in the nip, shown in Figure 4.9 *(b)*, in order to calculate the force on the blade. This analysis is based on a contraction in the ***x***-direction with volumetric strain of around 0.85, and assumes that there is no strain in the ***y***-direction. However, it is very unlikely that the material will compress this much in height without any lateral deformation (for example, see the cylindrical paste compression tests of Barnes (2001) or Stones (1999), where paste readily flowed radially when under an axial load). It might be more likely for the material to shear and flow around the blade tip – which is suggested by the fact that the device is used as a mixer. Furthermore, the authors acquired material data for volumetric strains of 0.01, and extrapolated these for use in their model for the 0.85 volumetric strain case without any comment on its validity. Unfortunately, little of use can be taken from their work.

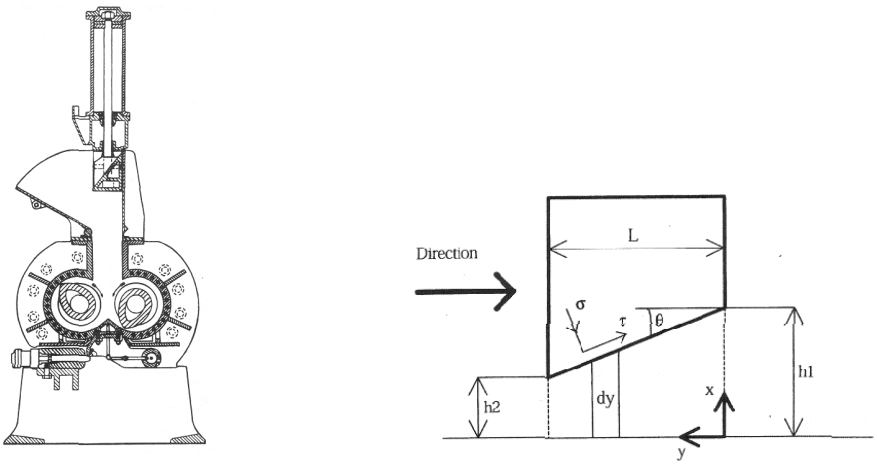

(a) The mixer (Perry and Green (1997a)) (b) Nip between blade and wall (Richardson et al. (2000))

Figure 4.9 The Banbury mixer

4.2 Beginnings of an understanding

We started this dissertation, in Chapter 1, by considering the basic design features and operation of the twin-screw radial screen extruder. In Section 4.1 we have reviewed the extent of the research which has been directly related to the extruder. Although some aspects of the extruder, such as flow in the screw feed and screen design, are reasonably well understood, there exists little knowledge of the conditions of flow in the extruder head and little idea of how these are affected by design and operation parameters.

It is useful at this point to reconsider the diagram of the extruder first presented in Section 1.2.1, represented in Figure 4.10 below. We can now see that the two aspects of the flow which have not previously been considered in any real detail are; ③ the flow into and along the region between the screen and the frustum core/blades, and ④ the flow out of the screen openings where a nip is developed between the blade and the screen. An analysis of these flows would give a model for the flow in an extruder head for the first time.

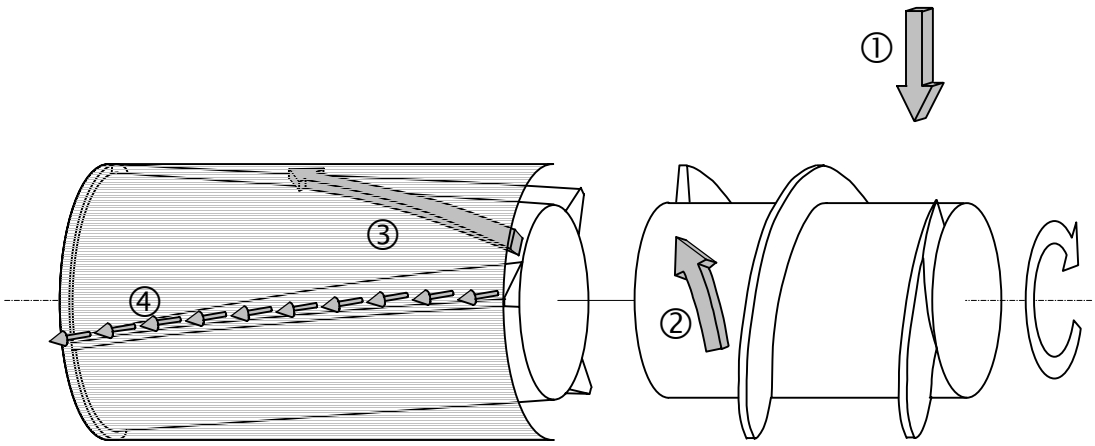

Figure 4.10 Exploded drawing of one half of a twin-screw radial screen extruder

The approach adopted for modelling the flow is essentially a combination of the upper bound method, which was outlined in Section 2.5.1, and the Benbow-Bridgwater method, outlined in Section 2.4. In summary, the upper bound method involves estimating a flow pattern and then analysing this to reach a stress distribution. Once we have estimated a suitable flow pattern, we may use the Benbow-Bridgwater analysis. If variables are introduced into the estimated flow pattern, the rate of energy dissipation may be minimised to find the most optimal, and thus realistic, flow pattern.

4.2.1 Proposed flow pattern I

A proposed flow pattern over the cross-section at some point along the extruder head has been developed, and is presented in Figure 4.11 below. This flow pattern has been based on the general principles of paste flow which have been presented in preceding Sections.

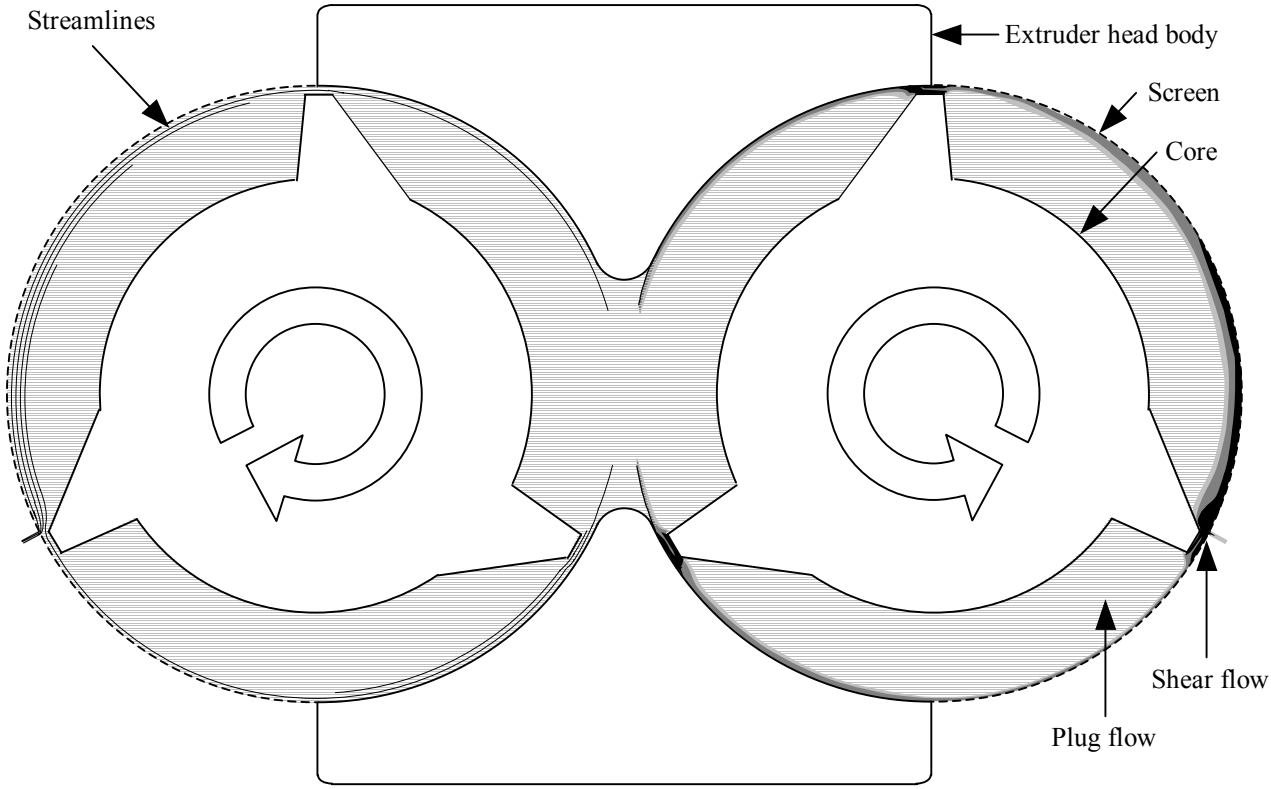

Figure 4.11 Proposed paste flow pattern over a cross-section of the extruder head I

Left hand side shows streamlines of flow relative to core. Right hand side shows strain rate.
paste material *low strain rate* *high strain rate*

The starting point for developing the flow pattern is recognition that the extruder head is rather similar to a three flighted screw extruder which has a large screw helix angle, tapered channels and a perforated barrel. As discussed in Section 4.1.1, Burbidge and Bridgwater (1995) modelled a screw extruder's channels as fully flooded with the paste flowing as a plug. It therefore seems appropriate to assume plug flow along the channel between two blades as the starting point for our flow pattern.

The literature reviewed in Section 4.1.2 suggested that as the blade passes a point on the screen there is a wave of high pressure and flow through the screen. Thus we can take the screen extrusion region to be immediately prior to the blade.

For material to flow through the screen, there must be some flow within what we have taken to be the paste plug. The interaction between the outermost surface of the paste plug and the screen is inducing this flow. It is likely that the shear stress on this paste surface would be sufficient to cause a shear flow towards the blade, and then through the screen. We saw from the model paste characterization in Section 3.4.3 that wall shear stresses can be sufficient to cause bulk shearing of the material.

Finally we use the observation from studies of twin-screw extruders, discussed in Section 4.1.1, that the two halves of the extruder head can be treated separately, but with some interaction – which we have assumed to be negligible.

The proposed flow pattern can be divided into two types of region; plug flow and shear flow. The plug flow regions represent the feed flow along the extruder head, labelled ③ in Figure 4.10. The shear flow regions represent the nip flow between the blades and the screen, which leads to flow through the screen die holes, labelled ④ in Figure 4.10. Ideally there would be no flow over the blade, and this would be a simpler situation to model. However, wearing of the blade tips is a major feature of industrial radial screen extruders, and the gap between the screen and the blade tip certainly becomes large enough for some material to slip between the two.

The proposed flow pattern is probably a plausible approximation of the flow in an actual extruder. However, modelling this flow with existing techniques would be particularly difficult. Any useful analysis of the stresses along complex shear planes, either by a Finite Element Method or some other approach, would require a well grounded material constitutive equation. As was explained in Chapter 2, and experienced in Chapter 3, such material data is rarely available. Consequently, further approximations are introduced which give a second proposed flow pattern which is more readily analysed by existing flow models. In particular, the second proposed flow pattern is amenable to analysis by the Benbow-Bridgwater approach, which was outlined in Section 2.4.

4.2.2 Proposed flow pattern II

The second proposed flow pattern, illustrated in Figure 4.12 overleaf, deviates from the first in that the paste is not sheared by the relative screen motion. Rather, the screen slips over the paste and the resulting shear stresses drive a flow pattern which might be approximately described as a combination of plug flow along the length of the extruder head, and tangential plug flow towards the nip between the screen and the blade.

Separating the flow pattern into two dominant plug flows represents a major approximation of the actual flow pattern, where the two dominant flows will interact to create a complex shearing pattern. The plug flow feed along the extruder head, labelled ③ in Figure 4.10 is further illustrated in Figure 4.13, and the plug flow tangentially into the nip between the blades and the screen, which leads to flow through the screen die holes, labelled ④ in Figure 4.10 is further illustrated in Figure 4.14.

This plug flow model can be approached using the same type of analysis as has already been applied to other paste extrusion situations. We choose the screw extruder model of Burbidge and Bridgwater (1995), discussed in Section 4.1.1, as our starting point. We proceed by developing the model and assessing it around the operating point of the industrial extruders with which we are interested. Following on from the modelling we choose suitable experimental programmes to aid in the model assessment.

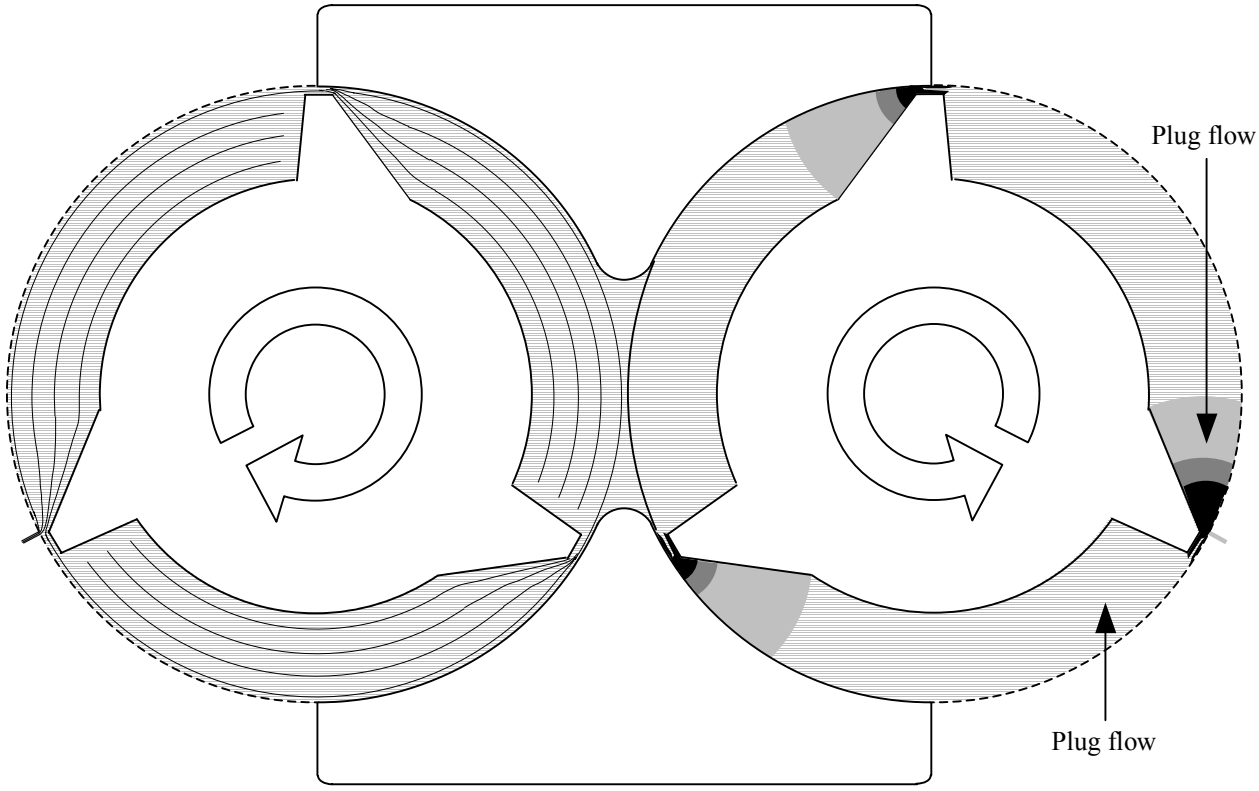

Figure 4.12 Proposed paste flow pattern over a cross-section of the extruder head II

Left hand side shows streamlines of flow relative to core. Right hand side shows strain rate.
paste material *low strain rate* *high strain rate*

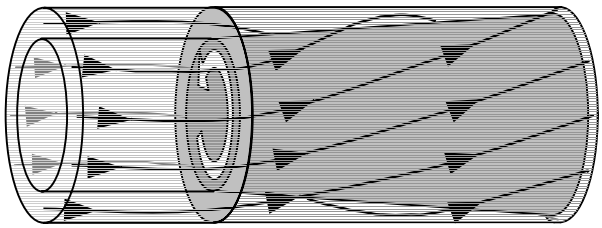

Figure 4.13 Paste flow between rotating core and screen

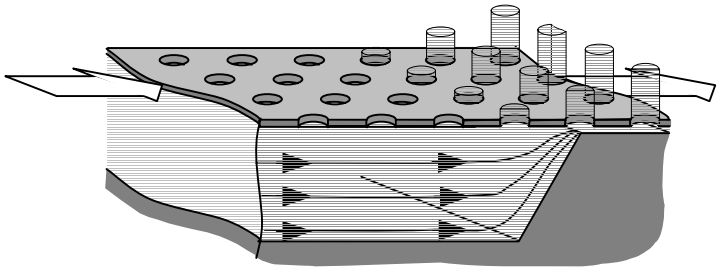

Figure 4.14 Paste flow into nip between blade and moving screen

4.3 Summary

This Chapter has presented the scope of the twin-screw radial screen extruder literature. The available knowledge of the paste flow within the extruder has been employed to propose a flow pattern for the paste within an extruder head. The proposed flow pattern shall form the basis of an upper bound flow model.

The flow pattern is based on the known flow properties of paste, especially the propensity of paste to slip at a wall. Assumptions have been made to develop a flow pattern which may be analysed using existing techniques, in particular the Benbow-Bridgwater model. The two most significant assumptions are; *(i)* that there is total slip at the walls, and *(ii)* that the flow may be separated into two pseudo-independent flows along the length of, and tangentially across, the extruder head.

Based on the proposed flow pattern, the parameters which are required to describe the paste flow may be found. These are listed in Table 4.2 along with their dimensions. More could be added to this list, for example if the screw feed had more than one blade. Also, new parameters could be defined which are a function of those already listed, and the extrudate velocity is not yet defined. Despite these uncertainties, a preliminary set of dimensionless groups may be constructed from some of these parameters.

These twenty six parameters have three different dimensions; pressure P, length L and time T. The Π theorem (*e.g.* Bridgman (1946)) states that the system may be completely described by twenty three dimensionless groups, based on three repeated parameters. A selection of such groups were formed using the screen diameter, D_s, the initial resistance to

change in cross-sectional area in the die entry, σ_0, and the extrudate velocity, V as the repeated variables. The resulting groups are presented in Table 4.3. No significant insight into the flow behaviour can be gained from the form of these groups due to their large number. However, the groups express the important factors which must be considered when analysing the paste flow in a radial screen extruder, and enable conditions to be compared between extruders of different scales.

Table 4.2 Parameters required to describe paste flow in a radial screen extruder

Parameter type	Parameter	Description	Dimension
Paste property	σ_0	Measure of initial resistance to change in cross-sectional area in the die entry	P
"	α	Measure of rate dependent resistance to change in cross-sectional area in the die entry	$P\ L^{-m}\ T^{m}$
"	m	Resistance to change in cross-sectional area in the die entry rate index	-
"	τ_0	Yield shear stress at wall	P
"	β	Rate dependence of shear stress at wall	$P\ L^{-m}\ T^{m}$
"	n	Shear stress at wall rate index	-
Operating condition	Q_0	Inlet flow rate into extruder head	$L\ T^{-1}$
"	S	Rotational speed of core/screen	T^{-1}
Screen geometry	L_{core}	Core/screen length	L
"	D_s	Screen diameter	L
"	D_{hole}	Screen hole diameter	L
"	L_{hole}	Length of screen holes, or screen thickness	L
"	$1-\lambda$	Open to total screen area ratio	-
Core geometry	D_0	Initial frustum core diameter	L
"	ϕ	Frustum core half angle	-
Blade geometry	W_{blade}	Gap between blade and screen	L
"	n_{blade}	Number of blades	-
"	ζ	Blade helix angle	-
"	θ	Blade nip angle	-
"	L_{blade}	Blade tip length	L
Dam geometry	L_{dam}	Length of dam at extruder exit	L
"	W_{dam}	Gap between dam and screen at extruder exit	L
Screw feed geometry	$D_{0\,feed}$	Diameter of screw feed core	L
"	$L_{core\,feed}$	Length of screw feed core or barrel	L
"	ζ_{feed}	Helix angle of screw feed blade	-
"	$D_{s\,feed}$	Diameter of screw feed barrel	L

Table 4.3 Proposed dimensionless groups to describe paste flow in a radial screen extruder

Group type	Group	Description
Paste property	$\frac{\alpha V^m}{\sigma_0}$	Ratio of rate dependent to initial resistance to change in cross-sectional area in the die entry
"	m	Dimensionless parameter
"	$\frac{\tau_0}{\sigma_0}$	Ratio of wall yield shear stress to initial resistance to change in cross-sectional area in the die entry
"	$\frac{\beta V^m}{\sigma_0}$	Ratio of wall rate dependent shear stress to initial resistance to change in cross-sectional area in the die entry
"	n	Dimensionless parameter
Operating condition	$\frac{\pi D_S S}{V}$	Ratio of relative velocity of screen to the core to extrudate velocity
Screen geometry	$\frac{L_{core}}{D_S}$	Ratio of screen length to diameter
"	$\frac{D_{hole}}{D_S}$	Ratio of screen hole diameter to screen diameter
"	$\frac{L_{hole}}{D_S}$	Ratio of screen hole length to screen diameter
"	$1-\lambda$	Dimensionless parameter
Core geometry	$\frac{D_0}{D_S}$	Ratio of frustum core initial diameter to screen diameter
"	ϕ	Dimensionless parameter
Blade geometry	$\frac{W_{blade}}{D_s}$	Ratio of blade gap to screen diameter
"	n_{blade}	Dimensionless parameter
"	ζ	Dimensionless parameter
"	θ	Dimensionless parameter
"	$\frac{L_{blade}}{D_s}$	Ratio of blade width to screen diameter

5 Extruder modules

This Chapter presents two novel pieces of apparatus which enable detailed observation of paste flow over the range of conditions met in screen extrusion. The design of these modules and the experimental procedures employed are detailed in this Chapter for reference in following Chapters.

Previously, in Section 4.1, we saw that very little quantitative information was available about the flow conditions in a screen extruder. Useful data were limited to only one publication, that by Shah *et al.* (1994). The extruder modules presented in this Section are the first systematic attempt to study the flow behaviour in a radial screen extruder under controlled conditions.

In Section 4.2 we divided the paste flow in a radial screen extruder into two aspects; the flow along the length of the extruder, and the tangential flow into the nip between the extruder blade and the screen. This Chapter is organised into two Sections. Section 5.1, describes an extruder module which is useful for studying both of these flow aspects, but has poor resolution when observing the flow into the nip. Section 5.2, describes another module which is less versatile, but provides better resolution when studying the plug flow of paste into a nip.

5.1 Rotating core module

5.1.1 Module design

The *rotating core module*, detailed in Figures 5.1 to 5.3 over the following pages, was designed to study both the feed flow ③ along the length of the extruder and the extrusion flow ④ in the nip between the blade and the screen, as were detailed in Figure 4.10. The

module design allowed for a wide variety of geometries and operating parameters, and allowed the measurement of the essential flow conditions.

The *rotating core module* was used in conjunction with a motor and a strain frame, arranged as shown in Figure 5.1. The module was designed for use within the available screw action strain frame, as was described previously in Section 2.4 and which was used for the characterization experiments of Chapter 3. The unit may readily be adapted for use with other strain frames. A locator (Figure 5.2, [18]) centred the module on the lower platform of the strain frame. The strain frame cross beam was used to drive a ram [2] through a feed barrel [3] containing paste on top of the module, thus providing a steady feed of paste to the module. The cross beam movement was controlled through a PC running Dartec Workshop 95 software, which programmed the strain frame controller (Modular 9500 Digital Control System, Dartec Ltd., Stourbridge, UK). A variable speed motor (Tasc Unit ID2/2, Laurence, Scott & Electromotors Ltd., Norwich, UK) and gear box (ElectroPower Gears ESR10, Laurence, Scott & Electromotors Ltd., Norwich, UK) assembly, located to the rear of the strain frame, was connected via a belt drive to power the rotating core. The motor speed was controlled manually.

The module was constructed around a framework of vertical struts and horizontal plates, shown in Figure 5.2. The lower spindle [16] was driven via a belt and pulley [17] by the motor. The lower spindle was connected to the upper spindle [9] through a 10 Nm torque transducer [15] (E300/RWT 1-2, Sensor Technology Ltd., P.O. Box 36, Banbury, UK) using sleeves [8]. A modified magnetic bicycle speedometer (CC-VL 100, Cat Eye Co., Ltd., Osaka, Japan), attached to the sleeve above the torque transducer, indicated the spindle rotational speed. The upper spindle was supported vertically upon a pre-loaded 10 kN force transducer [13] (SN1013210, Kistler Instruments Ltd., Alton, UK). Both of these transducers were connected through amplifiers (respectively; E301, Sensor Technology Ltd., P.O. Box 36, Banbury, UK and SN997660, Kistler Instruments Ltd., Alton, UK) to the strain frame controller which captured the data. A sleeve allowed interchangeable cores to be attached to the top of the upper spindle. This core was located centrally within a screen [6] attached to the underside of the uppermost plate. The screen shown in this case is a blank, but could be changed to perforated designs. Fixed centrally within the upper side of this plate is a stationary die [4] and core [5] arrangement which locates with the top end of the interchangeable core through a PTFE bearing. The

feed barrel [3] was screwed into the top plate to secure itself and to clamp the die in position. All construction was from stainless steel.

Figure 5.3 shows the extrusion region of the module in more detail. We see the feed barrel [3] which contains a reservoir of paste which is driven by the piston [2] into the extrusion region. The die [4] uses a web to support a central core. Paste must flow divergently around the central core and recombine after flowing over the webs to create an annulus of plug flow into the extrusion region. The die supported the interchangeable stationary core [5]; the diameter of which could be matched with the initial diameter of the interchangeable rotating core [7]. The experimental extrusion flow was thus created between the interchangeable rotating core - of initial diameter D_0, half-angle ϕ, and length, L, 50.0 mm - and the screen [6] - of measured diameter, D_s, 30.76 mm. The extrusion flow would leave the extruder through the end gap between the rotating core and the screen. An array of five pressure transducers, T1 – T5, of ranges up to either 0.69, 3.5, 6.9, or 35 MPa (XTM-190 series, Kulite Semiconductor Products Inc., Leonia, New Jersey, USA) were located in the blank screen at the positions shown. These transducers measured the radial stress at points along the length of the extruder. The transducers were connected through an amplifier (model CE227B, made in-house) to a dedicated PC which collected the data using a data acquisition program (DASYLab v.2.02.20, DASYTEC GmbH, Germany). The transducers were calibrated before use with a portable pressure calibrator (DPI 601, Druck Ltd., Leicester, UK).

Table 5.1 presents the range of practical operating conditions which were possible using the *rotating core module* with the model paste best fit parameters given in Table 3.5. Although it was often possible to achieve any desired value for a single group, there were often further limitations when controlling the values of more than one group. For comparison, the table also shows the conditions which might be expected in an industrial extruder using the data given in Appendix A.

The *rotating core module* enabled the measurement of the radial stress profile along the length of the screen, the axial force and the torque on the core over the whole range of possible experimental conditions. For illustrative purposes a set of sample results is now considered.

Table 5.1 Practical module operating condition and geometry

Group type	Operating condition	Module range	Typical industrial value
Paste property	$\alpha V^m/\sigma_0$ *	0 - 5	2.7
"	m	0.23	0.23
"	τ_0/σ_0	0	0
"	$\beta V^n/\sigma_0$ *	0 – 1.1	0.53
"	n	0.26	0.26
Operating condition	$\pi D_S N/V$ *	any	32
Screen geometry	L_{core}/D_s	1.6	1.7
"	D_{hole}/D_s	any	0.005
"	L_{hole}/D_s	any	0.005
"	$1-\lambda$	any	0.2
Core geometry	D_0/D_s	0.3 - 1	0.7
"	ϕ	0° - 11°	4°
Blade geometry	W_{blade}/D_s	0.006 – 0.03	0.01
"	n_{blade}	any	3
"	ζ	any	81°
"	θ	45° - 90°	47°
"	W_{blade}/D_s	0 - 0.03	0.03

** Here the extrudate velocity is taken as the axial velocity of paste flowing through the gap between the screen and the end of the core, with no flow through the screen.*

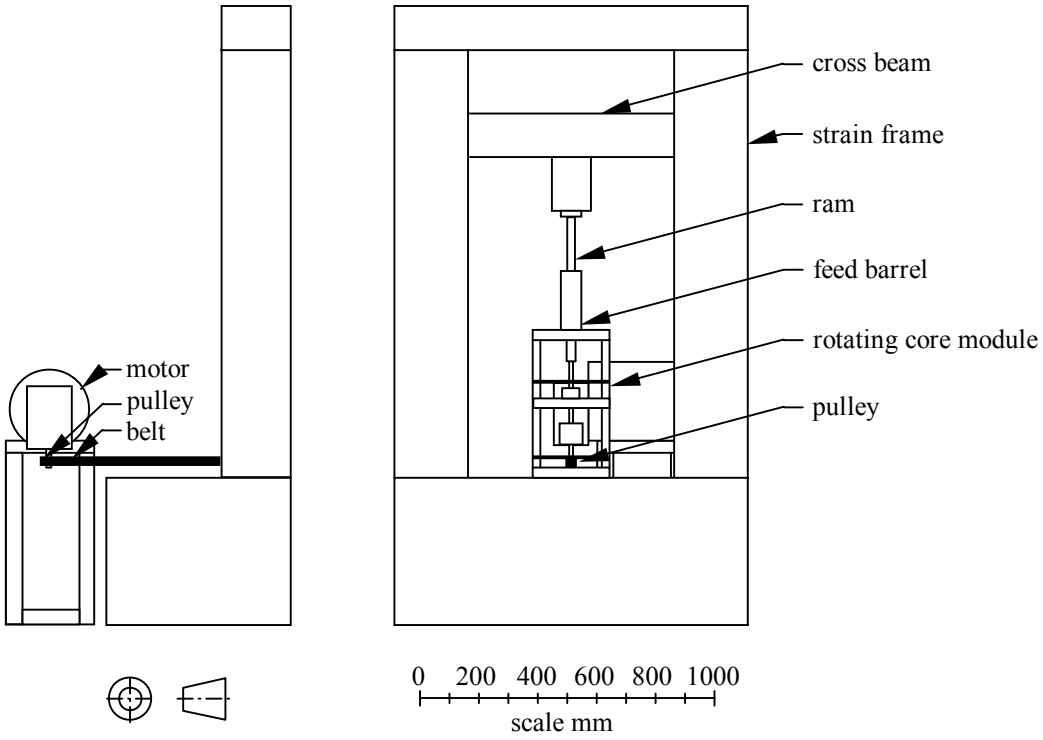

Figure 5.1 Rotating core module arrangement with motor and strain frame

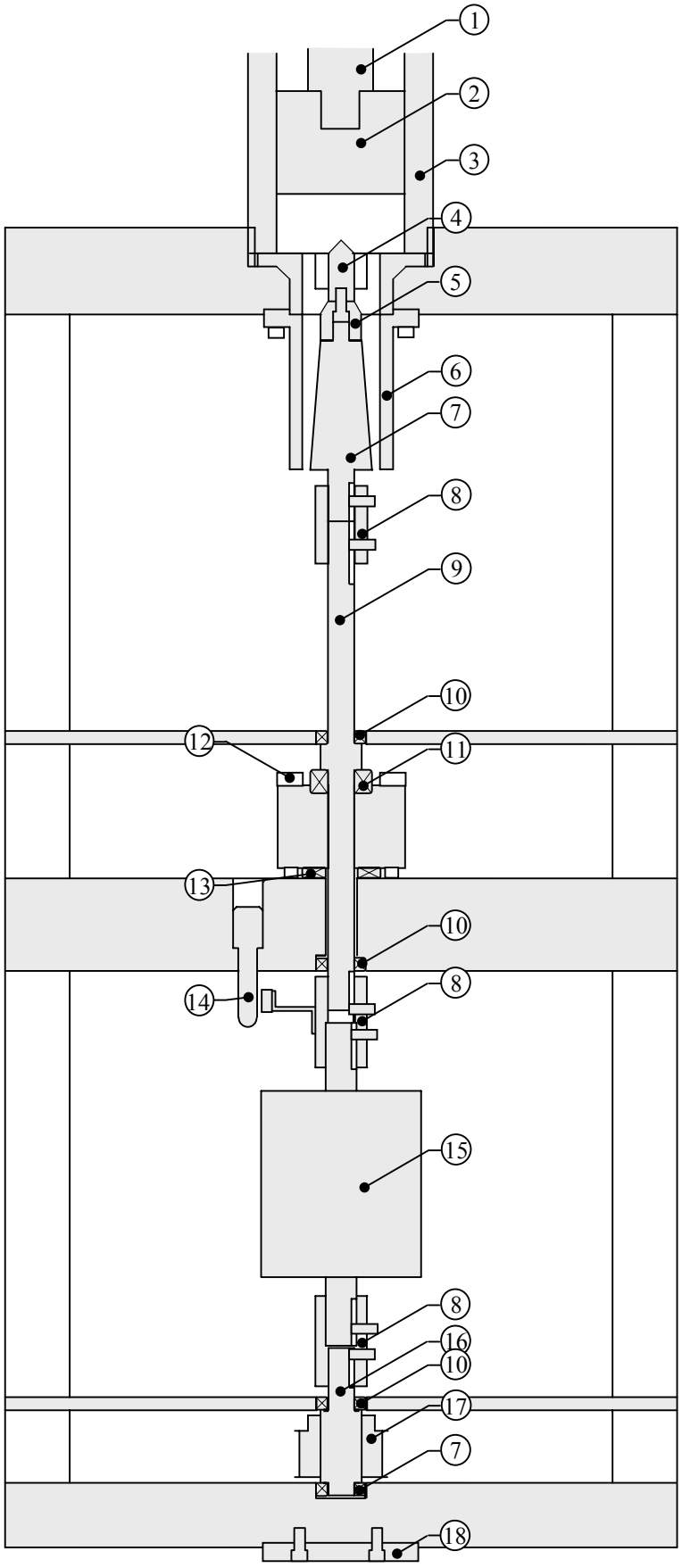

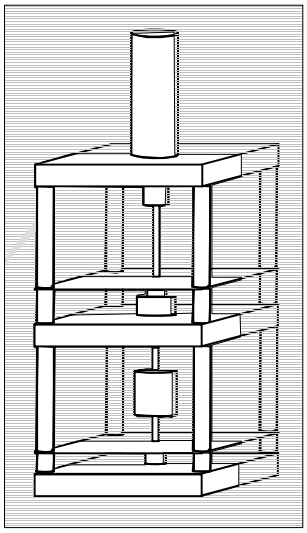

Plane of cross-section

Item	Description
18	Strain frame locator
17	Pulley
16	Lower spindle
15	Torque transducer
14	Speedometer
13	Force transducer
12	Pre-load bolts
11	Axial load bearing
10	Radial load bearing
9	Upper spindle
8	Sleeve
7	Core 2
6	Screen
5	Core 1
4	Die
3	Feed barrel
2	Piston
1	Ram

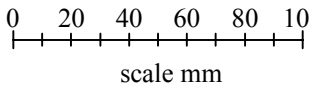

Figure 5.2 Cross-section through rotating core module

Area shaded is where module has been sectioned.

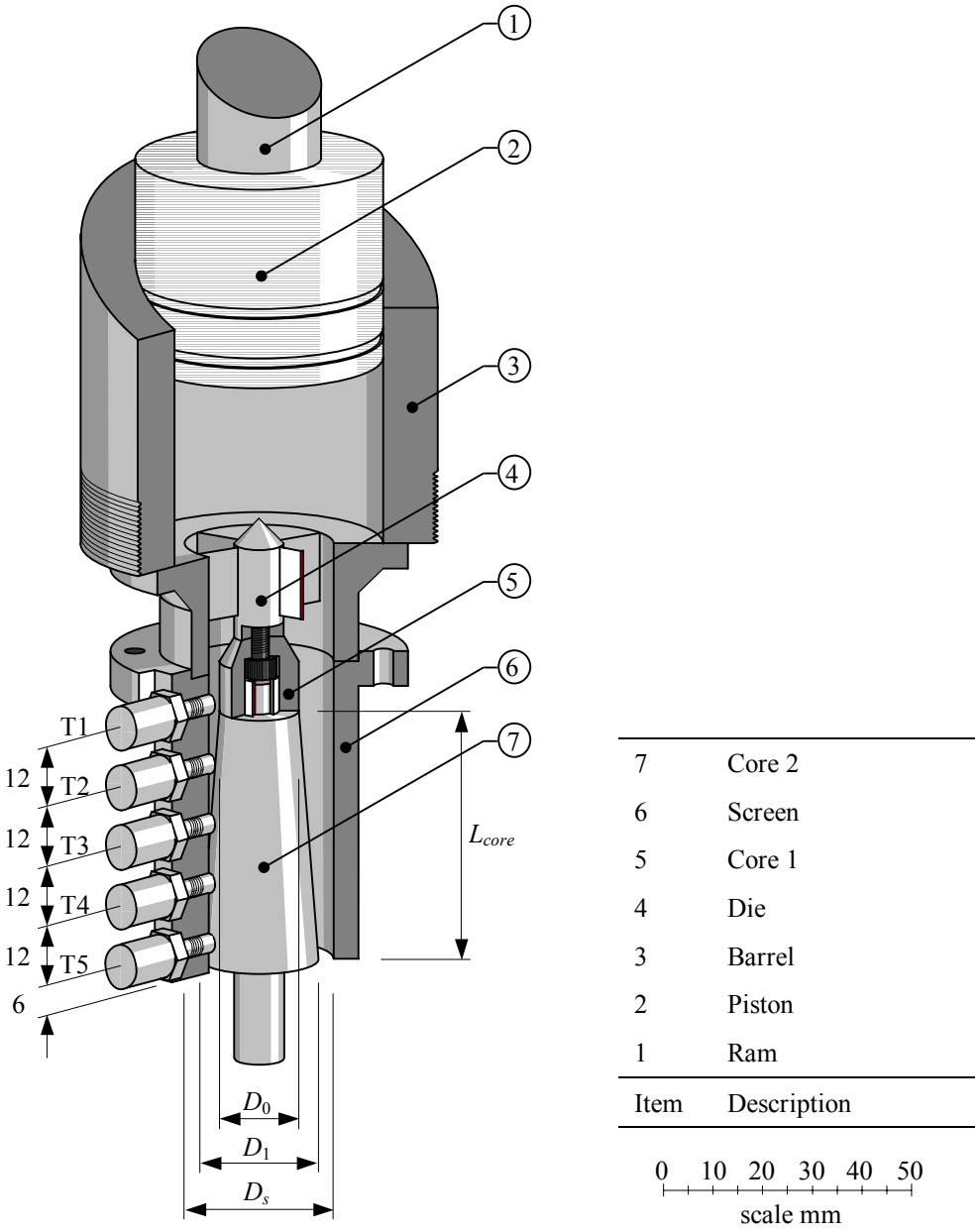

Figure 5.3 Cut away view of extrusion region of rotating core module

Dimensions shown in mm.

5.1.2 Sample *rotating core module* results

The barrel was loaded with 500 g of the model talc paste, weighed out on a balance (BA 6100 Sartorius balance, Sartorius Ltd., Edgewood, New York, USA). With a blank die at the end of the feed barrel, the paste was compacted manually into the barrel with a rod. A pre-compaction stress of 5 MPa was then applied for a few seconds using the strain frame apparatus, following which the barrel and blank die were removed from the module. A rotating die with an initial diameter, D_0, of 15 mm and final diameter, D_1, of 25 mm was located within the blank screen and fixed to the upper spindle. A stationary core of 15 mm diameter was attached to the webbed die, which was then inserted on top of the rotating core and clamped in position by re-attaching the barrel.

The core was rotated at 0.75 rotations/second and the piston driven at 0.4 mm/s. The following data were recorded at a frequency of 5 Hz: the axial force on the piston, the axial force on the rotating core, the torque on the rotating core, and the radial stress at five points along the screen length. The sample results are presented in Figure 5.4.

Firstly, in Figure 5.4 *(a)*, we see the profile of the axial force on the piston over the duration of the experiment. The stress increases as the paste is compacted and forced to flow through and fill the whole apparatus volume, until it reaches a peak and then a steady state flow region. The peak stress approached 5 MPa, the same as the stress which was found necessary in Section 3.4.1 to satisfactorily compact the paste. No output from the core axial force or spindle torque transducers is measured for some time, as evident in *(b)* and *(c)*. Only when enough paste has flowed to start filling the region between the screen and the core are a force and torque registered. Again these pass through a peak and settle at a steady value. There was noticeable noise in both of these readings; the detailed presentation in *(d)* shows that the noise is a periodic oscillation which was not present in the stress on the piston. The frequency of oscillation for both the force and torque data was measured at 0.75 Hz, which matches the rotational speed of the core. It was most likely that this oscillation was caused by a slight eccentricity of the rotating core. Figure 5.4 *(e)* shows a similar delay before the paste makes contact with the pressure transducers, and, as expected, the transducers give an output in sequence. Again the screen radial stress passes through a peak before reaching a steady state value. The axial variation of the steady state screen radial stress is shown in *(f)*, which shows a slightly convex decay from the initial value of 1.5 MPa to zero at the exit.

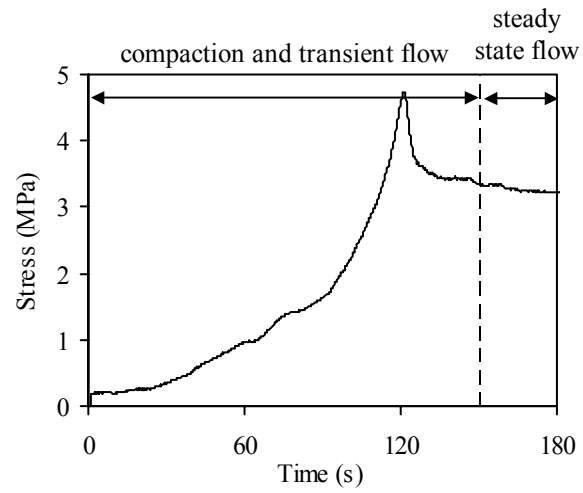

(a) Axial stress on piston against time

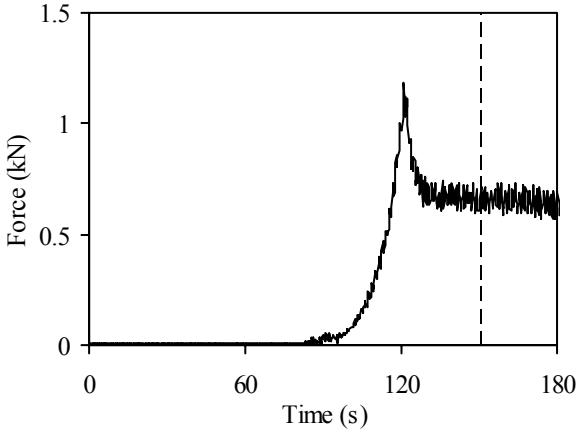

(b) Axial force on rotating core against time

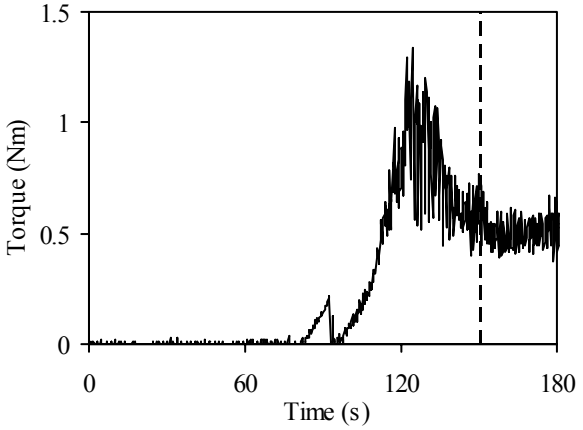

(c) Spindle torque against time

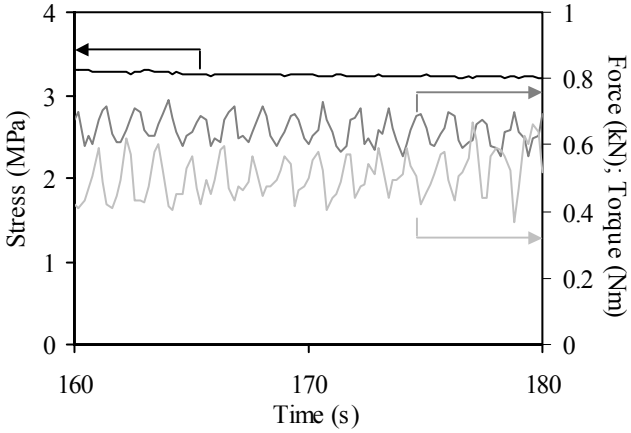

(d) Figures (a), (b) and (c) compiled

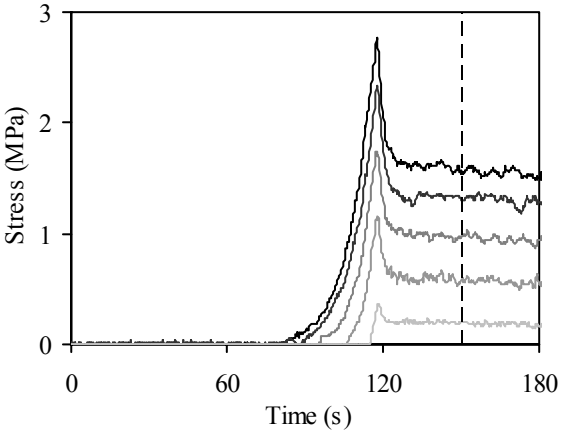

(e) Radial stress on screen against time

T1 T2 T3 T4 T5 *quartile.*

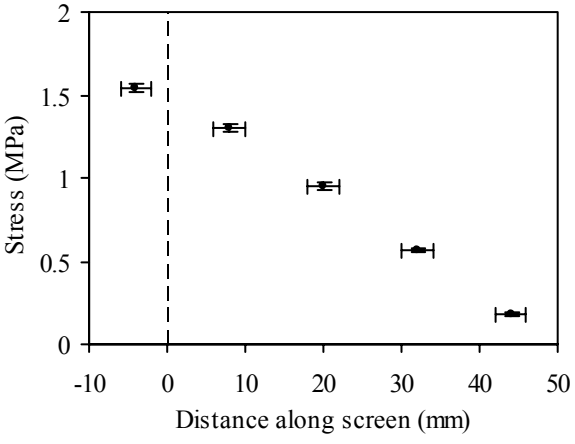

(f) Distribution of radial normal stress on screen

Stress error bars extend over 1st to 3rd

Distance error bars span transducer width.

axial stress on piston
axial force on rotating core
spindle torque

Figure 5.4 Sample results from a rotating core module experiment (no blade)
$\alpha V^m/\sigma_0 = 1.77$, $\beta V^n/\sigma_0 = 0.327$, $\pi D_s S/V = 23.2$, $D_0/D_s = 0.488$, $\phi = 5.71°$

5.2 Nip module

5.2.1 Module design

The *nip module*, detailed in Figures 5.6 to 5.8, was designed to study flow pattern ④ in the nip between the blade and the screen, (see Figure 4.10). The module design allowed for only a narrow variety of geometries and operating parameters, but enabled detailed measurement of the flow patterns and stress distributions.

The pressure transducers mounted in the screen of the *rotating core module* allowed the radial stress on the screen to be measured as the blade passed by, but the dimensions of the transducers were approximately the same as the dimensions of the nip between the blade and the screen. Thus precise measurements of the stress state in the nip could not be readily obtained with the *rotating core module*. Also, the *rotating core module* did not allow measurement of the flow through the screen or the leakage flow between the blade and screen. The tangential flow was generated in the *rotating core module* by the relative movement between the screen and the core. This could not be practically achieved on a larger scale, so based on the second assumed flow model detailed in Section 4.2.2, a plug flow feed into the nip was used. The module was designed with the objective of achieving plane-strain flow into a two-dimensional nip.

The module was designed for use with the same strain frame as the *rotating core module*, shown in Figure 5.5. The module consisted of a rectangular barrel with a wide variety of attachments which enabled many extruder geometries to be investigated. The strain frame cross beam was used to drive a rectangular piston down the barrel and so force the paste to flow through the extruder. A previous study by Bayfield (1997) similarly attempted to develop plane strain paste flow. It was reported that the achievement of plane strain flow was limited by two factors; *(i)* insufficient module wall strength which led to bowing of the walls and leakage of paste past the piston, and *(ii)* insufficient depth which led to wall end effects being very significant. This study was based on an apparatus 80 mm wide and 20 mm deep, constructed from 10 mm thick brass and polycarbonate. To reduce the significance of any end effects, the *nip module* was designed with the same 80 mm width, but with an increased depth of 60 mm. To reduce wall bending and leakage, all of the module was constructed from stainless steel with the barrel walls being 20 mm thick.

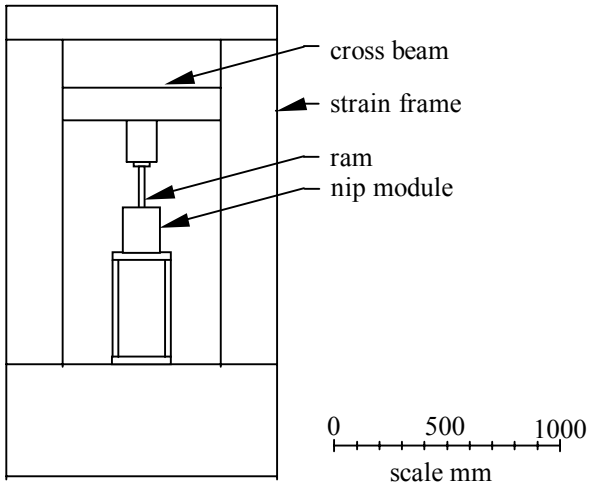

Figure 5.5 Nip module arrangement with strain frame

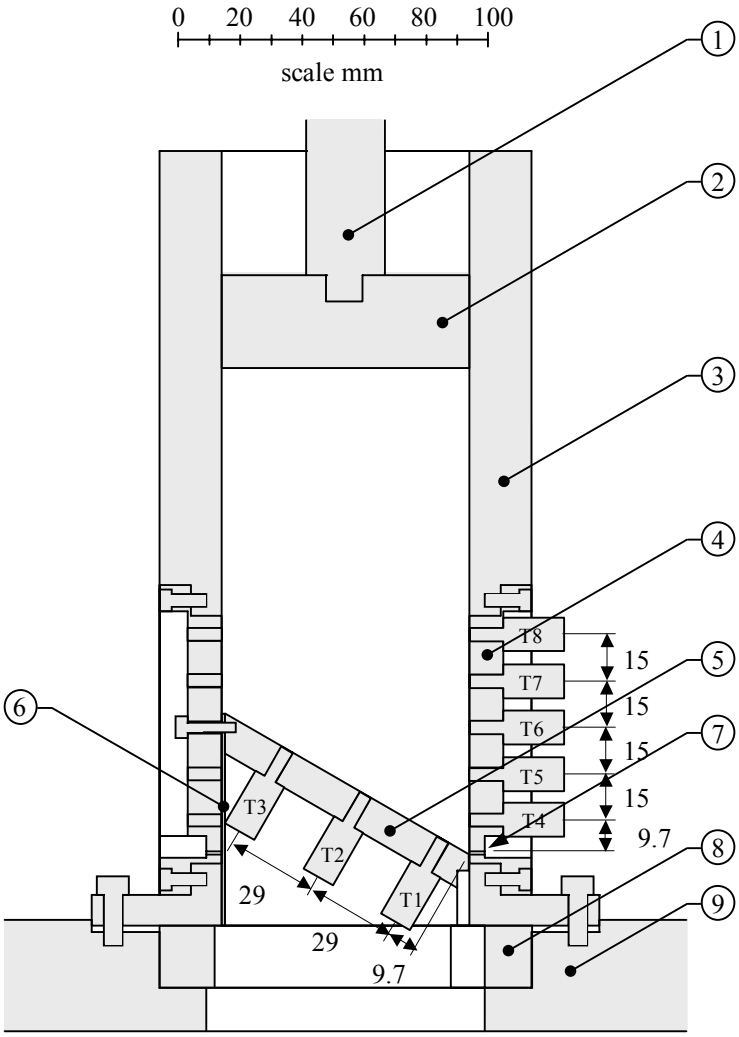

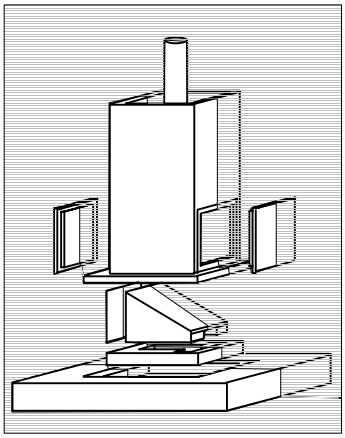

Plane of cross-section through exploded module

Item	Description
9	Base plate
8	Base insert
7	Side plate die slot
6	Spacer
5	Wedge
4	Side plate
3	Feed barrel
2	Piston
1	Ram

Figure 5.6 Cross-section through nip module

Area shaded is where module has been sectioned.

The *nip module* was based around the rectangular feed barrel [3] which was secured with bolts onto a base plate [9]. A variety of attachments could be used to create many different extruder geometries; one example is presented in Figure 5.6. The barrel has a window opening on either side into which side plates [4] are secured with bolts. A base insert [8] is clamped between the barrel and the base plate to support an internal wedge [5]. The angle between the wedge and the vertical barrel wall is the nip angle. The side plates are multi-use; to secure the wedge a bolt is inserted through the suitable side plate hole, and hence the other remaining holes are blocked. This flexible design potentially allows a wide range of plane strain flow patterns to be studied; here we shall only present the case of flow into a nip.

Figure 5.6 shows the module arrangement for extrusion into a nip of 60° with extrudate flow out of the side plate die slot only [7]. The side plate die slot has a height of 1.3 mm. The module was used to study three different nip flow conditions as illustrated in Figure 5.7; nip extrusion to the side, nip extrusion to the side and front, and nip extrusion to the front. When the spacer [6] is in place, both edges of the wedge are tight against the barrel and the front of the extruder is sealed. In this case, using a slotted side plate in the barrel allows paste to flow through the side of the extruder only, as shown in Figure 5.7 *(a)*. When the spacer is removed and a bolt used to pull the wedge tight against one wall, the paste can flow through the resulting 1.3 mm gap at the front of the extruder as well as through the side, as shown in *(b)*. The slotted barrel side plate is replaced with a blank side plate to allow flow through the front of the extruder only, as shown in *(c)*.

The mean axial stress on the piston was taken as the extrusion pressure. The array of pressure transducers, T1 – T8, were those used in the *rotating core module*, and measured the normal stress on one or both of the walls of the nip over a range of distances. Extrudate could be readily collected, allowing comparison of flow rates throughout the side and front flow case.

Preliminary experiments extruding the model talc paste through the module showed that extrudate flowing from the die slot had a significantly greater velocity in the middle than at the edges. An image of a length of this extrudate is shown in Figure 5.8 *(a)*. Much tearing of the extrudate edges is evident as the paste flows faster in the centre. This evidence suggested that the flow pattern was not very close to a plane-strain flow. A thin layer of petroleum jelly was smeared onto the facing barrel walls in Figure 5.6. This

enhanced wall slip at these surfaces and resulted in extrudate flow which could be well described as plug flow. An image of a length of this extrudate is shown in Figure 5.8 *(b)*. It can be seen that there is much less tearing at the wall and the sample looks as though it extruded as a plug.

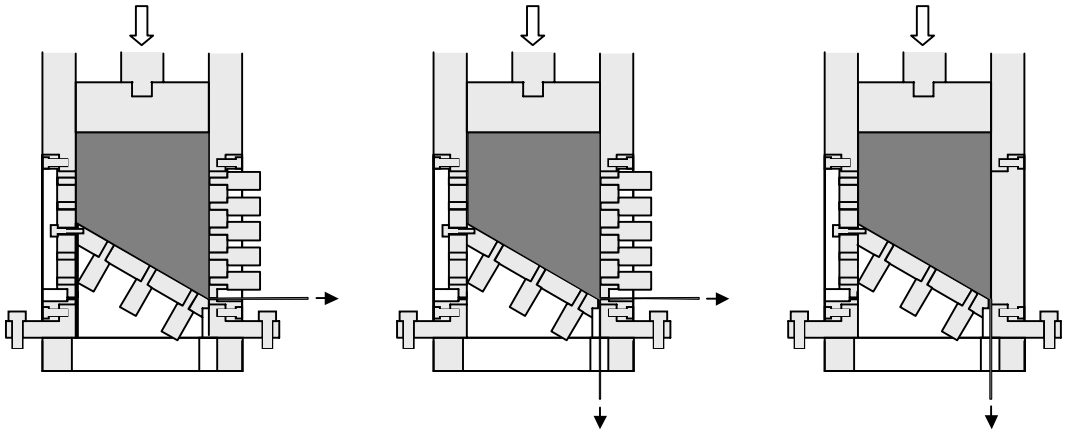

(a) Extrusion to the side *(b) Extrusion to the side and front* *(c) Extrusion to the front*

Figure 5.7 Cross-sections showing three nip extrusion flow conditions

Paste

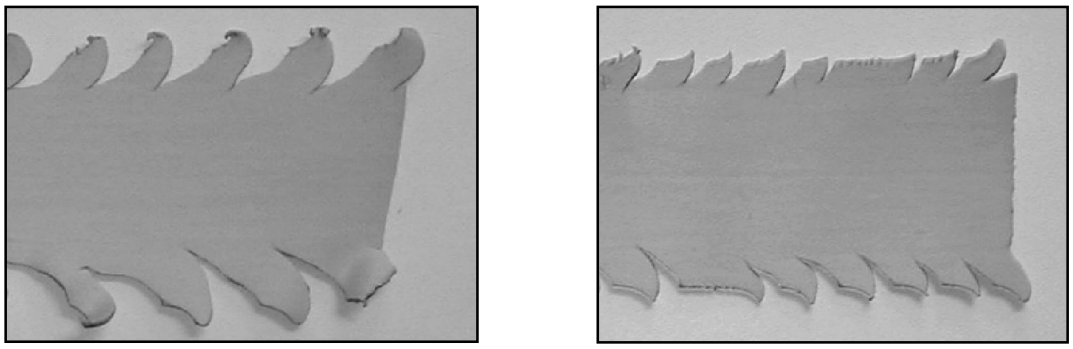

(a) No wall lubrication *(b) Barrel wall lubricated*

Figure 5.8 Nip module extrudate images

Left to right extrudate flow.

Table 5.2 overleaf presents the range of practical operating conditions which were possible using the *nip module* with the model paste best fit parameters given in Table 3.5. For comparison, the table also shows the conditions which might be expected in an industrial extruder using the data given in Appendix A.

The *nip module* enabled the measurement of the wall normal stress profile along the length of both surfaces to the nip, as well as the extrusion pressure over the whole range of possible experimental conditions. For illustrative purposes a set of sample results is now considered.

Table 5.2 Practical module operating condition and geometry

Group type	Operating condition	Module range	Typical industrial value
Paste property	$\alpha V^m/\sigma_0$ *	0 - 6	4.9
"	m	0.23	0.23
"	τ_0/σ_0	0	0
"	$\beta V^n/\sigma_0$ *	0 – 1.3	1.0
"	n	0.26	0.26
Screen geometry	W_{screen}/h	any	0.005
"	L_{screen}/h	any	0.005
"	$1-\lambda$	any	0.2
Blade geometry	W_{blade}/h	any	0.01
"	n_{blade}	1	3
"	ζ	90°	81°
"	θ	any	47°
"	L_{blade}/h	any	0.03

** Here the extrudate velocity is taken as the mean velocity of paste flowing through the die slots, or the radial extrudate velocity given in Table A.2.*

5.2.2 Sample *nip module* side flow results

The spacer and a 60° nip wedge were attached in the barrel, and a blank side plate fixed in the barrel window. The barrel was then bolted onto the base plate, sandwiching the base insert in place. The barrel was loaded with between 1250 and 1350 g of model talc paste, weighed out on a balance, then compacted manually with a rod. The paste was then pre-compacted to a stress of 5.2 MPa applied by the piston for a period of a few seconds. The blank side plate was replaced with a slotted side plate. The piston was then lowered to contact the paste, and then run at a constant velocity of 0.2 mm/s. Piston axial force and normal stress at the wall was measured at a frequency of 1 Hz. The sample *nip module* results are presented in Figure 5.9.

Firstly, in Figure 5.9 *(a)* we see the profile of the extrusion pressure over the duration of the experiment. The extrusion pressure increases as the paste is compacted and flow commences. After passing through a peak, the extrusion pressure reaches a steady value of 2.3 MPa at around 180 s. A similar pattern can be seen in both wedge and barrel wall normal stress plots, Figure 5.9 *(b)* and *(c)* respectively. The mean normal stress was calculated over the steady period for each wall position, and the resulting wall normal stress profile against distance from die entry is shown in Figure 5.9 *(d)*. The normal

stresses measured at the barrel wall and wedge surface are effectively equal, despite the difference in angle with respect to the piston driving force. The stress appears to decrease weakly and linearly as the entry is approached. The stress profile over the last 10 mm before the die entry is not known, and this may deviate from the quasi-linear trend.

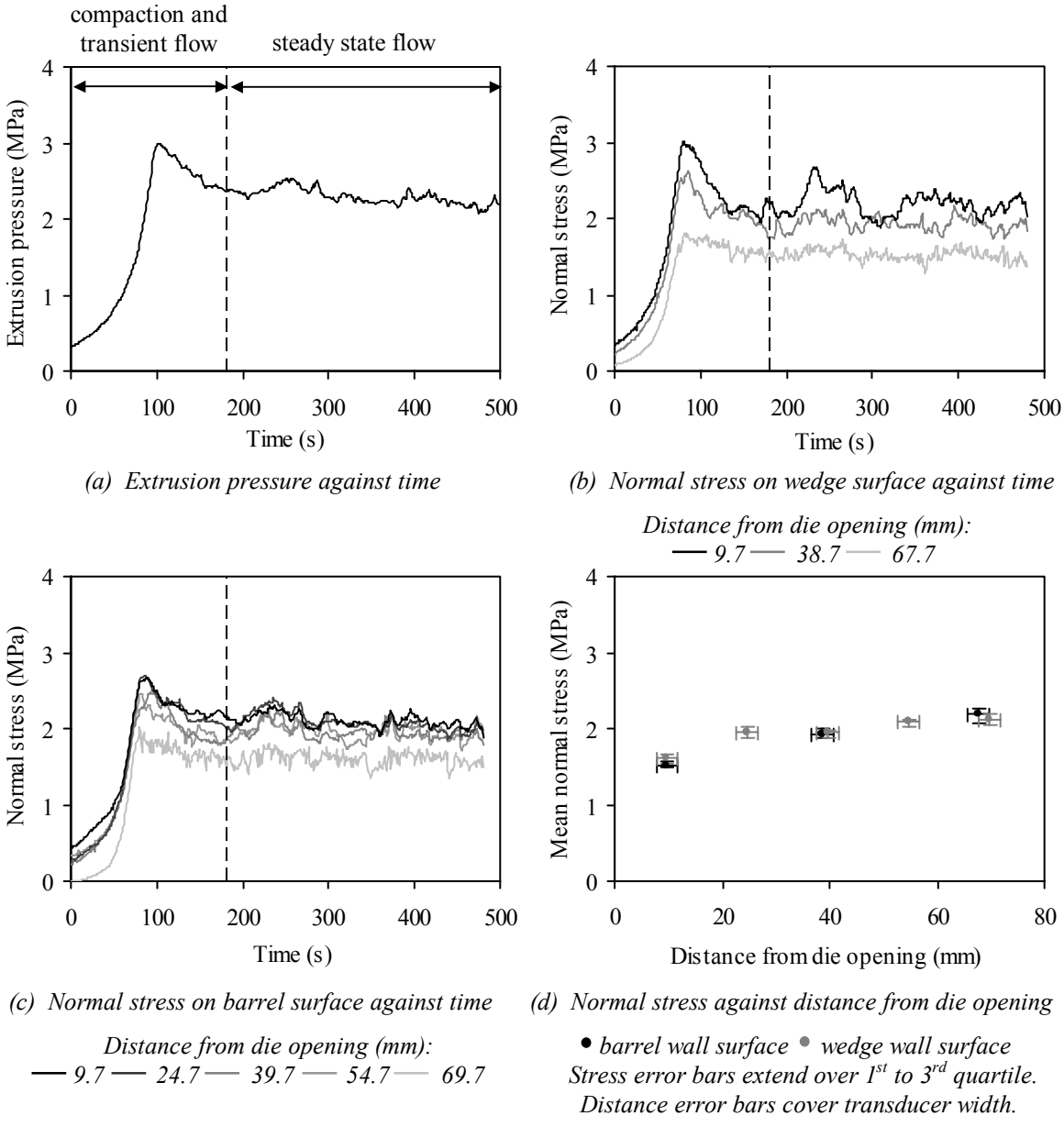

(a) Extrusion pressure against time

(b) Normal stress on wedge surface against time

(c) Normal stress on barrel surface against time

(d) Normal stress against distance from die opening

Figure 5.9 Sample results from a nip module experiment

$\alpha V^{*n}/\sigma_0 = 2.42$, $\beta V^{*n}/\sigma_0 = 0.467$, $D_0/D = 0.0163$, $L/D_0 = 0.0625$, $\theta = 60°$

5.3 Summary

This Chapter has detailed the design and use of two versatile extruder modules which may be used to investigate the flow of paste in the head of a radial screen extruder. The proposed flow pattern developed in Chapter 4 was used as a guide for the module design. The experimental use of the modules has been outlined in detail for reference in later Chapters. Finally, the ability of the modules to measure accurate stress distributions within various parts of a radial screen extruder head, which has never been achieved before, has been demonstrated.

6 Screen extruder flow model

In this Chapter we present a model for the flow of paste material in a single screw radial screen extruder with a screw feed. The Chapter contains two main parts. The first, Section 6.1, concerns the presentation and justification of the model. Then in Section 6.2 the model is assessed on its own terms, based on an industrial case.

We noted in Section 4.2 that the existing understanding of paste screw extrusion could be a suitable starting point for understanding radial screen extrusion. In this Chapter we present a model for the flow of paste in a single screw radial screen extruder with varying channel depth and a conical core. A single-screw extruder was chosen for simplicity, further development of the model might enables its use with twin-screw extruders. An upper bound modelling approach is used, where a flow pattern is assumed from which the stress distribution and rate of energy dissipation are calculated using the Benbow-Bridgwater approach. Flexibility in the assumed flow pattern enables an optimum flow pattern to be found based on a minimum work requirement. This model is the first reported flow model for radial screen extrusion.

The model is widely adaptable for use on many types of extrusion from simple screw extrusion with a parallel sided screw core to a full screw feed radial screen extruder. The model has not been extended to the twin-screw extruder case, but it is thought that the single screw model may still be able to give insight into twin-screw extruder operation. In the following Chapter we assess the model against experimental results obtained with the extruder modules discussed previously.

Throughout this Chapter, the notation is occasionally abbreviated to avoid excessively lengthy equations and enable clearer labelling of figures. For example, the number of blades on the extruder head, n_{blade}, might be abbreviated to n_{bl}.

6.1 Development of model

This model is a development of the model presented by Burbidge and Bridgwater (1995) for the flow of paste in a screw extruder with a constant channel depth. These authors applied the principle of mechanical equilibrium over an element of paste in the screw channel to analyse the flow, which was adequate for their case. Botten *et al.* (2002) have presented a continuation of this model for the case of non-constant screw depth. Again, they applied the principle of mechanical equilibrium and considered the forces due to shear stress at the walls and the normal direct stresses, but also included a force term associated with the deformation of the material. This might be considered to be a conflation of two principles – mechanical equilibrium and conservation of energy – even if it does lead to the same result in their case.

In order to present a coherent analysis we use only a conservation of energy analysis. The rate of work done in rotating the screw relatively to the barrel is balanced against the rate of work done against interfacial shear stresses, direct normal stresses and internal deformation. We consider a frustum screw with attached blade (or flight), illustrated in Figure 6.1 *(a)* overleaf, and balance the rate of work done on and by the shaded element.

6.1.1 Channel geometry

Unrolling a screw channel

For simplicity, we assume that the back edge of the blade is not inclined, although this assumption could be relaxed if it proved necessary. The screw shown has only a single blade, but the analysis is generalised to n_{blade} blades, although the analysis is only for the case of a screw with a constant pitch. We define two axes, the linear $\boldsymbol{x}$ axis along the length of the screw and the helical $\boldsymbol{l}$ axis along the barrel surface. These are shown in Figure 6.1 *(b)*, along with the frustum half angle, ϕ, and the helix angle of the screw ζ. The distance along the $\boldsymbol{l}$ axis and the $\boldsymbol{x}$ axis are related by,

$$\frac{x}{l} = \sin\zeta \tag{6.5}$$

To facilitate the analysis the element of paste is unrolled, following the approach of Darnell and Mol (1956), such that the helical $\boldsymbol{l}$ axis becomes linear and the curved surfaces are flattened, illustrated in Figure 6.1 *(c)*. This deviation from the true geometry gives a more approximate analysis, but simplifies all further calculations. The geometry of the channel element can now be readily calculated, as shown in Figures 6.2 to 6.6.

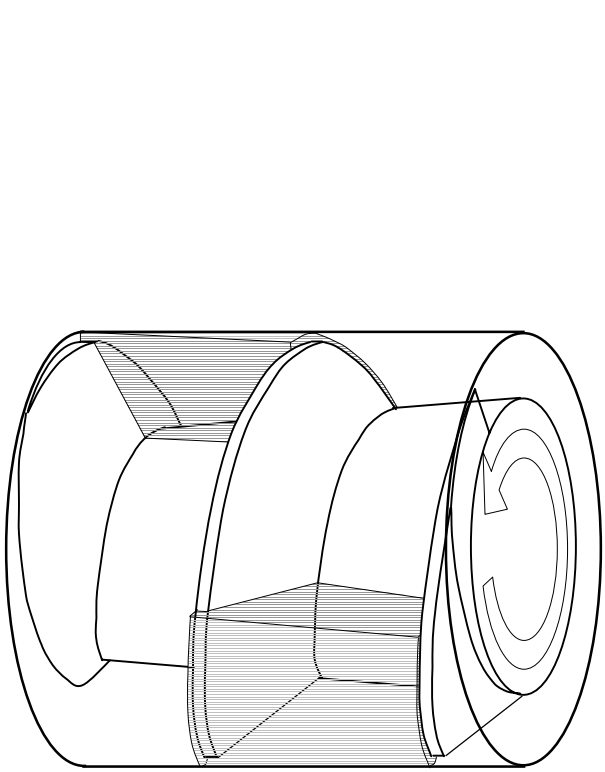

(a) Section of channel in a single screw extruder

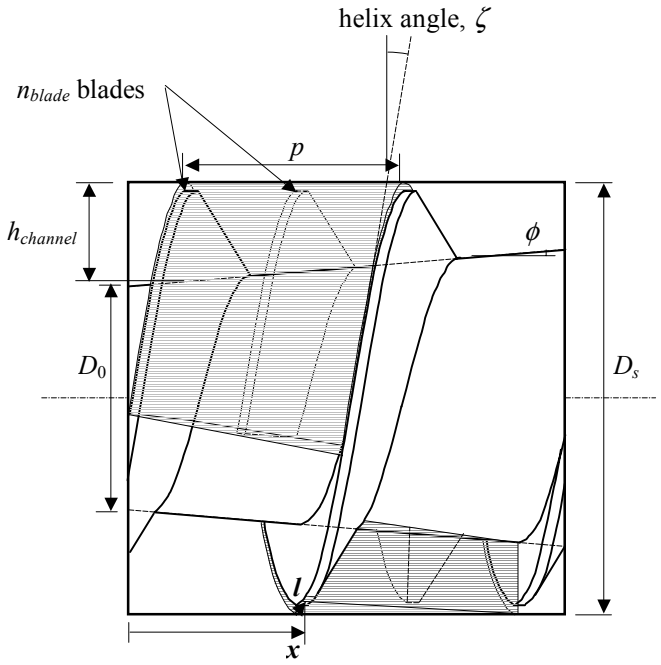

(b) Plan view of channels to be unrolled

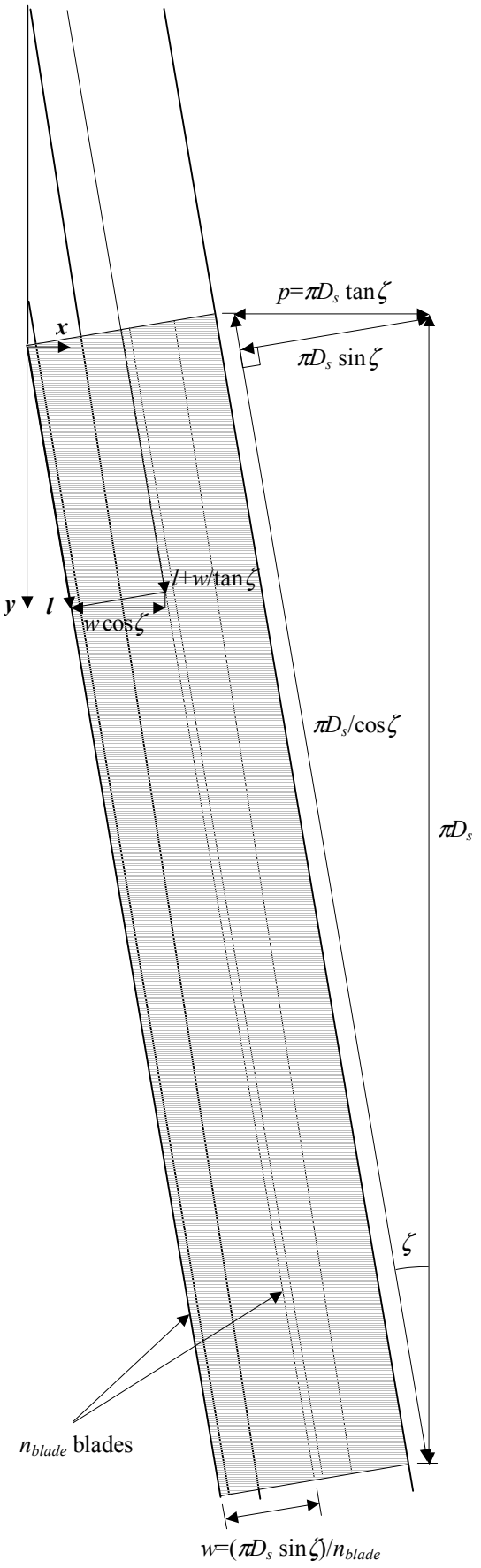

(c) Plan view of channels unrolled one revolution

Figure 6.1 A length of channel volume in a single screw screen extruder

Blade gap and screen extrusion holes geometry

The length of the blade tip and the nip angle formed between the blade and the screen vary depending on which channel cross-sectional plane is being considered. The length, L_{blade}, and angle, θ, on the plane perpendicular to the channel length axis $\boldsymbol{l}$ are required for our analysis. Often, values are only available for the length, L_{blade}', and angle, θ', on the plane perpendicular to the extruder length axis $\boldsymbol{x}$. Figure 6.2 below illustrates these respective geometries, and the conversions between the two are given by,

$$L_{blade} = L_{blade}' \sin\zeta \tag{6.6}$$

$$\theta = \tan^{-1}\left(\frac{\tan\theta'}{\sin\zeta}\right) \tag{6.7}$$

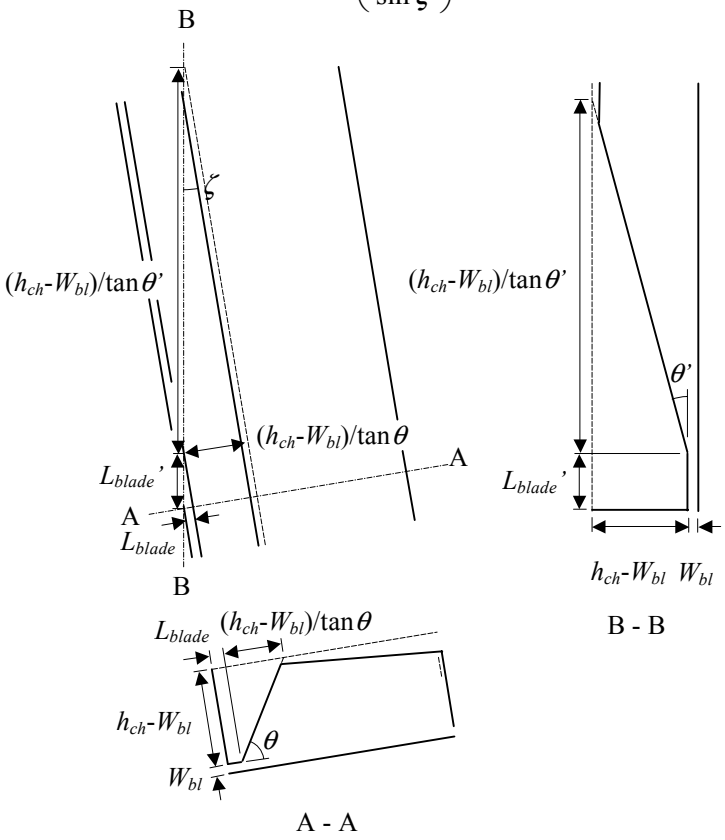

Figure 6.2 Nip angle and blade length of an infinitesimal length of unrolled channel surface

It is not known exactly how paste flows through the screen die holes. The proposed flow pattern presented in Section 4.2.2 assumed that paste is extruded through the region of the screen immediately in front of the passing blade. Given the little knowledge available, we assume that paste is extruded evenly through n_{row} rows of die holes in front of the blade. We assume that the hole rows are parallel to the blade edge, as the actual orientation of the hole rows on an extruder screen is not known. To simplify the analysis, the die hole rows are approximated by a single, parallel sided slot in the screen located

immediately in front of the blade, as shown in Figure 6.4 below. The width, W_{screen}', and length, L_{screen}', of this pseudo die slot are such that the die land surface area per screen length and cross-sectional area per screen length are equal to the total die hole surface area and cross-sectional areas per screen length respectively. The resulting dimensions are given by,

$$L_{screen}' = \frac{\pi D_{hole} L_{hole} n_{row}}{2 p_{hole}} \tag{6.8}$$

$$W_{screen}' = \frac{\pi D_{hole}^{\,2} n_{row}}{4 p_{hole}} \tag{6.9}$$

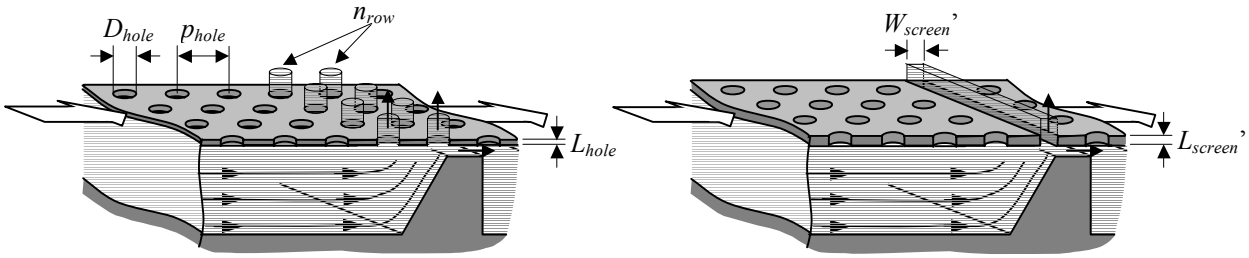

(a) Even flow through n_{row} die holes *(b) Flow through pseudo die slot*

Figure 6.3 Channel showing extrusion through screen die land

Channel core surface plane

The uppermost surface of an unrolled section of channel volume, as shown in Figure 6.4 *(a)* overleaf, is in contact with the channel core. The plane in which this surface lies in may be determined by considering the inclination of the core surface with respect to the extruder and channel axes, shown in Figure 6.4 *(b)* and *(c)*.

Through calculation of the lengths ac and df respectively, the angle of inclination in the ***l***-direction, χ, and the angle inclination in the ***w***-direction, ψ, may be expressed as,

$$\tan\chi = \sin\zeta \tan\phi \tag{6.10}$$

$$\tan\psi = \cos\zeta \tan\phi \tag{6.11}$$

With these angles, the height of the channel, $h_{channel}$, is given by,

$$h_{core} = h_0 - l\tan\chi - w\tan\psi \tag{6.12}$$

where the initial channel height, h_0, is,

$$h_0 = \frac{D_s - D_0}{2} \tag{6.13}$$

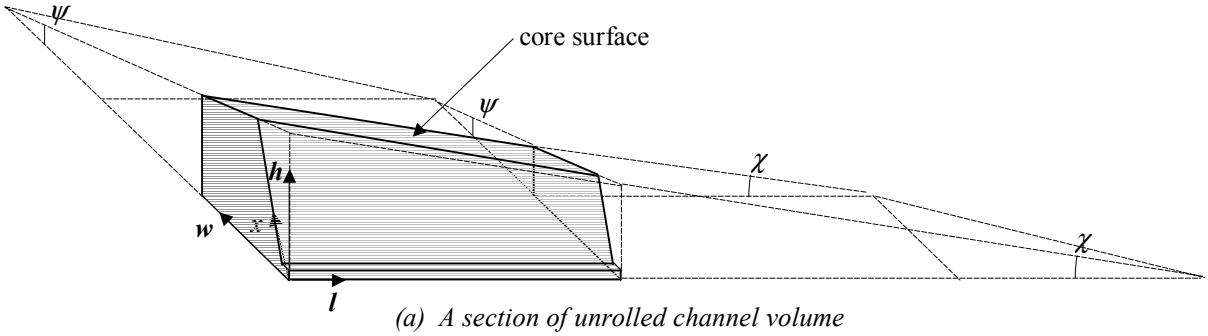

(a) A section of unrolled channel volume

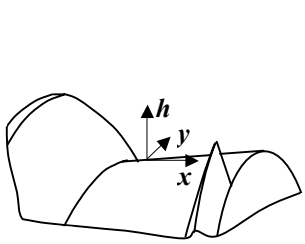

(b) Orientation of axes on channel

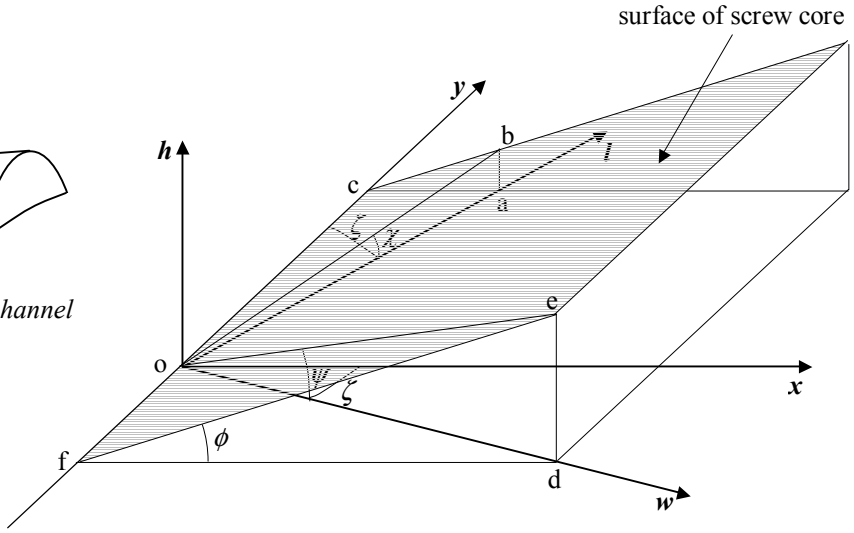

(c) Channel core surface orientation

Figure 6.4 Determination of channel volume core surface plane

Extruder exit

A radial screen extruder might typically have a dam at the end of the extruder head to restrict the over flow through the end, illustrated in Figure 6.5 below. Often the gap between the dam and the screen, W_{dam}, is the same as the gap between the blades and the screen, W_{blade}.

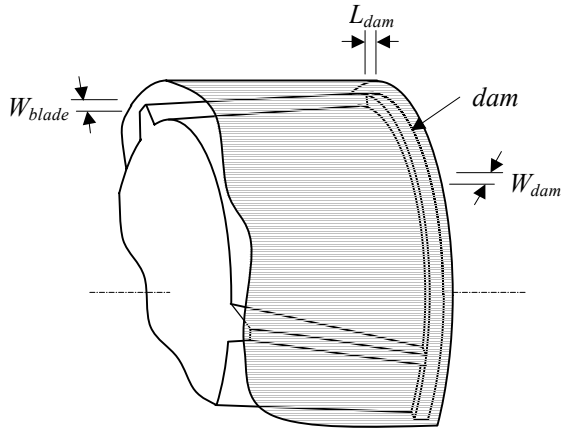

Figure 6.5 Section of extruder showing the exit dam

Cross-section geometry

The geometry of the channel cross-section normal to the longitudinal direction ***l*** is illustrated in Figure 6.6. Two possible geometries are shown depending on the dimensions in the vicinity of the nip. Various points across the channel cross-section are indicated with letters a through t. At the end of the channel we assume that the dam may be approximated as being perpendicular to the longitudinal direction without too much error. Letters u and v indicate the dam at the end of the channel. The lengths between pairs of points are listed in Table 6.1 overleaf. Also listed are the radial distances r_0 and r_1 away from point h, which will be used regularly throughout the analysis.

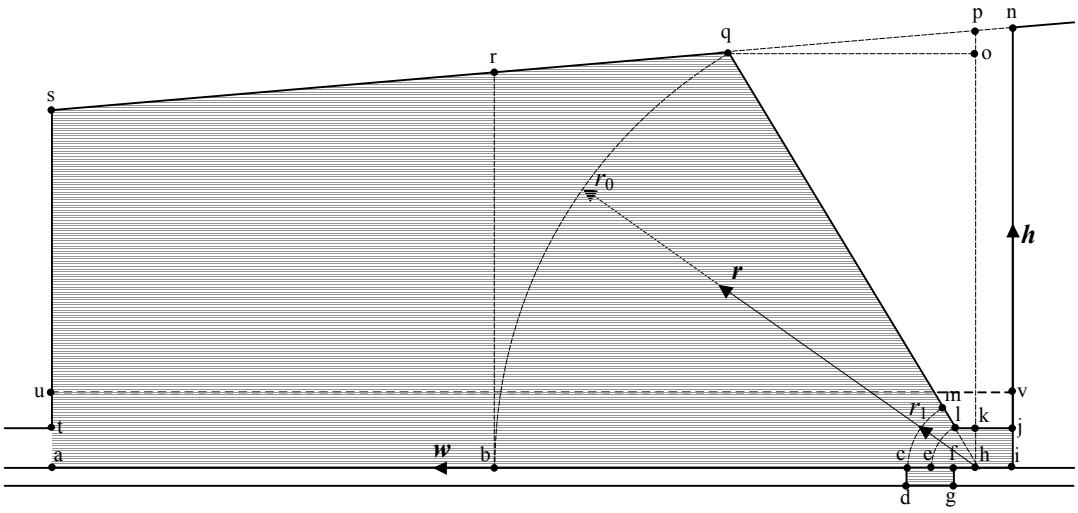

(a) $W_{screen}'+W_{blade}/\tan\theta > W_{blade}/\sin\theta$

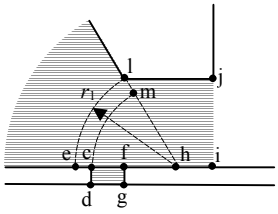

(b) $W_{blade}/\sin\theta > W_{screen}'+W_{blade}/\tan\theta$

Figure 6.6 Channel geometry; cross-section looking along length axis

Table 6.1 Channel cross-section dimensions

General perimeter lengths			
ai	w	in	h_0-$l\tan\chi$
ns	$w/\cos\psi$	sa	h_0-$l\tan\chi$-$w\tan\psi$
Perimeter section lengths			
ab	w-L_{blade}+$W_{blade}/\tan\theta$-r_0	bc	r_0-W_{screen}'-$W_{blade}/\tan\theta$
cf	W_{screen}'	dg	W_{screen}'
cd	L_{screen}'	fg	L_{screen}'
fh	$W_{blade}/\tan\theta$	lk	$W_{blade}/\tan\theta$
fi	L_{blade}	lj	L_{blade}
hi	L_{blade}-$W_{blade}/\tan\theta$	kj	L_{blade}-$W_{blade}/\tan\theta$
fl	W_{blade}	ij	W_{blade}
hc	W_{screen}'+$W_{blade}/\tan\theta$	hm	W_{screen}'+$W_{blade}/\tan\theta$
he	$W_{blade}/\sin\theta$	hl	$W_{blade}/\sin\theta$
hq	r_0	hb	r_0
qr	$r_0(1-\cos\theta)/\cos\psi$	rs	$(w-L_{blade}+W_{blade}/\tan\theta-r_0)/\cos\psi$
st	h_0-$l\tan\chi$-$w\tan\psi$-W_{blade}	ta	W_{blade}
au	W_{dam}	iv	W_{dam}
Radial distances from point h			
r_1	Maximum(hc/hm, he/hl) = Maximum(W_{screen}'+$W_{blade}/\tan\theta$, $W_{blade}/\sin\theta$)		
r_0	$(h_0-l\tan\chi-(L_{blade}-W_{blade}/\tan\theta)\tan\psi)/(\sin\theta+\cos\theta\tan\psi)$		

The cross-sectional area of the channel, A, may be expressed as,

$$A = \frac{1}{2}\mathrm{sa}(\mathrm{ai}-\mathrm{hi}) + \frac{1}{2}r_0((\mathrm{ai}-\mathrm{hi})\sin\theta - \mathrm{sa}.\cos\theta) + \mathrm{fi.ij} - \frac{1}{2}\mathrm{fh.fl} \tag{6.14}$$

which, written in full is,

$$\begin{aligned} A = {} & \frac{1}{2}\left(h_0 - l\tan\chi - w\tan\psi\right)\left(w - \left(L_{blade} - \frac{W_{blade}}{\tan\theta}\right)\right) \\ & + \frac{1}{2}\frac{h_0 - l\tan\chi - (L_{blade} - W_{blade}/\tan\theta)\tan\psi}{\sin\theta + \cos\theta\tan\psi}\begin{pmatrix}(w - (L_{blade} - W_{blade}/\tan\theta))\sin\theta \\ -(h_0 - l\tan\chi - w\tan\psi)\cos\theta\end{pmatrix} \\ & + L_{blade}W_{blade} - \frac{1}{2}\frac{{W_{blade}}^2}{\tan\theta} \end{aligned} \tag{6.15}$$

From this the rate of change of cross-sectional area over the length of the channel is found to be,

$$\frac{\mathrm{d}A}{\mathrm{d}l} = -\frac{\tan\chi}{\tan\theta+\tan\psi}\left(\left(w - \left(L_{blade} - \frac{W_{blade}}{\tan\theta}\right)\right)\tan\theta - (h_0 - l\tan\chi - w\tan\psi)\right) \tag{6.16}$$

An element of the cross-section perimeter next to the screen of width dw and length dl has area dA_{ai},

$$\mathrm{d}A_{ai} = \mathrm{d}w\mathrm{d}l \tag{6.17}$$

The corresponding perimeter element next to the core has area dA_{sq},

$$\mathrm{d}A_{sq} = \mathrm{d}w\mathrm{d}l/(\cos\chi\cos\psi) \tag{6.18}$$

6.1.2 Flow patterns

The paste velocity at any point is made up of three orthogonal components in the ***l***, ***w*** and ***h***-directions. Velocity in the ***l***-direction is associated with flow along the channel length parallel to the screen. Velocity in the ***w***-direction is associated with flow across the channel cross-section and parallel to the screen. Velocity in the ***h***-direction is flow perpendicular to the screen.

As was discussed in Section 4.2, we shall consider the paste flow in terms of its longitudinal and cross-sectional components, and over an element channel length we shall treat them as being independent from each other.

Flow along the channel length

Paste flow along the channel length is assumed to be towards the virtual apex made between the screen and the inclined channel core surface. It is also assumed that a distance l along the channel, the velocity in the ***l***-direction, v_l, is constant over the channel cross-section. This assumed velocity profile is illustrated in Figure 6.7.

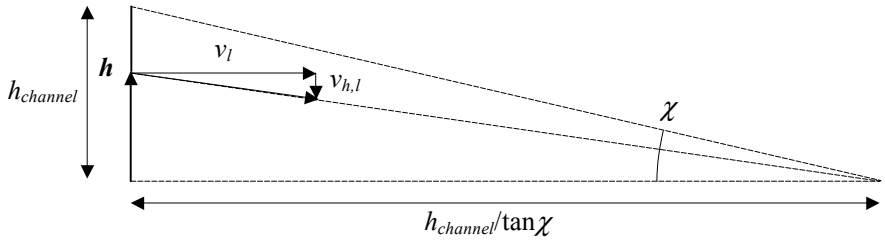

Figure 6.7 Assumed channel length flow pattern

The velocity in the ***l***-direction is given by,

$$v_l = Q_l / A \tag{6.19}$$

and by similar triangles the velocity in the ***h***-direction due to longitudinal flow, $v_{h,l}$, is given by,

$$\begin{aligned} v_{h,l} &= -v_l \frac{h}{h_{channel}} \tan\chi \\ &= -\frac{Q_l}{A}\frac{h}{h_{channel}} \tan\chi \end{aligned} \tag{6.20}$$

Flow across the channel cross-section

The paste flow across the channel cross-section was considered as six separate regions. These regions are bounded in Figure 6.8 below by fijl, cdgf, flmc (or fle depending on the geometry), bcmq (or celq), bqr and abrs. We characterise the paste flow in general by saying that a flow per unit depth of paste across the cross-section is Q_w from left to right in the figure towards the nip between the blade and screen. We also say that a fraction ε of the flow is extruded through the screen pseudo die land immediately prior to the nip. The remaining fraction (1-ε) flows through the gap between the blade and the screen.

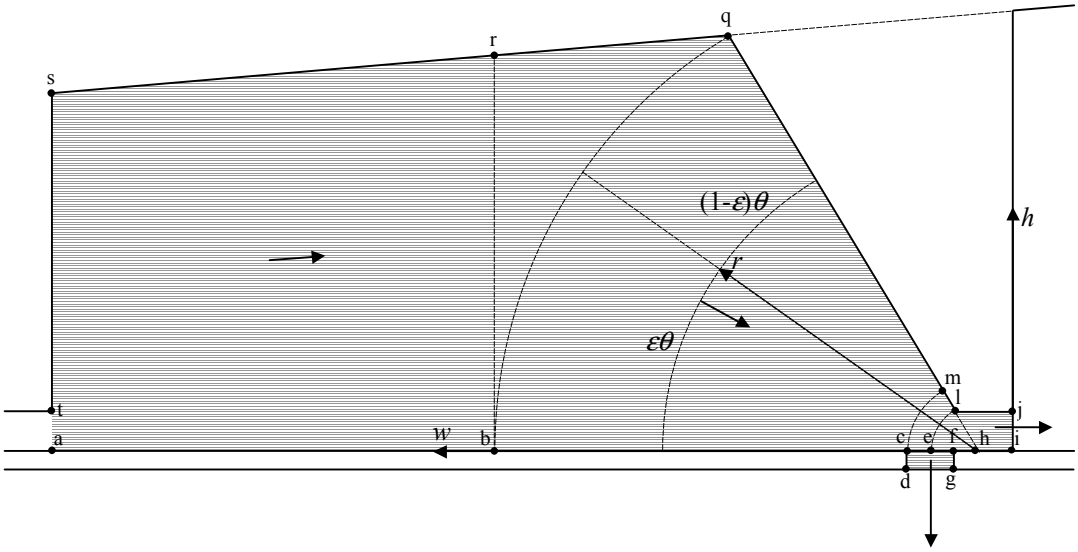

(a) Regions of flow

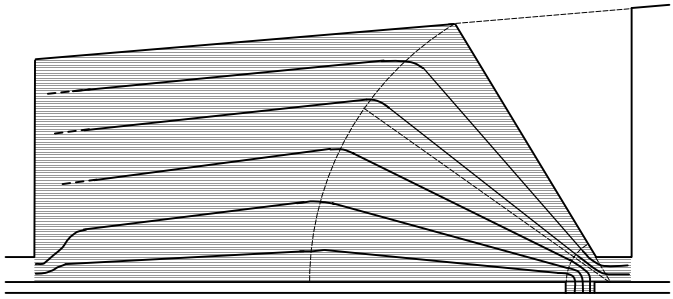

(b) Generalised flow scheme

Figure 6.8 Assumed channel cross-section flow pattern

Region abqs

Paste flow across the channel width is assumed to be away from the virtual apex made between the screen and the inclined channel core surface. It is also assumed that at a distance w across the channel, the velocity in the $\boldsymbol{w}$-direction, v_w, is constant over the channel height. This assumed velocity profile is illustrated in Figure 6.9.

The velocity in the w-direction is given by,

$$v_w = Q_w / h_{channel} \tag{6.21}$$

and by similar triangles the velocity in the ***h***-direction due to longitudinal flow, $v_{h,w}$, is given by,

$$\begin{aligned} v_{h,w} &= v_w \frac{h}{h_{channel}} \tan\psi \\ &= Q_w \frac{h}{h_{channel}^2} \tan\psi \end{aligned} \tag{6.22}$$

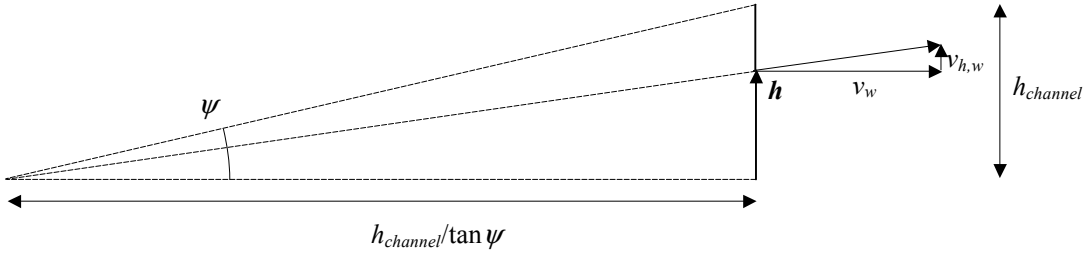

Figure 6.9 Assumed channel cross-section flow pattern over region abrs

Region brq

Paste is assumed to continue to flow away from the virtual apex made between the screen and the inclined channel core surface as a continuation of the flow from region abqs. A velocity discontinuity is assumed along the boundary bq as the flow pattern changes from that of region brq to that of region bflq (also see page 135A).

Region bflq

Paste is assumed to flow radially into the nip between the blade and the screen towards the point h. At a given distance *r* the flow has a constant velocity in the ***r***-direction, v_r. In this region a fraction ε of the flow passes through the screen and the remaining (1-ε) will flow between the screen and the blade. The radial velocity is given by,

$$v_r = -\frac{Q_w}{r\theta} \tag{6.23}$$

Along perimeter bf, the paste velocity in the ***w***-direction is equal to the radial velocity. Along perimeter lq the velocities in the ***w*** and ***h***-directions are given by,

$$v_w = -\frac{Q_w}{r\theta}\cos\theta \tag{6.24}$$

$$v_{h,w} = -\frac{Q_w}{r\theta}\sin\theta \tag{6.25}$$

In close proximity to the nip, where r is less than r_1, the flow pattern changes as paste has started to flow through the screen or past the blade. It is not clear what the flow pattern in this region might be. Although it is often only a small region, the paste velocity can be large which gives the region significance to the overall pressure profile. We assume that where paste is flowing against either the screen or blade surface the paste velocity remains constant and equal to the velocity at r_1 throughout the region.

Regions cdgf and fijl

We assume the paste to undergo plug flow through both the screen pseudo die and the gap between the blade and the screen. Through the screen the paste will have the same velocity in the ***w***-direction as the screen, and the velocity in the ***h***-direction is given by,

$$v_h = -\varepsilon Q_w / W_{screen}' \tag{6.26}$$

Throughout the gap between the blade and the screen the velocity in the ***w***-direction is given by,

$$v_w = -(1-\varepsilon) Q_w / W_{blade} \tag{6.27}$$

Flow over the exit dam, region aivu

We assume that the paste undergoes plug flow between the dam and the screen. The velocity in the ***l***-direction is given by,

$$v_l = \frac{Q_l}{W_{dam} w} \tag{6.28}$$

The paste is assumed to flow in the ***w***-direction at half the velocity of the relative screen velocity in the ***w***-direction,

$$v_w = \pi D_s S \sin\zeta / 2 \tag{6.29}$$

6.1.3 Calculation of paste slip velocities

In order to find the shear stresses acting on the paste, and thus conduct energy balances, the relative velocity of the paste to the channel boundaries must be found. Where the paste is in contact with the core and blade, the slip velocity is simply equal to the paste velocity. Where the paste is in contact with the screen, velocity triangles can be used to determine the relative velocities, as we show in Figure 6.10 overleaf. The magnitude of the barrel velocity, v_b, is given by,

$$|v_b| = \pi D_s S \tag{6.30}$$

The ***l***, ***w*** and ***h***-directional components of the paste slip velocities relative to the channel or screen walls are listed in Table 6.2 below. The slip velocity of the screen relative to the paste in the ***x*** and ***y***-directions, $v_{slip\ s,x}$ and $v_{slip\ s,y}$, respectively are,

$$v_{slip\ s,x} = -v_{slip\ \mathrm{ai},l} \sin\zeta - v_{slip\ \mathrm{ai},w} \cos\zeta \tag{6.31}$$

$$v_{slip\ s,y} = -v_{slip\ \mathrm{ai},l} \cos\zeta + v_{slip\ \mathrm{ai},w} \sin\zeta \tag{6.32}$$

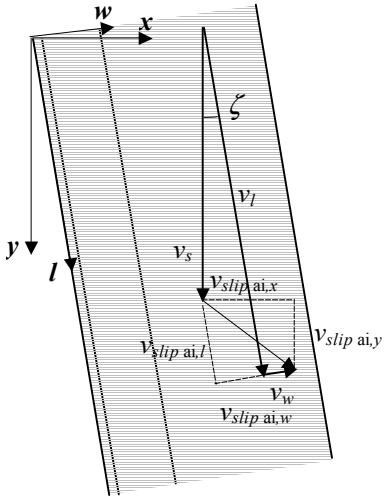

Figure 6.10 Slip velocity of paste relative to screen

Table 6.2 Paste slip velocities relative to channel and screen

Perimeter	***l*** component	***w*** component	$\boldsymbol{h}_l$ component	$\boldsymbol{h}_w$ component
ab	$Q_l/A - \pi D_S S\cos\zeta$	$-Q_w/h_{core} + \pi D_S S\sin\zeta$	0	0
bc†	$Q_l/A - \pi D_S S\cos\zeta$	$-Q_w/(r\theta) + \pi D_S S\sin\zeta$	0	0
qm†	Q_l/A	$-Q_w\cos\theta/(r\theta)$	0	$-Q_w\sin\theta/(r\theta)$
ql†	Q_l/A	$-Q_w\cos\theta/(r_1\theta)$	0	$-Q_w\sin\theta/(r_1\theta)$
be‡	$Q_l/A - \pi D_S S\cos\zeta$	$-Q_w/(r\theta) + \pi D_S S\sin\zeta$	0	0
ec‡	$Q_l/A - \pi D_S S\cos\zeta$	$-Q_w/(r_1\theta) + \pi D_S S\sin\zeta$	0	0
ql‡	Q_l/A	$-Q_w\cos\theta/(r\theta)$	0	$-Q_w\sin\theta/(r\theta)$
cd	0	0	0	$-\varepsilon Q_w/W_{screen}'$
fg	0	0	0	$-\varepsilon Q_w/W_{screen}'$
fi	$Q_l/A - \pi D_S S\cos\zeta$	$-(1-\varepsilon)Q_w/W_{blade} + \pi D_S S\sin\zeta$	0	0
lj	Q_l/A	$-(1-\varepsilon)Q_w/W_{blade}$	0	0
sq	Q_l/A	$-Q_w/h_{core}$	$-Q_l\tan\chi/A$	$Q_w\tan\psi/h_{core}$
st	Q_l/A	0	$-Q_l h\tan\chi/(Ah_{core})$	0
dam – ai	$Q_l/(W_{dam}w) - \pi D_S S\cos\zeta$	$\pi D_S S\sin\zeta/2$	0	0
dam – uv	$Q_l/(W_{dam}w)$	$-\pi D_S S\sin\zeta/2$	0	0

† *where* $W_{screen}' + W_{blade}/\tan\theta > W_{blade}/\sin\theta$ ‡ *where* $W_{screen}' + W_{blade}/\tan\theta < W_{blade}/\sin\theta$

6.1.4 Work rate equations

Stress state

The flow pattern is based on treating the longitudinal and cross-sectional contributions over an element as independent. This approach is now extended to analyse the rates of energy dissipation. We separate the work done by flow along the channel length from that by flow across the width. Thus, the rate of work done *on* the paste in the longitudinal direction is equal to the rate of work dissipated *by* the paste as it flows along the channel. Similarly, we assume that the rate of work done *on* the paste in the width direction is equal to the dissipation *by* the paste as it flows across the channel width.

These assumptions decouple the flow equations, enabling solutions to be readily found. The complexity of solving coupled equations, especially without reliable material parameters, was deemed to outweigh any improvement they would make to model.

We considered in Section 2.6 the practical approaches in dealing with stresses in pastes. The Section concluded that there is some justification in treating the material as isotropic, and it certainly simplifies the analysis. The paste is said to be under a pressure p, and this is separated into two parts p_l and p_w relating to longitudinal and cross-sectional flows respectively. We assume that the pressure associated with longitudinal flow, p_l, is constant over the channel cross-section and thus drops out of the cross-section work rate equations. The paste pressure at some point is then given by,

$$p = p_l + p_w \tag{6.33}$$

At a distance along the channel, the two components can be calculated separately and simply added to give the total pressure. It would be possible to calculate the variation of the longitudinal component over the cross-section, rather than just the average, but at this stage the increased complexity of this approach is not thought to be worthwhile. However, this does mean that our solution does not satisfy mechanical equilibrium – but since we are aiming for an approximate solution, we should not be too worried by this.

Rate of work done by paste

We consider the rate of work that is done over an element of the cross-section. The screen may be perforated, so we take the area of actual contact between paste and solid screen as a factor λ of the total screen area, where λ is given by,

$$\lambda = 1 - \frac{\pi D_{hole}{}^2}{2\sqrt{3}\, p_{hole}{}^2}. \tag{6.34}$$

Where we have a slip velocity in one direction, but are considering the rate of work done, $\underline{D}$, on an element of the slip plane of area dA in two perpendicular directions $\boldsymbol{x}$ and $\boldsymbol{y}$ we may write,

$$\underline{D} = |V||\tau|\mathrm{d}A\,. \tag{6.35}$$

$$\underline{D}_x = \frac{V_x^{\,2}}{|V|}|\tau|\mathrm{d}A \tag{6.36}$$

$$\underline{D}_y = \frac{V_y^{\,2}}{|V|}|\tau|\mathrm{d}A \tag{6.37}$$

We apply this principle over the perimeter surfaces ai, lj, and ql to separate the rate of work done in the longitudinal and cross-sectional planes. Over perimeter qs the slip velocities in the longitudinal and cross-sectional planes are not perpendicular unless the cross-section core to screen surface angle, ψ, is zero. However, in most cases angle ψ is likely to be small. We proceed to use this approach on this perimeter in the hope that the errors introduced are small.

Rate of work done in cross-sectional plane

The equations for the rate of work in the cross-sectional plane over the width of the channel are summarised in Table 6.3 overleaf. The work rates in the cross-sectional plane, dD_w/dl, are expressed as a function of distance in the $\boldsymbol{w}$-direction, and separated into different regions of the cross-section. The variation of stress with position is not considered over region fr_1, and a stress discontinuity is calculated at position b. In Table 6.4 the contributions of each portion of perimeter to the work rate per length in the longitudinal plane, dD_l/dl, are expressed.

The deformational flow into the nip is separated into two components related to the flows through the screen (ε) or between the blade and the screen (1-ε). The total work rate of each flow is equal to that expected from the initial dimensions at point b to the final dimensions of the screen pseudo-die or of the gap between the blade and screen. To match the form of the Benbow-Bridgwater equation (2.25), these are scaled logarithmically between the distances r_1 and r_0 to estimate the stress profiles (see addendum on page 135A). The yielding stresses for each flow, $\sigma_{y\ \varepsilon}$ and $\sigma_{y\ (1-\varepsilon)}$, respectively, are also separated, and are based on the respective velocities of the two flows. The yielding stress associated with deformational flow within region abrs, $\sigma_{y\ \mathrm{ba}}$, is assumed to be dependent on the local paste velocity in the $\boldsymbol{w}$-direction.

The assumed flow pattern along chord bq in Figure 6.8 is not kinematically admissible. In other words, continuity is not observed at any particular point along the chord – the mass flow in is different from the mass flow out – although mass flow does balance over the whole length of the boundary. This does not directly present itself as a problem in our analysis since the energy dissipation along the boundary, due to the associated slip velocity and shear stress at the discontinuity, is not included. We justify this on the grounds that the energy dissipation along the boundary is incorporated within the overall energy dissipation over the flow contraction as calculated from a Benbow-Bridgwater analysis.

Use of the Benbow-Bridgwater analysis to calculate the rate of energy dissipation over the flow contraction through the nip and out of the screen, or over the tip of the blade, represents a deviation away from an upper bound analysis. A true upper bound analysis would calculate the rate of energy dissipation based directly on the assumed strain field and the material's constitutive equation. However, when a true constitutive equation is not available, but Benbow-Bridgwater material parameters are (as is often the case), this approach appears to be a suitable compromise.

Table 6.3 Rate of cross-sectional work done over channel cross-section

Portion of channel width	Cross-sectional rate of work per length ($\mathrm{d}D_w/\mathrm{d}l$) balance
if	$(1-\varepsilon)Q_w\dfrac{\mathrm{d}p_w}{\mathrm{d}w} = -\tau_{\mathrm{lj}}v_{slip\,\mathrm{lj},w}\dfrac{\lvert v_{slip\,\mathrm{lj},w}\rvert}{\lvert v_{slip\,\mathrm{lj}}\rvert} - \lambda\tau_{\mathrm{fi}}v_{slip\,\mathrm{fi},w}\dfrac{\lvert v_{slip\,\mathrm{fi},w}\rvert}{\lvert v_{slip\,\mathrm{fi}}\rvert}$
fr$_1$ when, $W_{screen}' + \dfrac{W_{blade}}{\tan\theta} > \dfrac{W_{blade}}{\sin\theta}$	$Q_w p_{w,r1} = (1-\varepsilon)Q_w p_{w\,\mathrm{f}} + \int_{W_{blade}/\sin\theta}^{r_1} \tau_{\mathrm{ql}}\dfrac{v_{slip\,\mathrm{ql},w}^{\,2} + v_{slip\,\mathrm{ql},h}^{\,2}}{\lvert v_{slip\,\mathrm{ql}}\rvert}\mathrm{d}r$ $- L_{screen}'\tau_{\mathrm{cd}}v_{slip\,\mathrm{cd},h-w} - L_{screen}'\tau_{\mathrm{fg}}v_{slip\,\mathrm{fg},h-w}$
fr$_1$ when, $W_{screen}' + \dfrac{W_{blade}}{\tan\theta} < \dfrac{W_{blade}}{\sin\theta}$	$Q_w p_{w,r1} = (1-\varepsilon)Q_w p_{w\,\mathrm{f}} - \lambda\int_{W_{screen}'+\frac{W_{blade}}{\tan\theta}}^{r_1} \tau_{\mathrm{bc}}v_{slip\,\mathrm{bc},w}\dfrac{\lvert v_{slip\,\mathrm{bc},w}\rvert}{\lvert v_{slip\,\mathrm{ql}}\rvert}\mathrm{d}r$ $- L_{screen}'\tau_{\mathrm{cd}}v_{slip\,\mathrm{cd},h-w} - L_{screen}'\tau_{\mathrm{fg}}v_{slip\,\mathrm{fg},h-w}$
$r_1 r_0$	$Q_w\dfrac{\mathrm{d}p_w}{\mathrm{d}r} = \tau_{\mathrm{ql}}\dfrac{v_{slip\,\mathrm{ql},w}^{\,2} + v_{slip\,\mathrm{ql},h}^{\,2}}{\lvert v_{slip\,\mathrm{ql}}\rvert} - \lambda\tau_{\mathrm{bc}}v_{slip\,\mathrm{bc},w}\dfrac{\lvert v_{slip\,\mathrm{bc},w}\rvert}{\lvert v_{slip\,\mathrm{bc}}\rvert}$ $+ (1-\varepsilon)Q_w\sigma_{y\,(1-\varepsilon)}\dfrac{1}{r}\ln\!\left((1-\varepsilon)h_{channel\,\mathrm{b}}/W_{blade}\right)/\ln\!\left(r_0/r_1\right)$ $+ \varepsilon Q_w\sigma_{y\,\varepsilon}\dfrac{1}{r}\ln\!\left(\varepsilon h_{channel\,\mathrm{b}}/W_{blade}\right)/\ln\!\left(r_0/r_1\right)$
b	$Q_w p_{w\,\mathrm{b}+} = Q_w p_{w\,\mathrm{b}-} + \int_{L_{blade}-\frac{W_{blade}}{\tan\theta}+r_0\cos\theta}^{L_{blade}-\frac{W_{blade}}{\tan\theta}+r_0} \dfrac{\tau_{\mathrm{sq}}}{\cos\chi\cos\psi}\dfrac{v_{slip\,\mathrm{sq},w}^{\,2} + v_{slip\,\mathrm{sq},h-w}^{\,2}}{\lvert v_{slip\,\mathrm{sq}}\rvert}\mathrm{d}w$
ba	$Q_w\dfrac{\mathrm{d}p_w}{\mathrm{d}w} = \dfrac{\tau_{\mathrm{sq}}}{\cos\chi\cos\psi}\dfrac{v_{slip\,\mathrm{sq},w}^{\,2} + v_{slip\,\mathrm{sq},h-w}^{\,2}}{\lvert v_{slip\,\mathrm{sq}}\rvert}$ $- \lambda\tau_{\mathrm{ab}}v_{slip\,\mathrm{ab},w}\dfrac{\lvert v_{slip\,\mathrm{ab},w}\rvert}{\lvert v_{slip\,\mathrm{ab}}\rvert} + Q_w\sigma_{y\,\mathrm{ba}}\dfrac{w\tan\psi}{h_{channel}}$

The magnitude of a shear stress τ, caused by a slip of velocity v_{slip} is given by,

$$\tau = \tau_0 + \beta\left|V_{slip}\right|^n \tag{6.38}$$

The magnitudes of the yielding stresses are given by,

$$\sigma_{y\,\varepsilon} = \sigma_0 + \alpha\left|v_{slip\,\mathrm{cd}}\right|^m \tag{6.39}$$

$$\sigma_{y\,(1-\varepsilon)} = \sigma_0 + \alpha\left|v_{slip\,\mathrm{lj}}\right|^m \tag{6.40}$$

$$\sigma_{y\,\mathrm{ba}} = \sigma_0 + \alpha\left|\frac{Q_w}{h}\right|^m \tag{6.41}$$

Rate of work done in longitudinal plane

The work rate in the longitudinal, $\mathrm{d}D_l/\mathrm{d}l$, plane is equal to,

$$Q_l \frac{\mathrm{d}p_l}{\mathrm{d}l} = Q_l \sigma_{yl} \frac{1}{A} \frac{\mathrm{d}A}{\mathrm{d}l} + \text{frictional components} \tag{6.42}$$

where the yielding stress is determined using the local velocity in the ***l***-direction,

$$\sigma_{yl} = \sigma_0 + \alpha \left| \frac{Q_l}{A} \right|^m \tag{6.43}$$

All of the contributions to the frictional components around the perimeter of the channel cross-section are presented in Table 6.4 below.

Table 6.4 Rate of longitudinal work done over channel cross-section

Portion of channel width	Contribution to longitudinal rate of work ($\mathrm{d}D_l/\mathrm{d}l$)
if	$-L_{blade}\tau_{\mathrm{lj}} v_{slip\,\mathrm{lj},l} \dfrac{\left\lvert v_{slip\,\mathrm{lj},l} \right\rvert}{\left\lvert v_{slip\,\mathrm{lj}} \right\rvert} - \lambda L_{blade}\tau_{\mathrm{fi}} v_{slip\,\mathrm{fi},l} \dfrac{\left\lvert v_{slip\,\mathrm{fi},l} \right\rvert}{\left\lvert v_{slip\,\mathrm{fi}} \right\rvert}$
fr_1 when, $W_{screen}' + \dfrac{W_{blade}}{\tan\theta} > \dfrac{W_{blade}}{\sin\theta}$	$-\displaystyle\int_{W_{blade}/\sin\theta}^{r_1} \tau_{\mathrm{ql}} v_{slip\,\mathrm{ql},l} \frac{\left\lvert v_{slip\,\mathrm{ql},l} \right\rvert}{\left\lvert v_{slip\,\mathrm{ql}} \right\rvert} \mathrm{d}r$
fr_1 when, $W_{screen}' + \dfrac{W_{blade}}{\tan\theta} < \dfrac{W_{blade}}{\sin\theta}$	$-\lambda \displaystyle\int_{W_{screen}' + \frac{W_{blade}}{\tan\theta}}^{r_1} \tau_{\mathrm{bc}} v_{slip\,\mathrm{bc},l} \frac{\left\lvert v_{slip\,\mathrm{bc},l} \right\rvert}{\left\lvert v_{slip\,\mathrm{ql}} \right\rvert} \mathrm{d}r$
$r_1 r_0$	$-\displaystyle\int_{r_1}^{r_0} \tau_{\mathrm{ql}} v_{slip\,\mathrm{ql},l} \frac{\left\lvert v_{slip\,\mathrm{ql},l} \right\rvert}{\left\lvert v_{slip\,\mathrm{ql}} \right\rvert} \mathrm{d}r - \lambda \int_{r_1}^{r_0} \tau_{\mathrm{bc}} v_{slip\,\mathrm{bc},l} \frac{\left\lvert v_{slip\,\mathrm{bc},l} \right\rvert}{\left\lvert v_{slip\,\mathrm{bc}} \right\rvert} \mathrm{d}r$
b	$-\displaystyle\int_{L_{blade} - \frac{W_{blade}}{\tan\theta} + r_0 \cos\theta}^{L_{blade} - \frac{W_{blade}}{\tan\theta} + r_0} \frac{\tau_{\mathrm{sq}}}{\cos\chi\cos\psi} \frac{v_{slip\,\mathrm{sq},l}^{\,2} + v_{slip\,\mathrm{sq},h-l}^{\,2}}{\left\lvert v_{slip\,\mathrm{sq}} \right\rvert} \mathrm{d}w$
ba	$-\displaystyle\int_{L_{blade} - \frac{W_{blade}}{\tan\theta} + r0}^{w} \frac{\tau_{\mathrm{sq}}}{\cos\chi\cos\psi} \frac{v_{slip\,\mathrm{sq},l}^{\,2} + v_{slip\,\mathrm{sq},h-l}^{\,2}}{\left\lvert v_{slip\,\mathrm{sq}} \right\rvert} \mathrm{d}w$ $-\lambda \displaystyle\int_{\mathrm{L_{blade}} - \frac{\mathrm{W_{blade}}}{\tan\theta} + r0}^{w} \tau_{\mathrm{ba}} v_{slip\,\mathrm{ba},l} \frac{\left\lvert v_{slip\,\mathrm{ba},l} \right\rvert}{\left\lvert v_{slip\,\mathrm{ba}} \right\rvert} \mathrm{d}w$
a	$-\displaystyle\int_{W_{blade}}^{h} \tau_{\mathrm{st}} \left\lvert v_{slip\,\mathrm{st}} \right\rvert \mathrm{d}h$

Torque

For a given rotational speed between the core and the screen, whether it is the core or the screen which is actually moving, the same flow pattern will be developed, and work will be done at the same rate. Therefore, the torque on the screen is equal to the torque on the core. It is simpler to use the model to predict the torque on the screen, and then use that to infer the torque on the core.

The rate of change of torque on the screen per unit channel length, $\mathrm{d}T/\mathrm{d}l$, may be determined by balancing the work rate per channel length done by the screen with the work done on the paste in all of the channels. The work rate per channel length done by the screen is simply equal to the product of torque per length and rotational speed. The work rate per unit length done on the paste in a single channel by the screen may be determined by integrating the work done on an element over the screen width.

The resulting balance gives,

$$2\pi S\frac{\mathrm{d}T}{\mathrm{d}l}=n_{blade}\lambda\int_0^w\tau_{\mathrm{ai}}v_{slip\,b,y}\frac{\left|v_{slip\,\mathrm{b},y}\right|}{\left|v_{slip\,\mathrm{ai}}\right|}\mathrm{d}w \tag{6.44}$$

This may be separated into the appropriate cross-section sections, as expressed in terms of slip velocities of Section 6.1.3 to give,

$$2\pi S\frac{\mathrm{d}T}{\mathrm{d}l}=n_{blade}\lambda\left(\begin{array}{l}\displaystyle\int_0^{L_{blade}}\tau_{\mathrm{fi}}\left(-v_{slip\,\mathrm{fi},l}\cos\zeta+v_{slip\,\mathrm{fi},w}\sin\zeta\right)\frac{\left|-v_{slip\,\mathrm{fi},l}\cos\zeta+v_{slip\,\mathrm{fi},w}\sin\zeta\right|}{\left|v_{slip\,\mathrm{fi}}\right|}\mathrm{d}w\\ \displaystyle+\int_{W_{screen}'+\frac{W_{blade}}{\tan\theta}}^{r_0}\tau_{\mathrm{cb}}\left(-v_{slip\,\mathrm{cb},l}\cos\zeta+v_{slip\,\mathrm{cb},w}\sin\zeta\right)\frac{\left|-v_{slip\,\mathrm{cb},l}\cos\zeta+v_{slip\,\mathrm{cb},w}\sin\zeta\right|}{\left|v_{slip\,\mathrm{cb}}\right|}\mathrm{d}r\\ \displaystyle+\int_{r_0+L_{blade}-\frac{W_{blade}}{\tan\theta}}^{w}\tau_{\mathrm{cb}}\left(-v_{slip\,\mathrm{ba},l}\cos\zeta+v_{slip\,\mathrm{ba},w}\sin\zeta\right)\frac{\left|-v_{slip\,\mathrm{ba},l}\cos\zeta+v_{slip\,\mathrm{ba},w}\sin\zeta\right|}{\left|v_{slip\,\mathrm{ba}}\right|}\mathrm{d}w\end{array}\right) \tag{6.45}$$

An additional component to the torque, ΔT_{dam}, is introduced over the dam region at the end of the extruder. It can be found from,

$$2\pi S\Delta T_{dam}=n_{blade}\lambda L_{dam}w\tau_{dam-\mathrm{ai}}\left(-v_{slip\,dam\text{-}\mathrm{ai},l}\cos\zeta+v_{slip\,dam\text{-}\mathrm{ai},w}\sin\zeta\right)\frac{\left|-v_{slip\,dam\text{-}\mathrm{ai},l}\cos\zeta+v_{slip\,dam\text{-}\mathrm{ai},w}\sin\zeta\right|}{\left|v_{slip\,dam\text{-}\mathrm{ai}}\right|} \tag{6.46}$$

Screen axial force

No work is done in the axial direction by the screen. Thus it is not possible to find the total force on the screen in the axial direction as energy balanced, as was used to find the torque. Instead, we apply mechanical equilibrium to the extruder and a force balance in the axial direction over an element of the screen gives,

$$\frac{\mathrm{d}F_{screen}}{\mathrm{d}l} = n_{blade}\lambda\int_0^w \tau_{\mathrm{ai}}\frac{\left|v_{slip\,\mathrm{ai},x}\right|}{\left|v_{slip\,\mathrm{ai}}\right|}\mathrm{d}w \tag{6.47}$$

This may be separated into the appropriate cross-section sections, as expressed in terms of slip velocities of Section 6.1.3 to give,

$$\frac{\mathrm{d}F_{screen}}{\mathrm{d}l} = -n_{blade}\lambda\left(\begin{array}{l}\displaystyle\int_0^{L_{blade}} \tau_{\mathrm{fi}}\frac{-v_{slip\,\mathrm{fi},l}\sin\zeta - v_{slip\,\mathrm{fi},w}\cos\zeta}{\left|v_{slip\,\mathrm{fi}}\right|}\mathrm{d}w \\ \displaystyle+\int_{W_{screen}'+\frac{W_{blade}}{\tan\theta}}^{r_0} \tau_{\mathrm{cb}}\frac{-v_{slip\,\mathrm{cb},l}\sin\zeta - v_{slip\,\mathrm{cb},w}\cos\zeta}{\left|v_{slip\,\mathrm{cb}}\right|}\mathrm{d}r \\ \displaystyle+\int_{r_0+L_{blade}-\frac{W_{blade}}{\tan\theta}}^{w} \tau_{\mathrm{cb}}\frac{-v_{slip\,\mathrm{ba},l}\sin\zeta - v_{slip\,\mathrm{ba},w}\cos\zeta}{\left|v_{slip\,\mathrm{ba}}\right|}\mathrm{d}w\end{array}\right) \tag{6.48}$$

An additional component to the axial force on the screen, $\Delta F_{screen\text{-}dam}$, is introduced over the dam region at the end of the extruder. It can be found from,

$$\Delta F_{screen-dam} = n_{blade}\lambda L_{dam}\,w\,\tau_{dam-\mathrm{ai}}\frac{\left|-v_{slip\,dam\text{-}\mathrm{ai},l}\sin\zeta - v_{slip\,dam\text{-}\mathrm{ai},w}\sin\zeta\right|}{\left|v_{slip\,dam\text{-}\mathrm{ai}}\right|} \tag{6.49}$$

Core axial force

The force on the core may be estimated by carrying out a force balance over the whole extruder, as shown in Figure 6.11 overleaf. The balance gives us,

$$F_{core} = \int p\mathrm{d}A\Big|_{l=0}\cos\zeta - F_{screen}$$

The integral of pressure over area might be approximated to,

$$\int p\mathrm{d}A\Big|_{l=0} = n_{blade}\left(\begin{array}{l}\displaystyle\int_0^{L_{blade}} pW_{blade}\mathrm{d}w + p_{r_1}\left(\frac{r^2\theta}{2} - \frac{W_{blade}^{\ 2}}{2\tan\theta}\right) + \int_{r_1}^{r_0} pr\theta\mathrm{d}r \\ \displaystyle+ p_{b+}\frac{r_0^{\ 2}}{2}\left((2-\cos\theta)\sin\theta - \theta - (1-\cos\theta)^2\tan\psi\right) + \int_{r_0+L_{blade}-\frac{W_{blade}}{\tan\theta}}^{w} ph_{channel}\mathrm{d}w\end{array}\right) \tag{6.50}$$

where the pressures over the areas bounded by either flmc or fle (flmc if W_{screen}'$+W_{blade}/\tan\theta > W_{blade}/\sin\theta$, fle otherwise) are assumed to be equal to p_{r1} and p_{b+} respectively.

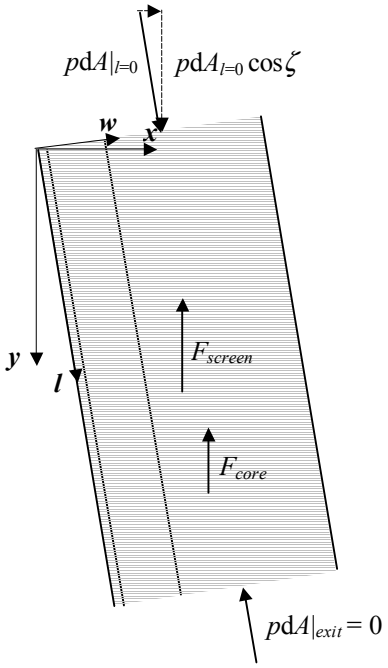

Figure 6.11 Force balance over a section of channel

6.1.5 Boundary conditions

Boundary conditions must be specified to enable all of the equations presented over the previous four Sections to be solved to give a pressure distribution and flow pattern over the whole extruder channel. Mechanical equilibrium over the channel cross-section would require something like,

$$p\big|_{l,w=w} = p\big|_{l=l+w/\tan\zeta,w=0} \tag{6.51}$$

and conservation of mass would require something like,

$$\frac{\mathrm{d}Q_l}{\mathrm{d}l} = \left((1-\varepsilon)Q_w\right)\big|_{l+w/\tan\zeta} - Q_w \tag{6.52}$$

However, both of these boundary conditions would require iterative stages towards finding a possible solution. Given the many assumptions already made in the model it was thought appropriate, at least in the first instance, to use simplified approximate boundary conditions,

$$p\big|_{l,w=w} = p\big|_{l,w=0} \tag{6.53}$$

$$\frac{\mathrm{d}Q_l}{\mathrm{d}l} = -\varepsilon Q_w \tag{6.54}$$

Further to these conditions, we assume that the developed flow pattern will be that which minimises the rate of work dissipation, and thus that which minimises the rate of work input by the relative tangential motion of the screen. Thus, over a cross-section of the channel the flow rate across the cross-section, Q_w, and the fraction of this flow which passes through the screen, ε, may be determined by making the pressure at either side of the channel equal and by minimising the rate of work done by the screen.

We assume that the paste pressure at the extruder exit, $p_{l=l,w=0}$, is determined by the flow through the channel exit gap by this energy balance,

$$\begin{aligned} Q_l p\big|_{l=l,w=0} &= Q_l \sigma_{y\,exit} \ln\left(\frac{A_l}{W_{dam} w}\right) \\ &+ \lambda L_{dam} w \tau_{dam-\mathrm{ai}} v_{slip\,dam-\mathrm{ai},l} \frac{\left|v_{slip\,dam-\mathrm{ai},l}\right|}{\left|v_{slip\,dam-\mathrm{ai}}\right|} \\ &+ L_{dam} w \tau_{dam-\mathrm{uv}} v_{slip\,dam-\mathrm{uv},l} \frac{\left|v_{slip\,dam-\mathrm{uv},l}\right|}{\left|v_{slip\,dam-\mathrm{uv}}\right|} \end{aligned} \tag{6.55}$$

where the paste slip yielding stress, $\sigma_{y\,exit}$, is given by

$$\sigma_{y\,exit} = \sigma_0 + \alpha\left(\frac{Q_l}{W_{dam} w}\right)^m \tag{6.56}$$

For the case of a screw feed to the extruder, the model can be used to analyse the flow in both the feed and the extruder head simultaneously. This approach required the inlet flow rate to be found by matching the work rate done by the paste at the screw feed channel exit to the work rate at the extruder channel entrance. For a simple screw feed of constant core thickness, no leakage over the flights, negligible flight width, the work rate at the screw feed channel exit may be found using the preceding analysis and the equations presented in Table 6.3. These equations may be summed, and simplified to give,

$$Qp = -l\left(\begin{aligned} &(2h_{ch} + w)\tau_{core}\frac{Q}{h_{ch} w} \\ &+ w\tau_{barrel}\left(\frac{Q}{h_{ch} w} - \pi D_s S\cos\zeta\right)\frac{\left|\frac{Q}{h_{ch} w} - \pi D_s S\cos\zeta\right|}{\sqrt{(\pi D_s S\sin\zeta)^2 + \left(\frac{Q}{h_{ch} w} - \pi D_s S\cos\zeta\right)^2}} \end{aligned}\right) \tag{6.57}$$

where all of the symbols refer to the screw feed geometry and the shear stresses at the core, τ_{core}, and barrel, τ_{barrel}, walls respectively are,

$$\tau_{core} = \tau_0 + \beta\left(\frac{Q}{h_{ch}w}\right)^n \tag{6.58}$$

$$\tau_{barrel} = \tau_0 + \beta\left((\pi D_s S\sin\zeta)^2 + \left(\frac{Q}{h_{ch}w} - \pi D_s S\cos\zeta\right)^2\right)^{\frac{n}{2}} \tag{6.59}$$

6.1.6 Special cases

The geometry of the extrusion modules previously described in Chapter 5 requires two special cases to be considered, relating to operation of the *rotating core module* without any blades and to all cases of flow in the *nip module*

Rotating core module with no blade

This situation may be unrolled, as with the bladed core in Section 6.1.1, to give a bounded channel, shown in Figure 6.12. The channel width, w, is given by,

$$w = \pi D_s \tag{6.60}$$

and the height, $h_{channel}$, of the channel at a distance l along the length is given by,

$$h_{ch} = h_0 - l\tan\phi \tag{6.61}$$

where the initial height, h_0, is given by,

$$h_0 = \frac{D_s - D_0}{2} \tag{6.62}$$

The channel cross-sectional area, A, is given by,

$$A = h_{channel}w \tag{6.63}$$

and the rate of change of area with longitudinal position is given by,

$$\frac{\mathrm{d}A}{\mathrm{d}l} = -w\tan\phi \tag{6.64}$$

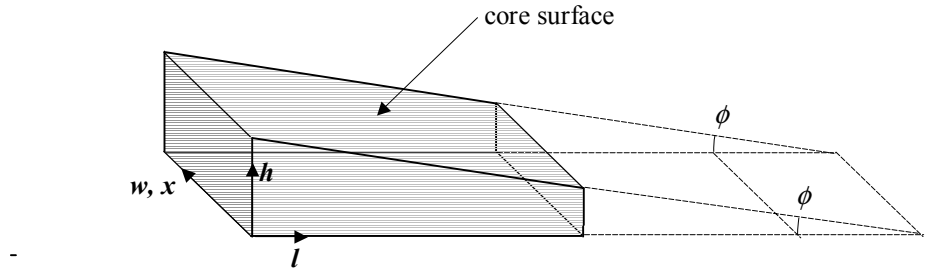

Figure 6.12 Unrolled channel from bladeless extruder

In this special case of no blade, there is no friction on either of the vertical sides of the channel. It is assumed that there is no flow through the screen in this case. As in the main

analysis, the velocity in the ***l***-direction is assumed constant over the channel cross-section. Thus, the velocities in the ***l*** and ***h***-directions, v_l and v_h respectively, are given by,

$$v_l = \frac{Q_0}{w h_{ch}} \tag{6.65}$$

$$v_h = -\frac{h}{h_{ch}} \frac{Q_0}{w h_{ch}} \tan\phi \tag{6.66}$$

The work in the ***w***-direction done by the screen on the paste is assumed to be equal to the work in the ***w***-direction done by the paste against the core. Thus the velocity in the ***w***-direction, v_w, is half of the relative velocity of the screen to the core,

$$v_w = -\frac{\pi D_s S}{2} \tag{6.67}$$

Balancing the rate of work done in the longitudinal direction enables us to write an expression for the rate of change of paste pressure over the channel length, dp/dl,

$$\begin{aligned} Q_0 \frac{dp}{dl} = Q_0 \sigma_y \frac{1}{A}\frac{\mathrm{d}A}{\mathrm{d}l} - w\tau_{screen} \frac{\left(\frac{Q_0}{h_{ch}w}\right)^2}{\left(\left(\frac{Q_0}{h_{ch}w}\right)^2 + \left(-\frac{\pi D_s S}{2}\right)^2\right)^{\frac{1}{2}}} \\ - \frac{w\tau_{core}}{\cos\phi} \frac{\left(\frac{Q_0}{h_{ch}w}\right)^2 + \left(-\frac{Q_0}{h_{ch}w}\tan\phi\right)^2}{\left(\left(\frac{Q_0}{h_{ch}w}\right)^2 + \left(-\frac{Q_0}{h_{ch}w}\tan\phi\right)^2 + \left(-\frac{\pi D_s S}{2}\right)^2\right)^{\frac{1}{2}}} \end{aligned} \tag{6.68}$$

where the core and screen wall shear stresses, τ_{core} and τ_{screen} respectively, are given by,

$$\tau_{core} = \tau_0 + \beta\left(\left(\frac{Q_0}{h_{ch}w}\right)^2 + \left(-\frac{Q_0}{h_{ch}w}\tan\phi\right)^2 + \left(-\frac{\pi D_s S}{2}\right)^2\right)^{\frac{n}{2}} \tag{6.69}$$

$$\tau_{screen} = \tau_0 + \beta\left(\left(\frac{Q_0}{h_{ch}w}\right)^2 + \left(\frac{\pi D_s S}{2}\right)^2\right)^{\frac{n}{2}} \tag{6.70}$$

and the yielding stress, σ_y, is given by,

$$\sigma_y = \sigma_0 + \alpha\left(\frac{Q_0}{h_{ch}w}\right)^m \tag{6.71}$$

The paste pressure is taken as being zero at the extruder exit. Balancing the rate of work done in the ***x***/***w***-direction enables us to write an expression for the rate of change of screen/core torque per channel length, dT/dl,

$$2\pi S\frac{dT}{dl}=w\tau_{screen}\frac{\left(-\frac{\pi D_s S}{2}\right)^2}{\left(\left(\frac{Q_0}{h_{ch}w}\right)^2+\left(-\frac{\pi D_s S}{2}\right)^2\right)^{\frac{1}{2}}} \tag{6.72}$$

Force balances give the axial force on the screen and the core, F_{screen} and F_{core} respectively, to be,

$$F_{screen}=w\tau_{screen}\frac{\left(\frac{Q_0}{h_{ch}w}\right)}{\left(\left(\frac{Q_0}{h_{ch}w}\right)^2+\left(-\frac{\pi D_s S}{2}\right)^2\right)^{\frac{1}{2}}} \tag{6.73}$$

$$F_{core}=wh_0p_0-F_{screen} \tag{6.74}$$

Nip module

The profile of paste pressure over radial distance from the nip, as well as the extrusion pressure, may be found using the main analysis presented. Appropriate selection of variables enables the *nip module* flow to be modelled without distorting any of its geometry. It is assumed that there is no friction on the side walls of the barrel in the *nip module*. If the module has dimensions listed in Table 6.5 below then it may be modelled using the previous analysis with the variables listed in Table 6.6 overleaf.

Table 6.5 Nip module parameters

Nip module parameter	Symbol
Barrel width	W_0*
Barrel depth	L_0*
Nip angle between wedge and barrel wall	θ*
Length of blade die land	L_{blade}*
Width of blade die land	W_{blade}*
Length of screen die land	L_{screen}*
Width of screen die land	W_{screen}*
Paste flow rate	Q_0*
Fraction of paste flowing through screen	ε*

Table 6.6 Equivalent screen extruder flow model and nip module parameters

Screen extruder model parameter	Value to model *nip module*
D_0	$(W_0^*/\sin\theta^*+L_{blade}^*)/\pi - 2W_0^*$
L_{core}	L_0^*
ϕ	0
n_{blade}	1
ζ	90°
θ	θ^*
L_{blade}	L_{blade}^*
W_{blade}	W_{blade}^*
D_s	$(W_0^*/\sin\theta^*+L_{blade}^*)/\pi$
L_{screen}'	L_{screen}^*
W_{screen}'	W_{screen}^*
S	0
Q_l	0
Q_w	Q_0^*/L_0^*
ε	ε^*
λ	1
p_l	0

6.2 Assessment of the screen extruder model

The screen extruder model presented in Section 6.1 may be used in conjunction with feed screw geometry, operating speed and Benbow-Bridgwater material parameters to model a whole single-screw extruder. The model can predict the flow rate; the screw feed and extruder work rates; the extruder core and screw core torques; the axial force on the extruder core; the flow rates through the screen and over the blade along the extruder channel length, and the paste pressure profile over the extruder channel length and width.

In this Section we assess the performance of the model on its own terms without comparison to any experimental data. Model predictions are considered for the case of a single screw extruder based on the industrial extruder presented in Appendix A. The model is used with the model paste Benbow-Bridgwater material parameters found in Chapter 3. The variation of the model predictions are considered over a number of key parameters. Chapter 7 considers the performance of the model when compared to results from the extruder modules previously presented in Chapter 5.

6.2.1 Obtaining solutions

The large number of equations in the screen extruder model makes an analytical solution an unviable option for most extruder geometries. For this study the model equations were implemented numerically using MS Excel97, although a number of other commercial mathematical software packages might have been used equally well. Essentially the model is implemented as an approximate *ad hoc* Eulearian finite difference analysis. Six points along the extruder length were considered. Initial values of extruder total flow rate, cross-sectional flow rates and fractions of cross-sectional flow through the screen were selected on the basis of what might be considered a reasonable flow pattern. The integral Excel97 'solver' function was used to minimise the total work rate subject to the boundary conditions outlined in Section 6.1.5. The *solver* was usually able to find a feasible solution within a few minutes. Starting from a variety of initial conditions, the *solver* would converge to the same solution.

Sensitivity to flow pattern

The total rate of work done by the extruder was not a strong function of the precise flow pattern. The optimum flow pattern was found for the extruder geometry and operating speed outlined in the following Section (where $n_{row} = 1$). Along with the inlet flow and the cross-sectional flow along the channel length, the optimum flow pattern included the fraction of cross-sectional flow which passed through the screen, ε, along the channel length. To test the sensitivity of the optimum flow pattern, the optimum distribution of ε along the channel length found in Section 6.2.2 (for the best fit material parameter case) was scaled and used as fixed values whilst the new minimum possible total extruder work rate was found. Figure 6.13 overleaf shows the variation of the total work rate as the flow distribution scaling factor is varied from no flow through the screen, to twice the optimum flow passing through the screen. A minimum clearly exists, but the variation from no flow through the screen to the optimum is only 0.2 per cent of the total work rate. Thus the model might be expected to be a poor predictor of exact flow patterns. Comparison with experimental data must be conducted to establish the validity of the predicted flow patterns. Some limited experimental data is presented in the next Chapter. A similar modelling approach was used to predict the flow pattern through a circular barrel with an asymmetrical die arrangement by Martin *et al.* (2001) where similar problems were found.

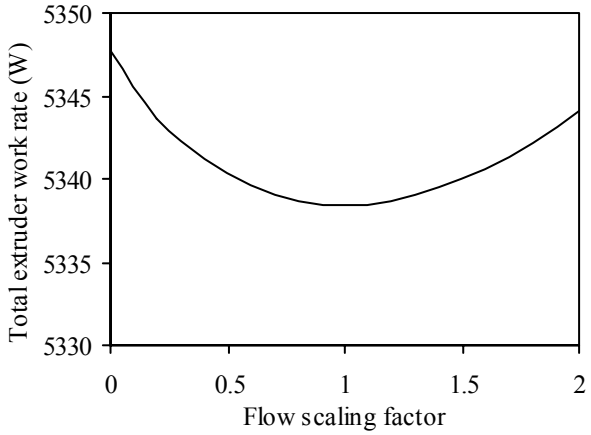

Figure 6.13 Variation of minimum total extruder work rate with flow pattern

Sensitivity to number of numerical elements

It was noted above that only five numerical elements along the length of the extruder were used. This precise number was used in order to give data at positions comparable to the experimental data, which is presented in Chapter 7. The number of longitudinal elements was varied for the sample model case in Section 6.2.2 (for the best fit material parameter case). Figure 6.14 shows that the sensitivity of the solution to the number of elements is not great when the number of elements is five or more. The solution appears to level out at around ten elements. Small changes in the magnitude of the flow pattern were observed, but there were no significant changes in the flow distribution. The reduced accuracy of using five elements was deemed acceptable in light of the much reduced computation time; the computation time to find a solution was approaching sixty minutes when twenty elements were used.

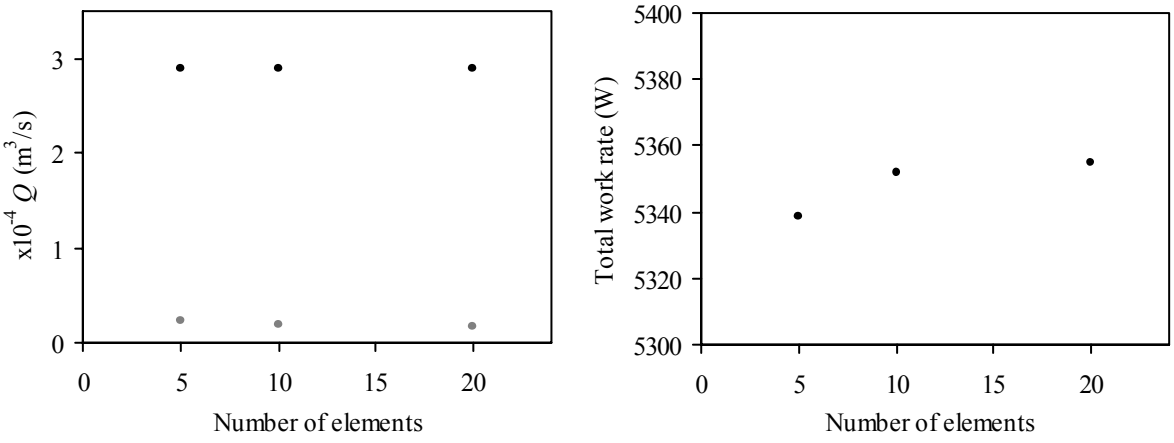

(a) Extruder flow rate against number of elements *(b) Total work rate against number of elements*

• *inlet flow rate* • *extrusion through screen*

Figure 6.14 Variation of minimum total extruder work rate with number of longitudinal elements

Other aspects of accuracy and model limitations

Some special cases of extruder geometry, such as the *nip module* flow described in Section 6.1.6, may be solved analytically. Comparison of sample analytical results with numerical results suggested that the numerical accuracy to within ±10 per cent. Given the approximations within the model, this degree of accuracy was deemed acceptable when compared against the convenience of using Excel97 over some other packages.

The most immediate limitation of the model is that there is no indication of how many rows of screen die holes the paste is extruded through. Perhaps with further experimental observation a suitable value could be determined. There is currently little theoretical work to indicate the likely flow pattern. To obtain sample results, in the first instance we assume extrusion through only a single row of screen holes. The variation of model prediction is then considered as the number of screen hole rows is increased.

6.2.2 Sample results for a typical extruder

To test the model on a realistic extruder, a single screw version of the Syngenta Herbicide Plant extruder was used, the dimensions and operating speed of which are outlined in Table A.2. The lower bound, best fit, and upper bound Benbow-Bridgwater model talc paste parameters (Table 3.5) were used. In the first instance we assume that paste is only extruded through the first row of die holes in front of the blade. The model predictions for this case are shown in Figure 6.15 and Table 6.7 overleaf.

Figure 6.15 *(a)* shows the profile of the paste pressure next to the screen over the whole length and width of one of the three extruder channels. The shapes of the profiles relating to the three different paste material Benbow-Bridgwater parameters appear similar, with the boundary cases being between twenty to forty per cent larger or smaller than the best fit parameter case. This represents a large variation in prediction and highlights how the uncertainty in the material characterization limits any modelling technique. From this point forward, unless otherwise stated, only the model predictions based on the best fit material parameters will be discussed.

Over the channel cross-section, the paste pressure increases almost linearly from a positive value to a peak. This peak marks the start of the nip radial flow region. The pressure decreases in a logarithmic fashion over the nip region. Finally the pressure decreases linearly over the length of the extruder blade, until it reaches the same value as at the start. These initial and final pressures were determined by the longitudinal flow of the paste. The channel cross-sectional pressure profile shape does not appear to vary

markedly along the channel length. The initial/final pressure and the height of the peak above the initial/final pressure vary along the channel length.

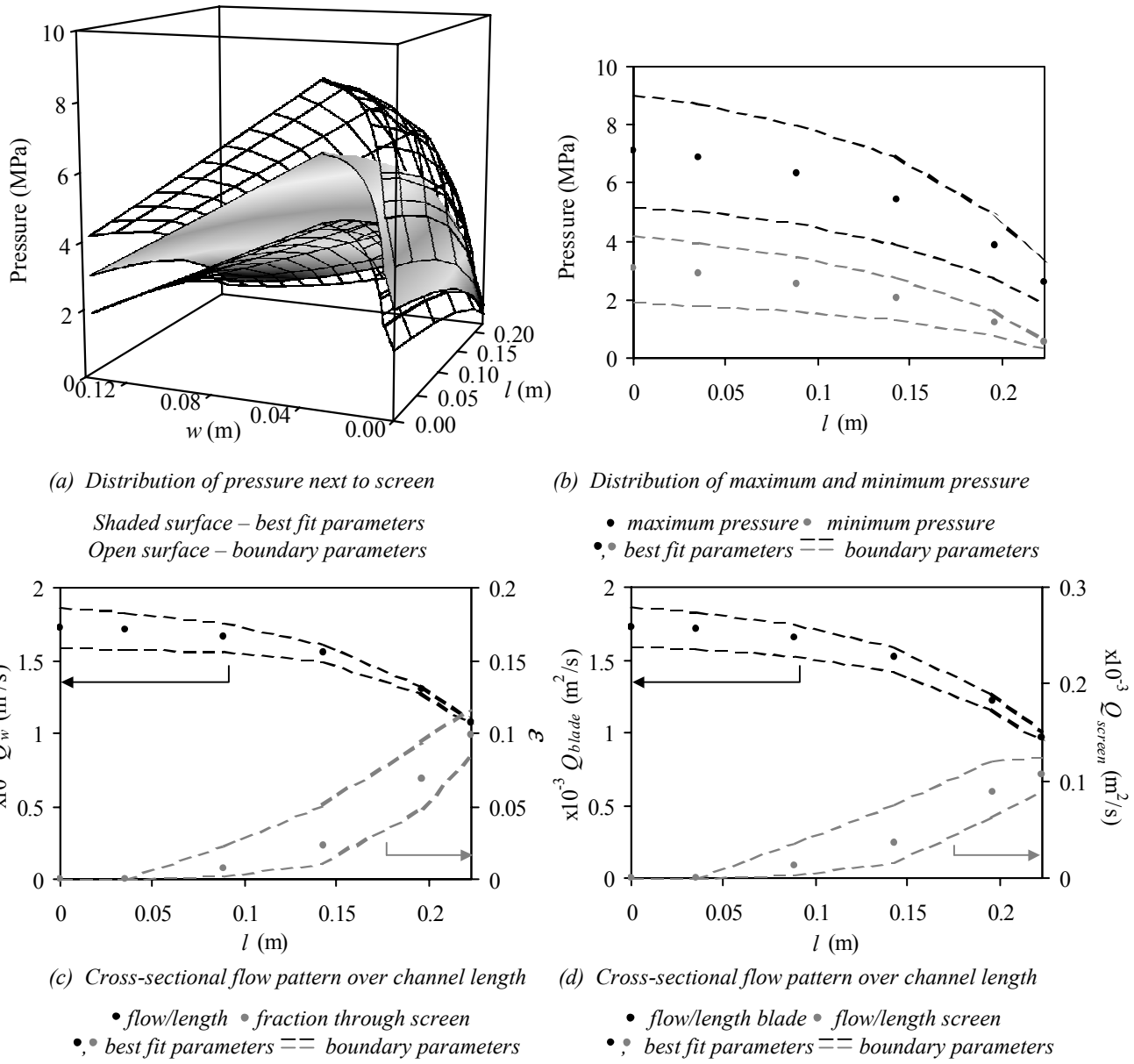

(a) Distribution of pressure next to screen

(b) Distribution of maximum and minimum pressure

(c) Cross-sectional flow pattern over channel length

(d) Cross-sectional flow pattern over channel length

Figure 6.15 Sample screw extruder model results

Table 6.7 Sample screw extruder model results

	Lower bound parameters	Best fit parameters	Upper bound parameters
Inlet flow rate (m^3/s)	2.91×10^{-4}	2.89×10^{-4}	2.86×10^{-4}
Screen extrudate flow rate (m^3/s)	2.77×10^{-5}	1.48×10^{-5}	0.84×10^{-5}
Screw feed work rate (W)	2.67	3.74	4.82
Extruder head work rate (W)	3860	5340	7120
Screen/core torque (Nm)	410	566	756
Extruder screen axial force (N)	998	143	1940
Extruder core axial force (N)	26200	37000	48100

Figure 6.15 *(b)* shows the variation of the initial/final pressure and the peak pressure along the channel length. Both decrease along the length of the channel in a logarithmic fashion, as expected from the analysis. The final value of the minimum cross-sectional pressure is determined by the dam outlet conditions. The difference between the peak pressure and the minimum pressure decreases slightly over the length of the extruder.

Figure 6.15 *(c)* shows the total cross-sectional paste flow rate per unit length of channel over the entire channel length, along with the fraction of this flow which is extruded through the screen. The cross-sectional flow rate decreases along the length of the extruder, although the fraction being extruded through the screen increases. Figure 6.15 *(d)* shows the actual flow rates per length between the blade and screen, and through the screen over the channel length. It can be seen that the decrease in total flow rate is not as significant as the increase in fraction flowing through the screen, thus the flow rate through the screen increases over the length of the channel and the flow rate over the blade decreases. However, the flow rate through the screen is at least an order of magnitude less than the flow rate over the blade in this case – representing an ineffective extruder. In actual fact, the distance between the dam and the screen on the industrial extruder is probably less than that listed in Table A.2. This might reduce the total flow rate, but encourage a greater fraction of the paste to flow through the screen.

Some of the overall extruder operating conditions are listed in Table 6.7. The twin-screw extruder flow rate for the industrial plant listed in Table A.2 is approximately 4.2×10^{-5} m^3/s, assuming a paste density of 2000 kg/m^3. The inlet flow rate predicted by the model is 2.9×10^{-4} m^3/s, an order of magnitude higher than the flow rate through each barrel of the industrial extruder. Again, more resistance to flow at the dam might decrease the flow rate predicted by the model. Also the industrial extruder flow rate is based on the industrial paste, which may present more resistance to flow than our model paste.

As was noted in Figure 6.15 *(d)*, that very little of the paste is flowing through the screen. In total, only around five per cent of the paste flowing into the extruder is extruded through the screen. The effect of varying the dam conditions is considered further in Section 6.2.3.

The extruder head work rate is around 5 kW. This seems a reasonable value when it is considered that the industrial twin-screw industrial extruder is powered by a single 20 kW motor. The work rate of the screw feed is almost negligible when compared to the work

rate of the extruder head. This suggests that the work rate required to move the paste along the length of the extruder channel is much less than the work rate required to move the paste across the channel cross-section.

Variation with number of active rows of extrusion holes

The previous model prediction results were based on paste flowing through only the first row of screen die holes in front of the extruder blade. Now we consider the effect of increasing the number of rows. Figure 6.16 presents the variation of a number of the predicted flow characteristics with number of screen extrusion rows; from one to nine rows. At one row the pseudo screen die width is 0.23 mm; at nine rows the pseudo die width is 2.1 mm; the gap between the blade tip and the screen is 1.4 mm. If more than nine screen rows were used, all of the paste was extruded before the end of the extruder. These cases have not been considered here.

Figure 6.16 *(a)* and *(b)* show the variation of the maximum and minimum pressures respectively over the length of the extruder channel for a variety of screen extrusion rows. Both the maximum and minimum pressures decrease over the whole of the channel length as the number of extrusion rows is increased. The maximum pressure decreases most at the end of the channel whereas the minimum pressure decreases most at the start of the channel.

Figure 6.16 *(c)* and *(d)* show the variation of the flow rates per length over the blade and through the screen respectively over the length of the extruder channel for a variety of screen extrusion rows. The flow rate per length over the blade changes little over the first half of the channel length, but then decreases greatly at the channel exit as the number of extrusion rows is increased. As the number of rows is increased from one to nine, the flow per unit length over the blade decreases by almost fifty per cent. Correspondingly, the flow per unit length through the screen also changes little over the first half of the screen length, with practically no screen extrusion at all over the first third of the channel length. Towards the end of the channel a significant amount of paste is flowing through the screen. With nine extrusion rows the flow rate per length through the screen is almost equal to the flow rate per length over the blade.

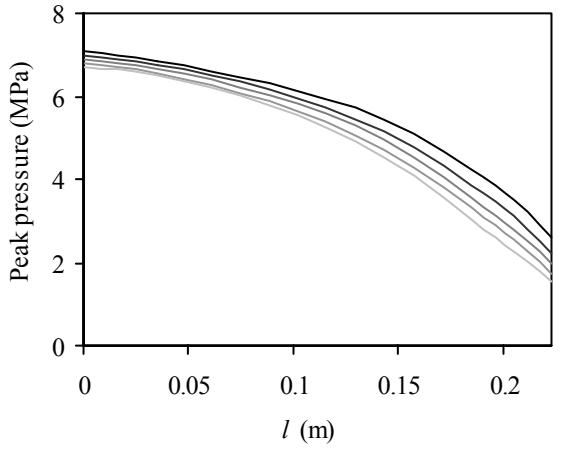

(a) Peak pressure over channel length

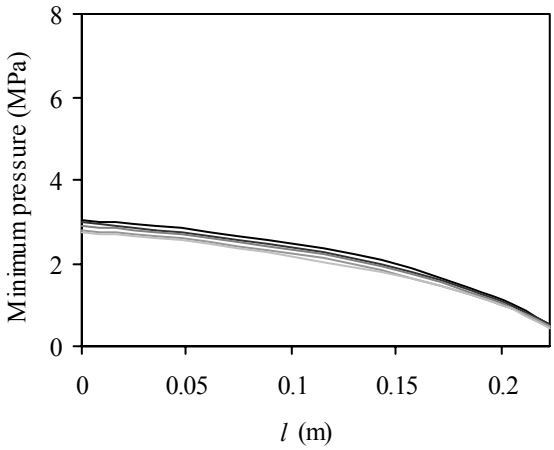

(b) Minimum pressure over channel length

n_{row}: — *1* — *3* — *5* — *7* — *9*

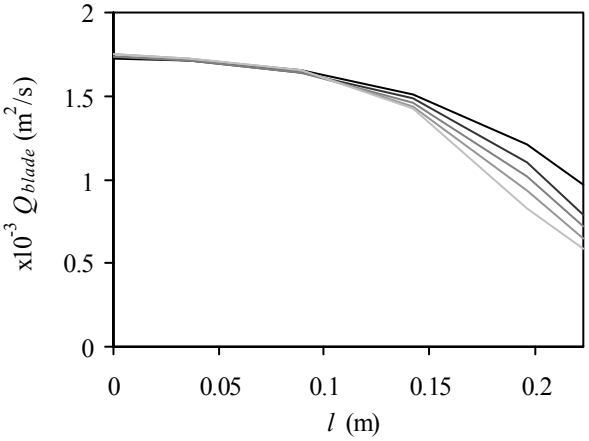

(c) Cross-sectional blade flow over channel length

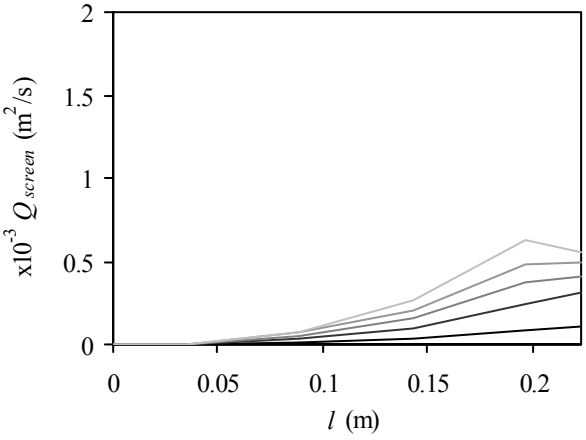

(d) Cross-sectional screen flow over channel length

n_{row}: — *1* — *3* — *5* — *7* — *9*

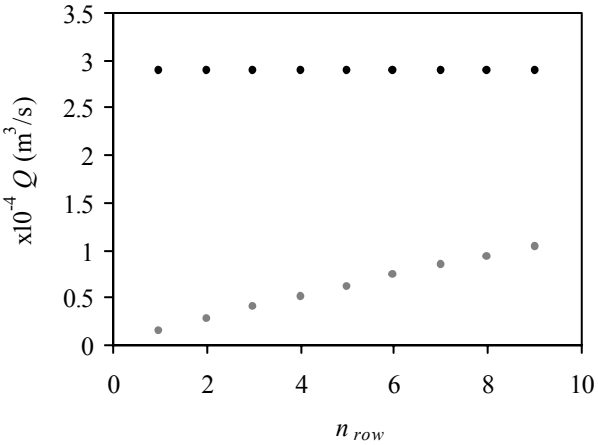

(e) Extruder flow rates against number of rows

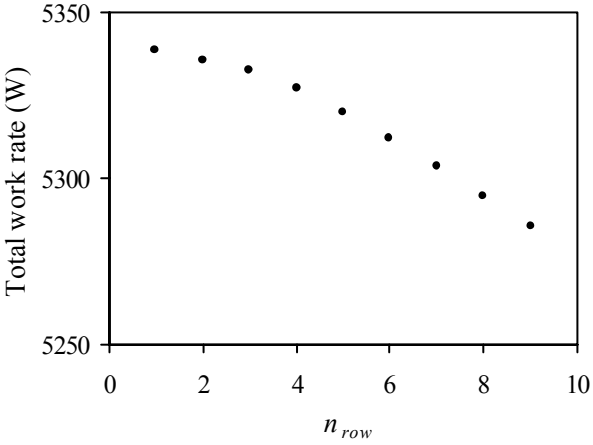

(f) Extruder total work rate against number of rows

• *inlet flow rate* • *extrusion through screen*

Figure 6.16 Variation of model results with number of screen hole extrusion rows

Figure 6.16 *(e)* indicates that the total flow rate through the extruder varies very little as the number of extrusion rows is increased. It also shows the flow rate through the screen increasing almost linearly with the number of extrusion rows, from practically zero to around one third of the total throughput.

Figure 6.16 *(f)* shows the predicted rate of work done by the extruder decreases slightly as the number of screen extrusion rows is increased. However, the total decrease as the number of rows increases from one to nine is only around two percent.

Considering all of the charts in Figure 6.16, it is noted that varying the number of screen extrusion rows impacts markedly on the flow pattern within the extruder, and thus on the amount of material which is actually extruded through the screen. This variation is significant when compared to the range of prediction given by the boundary paste parameters. The number of screen extrusion rows produces noticeable changes in the paste pressure profile, although the changes are at most of the same magnitude as the range of prediction given by the boundary paste parameters. The number of screen extrusion rows has little impact, of the order of a few per cent, on either the input flow rate to the extruder head or the extruder work rate.

6.2.3 Variation with extruder parameters

The performance of the extruder model was assessed in the previous Section for a single set of extruder geometry and operating parameters. This Section considers the response of the model to variation in some of these parameters. With over twenty possible parameters to vary, there is a great deal of scope for change. Here only four parameters are considered, primarily for illustrative purposes. Further validation of the model would be required before an extensive study of its predictions over the range of parameters.

The model is used with a fixed rotational extruder speed, from which the flow rate and work rate are found. The model could be used at a fixed flow rate, or work rate and the other parameters found respectively, although the solutions might prove to be more elusive. The model performance is considered as the speed operating condition, and three geometry conditions are varied. In each case the extruder conditions outlined previously in Section 6.2.2, using the best fit material parameters, are taken as a starting point from which one parameter is varied in turn. The response of some of the extruder conditions are show in Figures 6.17 to 6.20 over the following pages.

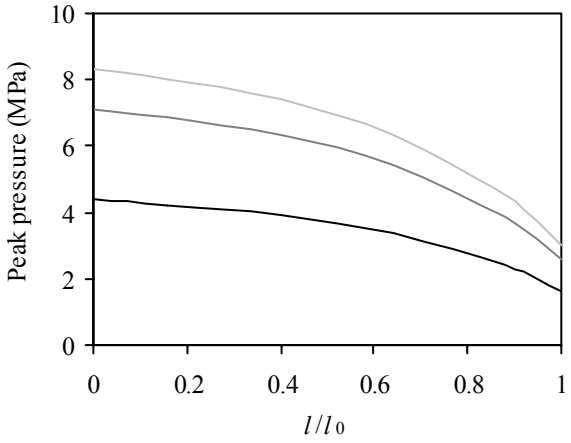

(a) Peak pressure over channel length

S (rpm): — *10* — *90* — *180*

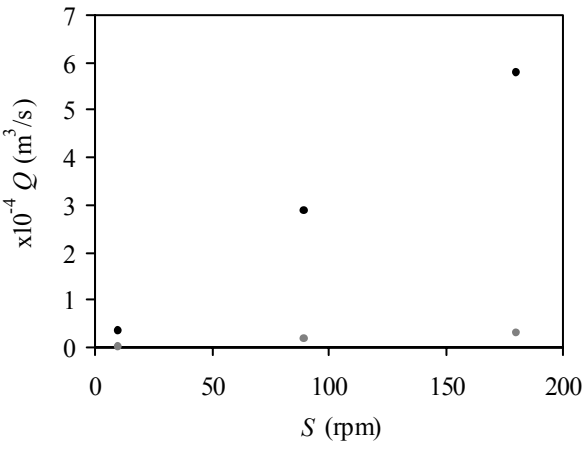

(b) Extruder flow rate

• *total flow* • *flow through screen*

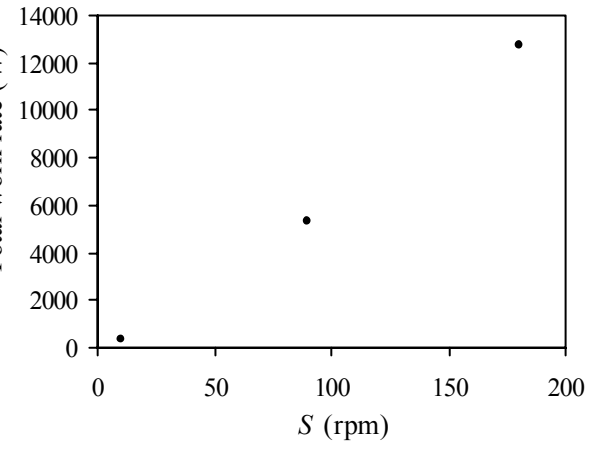

(c) Total extruder work rate

Figure 6.17 Model response to speed

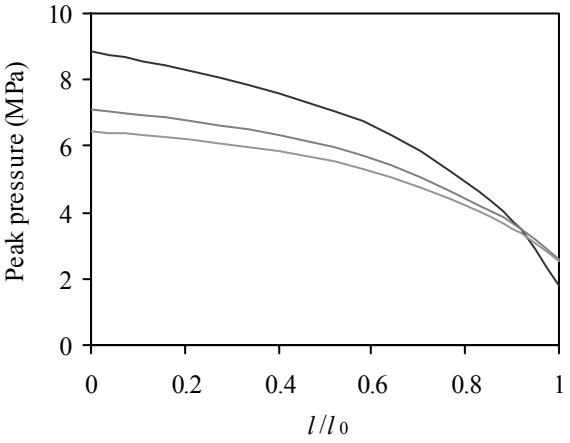

(a) Peak pressure over channel length

n_{blade}: — *1* — *3* — *5*

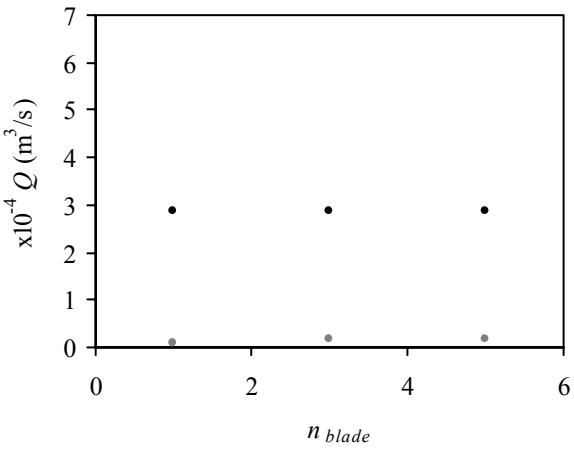

(b) Extruder flow rate

• *total flow* • *flow through screen*

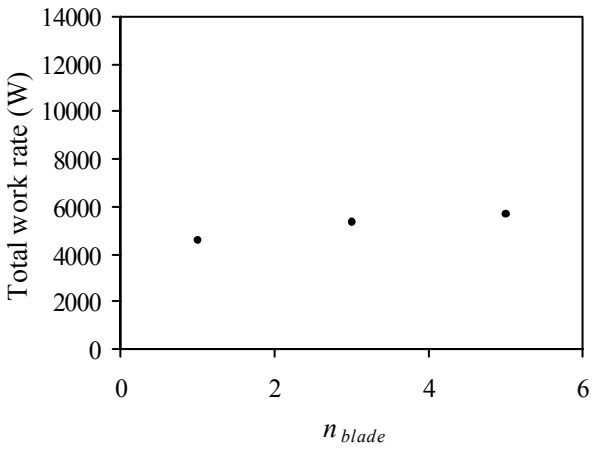

(c) Total extruder work rate

Figure 6.18 Model response to number of blades

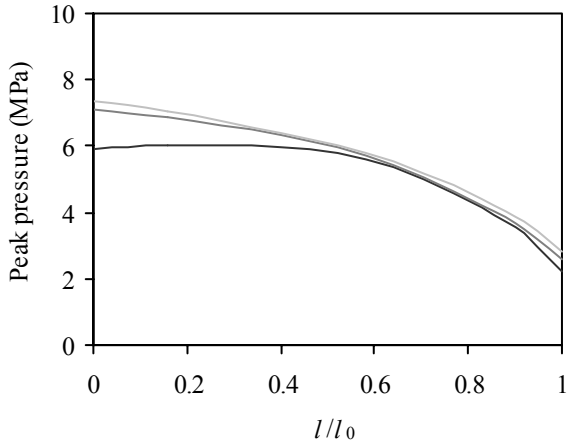

(a) Peak pressure over channel length

ζ (°): — 70 — 81 — 90

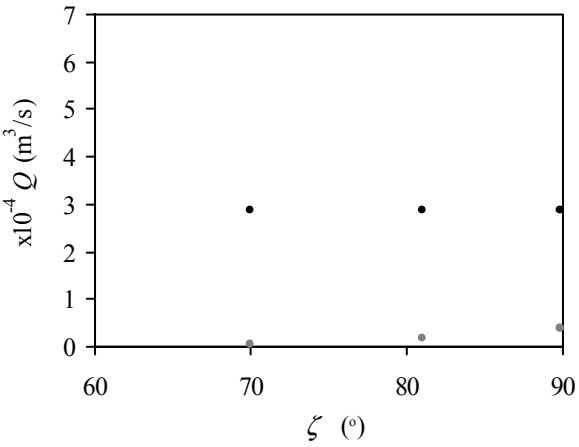

(b) Extruder flow rate

• total flow • flow through screen

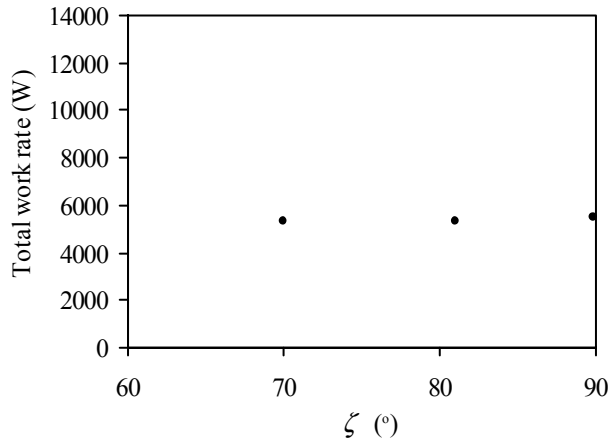

(c) Total extruder work rate

Figure 6.19 Model response to blade helix angle

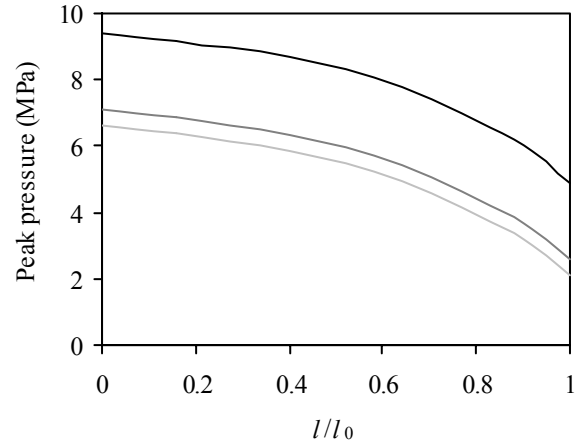

(a) Peak pressure over channel length

W_{blade}(m): — 0.0001 — 0.00135 — 0.0039

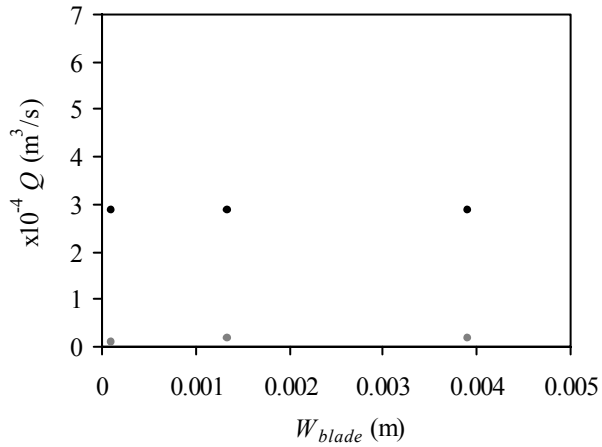

(b) Extruder flow rate

• total flow • flow through screen

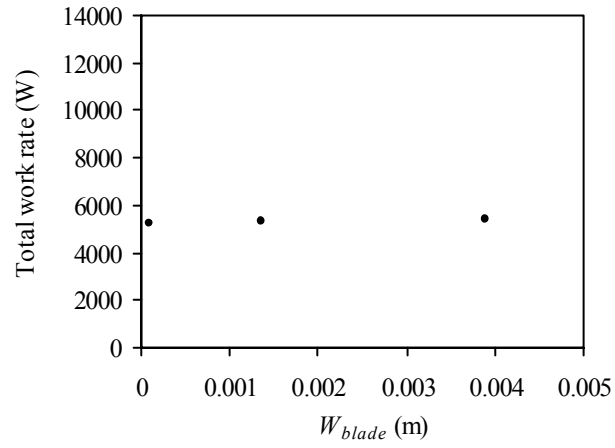

(c) Total extruder work rate

Figure 6.20 Model response to blade-screen gap

Over the relatively small range of parameters which have been varied, it has been generally apparent that the nature of the extrusion flow is generally constant. The extrusion flow through the screen always starts near zero at the inlet end of the channel, rising along the channel length (which may support a practice used by the sponsoring company of blanking the first third of the screen off). The magnitude of the extrusion flow does not appear to be very sensitive to the geometrical parameters, although the flow rate does appear to increase linearly with extruder speed. It is very apparent that with the extruder parameters used very little of the material is extruded through the screen. Increasing the number of screen hole extrusion rows would increase the screen extrusion rate as was seen in the previous Section, but the rate still appears low when compared to industrial flow rates.

A more rigorous study of the model performance might require the development of some sort of extruder effectiveness parameter, perhaps relating the work rate to the extrusion rate through the screen. An industrial extruder is typically limited by its power rating, thus some of the speeds and flow rates predicted here may not be realistically achievable. More useful results might be obtained by setting the total extruder work rate as the operating condition, rather than the speed. Without performance parameters, concise conclusions as to the change in operation as the conditions are changed is difficult. A few observations based on Figures 6.17 to 6.20 are made.

Figure 6.17 suggests that the flow rate through the extruder and screen, as well as the power requirement, increase linearly with extruder speed. This indicates that increasing the power rating of an extruder might increase its throughput linearly, but not improve its efficiency in any way. The number of blades has an effect on the performance up to a point, as shown in Figure 6.18. Moving from one to three blades reduces the peak screen pressure and increases the extrusion flow rate, although at a slight increase in power consumption. Moving from three to five further increases the power consumption, but does not appear to improve upon the peak stress or screen extrusion rate.

It appears from Figure 6.19 that increasing the blade helix angle towards a straight blade increases the screen flow rate significantly, with little penalty in terms of peak screen pressure, which might lead to more screen wear, or power consumption. Decreasing the gap between the blade tip and the screen, shown in Figure 6.20, also increases the extrusion rate through the screen with little power penalty, although the peak stress does increase markedly.

6.3 Summary

In this Chapter we have presented a novel extension to the previous ram and screw extruder methods to model the paste flow in a single-screw radial screen extruder. A combination of the upper bound method and the Benbow-Bridgwater method was used. It has been demonstrated that the principle of applying a minimum energy requirement can be used to model complex flows of paste – albeit in a simplified form.

The new model is based on a large number of assumptions, some which are very major. Assumptions are involved in all three stages of the model; *(i)* in the determination of material parameters, *(ii)* establishing the flow equations, and *(iii)* solving the flow equations. These assumptions are considered in more detail in Chapter 8, where the model can be assessed against experimental data.

The model has been shown to produce realistic predictions for the paste flow within a typical industrial extruder. The principal shortcoming of the current model is the lack of attention to flow through the screen in the region immediately in front of a blade. Consequently, the number of screen holes through which extrusion occurs has to be guessed. Future work proposed in Section 8.4 addresses how this shortcoming might be addressed. There appear to be two main limitations to the model; *(i)* the lack of well defined and accurate material parameters limits the quality of even the most rigorous model, and *(ii)* the total work rate appears to be only a very weak function of flow pattern, thus optimum flow pattern found by applying the minimum work requirement may be susceptible to error due the influence of factors which were assumed negligible.

The model has yet to be demonstrated to be of direct industrial use. However, the model predictions over the limited range of parameters considered do appear to show some optimum design parameters. For example, it appears that the screen throughput can be maximised by using a set of three straight blades, with very little extra work requirement. This is a result which appears to be consistent with industrial experience.

Finally, it is worth noting that this model may be implemented using a ubiquitous software package on any modern PC. Only a little effort is required to obtain predictions once the model has been set-up. Supposing that the model does give insight into the design and operation of industrial extruders, transferring the model for use in industry would be a simple step.

7 Extruder module results

The previous three Chapters have considered; *(i)* a possible flow pattern within a radial screen extruder, *(ii)* extruder modules capable of investigating these flows in a laboratory, and *(iii)* the development of a flow model which can predict the flow pattern and stress states in industrial extruders and the extruder modules. In this Chapter we present results obtained from the modules, using the model paste described in Chapter 3, for experimental conditions similar to those of an industrial extruder. These are compared to flow model predictions using the Benbow-Bridgwater material parameters. These results are the first detailed experimental examination of the physical conditions within radial screen extruders.

Three basic experimental arrangements are presented;

- *Rotating core module* – stationary with no blade, Section 7.1. A study of the flow of paste between the core and screen surface along the length of the extruder for a variety of core geometries.
- *Nip module* – Section 7.2. A study of piston driven flow of paste into a nip formed by a blade and screen for a variety of blade and die geometries.
- *Rotating core module* – single blade, Section 7.3. A study of the flow of paste along the length of the extruder channel formed by a single blade attached to a parallel sided core. A range of rotational speeds and blade geometries were used.

Some aspect of the model approach and assumptions are considered through an assessment of model predictions results compared to experimental results. However, we leave a more general consideration of the model performance until Chapter 8.

7.1 Rotating core module – stationary with no blade

7.1.1 Experimental program

Thirty six experimental runs were performed using the *rotating core module*, described in Section 5.1, with a stationary core and no blade. The model talc paste described in Chapter 3 was used for all of the runs. The paste was always prepared on the same day as the experiments. The experimental method followed that previously described in Section 5.1. All experiments were carried out with a blank screen with no perforations, of length L = 0.050 m and diameter D_s = 0.0308 m. Each experimental run was carried out at a constant rate, reported in terms of the extrudate velocity at the extruder exit. The experimental program is outlined in Table 7.1.

Table 7.1 Experimental program for rotating core module – stationary with no blade

L_{core}, m	D_s, m	D_0, m	ϕ, deg	V, m/s	L_{core}, m	D_s, m	D_0, m	ϕ, deg	V, m/s
0.05	0.0308	0.01	0	0.0016	0.05	0.0308	0.015	5.7	0.016
				0.0057					0.022
				0.02					0.03
			2.9	0.01				8.5	0.022
				0.016					0.035
				0.025					0.055
			5.7	0.016			0.02	2.9	0.01
				0.022					0.016
				0.03					0.025
			8.5	0.022				5.7	0.016
				0.035					0.022
				0.055					0.03
			11.3	0.035			0.025	0	0.0016
				0.044					0.0057
				0.055					0.02
								2.9	0.01
									0.016
									0.025
							0.03	0	0.0016
									0.0057
									0.02

7.1.2 Results

For all but the 0.03 m inlet core diameter, D_0, experiments, the paste was observed to flow steadily and evenly between the core and the screen. Where an initial core diameter of 0.03 m was used, the gap between the core and screen was only 0.0004 m along the whole length of the extruder. The flow between the core and the screen was observed to be very uneven in these cases, presumably because any slight eccentricity of the core would significantly change this gap distance. Results from these experiments were deemed to be unreliable, and are not presented here. For the rest of the data, steady state values of the screen pressures and axial force on the core were calculated from each run. Figures 7.1 to 7.3 present these experimental data in comparison with predictions obtained from the screen extruder model outlined in Section 6.1.6 using the boundary and best fit material parameters presented in Section 3.4.

Initially we consider the case of an inlet core diameter of 0.01 m. The profiles of the paste screen pressure along the length, l, of the extruder are presented against extrudate velocity, V, and core half-angle, ϕ, in Figure 7.1 *(a)* to *(e)*. A number of significant features stand out. The profile of pressure over length tends to change from linear for low half-angles to logarithmic at larger half-angles. This is in agreement with what we expected from our lower bound energy model presented in Section 2.4.2. The extrudate velocity does not appear to be a significant variable over the range of interest, with the data indicating practically no significant variation. The magnitude of the pressures increases markedly as the half-angle is increased, and thus the cross-sectional area reduction is increased.

Figure 7.1 *(f)* shows the corresponding variation of the axial force on the extruder core over the range of extrudate velocity and half-angle. Again, the velocity dependence is very weak over the ranges considered, whereas the force increases considerably from practically zero to 3 kN as the half-angle is increased. The model predictions generally over-predict the axial force, with the data lying slightly below the model lower bound prediction.

These data indicate that over the ranges of interest the rate effects are negligible in comparison to the effect of change in cross-sectional area, expressed here in terms of the core half-angle.

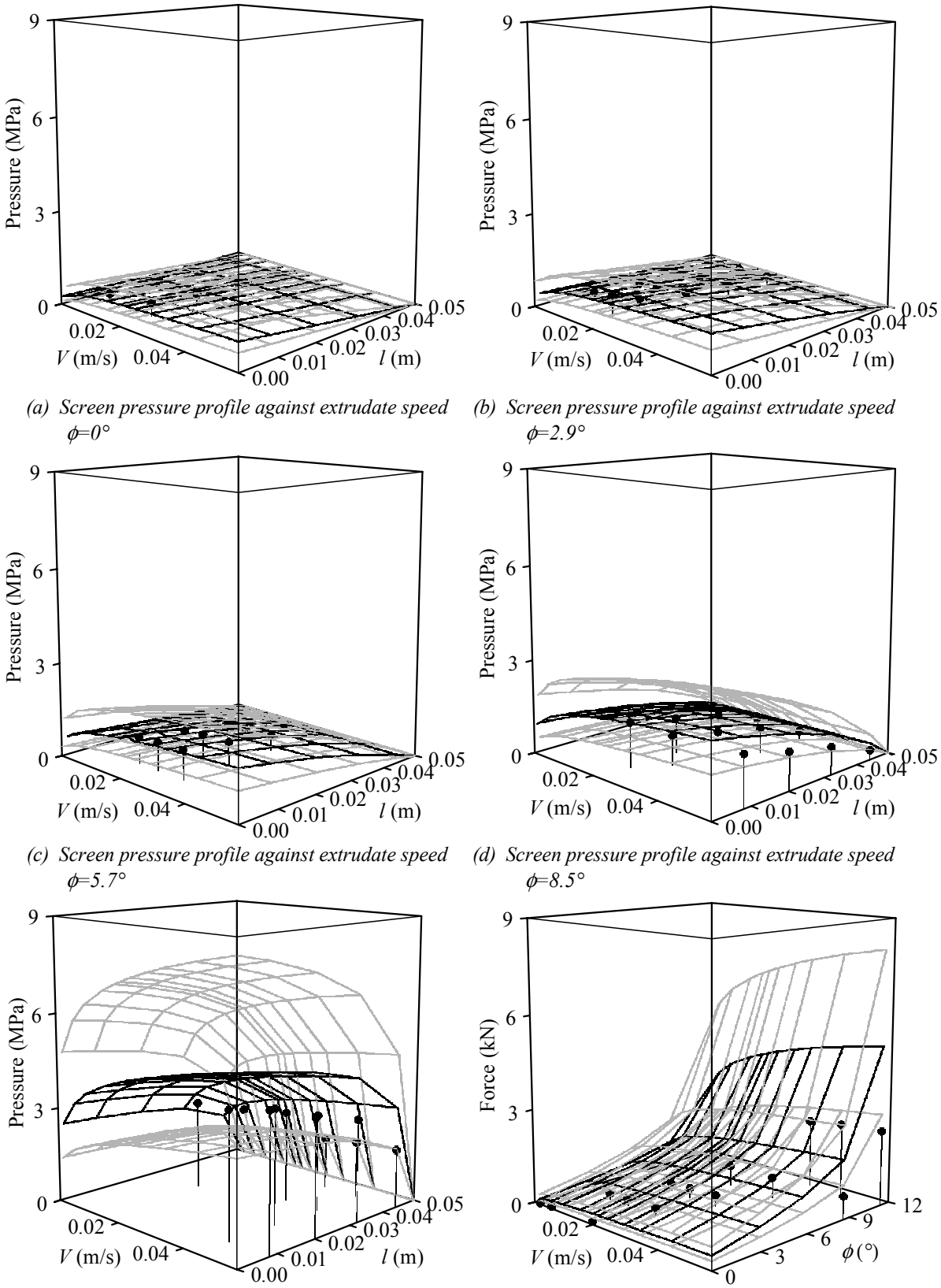

(a) Screen pressure profile against extrudate speed ϕ=0°

(b) Screen pressure profile against extrudate speed ϕ=2.9°

(c) Screen pressure profile against extrudate speed ϕ=5.7°

(d) Screen pressure profile against extrudate speed ϕ=8.5°

(e) Screen pressure profile against extrudate speed ϕ=11.3°

(f) Core force against half-angle and extrudate speed

Figure 7.1 Stationary core module with no blade results for D_0 = 0.01 m

• *experimental value*

model result: — *best fit parameters* — *boundary parameters*

The axial pressure profile shape appears to be more linear the smaller the half-angle. Having established this trend, only the variation of pressure profile magnitude is considered to enable the effect of a wider range of parameters to be presented. The screen pressure data from the first transducer leading away from the entrance (l = 0.008 m) was taken as a characteristic value for the whole pressure profile. Figure 7.2 shows the variation of the stress at this single position over the whole experimental ranges of extrudate velocity, core initial diameter and core half-angle. Figure 7.3 shows the corresponding data for axial force on the core.

In Figure 7.2 again it is apparent that the pressure is not sensitive to the extrudate velocity over most of the ranges considered, although as the initial core diameter increases the velocity does appear to have become more significant. This might be taken as evidence that rate dependence is more significant when there is an increase in surface area, thus the boundary work-rate rate dependence is more significant than the deformational work-rate rate dependence. The pressure is seen to increase with half-angle for all of the initial core diameters, and now we also see the pressure increasing as the initial core diameter increases. This increase might have been caused by the increase in core surface area. As the core inlet diameter approaches the screen diameter the pressure is seen to increase very rapidly.

As for the pressure profiles of Figure 7.1, the best fit parameter model predictions are generally close to the experimental data, with the experimental data always within the boundary parameter predictions. This was no longer the case when the inlet core diameter and the core-half angle are first increased. In these cases the measured pressure rises very rapidly and the model substantially under-predicts the experimental data.

A similar picture is apparent for the corresponding core axial force data presented in Figure 7.3. The experimental data follow a similar pattern; *i.e.* they are not sensitive to extrudate velocity, and they increase with half-angle and initial core diameter. However, the model predictions tend to over-predict the experimental data for the smaller initial core diameters, but then under-predict for the larger initial core diameters.

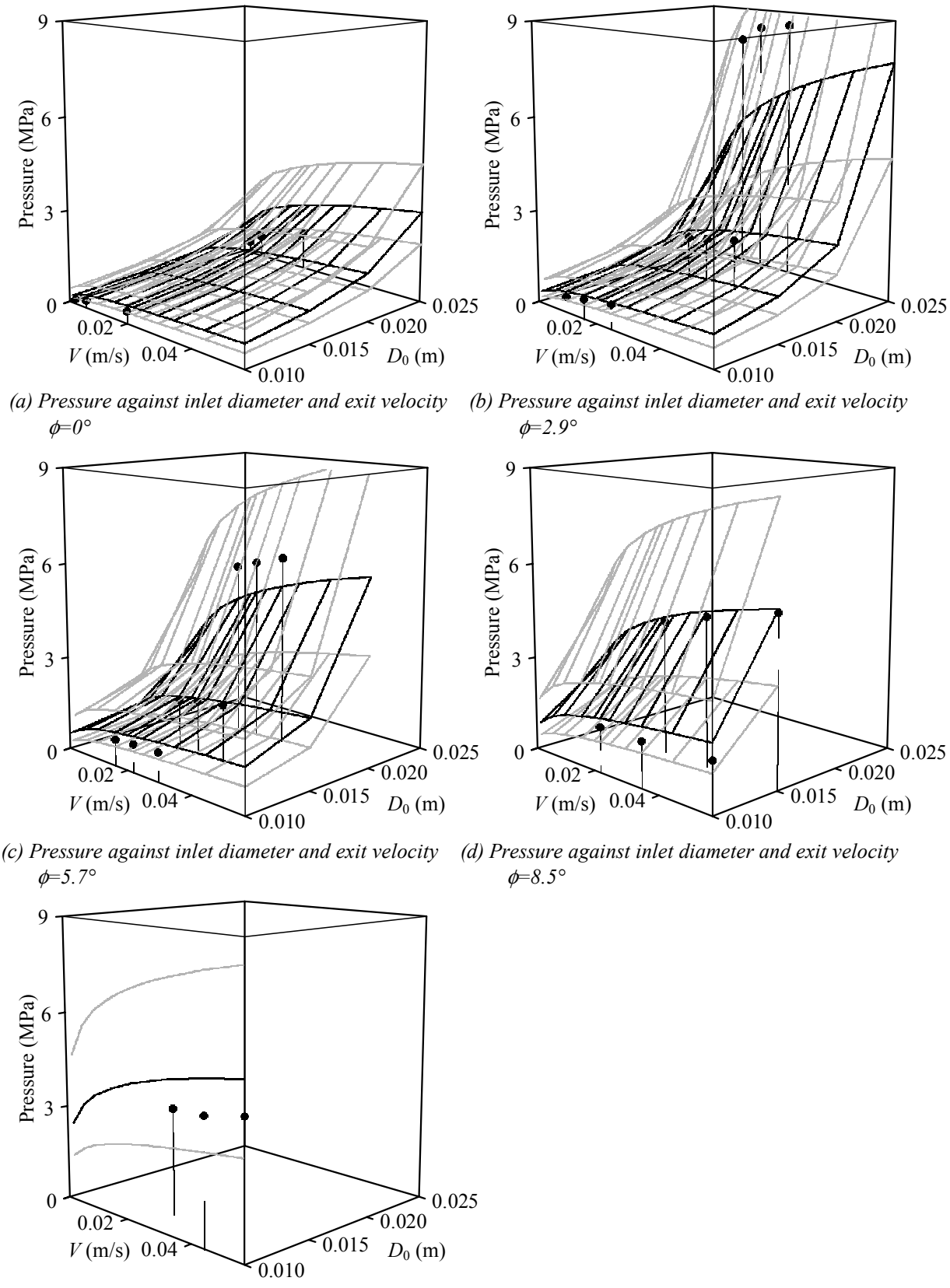

(a) Pressure against inlet diameter and exit velocity ϕ*=0°*

(b) Pressure against inlet diameter and exit velocity ϕ*=2.9°*

(c) Pressure against inlet diameter and exit velocity ϕ*=5.7°*

(d) Pressure against inlet diameter and exit velocity ϕ*=8.5°*

(e) Pressure against inlet diameter and exit velocity ϕ*=11.3°*

Figure 7.2 Stationary core module with no blade: screen pressure results at l = 0.008 m

● *experimental value*

model result: — *best fit parameters* — *boundary parameters*

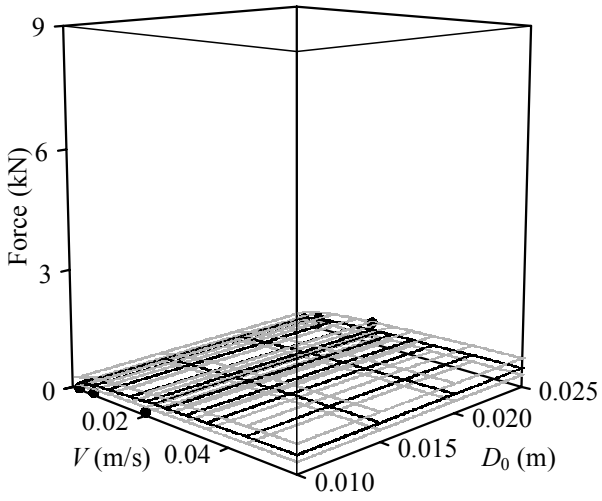

(a) Force against inlet diameter and exit velocity ϕ=0°

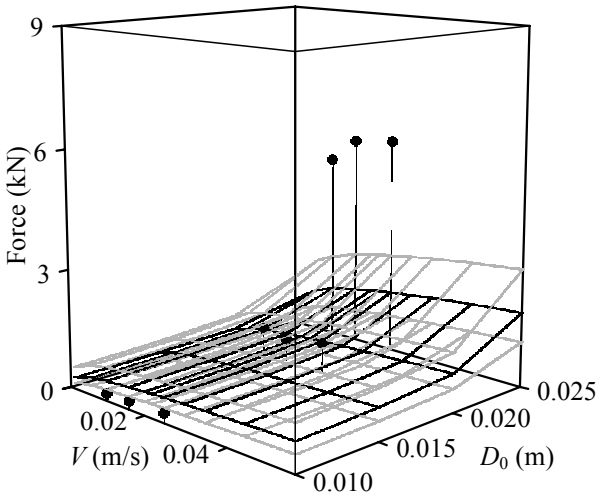

(b) Force against inlet diameter and exit velocity ϕ=2.9°

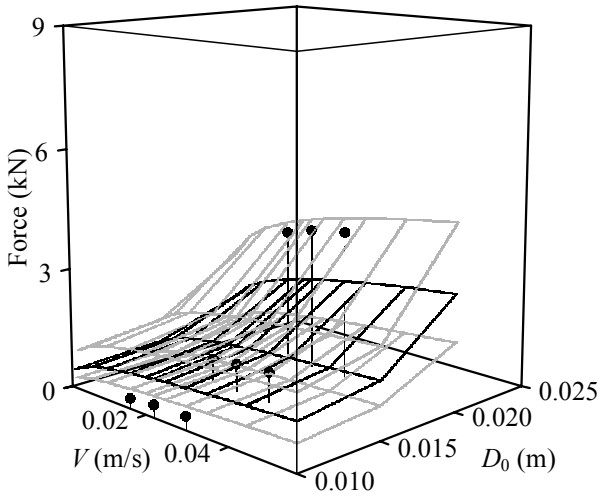

(c) Force against inlet diameter and exit velocity ϕ=5.7°

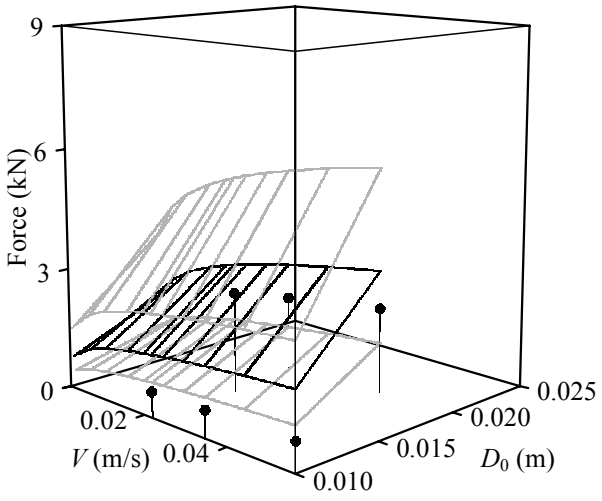

(d) Force against inlet diameter and exit velocity ϕ=8.5°

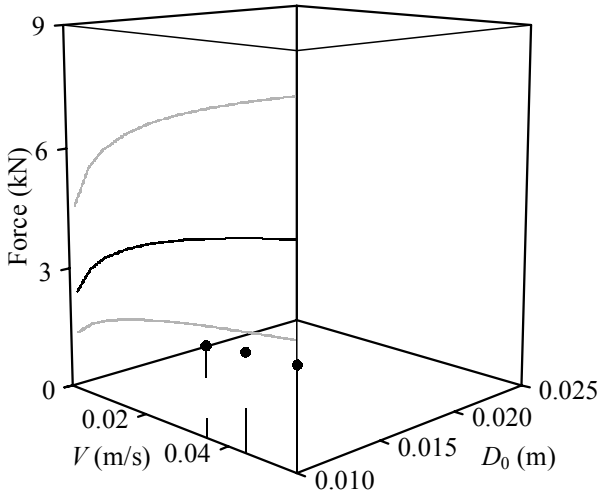

(e) Force against inlet diameter and exit velocity ϕ=11.3°

Figure 7.3 Stationary core module with no blade core: axial force results

● *experimental value*

model result: — *best fit parameters* — *boundary parameters*

7.2 Nip module

7.2.1 Experimental program

Thirty-six experimental runs were carried out using the *nip module* described in Section 5.2. The model talc paste described in Chapter 3 was used for all of the runs, and the paste always used on the same day as it was prepared. The experimental method followed that previously described in Section 5.2. Each experimental run was carried out at constant rate, reported in terms of the mean extrudate velocity at the extruder exits. Where both barrel (screen) and wedge (blade) dies were used, the extrudate was collected from each over the duration of the whole experiment and then weighed. From this data the mean fraction of flow through each die land over the course of the run was calculated. Three flow patterns were investigated where paste may flow only through the barrel (screen) die land, both the barrel (screen) and wedge-barrel (blade), or the wedge-barrel (blade) die lands. When used, the screen and blade die lands were nominally identical, as outlined in Table 7.2 *(a)*. Each of these three basis flow conditions was studied under the nip angle, θ, and mean extrudate velocity, V, conditions outlined in Table 7.2 *(b)*.

Table 7.2 Experimental program for nip module

(a) Die land geometries

Die land dimension	Screen flow	Screen and blade flow	Blade flow
W_{screen}, m	0.0013	0.0013	0
L_{screen}, m	0.0050	0.0050	N/A
W_{blade}, m	0	0.0013	0.0013
L_{blade}, m	N/A	0.0050	0.0050

(b) Operating conditions

θ, deg.	V, m/s
45	0.0012
	0.012
	0.12
60	0.0012
	0.012
	0.12
75	0.0012
	0.012
	0.12
90	0.0012
	0.012
	0.12

7.2.2 Results

Steady state values of the screen and blade pressures and the extrusion pressure on the piston were found from each run. Figures 7.4 to 7.5 present these experimental data in comparison with predictions obtained from the screen extruder model outlined in Section 6.1.6 using the boundary and best fit material parameters presented in Section 3.4.

Figure 7.4 shows the complete set of experimental data for the screen and blade flow case. Parts *(a)* to *(d)* show the pressure profile of the paste on the screen and blade walls as a function of radial distance from the nip, over the experimental range of mean extrudate velocities and nip angles. The first feature to note is that the pressure on the blade and on the screen surface at comparable radial positions are approximately equal. This gives weight to the validity of the radial flow assumption used in the modelling of Section 6.1.6. The shape of the pressure profile along the radial distance appears to be logarithmic in shape, again in agreement with the nature of the model. A strong dependence on mean extrudate velocity is apparent between the 0.0012 m/s and 0.012 m/s data sets, but the dependence on velocity between the 0.012 m/s and 0.12 m/s data is considerably smaller. A slight decrease in the pressure magnitudes is apparent as the angle of the nip between the blade and screen is increased. The model predictions follow the same trends as the experimental data, with the data always falling within the boundary predictions. The model appears to over-predict the stresses somewhat.

The significant velocity dependence at low velocities, and the slight dependence on nip angle can be seen again when the extrusion pressure is plotted in Figure 7.4 *(e)*. Only the case of nominally identical screen and blade die lands has been considered at this stage. For such a case, the model predicts the flow to be equally divided between the two die lands, thus the fraction of flow through the screen, ε, is 0.5. Figure 7.4 *(f)* shows that for our conditions this appears to hold true experimentally. Whether the model is able to successfully predict the flow distribution for non-similar die lands remains to be seen.

Figure 7.5 shows the extrusion pressure variation over nip angle and mean extrudate velocity for all three flow conditions; screen flow, screen and blade flow, and blade flow. It is apparent that the extrusion pressure is not greatly changed by the choice of flow pattern, so long as the mean extrudate velocity is the same. The same sensitivity to mean extrudate velocity and nip angle are evident as were described for Figure 7.4 *(a)* to *(e)*.

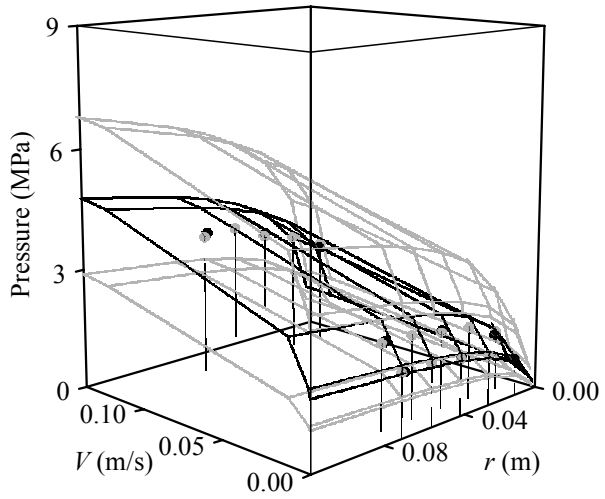

(a) Wall pressure profile against extrudate speed
θ=45°● blade wall● screen wall

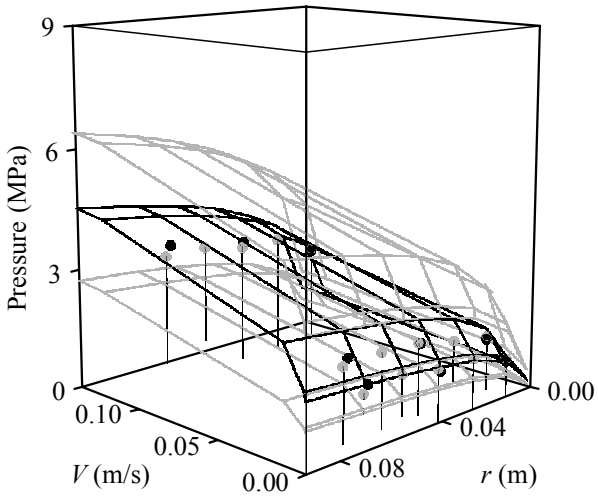

(b) Wall pressure profile against extrudate speed
θ=60● blade wall● screen wall

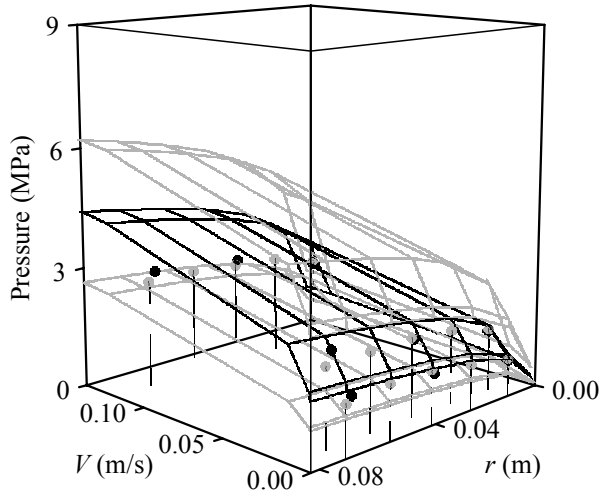

(c) Wall pressure profile against extrudate speed
θ=75°● blade wall● screen wall

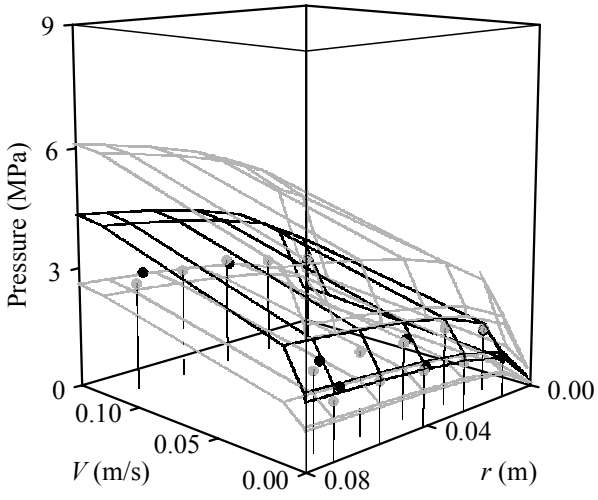

(d) Wall pressure profile against extrudate speed
θ=90● blade wall● screen wall

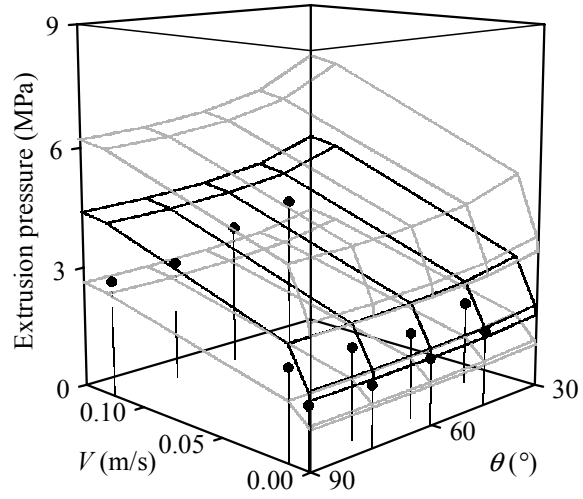

(e) Piston extrusion pressure against nip angle and extrudate speed

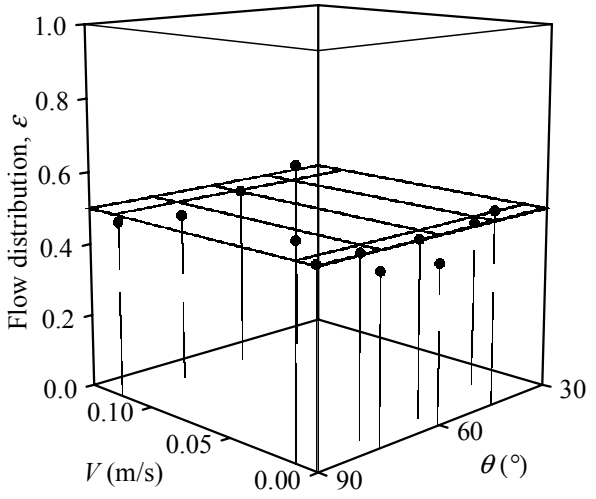

(f) Flow distribution against nip angle and extrudate speed

Figure 7.4 Nip module results for screen and blade flow case

● experimental value
model result: — best fit parameters — boundary parameters

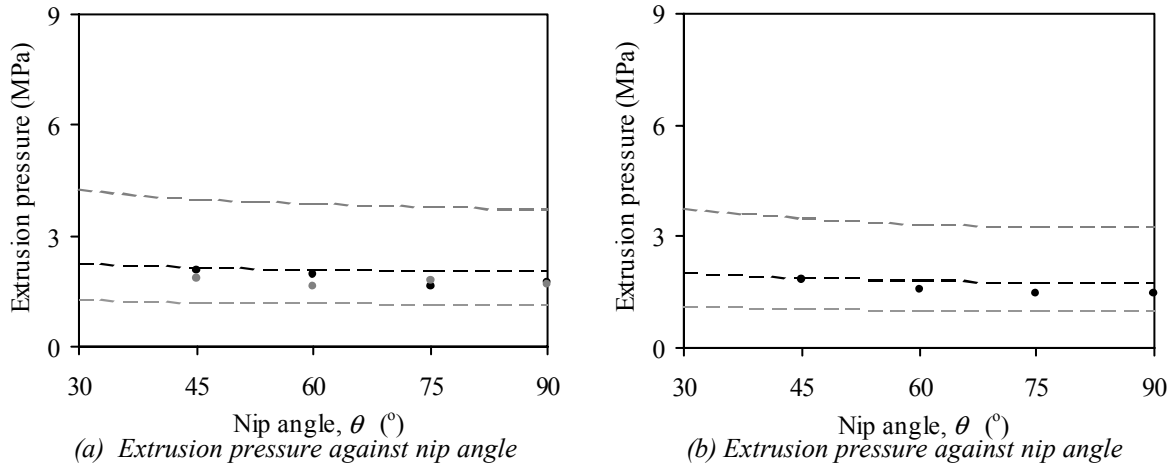

(a) Extrusion pressure against nip angle

V=0.0012 m/s, ● screen flow ● blade flow

(b) Extrusion pressure against nip angle

V=0.0012 m/s, ● screen and blade flow

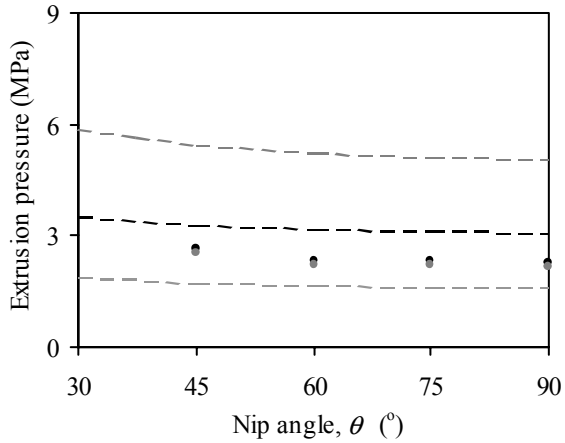

(c) Extrusion pressure against nip angle

V=0.012 m/s, ● screen flow ● blade flow

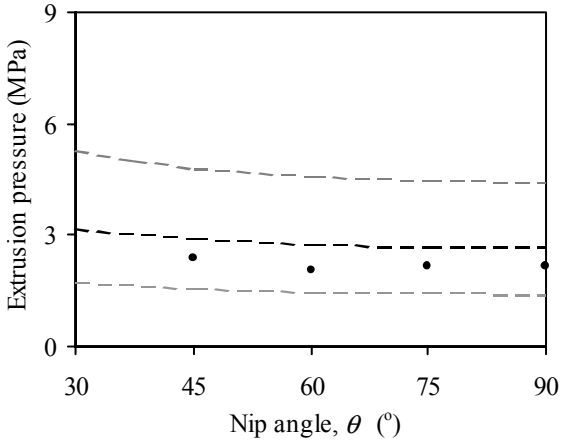

(d) Extrusion pressure against nip angle

V=0.012 m/s, ● screen and blade flow

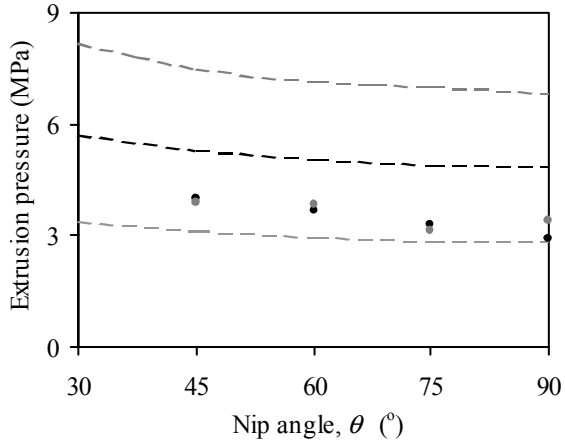

(e) Extrusion pressure against nip angle

V=0.12 m/s, ● screen flow ● blade flow

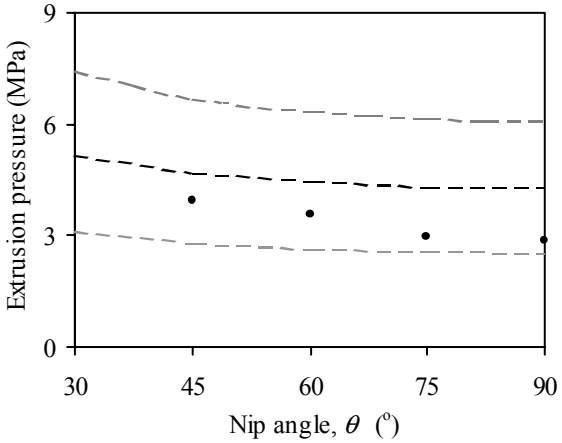

(f) Extrusion pressure against nip angle

V=0.12 m/s, ● screen and blade flow

Figure 7.5 Nip module extrusion pressure results

(a), (c) and (e) show data for both the screen flow geometry and the blade flow geometry
(b), (d) and (f) show data for combined screen and blade flow geometry
● experimental value
model result: — best fit parameters — boundary parameters

7.3 Rotating core module – single blade

7.3.1 Experimental program

Fourteen experimental runs were carried out using the *rotating core module* described in Section 5.1 with a single blade attached to a parallel-sided rotating core. The model talc paste described in Chapter 3 was used for all of the runs, the paste always being prepared on the same day as the experiments. The experimental method followed that previously described in Section 5.1. All experiments were carried out with a blank screen with no perforations, of length $L = 0.050$ m and diameter $D_s = 0.0308$ m. The core was parallel sided ($\phi = 0$) with diameter $D_0 = 0.025$ m. A variety of blade geometries and flow conditions were used, although all blades had tip length $L_{blade} = 0.0006$ m. Each experimental run was carried out at three different rates, each of sufficient duration to enable a steady state flow condition to be developed. The flow rate and rotational speed are reported in terms of the velocity of the paste along the channel length, v_l (assuming the paste fills the whole channel and undergoes plug flow), and the ratio of the tangential screen velocity relative to the core, v_s, to the paste velocity – v_s/v_l. Control experiments were also conducted where a nominally identical core was used, but with no blade attached. The experimental program is outlined in Table 7.3.

Table 7.3 Experimental program for rotating core module –with single blade

S (rpm)	$\{v_{l1}, v_{l2}, v_{l3}\}$ (m/s) $\{v_s/v_{l1}, v_s/v_{l2}, v_s/v_{l3}\}$	W_{blade} (m)	θ (degrees)
200	{ 0.0156, 0.00782, 0.00391} {20.6, 41.2, 82.4}	0.0010	45
			60
			75
		0.0006	45
			60
			75
		No blade	
100	{ 0.0156, 0.00782, 0.00391} {10.3, 20.6, 41.2}	0.0010	45
			60
			75
		0.0006	45
			60
			75
		No blade	

$D_s = 0.0308$ m, $D_0 = 0.025$ m, $\phi = 0$, $L_{core} = 0.050$ m, $L_{blade} = 0.0006$ m, blank screen

7.3.2 Results

Paste flow

When no blade was used the paste was observed to flow evenly as a plug out the end of the extruder, rotating if being extruded around a rotating core, as illustrated in Figure 7.6 *(a)*. When the single blade was present the paste was seen to flow through only a small region of the annulus between the screen and core, illustrated in Figure 7.6 *(b)*, and so the extrusion channel was not flooded. This region rotated with time, apparently synchronised with the rotation of the blade. It was supposed that the paste was predominantly flowing along the length of the extruder in the region in front of the blade, although no direct evidence for this was obtained.

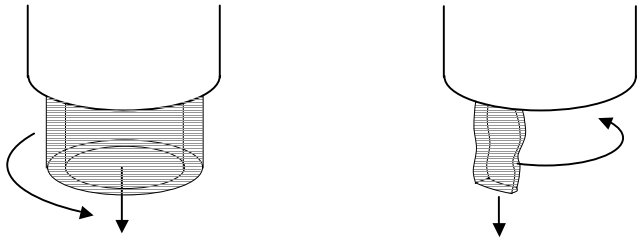

(a) No blade *(b) Single blade*

Figure 7.6 Observed paste flow pattern out of rotating core module

Control experiments with no attached blade

In Section 5.1 sample rotating core results were presented for the case of a rotating core with no blade. Steady state values were found for the axial force on the core, the spindle torque and the paste pressure on the screen along the extruder length. The extruder considered in Section 5.1 had a core inlet diameter, D_0, of 0.015 m and a core half angle, ϕ, of 5.7º. For this case, the variation of screen pressure over the extruder length was slightly convex and tended towards zero at the extruder exit. The control experiments considered in this Section used a parallel sided core (the core half-angle was zero). In this case the variation of screen pressure along the extruder length was consistently linear, again tending towards zero at the extruder exit. The gradient of the screen pressure along the extruder length was found by linear regression. The complete set of control experiment results, which correspond to the single blade experiments which follow, are presented in Figure 7.7.

We see in this figure that there is, in general terms, a reasonable agreement between the experimental results and the model predictions. The magnitude of the experimental core force,

torque and screen stress profile gradient all decrease as the relative screen velocity is increased or as the channel velocity is decreased. There is an apparent disagreement between the experimental and model results for the torque data. The predicted torque increases as the relative screen velocity increases, contrary to the experimental data. It is thought that a slight eccentricity of the core (measured at ~ 8 μm) was sufficient to effectively reduce the area of contact with the experimental core. This effect seemed to became more significant as the relative screen velocity increased. A reduced contact area might have led to reduced magnitudes of core force, torque and profile gradient. However, without knowing the precise flow pattern which occurred, any predictions of how the parameters would change are largely speculative.

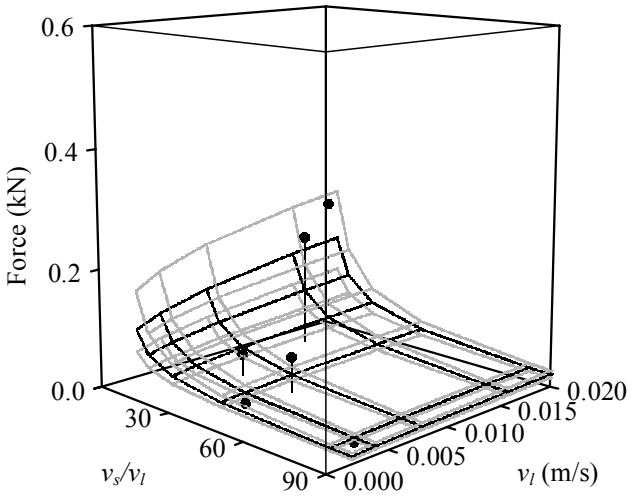

(a) Core force against screen and paste velocity

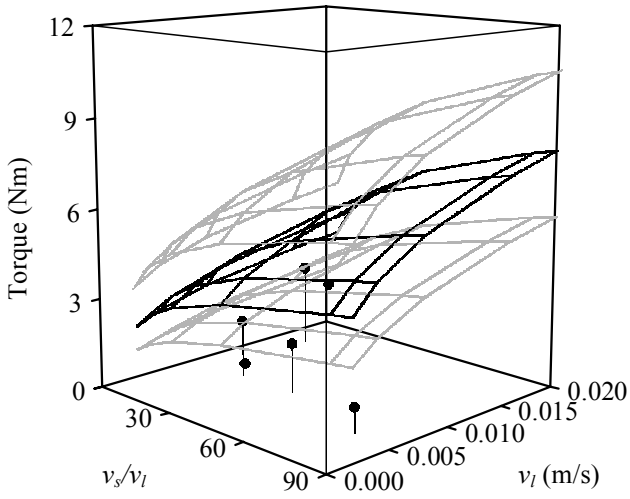

(b) Torque against screen and paste velocity

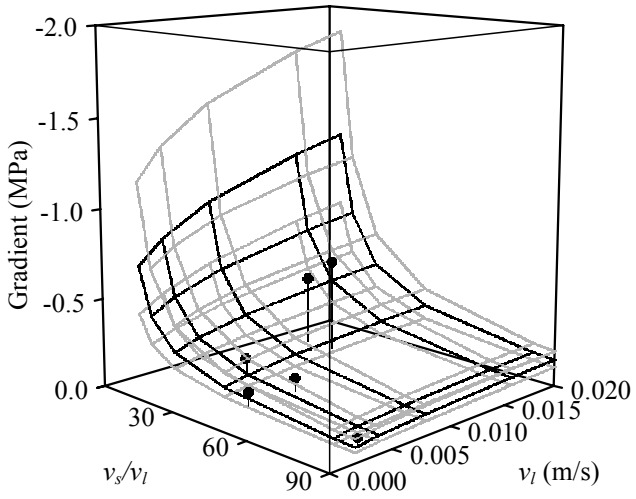

(c) Screen pressure gradient against screen and paste velocity

Figure 7.7 Control results for rotating core with no blade attached

● *experimental value*

model result: — *best fit parameters* — *boundary parameters*

Single blade pressure profiles

The previous Section considered the case of a rotating core with no blade attached. Now the effect of an attached blade is studied. Figure 7.8 shows the complete data set for a typical experimental run with a single blade attached. Parts *(a)*, *(b)* and *(c)* clearly show the effect of the three different flow rates on the extrusion pressure, axial force on the core and the spindle torque, respectively. These figures suggest that steady state conditions have been reached within each period. Part *(d)* shows the paste pressure against the screen over a steady state period for the first flow rate, Q. The pressure shows a cyclic pattern, corresponding to the rotation of the core. Data recorded over fifteen periods were averaged and plotted as mean radial screen stress profiles in *(e)*. A clear difference exists between the transducer upstream of the core, giving a weak variation in stress, and the four transducers downstream, which show a distinct peak and minimum as the blade passed. The extruder flow model of Section 6.1 suggests that the peak stress occurs at the boundary of the radial nip flow region. Following this, the peak experimental stress is assumed to be at the corresponding position across the extruder channel width. The increase in stress before the peak is more gradual than the decay afterwards. The magnitude of the peak stress is greatest at the start of the core, and decreases along its length. Part *(f)* shows that this decrease is almost linear, whereas the minimum stress decreases rapidly at first before levelling off at a low value.

The difference in magnitude between the peak and minimum stresses seen in Figure 7.8 *(f)* lends evidence to the notion that paste will flow through the screen of an extruder in the region of the nip between the blade and screen. Large stresses associated with the flow over the blade mean that it becomes energetically favourable for paste to flow through the screen instead. The rapid decay of the minimum stress along the extruder length to a relatively constant, and low, value is compatible with the observation of paste flowing along the length of the extruder predominantly in the region immediately prior to the blade. A region of channel behind the blade absent of paste would explain the low, and constant, stress readings. Over this period the pressure on the screen at the transducer locations would be low, increasing once the paste made contact again. The filled region of channel was estimated by using the point at which the stress started to increase as the boundary of the filled region. The result of this is presented in Figure 7.9. Some paste will be present throughout the channel due to flow over the blade. We do not pursue the specifics of the flow in the module extruder in further detail at this point, since the principal aim of this study has been the flow of paste in an industrial screen extruder.

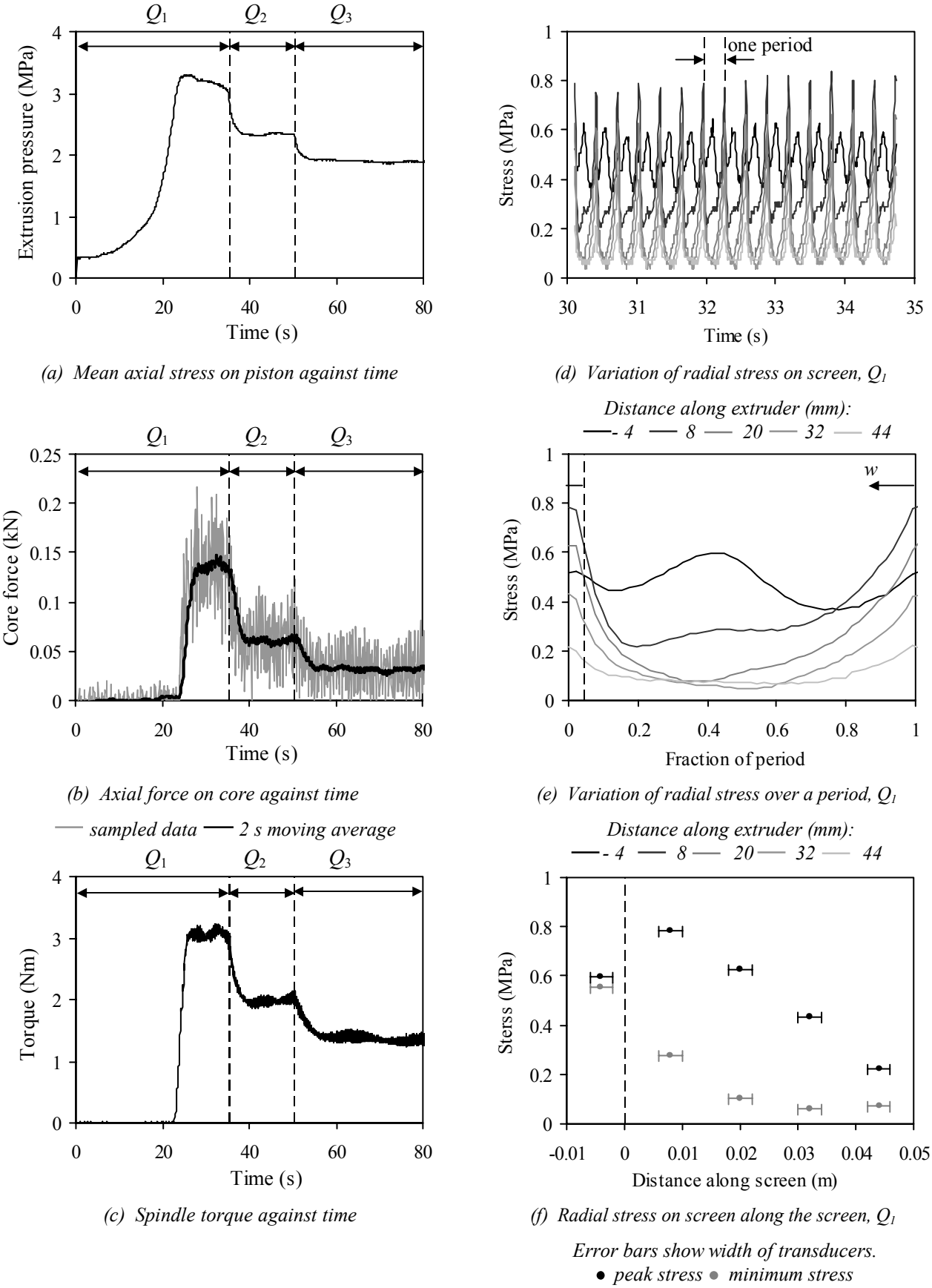

(a) Mean axial stress on piston against time

(d) Variation of radial stress on screen, Q_1

(b) Axial force on core against time

(e) Variation of radial stress over a period, Q_1

(c) Spindle torque against time

(f) Radial stress on screen along the screen, Q_1

Figure 7.8 Sample results from the rotating core module with single blade

$\theta = 45°$, $S = 200$ rpm, $D_s = 0.0308$ m, $L_{core} = 0.05$ m, $D_0 = 0.025$ m, $\phi = 0$.
$W_{blade} = 0.0006$ m, $L_{blade} = 0.0006$ m.

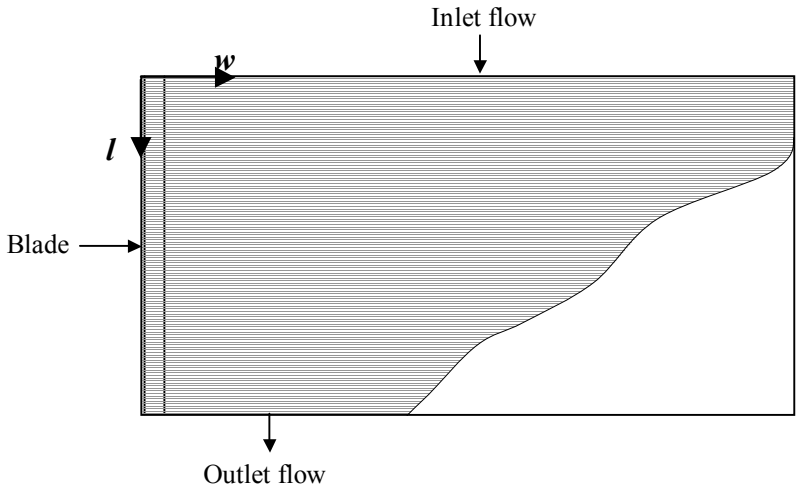

Figure 7.9 Supposed paste filled region of extruder channel for sample extrusion

The results of the single blade *rotating core module* experiments are shown in comparison to the flow model predictions in Figures 7.10 to 7.15. Figure 7.10 shows the profile of the paste pressure on the screen over the width of the extruder channel at the four pressure transducer locations along the length of the screen. Over the range of operating conditions the nature of the pressure profile remains constant. From a minimum, the pressure rises gradually, at a slightly increasing rate, until a peak pressure is reached. It is supposed that this peak pressure is associated with the onset of radial flow into the blade/screen nip, although no direct evidence of the relative location of the experimental pressure peak and the blade was available. The peak in the pressure is relatively steep, with the pressure decaying immediately after it is reached. The pressure decay after the peak is faster than the pressure increase building up to the peak. The shape of the pressure profile over the channel width does not appear to vary greatly over the channel length. The profile appears to be scaled depending on the position along the length, with the magnitude being greatest at the channel entrance. Where the paste longitudinal channel velocity is low, the profile minima tend to collapse to around zero, which as we previously noted is probably due to an unfilled region in the extruder channel behind the blade. The magnitude of the stresses appear to increase as the paste longitudinal channel velocity is increased, but show apparently little sensitivity to the relative screen velocity.

The pressure profiles predicted by the extrusion flow model share some characteristics with the experimental profiles. For clarity, in this figure only the model predictions using the best fit paste material parameters are shown. Like the experimental data, the pressure increases gradually across the width of the channel as the paste flows towards the blade/screen nip. The profile reaches a peak where radial flow into the nip starts. The profile then decreases rapidly to the pressure minimum at the trailing edge of the blade. As with the experimental data, the

model profiles are offset depending on the position along the length of the channel. The nearer the channel entrance, the greater the profile offset.

The absolute performance of the model appears to be very limited. Whilst the minima of the profiles appear to bear some resemblance to the experimental values, the profile peaks appear to be a factor of 3 to 10 greater. The trends of the experimental and model profiles are seen more clearly when the profile maximum and minimum are plotted along the extruder length, as shown in Figure 7.11.

The variation of the profile peaks and minima along the channel length appear linear for both the experimental data and the model. The experimental minima approach the model lower bound predictions, with both approaching zero towards the channel exit Again the absolute discrepancy between the experimental and model peak values can be seen. Another feature of the discrepancy also appears in this figure. Both the experimental peaks and minima are tending, with different gradients, towards zero at the channel exit. However, the model peaks and minima vary with the same gradient along the channel length to different values at the channel exit. Put in an alternative way, the experimental pressure profile over the channel width is scaled depending on the position along the channel length, whereas the predicted model pressure profile over the channel width is offset depending on the position along the channel length.

We see from Figure 7.11 that the pressure profile over the whole of the channel may be characterized by the gradient and exit value along the channel length of the peaks and minima across the channel width. These values were found by linear regression for all of the experimental and model prediction data. The minima were not considered in much further detail because their tendency to drop to zero, or sometimes even small negative values made analysis of the gradients along channel length and exit values impractical. Gradient and exit value data for the profile maxima are presented following some consideration of the torque and axial force on the extruder core.

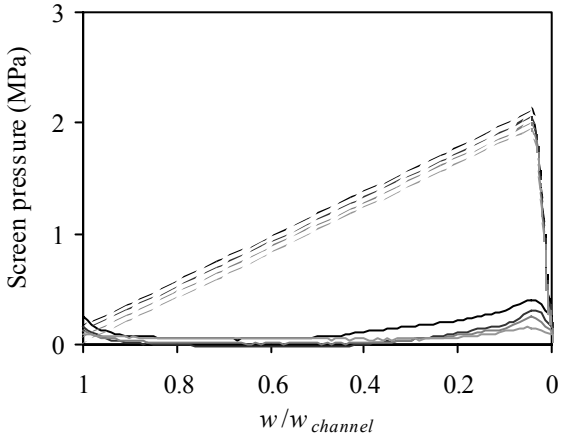

(a) Screen pressure profile over width
v_l = 0.00391 m/s, v_s/v_l = 41.2

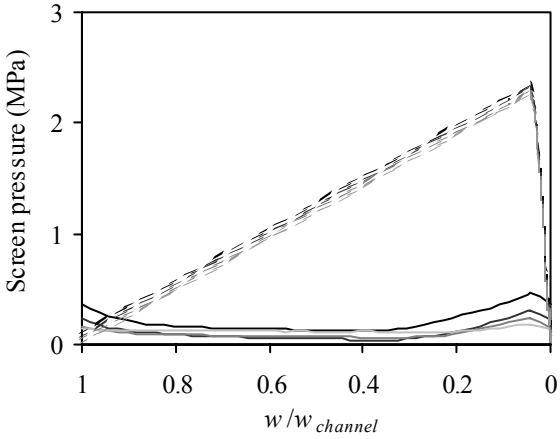

(b) Screen pressure profile over width
v_l = 0.00391 m/s, v_s/v_l = 82.4

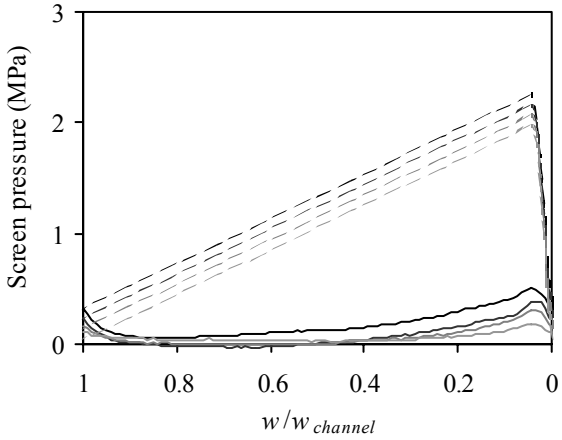

(c) Screen pressure profile over width
v_l = 0.00782 m/s, v_s/v_l = 20.6

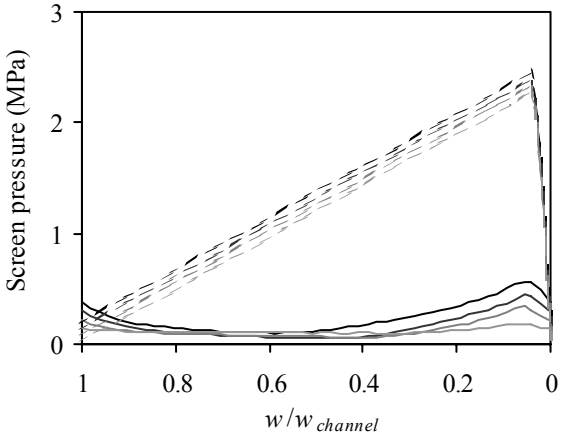

(d) Screen pressure profile over width
v_l = 0.00782 m/s, v_s/v_l = 41.2

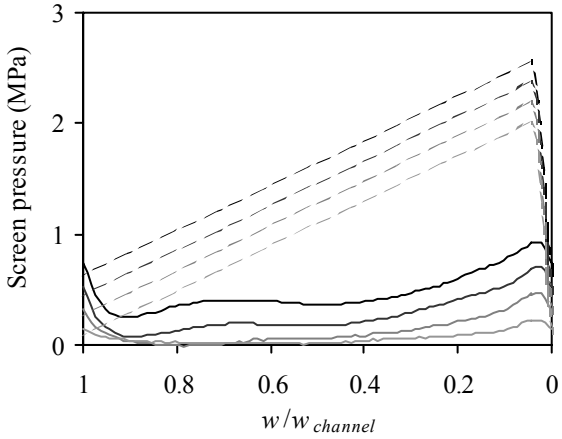

(e) Screen pressure profile over width
v_l = 0.0156 m/s, v_s/v_l = 10.3

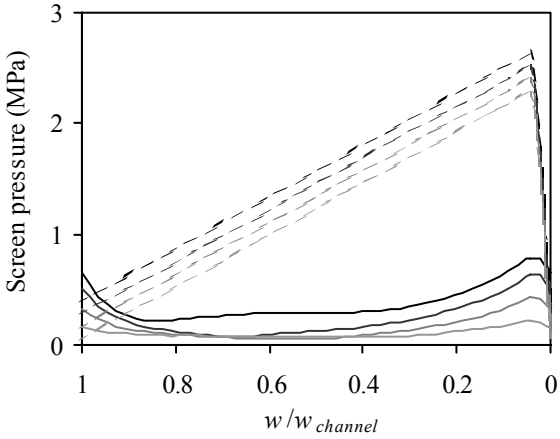

(f) Screen pressure profile over width
v_l = 0.00156 m/s, v_s/v_l = 20.6

Figure 7.10 Profile of paste pressure on screen over extruder channel area

θ = 45°, D_s = 0.0308 m, L_{core} = 0.05 m, D_0 = 0.025 m, ϕ = 0, W_{blade} = 0.0006 m, L_{blade} = 0.0006 m.
— *experimental* – – *model (best fit parameters)*
Distance along extruder (mm): — *4* — *8* — *20* — *32* — *44*

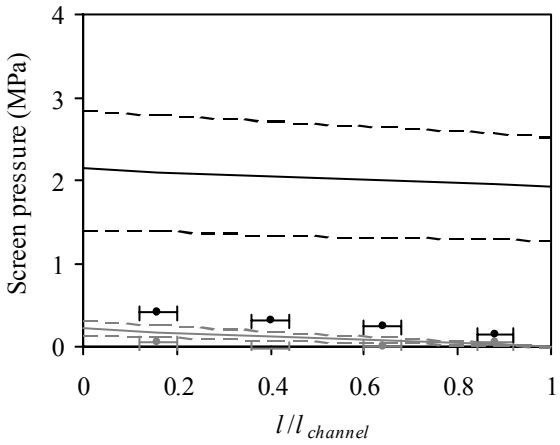

(a) Screen pressure profile over length
v_l = 0.00391 m/s, v_s/v_l = 41.2

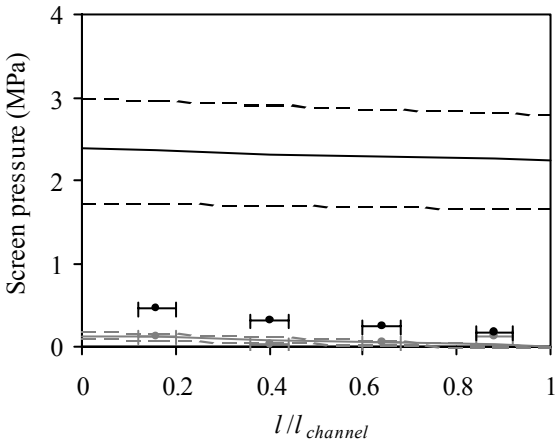

(b) Screen pressure profile over length
v_l = 0.00391 m/s, v_s/v_l = 82.4

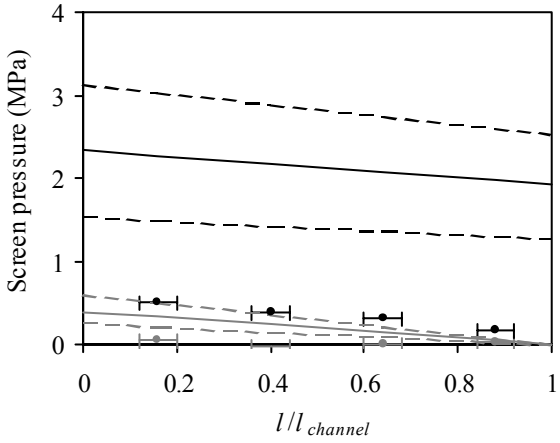

(c) Screen pressure profile over length
v_l = 0.00782 m/s, v_s/v_l = 20.6

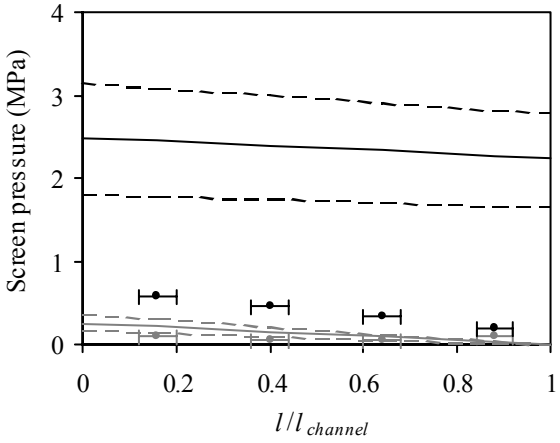

(d) Screen pressure profile over length
v_l = 0.00782 m/s, v_s/v_l = 41.2

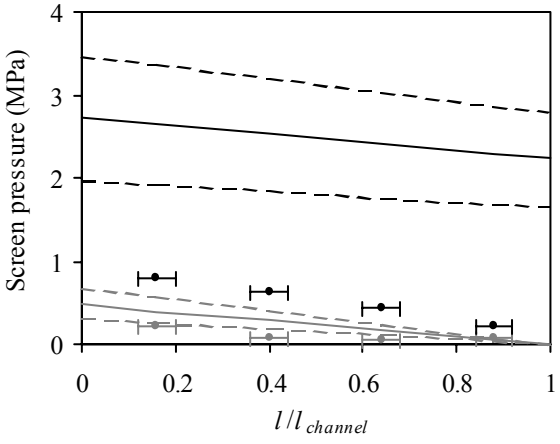

(e) Screen pressure profile over length
v_l = 0.0156 m/s, v_s/v_l = 10.3

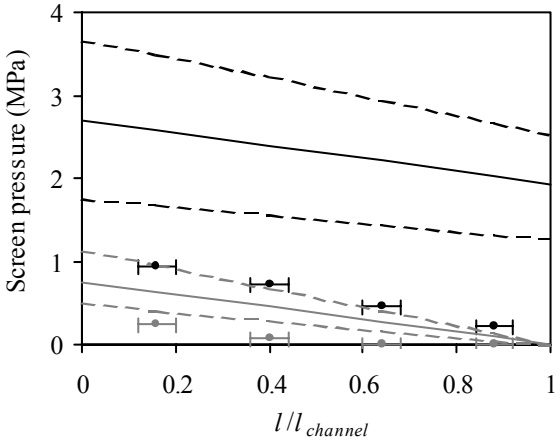

(f) Screen pressure profile over length
v_l = 0.00156 m/s, v_s/v_l = 20.6

Figure 7.11 Peak and minimum paste pressure on screen over extruder channel length

θ = 45°, D_s = 0.0308 m, L_{core} = 0.05 m, D_0 = 0.025 m, ϕ = 0, W_{blade} = 0.0006 m, L_{blade} = 0.0006 m.
Experimental:● peak stress ● minimum stress.
Model: —— best fit parameters – – boundary parameters
Error bars represent diameter of pressure transducers.

The axial force on the extruder core is considered for all of the experimental conditions in Figure 7.12. The experimental forces appear to be similar to those obtained when no blade was being used. This might not be a great surprise if we consider that the actual flow along the length of the extruder does not probably change as much between the two cases. The force increases with longitudinal channel velocity and decreases with relative screen velocity, rapidly at low relative screen velocities. The decrease at low relative screen velocities is expected from the model, but not the observed decrease at the larger screen velocities. Perhaps, again, this is due to a loss of contact between the paste and the core.

The model predictions agree reasonably well for the no blade case, whereas the model predictions have increased greatly with the introduction of the blade, but the experimental data show little change. The axial force on the core was obtained in Section 6.1.4 by a force balance including the axial force on the screen and the axial force over the paste at the extruder entrance. The axial force on the paste was found using the paste pressure over the channel cross-section. The introduction of the blade increased the paste pressure over the cross-section due to the flow over the blade. This increase gives a larger axial force over the paste at the channel entrance. Thus if the screen axial force is unchanged the core force increases, which is what we observe. Given that a rigorous analysis of the stress state of the paste was not carried out, perhaps it should not be surprising that the model core force predictions are inaccurate.

The torque experimental data, presented in Figure 7.13, appears largely unaffected by the introduction of the blade, as was found with the force data. This is more surprising given the significant impact the blade must have on the cross-sectional flow. However, in this case the model predictions also remain largely unchanged. The boundary shear stress calculated using the Benbow-Bridgwater parameters was seen in Figure 3.12 to level off as the slip velocity increased. This effect might mitigate the increase in slip velocity against the screen by the introduction of the blade, leaving the torque values little changed. Again it is striking how the nip angle and the gap between the blade and the screen make little difference to either the experimental or model prediction torques.

The peak cross-sectional stress gradient along the length of the extruder, shown in Figure 7.14 agrees reasonably well with the model predictions. The peak stress gradients are larger for this case with the attached blade than they were for the no blade control case, although the model predictions have increased less. Again, both the experimental

and predicted data indicate no significant change of gradient with nip angle or blade-screen gap. There is also relatively little change with longitudinal paste velocity – it is the relative screen velocity which dominates the magnitude of the gradient.

A significant shortcoming of the extrusion flow model is apparent in Figure 7.15, where the cross-sectional peak stresses at the extruder exit are shown. The experimental peak exit stresses remain uniformly low, close to zero, whereas the model predictions are of the order of one to two MPa, and vary significantly over screen-blade gap and relative screen velocity. This same problem was highlighted at the beginning of the discussion of results regarding Figure 7.10. Here we noted that the experimental peak stress profile along the channel length underwent a change in *gradient* as the operating condition was changed, with the profile always tending towards zero at the channel exit. In contrast, we noted that the predicted peak stress profile along the channel length underwent a change in *offset* and *gradient* as the operating condition was changed. The results presented in Figure 7.14 and Figure 7.15 confirm that this is the case over the whole of the experimental range considered.

7.4 Discussion of results

7.4.1 Experimental results

The three experimental module arrangements have provided the first quantitative data on the flow patterns and stress states within radial screen extruders – as well as some useful qualitative information. The purpose of the module experiments was two-fold; *(i)* to investigate the types of flow pattern which develop within the extruders, and *(ii)* to provide data which can be compared to model predictions based on assumed flow patterns.

Observations from the first two module arrangements – the *rotating core module* with a stationary core, and the *nip module* – suggested that the experimental flow patterns matched the expected flow patterns. The paste was observed to flow evenly, and apparently as a plug, from die land exits of both extruders. The measured pressures on the barrel and wedge walls of the *nip extruder* were found to lie on the same curve – evidence that the paste was undergoing radial plug flow towards the nip.

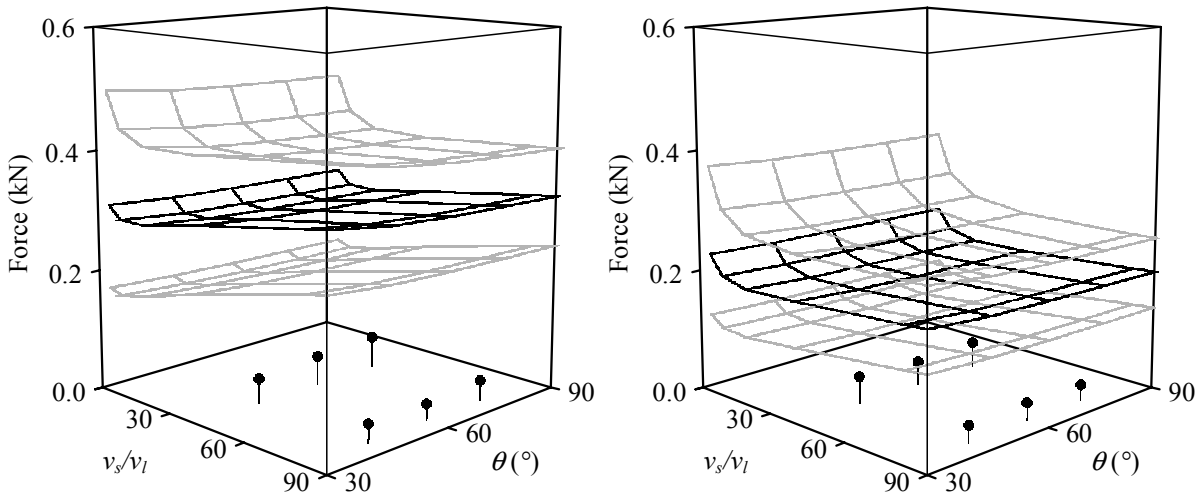

(a) Core force against screen velocity and nip angle W_{blade} *= 0.0006 m,* v_l *= 0.00391 m/s*

(b) Core force against screen velocity and nip angle W_{blade} *= 0.001 m,* v_l *= 0.00391 m/s*

(c) Core force against screen velocity and nip angle W_{blade} *= 0.0006 m,* v_l *= 0.00782 m/s*

(d) Core force against screen velocity and nip angle W_{blade} *= 0.001 m,* v_l *= 0.00782 m/s*

(e) Core force against screen velocity and nip angle W_{blade} *= 0.0006 m,* v_l *= 0.0156 m/s*

(f) Core force against screen velocity and nip angle W_{blade} *= 0.001 m,* v_l *= 0.0156 m/s*

Figure 7.12 Rotating core module axial force on core results

• *experimental value*

model result: — *best fit parameters* — *boundary parameters*

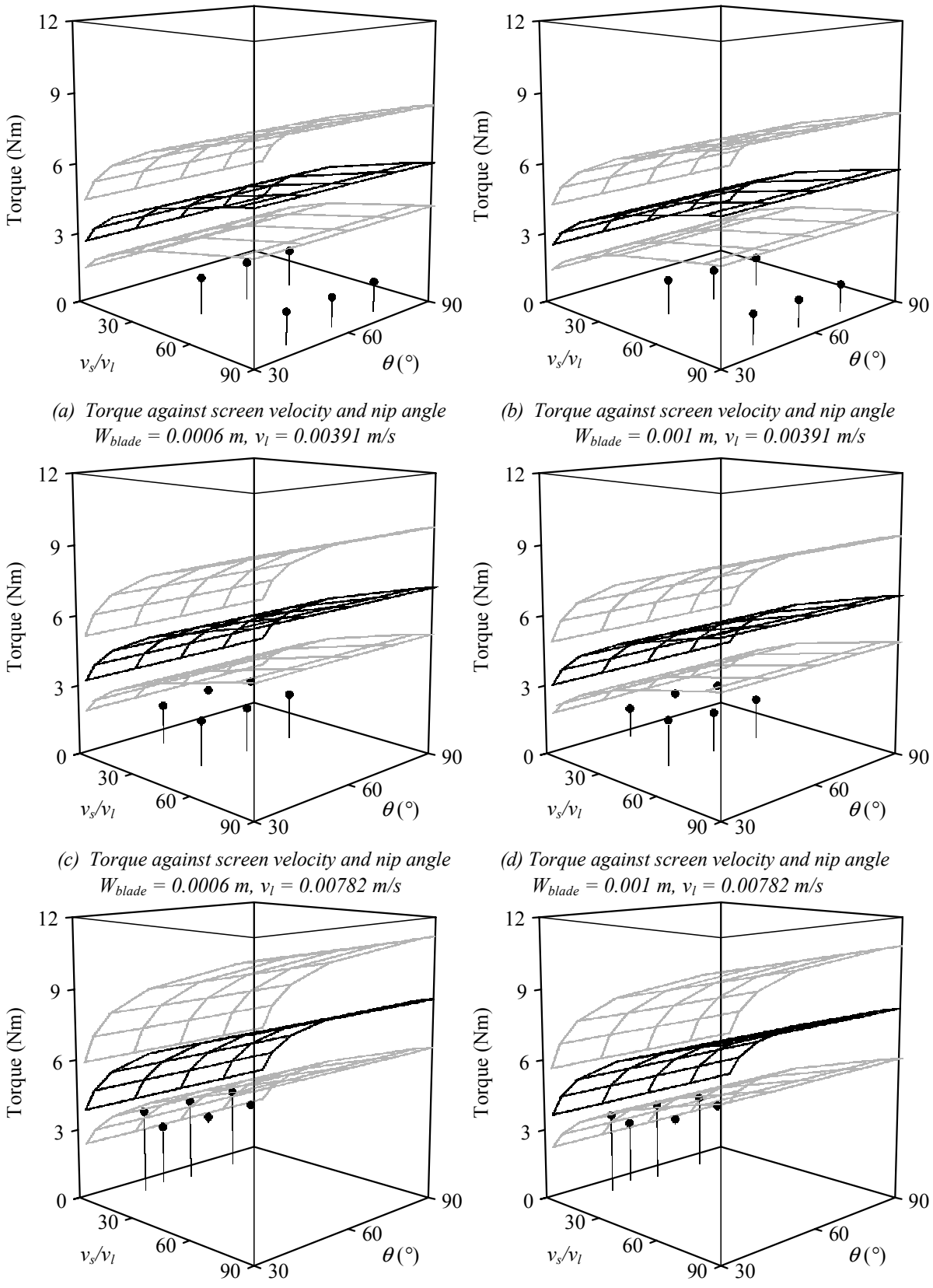

(a) Torque against screen velocity and nip angle
W_{blade} = 0.0006 m, v_l = 0.00391 m/s

(b) Torque against screen velocity and nip angle
W_{blade} = 0.001 m, v_l = 0.00391 m/s

(c) Torque against screen velocity and nip angle
W_{blade} = 0.0006 m, v_l = 0.00782 m/s

(d) Torque against screen velocity and nip angle
W_{blade} = 0.001 m, v_l = 0.00782 m/s

(e) Torque against screen velocity and nip angle
W_{blade} = 0.0006 m, v_l = 0.0156 m/s

(f) Torque against screen velocity and nip angle
W_{blade} = 0.001 m, v_l = 0.0156 m/s

Figure 7.13 Rotating core module spindle torque results

• *experimental value*

model result: — *best fit parameters* — *boundary parameters*

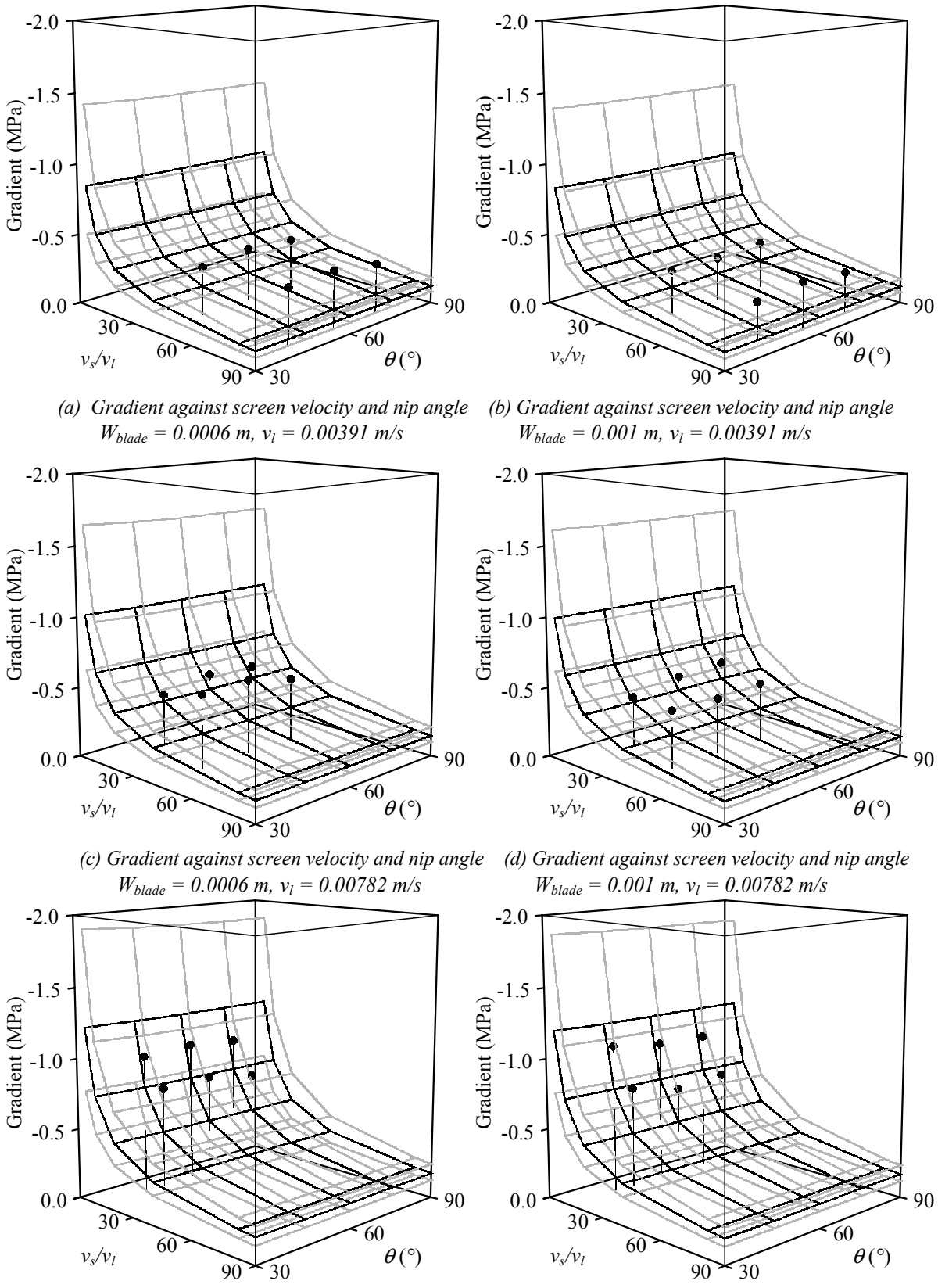

(a) Gradient against screen velocity and nip angle W_{blade} *= 0.0006 m,* v_l *= 0.00391 m/s*

(b) Gradient against screen velocity and nip angle W_{blade} *= 0.001 m,* v_l *= 0.00391 m/s*

(c) Gradient against screen velocity and nip angle W_{blade} *= 0.0006 m,* v_l *= 0.00782 m/s*

(d) Gradient against screen velocity and nip angle W_{blade} *= 0.001 m,* v_l *= 0.00782 m/s*

(e) Gradient against screen velocity and nip angle W_{blade} *= 0.0006 m,* v_l *= 0.0156 m/s*

(f) Gradient against screen velocity and nip angle W_{blade} *= 0.001 m,* v_l *= 0.0156 m/s*

Figure 7.14 Rotating core module peak stress profile gradient results

• *experimental value*

model result: — *best fit parameters* — *boundary parameters*

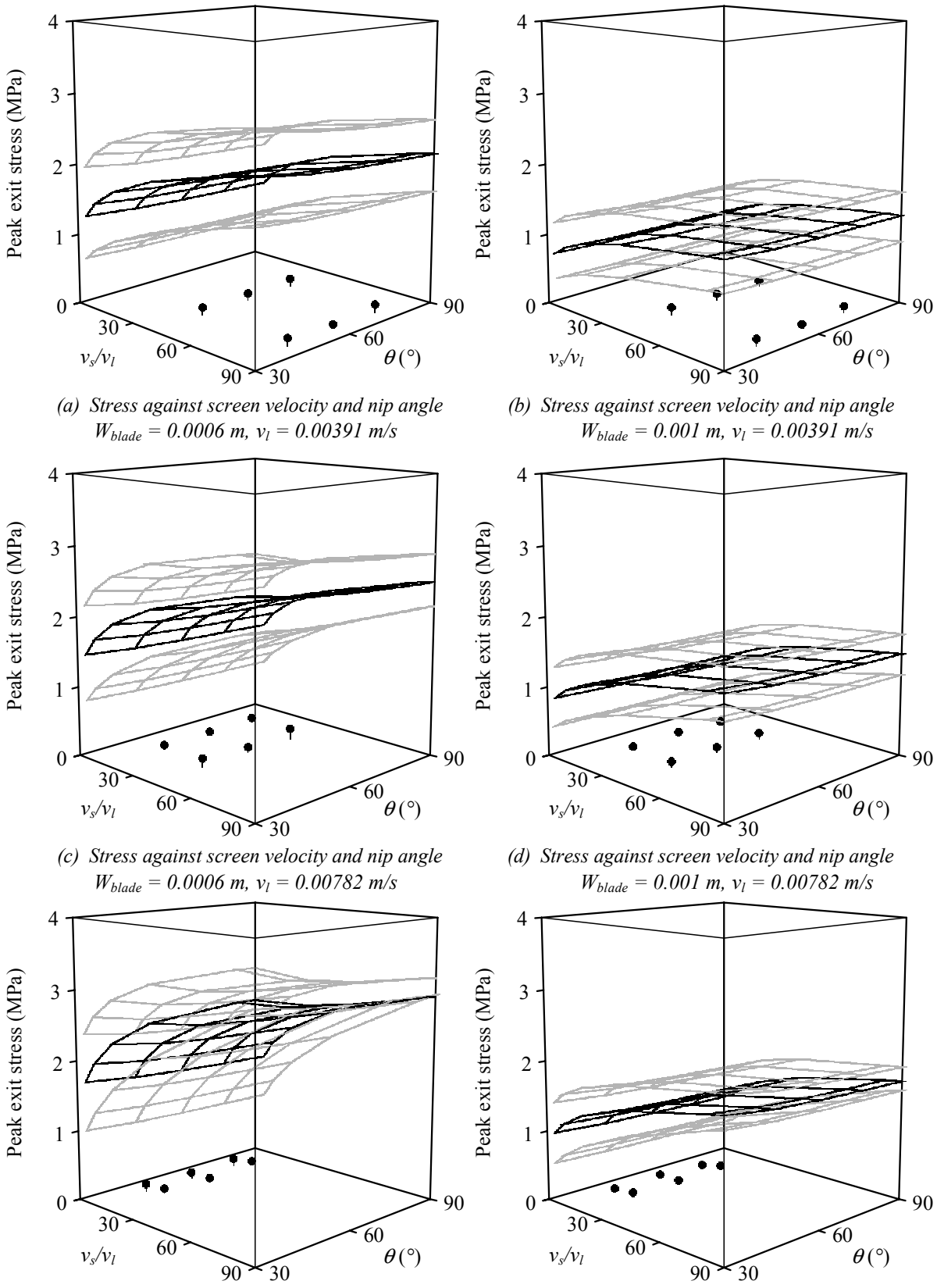

(a) Stress against screen velocity and nip angle
W_{blade} = 0.0006 m, v_l = 0.00391 m/s

(b) Stress against screen velocity and nip angle
W_{blade} = 0.001 m, v_l = 0.00391 m/s

(c) Stress against screen velocity and nip angle
W_{blade} = 0.0006 m, v_l = 0.00782 m/s

(d) Stress against screen velocity and nip angle
W_{blade} = 0.001 m, v_l = 0.00782 m/s

(e) Stress against screen velocity and nip angle
W_{blade} = 0.0006 m, v_l = 0.0156 m/s

(f) Stress against screen velocity and nip angle
W_{blade} = 0.001 m, v_l = 0.0156 m/s

Figure 7.15 Rotating core module peak stress at extruder channel exit results
• experimental value
model result: — best fit parameters — boundary parameters

The observed flow pattern for the *rotating core module* with a single blade did not appear to match the proposed flow pattern very well. The flow pattern within the extruder head could not be observed very well, but it was apparent that the head was not fully flooded. Presumably this was a consequence of longitudinal paste deformation as paste was forced against the rotating blade. The implications of the observed flow pattern are not clear. If the observed flow pattern is representative of that within an industrial extruder, then the assumed flow pattern used in the model of Chapter 6 is not very valid. However, it may be the case that the observed flow pattern was a facet of the experimental arrangement. In this case it is still not known how the flow pattern within an industrial extruder compares with that assumed. With hindsight, it may have been more useful to have used an experimental arrangement which promoted the flooding of the extruder head – such as the inclusion of a dam at the end of the extruder module, or the use of a frustum core.

It was noted in Chapter 3 that the model paste could be described as being *badly-behaved*. The model paste was found to have a relatively weak yield stress dependence, and thus had a propensity to shear rather than undergo plug flow. Whilst the model paste did not flow as expected in the *rotating core module* extruder head, it may be the case that more *well-behaved* pastes would follow the proposed flow pattern more closely.

7.4.2 Model predictions

When the experimental flow pattern was close to the flow pattern assumed in the model, the model predictions of flow distribution and paste pressure matched the measured values reasonably well. Usually the experimental data lay within the predictions given by the boundary sets of material parameters. Often, the experimental data was close to the model predictions given by the best fit set of material parameters. Typically the experimental values may deviate from these best fit parameter model predictions by thirty per cent. Further statistical analysis of the fit is not very appropriate given the accepted uncertainty in the model predictions.

For the case of the *rotating core module* with a single blade, where the experimental flow pattern appeared considerably different from the flow pattern assumed in the model, the model predictions were still encouraging. The modelling approach was based on an upper bound method, where if the assumed flow pattern is not the actual flow pattern the model provides an over-prediction of the stress distribution and total rate of energy

dissipation. This was found to be the case our model, stress distribution predictions were sometimes an order of magnitude larger than those measured.

The model predictions did have the same general form, and display the same trends, as the experimental data. With both, the screen pressure was found to gradually increase up to a peak (thought to be located at the point where radial flow into the nip begins) and then decay rapidly as the blade passed. The same forms of longitudinal stress distributions were found. Neither the width of the gap between the blade tip and the screen, nor the nip angle, were found to be sensitive parameters for either the model or experimental data. However, the experimental data and model predictions were all strongly dependent on the relative velocity of the screen to the (notional) longitudinal velocity of the paste. These findings are encouraging, and indicate that, with further development of both the model and the experimental arrangement, better agreement between the two might be found.

It was noted in Section 7.3.2, for the case of the *rotating core module* with a single blade attached, that the over-prediction of the axial force on the core was greater than the over-predicted of the torque on the core. It was mentioned in this Section that this was possibly a consequence of the assumed hydrostatic stress state adopted in the model. It is perhaps notable that this is the only occasion on which the assumed stress state has obviously caused an inaccuracy in the model predictions.

7.5 Summary

In this Chapter we have presented a selection of experimental and model results for the type of flows which are thought to be important within radial screen extruders. Three different module arrangements were used to investigate different aspects of extruder flow; *(i)* longitudinal flow along the extruder head, *(ii)* tangential flow into a nip, and *(iii)* the total flow pattern in a scaled down radial screen extruder (with a blank screen). The model paste presented in Chapter 3 was used for all of this work.

Under all of the conditions studied, the modules yielded good qualitative and quantitative information about the flow patterns and stress distributions which developed within the modules. The observed flow patterns were compared to the proposed flow pattern presented in Section 4.2. The first two module arrangements gave the expected flow patterns. However, the observed flow pattern in the scaled down radial screen extruder was significantly different from that proposed. The principal feature which had been omitted in the proposed flow pattern was longitudinal deformation of the paste as it

was pushed against the rotating blade. This led to unfilled regions within the extruder head. It was not clear whether or not this would also be a feature of flow in an industrial radial screen extruder.

Reasonable agreement between experimental data and model predictions was found when the observed flow pattern matched the model's assumed flow pattern (module arrangements *(i)* and *(ii)*). There was agreement between the trends of the experimental data and the model predictions module arrangement *(iii)*, but no absolute agreement.

It was found that neither the model nor experimental data were strongly dependent on the width of the gap between the blade tip and the screen, or the nip angle. The experimental data and model predictions were all found to be strongly dependent upon the relative velocity of the screen to the (notional) longitudinal velocity of the paste.

8 Conclusions and discussion

8.1 Restatement of aims

The radial screen extrusion operation is an integral part of the production process for the manufacture of many granular products. This project has been specifically concerned with the production of an agrochemical water dispersible granule. The project aim has been to improve granule product quality and reduce production costs by developing better extruder design and operation criteria. This was approached through considering the paste material flow through the extruder. The particular aims stated in Chapter 1 were,

(a) Identify the important features of twin-screw radial screen extruders, thus single out the important operation and design parameters.

(b) Develop and verify a model of the material flow within a screen extruder based on these parameters.

(c) Identify the important trends in, and modes of, flow behaviour over the range of parameters.

(d) Relate these trends to extruder lifetime, operating costs and product quality.

A schematic representation of the project progression from these aims is shown in Figure 8.1 overleaf. Two main themes developed; the modelling of paste materials, and the modelling of paste flow in a screen extruder. To begin with, in Section 8.2, an overview of the project is presented. Section 8.3 pays particular attention to the development of the radial screen extruder flow model and the experimental results respectively. Finally, in Section 8.4, some consideration is given to possible future work which would develop this project or address issues which have been raised in its course.

8.2 Project overview

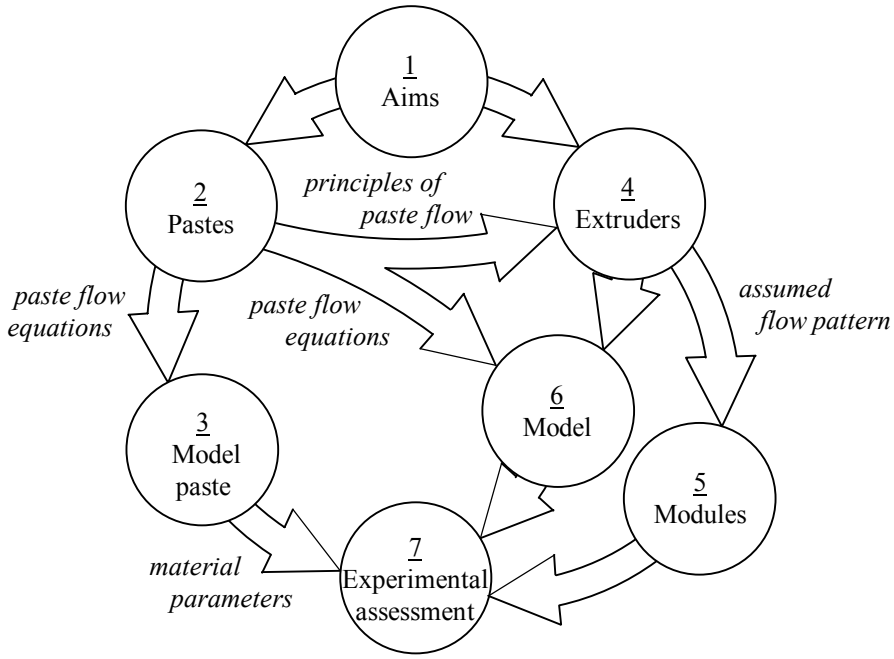

Figure 8.1 Schematic of project progression

Dissertation Chapters are indicated by number.

The literature related to general paste extrusion was reviewed in Chapter 2. It was noted that many techniques have been used to describe paste flow, ranging from multi-phase microscopic models to single-phase constitutive models. Typical paste properties were discussed; following on from these a general set of flow characteristics was established. The principal characteristic was that pastes frequently exhibit plug flow, with slip at the duct walls caused by local phase redistribution. However, a particular paste will only adhere to the general paste flow characteristics to a greater or lesser extent. Some pastes might be though of as being *well-behaved*, whilst others might be thought of as being *badly-behaved*. At this point it was decided to follow the Benbow-Bridgwater flow model, based on a lower bound ideal work equation, for the succeeding analysis. This approach was chosen over other, more precise approaches, especially the FEM modelling, which has become increasingly popular for paste extrusion analyses, because only very approximate constitutive equations can be found for most paste materials. This uncertainty means that a more precise modelling approach would not necessarily give a more accurate solution, in spite of the expense of increased complexity.

In Chapter 3, a model paste, based on an industrial material, was characterized by axisymmetric extrusion to obtain material parameters based on the Benbow-Bridgwater model. The characterization was conducted over a wide range of area reductions and

extrudate velocities to yield parameters which would remain valid for flow through the geometry of a radial screen extruder. The flow curves obtained suggested that flow in the die land region involved bulk shearing as well as wall slip. Conventional rheological approaches, including Mooney plots, to determine the relative amount of bulk shearing proved inconclusive. The model paste was relatively *badly-behaved*, although it was recognised that this was a necessary trade off in order to use an industrially relevant material. Three sets of material parameters were generated; one being the parameter group which best fitted the characterization data, the other two being parameter groups which bounded the data.

The literature specifically related to radial screen extrusion was reviewed in Chapter 4. Some research has been conducted into screen extruders as a process operation, for example, considering the product quality as a function of the composition of the feed material. However, very little research has been conducted into the actual flow patterns or stress states within a the extruder. A small body of literature relating to screw extrusion of pastes gave useful guidance on some aspects of flow in a radial screen extruder. Based on this literature, and the general principles of paste flow outlined in Chapter 2, an approximate paste flow pattern was proposed for a radial screen extruder. Two important aspects to the flow were identified; the flow along the length of the extruder, and the tangential flow towards the nip between the screen and a blade where paste is then extruded through the screen. The geometrical and operational parameters which would affect this flow pattern were identified, and a suitable set of dimensionless groups proposed.

Two laboratory scale extruder modules were presented in Chapter 5. These were designed to investigate in detail aspects of the proposed flow pattern from Chapter 4. The *rotating core module* was a versatile miniature version of a radial screen extruder with which stress states around the extruder could be measured over a wide range of operating conditions. The *nip module* enabled detailed measurement of flow patterns and stress states in the region of a nip. The modules were designed to be operable over the parameter ranges expected in an industrial extruder. Sample results from both modules were presented.

An approximate paste flow model for a single-screw radial screen extruder was presented in Chapter 6. The model was based on the paste flow principles and equations described in Chapter 2, along with the paste flow pattern within the extruder proposed in Chapter 4. The model represents the first attempt to extend the Benbow-Bridgwater

method to the geometry of a radial screen extruder. The modelling approach featured minimising the energy requirement and solutions were generated numerically.

The flow model was assessed on its own terms using the model paste material parameters from Chapter 3, and data from the industrial extruder outlined in Appendix A. The model was found to produce satisfactory numerical solutions using a relatively small number of elements, and no significant problems with convergence were found. The model proved able to predict extruder work rates, flow rates and pressure distributions of the expected order of magnitude. The main shortcoming of the model was the lack of consideration given to the extrusion pattern through the screen in the immediate vicinity of the nip. Further work into this area must be conducted before the model can be considered complete.

Finally, the model paste, described and characterized in Chapter 3, was extruded through both of the modules of Chapter 5, and the results compared with predictions given by the model in Chapter 6. The experimental and model results were presented and compared in Chapter 7. Three types of experiment were conducted. Paste was extruded through the *rotating core module* in two arrangements, both used a blank (no perforations) screen; *(i)* a stationary core of various initial diameters and half-angles, and no blade attached, and *(ii)* a rotating parallel sided core of fixed diameter and a single blade attached, which was of various dimensions. The other type of experiment extruded paste through the *nip module* with a variety of nip angles and die arrangements.

The model predictions agreed reasonably well for the stationary *rotating core module* and the *nip module* cases, with the experimental results consistently lying between the model predictions using the boundary material parameters. The paste flowed evenly through the apparatus and appeared to be predominantly undergoing plug flow.

When the *rotating core module* was used with a single blade, the paste appeared to flow along the extruder predominantly in the region immediately prior to the blade. A significant part of the extruder head was clearly not flooded with paste. These observations indicate that the usual principles of paste flow were not being followed; correspondingly the model predictions generally did not agree well with the experimental results, although there was a correspondence between the trends within the experimental and model data. It was thought that two flow effects occurred which were not accounted for in the model; longitudinal extensional flow and tangential shearing.

Further experimental work ought to be carried out before a full assessment of the model is made. It would be worthwhile extruding a *well-behaved* paste through the

rotating core module with an attached blade, and investigating whether the same flow results are observed and whether the model predictions are in any better agreement with the experimental data. If the same problems were encountered then further development of the model would have to be considered. If the paste were to remain *well-behaved*, the model could be assessed on its own terms and further development considered. For example, the unaddressed problem of flow through the screen into the nip region could be considered.

The flow model and the experimental results are considered in more detail over the following Section. In the final Section, some more suggestions are made as to how this work could be usefully extended.

8.3 Discussion

The problem of understanding the *mechanics of paste flow in radial screen extruders* has been addressed on two fronts. The first step has been to understand the general mechanics of paste flow; only once these were established could the specific case of the radial screen extruder be addressed.

8.3.1 General mechanics of paste flow

Pastes are multi-phase mixtures (usually including a solid and liquid-phase) which are characteristic for possessing a yield stress dominant behaviour. A paste may be easily deformed, but after deformation will retain its shape under its own weight. The mechanics of paste flow may be modelled with different degrees of detail – from the microstructural level (*e.g.* Yuan *et al.* (2001)) to bulk-averaged flow properties (*e.g.* Benbow and Bridgwater (1987b)). The particular approach adopted is usually tailored to a specific application.

The complexity of the flows within a radial screen extruder might demand a detailed micro-structural paste model, if all of the flow features are to be properly understood. However, such an approach is currently beyond the state of the art – the approximate model of Benbow and Bridgwater (1987b) was adopted since this offered a practical approach to measuring useful paste material parameters.

Benbow-Bridgwater characterization

The Benbow-Bridgwater model is based on axisymmetric extrusion, and assumes that the paste undergoes plug flow in the die land. The model characterizes a paste using a

bulk yield stress term, σ_0, and bulk yielding rate dependence terms, α and m, based on the extrudate velocity, V, such that the yielding stress, σ, is given by,

$$\sigma = \sigma_0 + \alpha V^m \tag{8.1}$$

The interaction between the bulk paste and the die land wall is characterized with a shear yield stress, τ_0, and shear rate dependence terms, β and n, based on the slip velocity, also V, such that the shear stress at the interface, τ, is given by,

$$\tau_w = \tau_0 + \beta V_{slip}^n \tag{8.2}$$

A talc-based model paste material, based on an industrially used paste, was selected for use in this project. Characterization data was found for this material, and Benbow-Bridgwater parameters fitted. The bulk yield and boundary slip behaviour and Benbow-Bridgwater characterization were presented in Figure 3.17 *(a)* and Figure 3.16 *(c)* respectively, reproduced here in Figure 8.2. A significant degree of variation can be seen amongst the data in both of these plots.

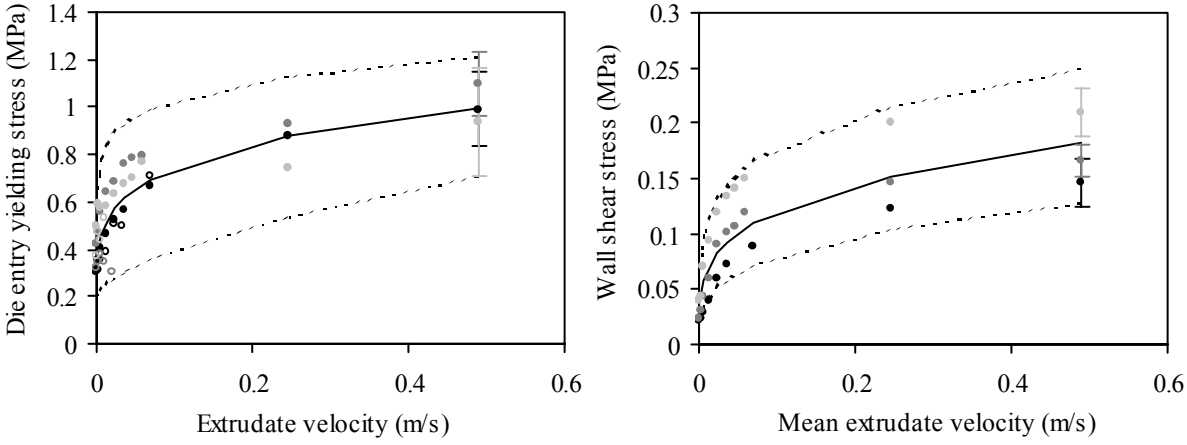

(a) Die entry yielding stress against extrudate velocity *(b) Wall shear stress against extrudate velocity*

Figure 8.2 Characterization of model paste

Selected error bars bound regions of possible values.
● ● ● capillary diameter D = 1, 2, 3 mm respectively
○ ○ ○ capillary diameter D = 8, 15, 20 mm respectively
—— best fit Benbow-Bridgwater model --- boundary Benbow-Bridgwater model

Some of the variation seen in the die entry yielding stress data (Figure 8.2 *(a)*) may be caused by the use of the extrudate velocity as the rate term in the Benbow-Bridgwater characterization. The possible limitations of using the extrudate velocity to represent rate effects have previously been noted twice (Zheng *et al.* (1992) and Blackburn *et al.* (2000)). By dimensional analysis, the rate term should appear in the form $(V/D)^x(D_0/D)^y$, where D is the die land diameter, D_0 is the barrel diameter and x and y are

unknown indices. However, attempts to fit the data to one curve by using this rate term and adjusting the indices were unsuccessful.

It is apparent from Figure 8.2 *(b)* that the Benbow-Bridgwater characterization data did not collapse onto a single flow curve. Many reasons for this were considered, mainly relating to the possibility of bulk material shearing in the die land in combination with wall slip. Mooney diagrams were constructed (Mooney (1931)), but these gave physically unrealistic results.

Similar problems have been experienced in other studies (*e.g.* Adams *et al.* (1995), or Khan *et al.* (2001)). A physically grounded explanation for this occurrence has not yet been proposed. It was noted in another study using a similar talc-based paste (Formstone (1995)) that the microstructure of the paste varied over the die land cross-section. SEM images indicated that talc platelets near the wall had become orientated parallel to the wall, whereas the platelets in the centre were orientated perpendicularly to the direction of flow. A central assumption of the Mooney analysis (which is based on the Weissenberg-Rabinowitsch equation, Rabinowitsch (1929)) is that the direct stress acting in the direction of flow is constant over the die land cross-section. Variation in the material microstructure would conceivably lead to a non-constant stress distribution, and thus invalidates the Mooney analysis.

It was shown in Figure 3.18 that the best fit Benbow-Bridgwater parameters predicted a wall shear stress greater than the estimated bulk shear yield stress once the slip velocity exceeded 0.01 m/s. It seems likely that a combination of shearing in the bulk material, variable material properties over the die land, and experimental error made a single flow curve unobtainable. In particular, it appears that the relatively high liquid-phase fraction – and correspondingly low solids fraction – of the model paste (the model paste solids fraction was 0.49, compared to 0.60 for other pastes modelled using this approach) resulted in a paste with relatively low σ_0 parameters, and consequently sheared quite readily. An approach was adopted where three sets of Benbow-Bridgwater characterization parameters were fitted; one is the best fit parameter set, the other two bound the data to give boundary parameter sets.

Approximate stress states

In order to model the paste flow in the complex geometry of a radial screen extruder, an approach was adopted for determining the material stress state. This might be done rigorously through the use of techniques such as the Mohr's circle, used in granular

materials (Nedderman (1992)), or the pore pressure/effective stress model, used in soil mechanics (Atkinson (1993)). It would be expected that a yield stress dominated material would exhibit noticeably different values of principal stresses. However, studies which have attempted to resolve between, say, the axial and radial stresses during axisymmetric extrusion (Amarasinghe (1998a) using soap and an alumina based paste) have not been able to distinguish the difference between the stresses.

For the purposed of this project it was assumed that the stress state could be approximated as isotropic. That is, the stress is the same in all directions, and the paste is treated as a *pseudo-fluid*. This assumption is likely to be more valid for a wetter paste where a significant component of the stress is transmitted through the isotropic pore pressure. Compaction experiments for the dry talc material and the talc-based paste were shown in Figures 3.3 and 3.8 respectively, and are reproduced here in Figure 8.3.

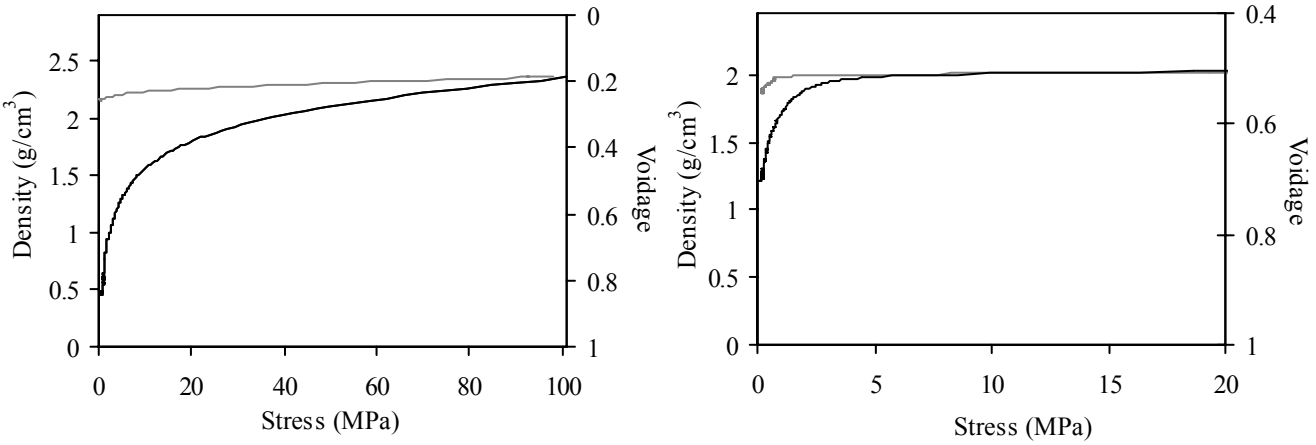

(a) Density and voidage of Micro-Talc AT Extra *(b) Density and voidage of model paste*

Figure 8.3 Compaction experiments

compaction curve *relaxation curve*

The dry talc material is still compacting, even at stresses of 100 MPa, whereas the paste became incompressible at just 5 MPa. It was thought the this was due to the liquid-phase in the paste transmitting the stress, thus preventing the solid particles from undergoing further compaction. In such a situation, the difference between the greatest and smallest principal stresses might not be large. Whilst the high liquid-phase content made the paste *badly-behaved* with regard to capillary flow, it appears that it may cause the paste to behave better with regard to the assumed stress state.

8.3.2 Paste flow in a radial screen extruder

Flow patterns

The paste flow in a radial screen extruder was separated into four main components, as illustrated in Figure 1.7, and reproduced here as Figure 8.4. Flow ① from the hopper onto the screw feed was believed to be relatively unproblematic, and flow ② along the screw feed is reasonably well understood. This project focused on flows ③ and ④ – the flow along the length of the extruder head, and the flow out of the extruder head through the screen respectively.

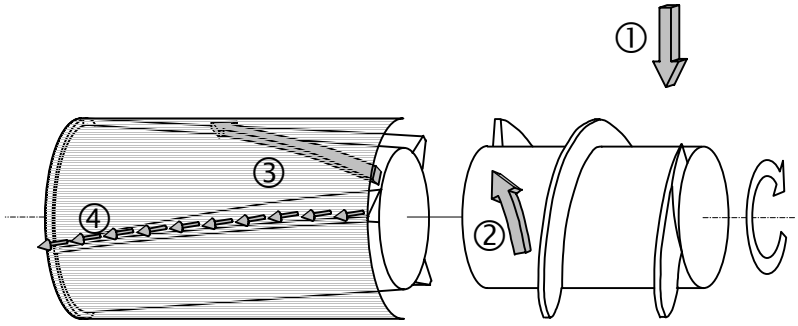

Figure 8.4 Exploded drawing of one half of a twin-screw radial screen extruder

The more complex modelling techniques, such as the Finite Element Method (*e.g.* Horrobin (1999)), were sidelined on the grounds that the high degree of detail in the techniques was not sympathetic to the quality of the available material parameters. Instead, an upper bound approach was used where the flow pattern is estimated and the resulting stress distribution calculated (from which the rate of energy dissipation, forces and torques *etc.* can be found). This approach results in an over-prediction of the stress distribution, and does not satisfy mechanical equilibrium. However, by introducing some flexibility into the assumed flow pattern the total energy dissipation rate may be minimised to find the most optimal flow pattern.

A flow pattern was assumed based on the previous knowledge of paste flow in extruders. The principles of the Benbow-Bridgwater analysis were applied to calculate the stress distribution from the assumed flow pattern.

Proposed flow pattern

The similarity between the extruder head and a screw extruder was noted, and consequently the flow in a screw extruder was taken as the starting point of the proposed flow pattern. The extruder head was assumed to be fully flooded, and the extrusional flow through the screen was assumed to occur only in the immediate vicinity of a blade. The

interaction between the twin-screws was assumed to be negligible – the flow was modelled for the case of a single-screw extruder only, with the hope that this would still provide insight into the behaviour of twin-screw extruders. The Benbow-Bridgwater model is suitable for use with paste flows where the flow is primarily due to slip at the wall. The proposed flow pattern was compromised to account for this; there appeared to be the possibility of bulk paste being sheared as a consequence of the very fast relative screen velocity, but a complete wall slip case was used to allow analysis by the Benbow-Bridgwater model. A cross-sectional view of the proposed flow pattern was presented in Figure 4.12, and is reproduced here as Figure 8.5.

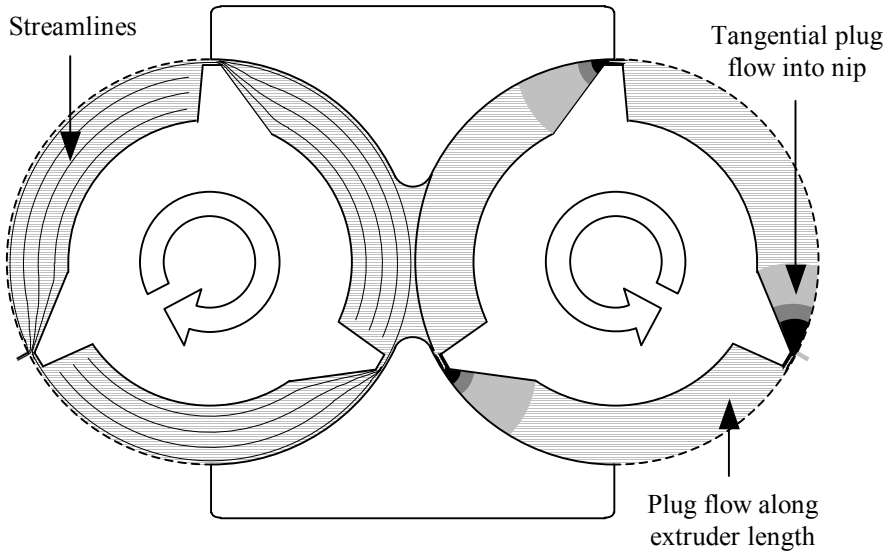

Figure 8.5 Proposed paste flow pattern over a cross-section of the extruder head II

Left hand side shows streamlines of flow relative to core. Right hand side shows strain rate.
paste material *low strain rate* *high strain rate*

Modelling the flow pattern

A major assumption was required in order to model the proposed flow pattern using the Benbow-Bridgwater method. The two identified contributions to the flow pattern – the longitudinal plug flow, and the tangential plug flow into the nip – had to be analysed independently in order to decouple the flow equations. Consequently, the two contributions of flow were essentially analysed separately as two types of flow reproduced overleaf in Figure 8.6 from the original Figures 4.13 and 4.14.

In order to reduce the impact of this approximation, the flow was considered over elemental lengths of the extruder head. But over each element the two flows were treated as independent – there was no transfer of mass or energy from one direction to the other.

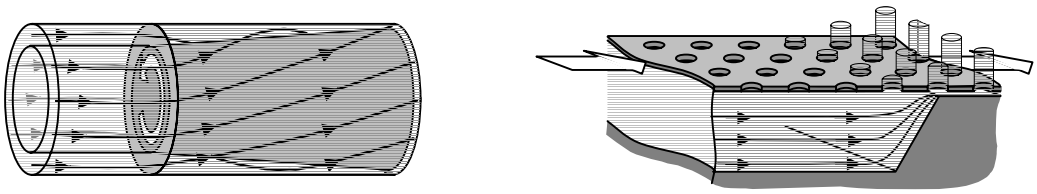

(a) Longitudinal paste flow between core and screen *(b) Tangential paste flow into nip*

Figure 8.6 Paste flow between rotating core and screen

The fraction of paste flowing across the channel cross-section was treated as a variable, which could be adjusted in order to minimise the total extruder energy dissipation rate. The specific paste flow pattern into the nip and either through the screen or over the blade has not yet been developed.

8.3.3 Model solutions

Finding solutions

Flow equations were developed to represent the assumed flow pattern. These were solved numerically with the use of approximate boundary conditions. The model was successfully implemented using an MS Excel 97 spreadsheet, and the minimum energy requirement could be found using the proprietary 'solver' function.

Minimum energy dissipation rates were found for a fixed operating speed by varying the total extruder throughput, the cross-sectional flow rate, and fraction of cross-sectional flow flowing through the screen over the extruder length. However, it was found that the total extruder work rate was quite insensitive to changes in the cross-sectional flow pattern. Consequently, the effect of approximations used in the model may have a significant impact on the actual flow pattern.

Validation of solutions

Model predictions using the Benbow-Bridgwater parameters for the model paste, and the geometry and operating conditions of a real industrial extruder, appeared to be realistic. The magnitudes of the work rate and the screen pressure distribution were close to the expected values. The flow pattern appeared to under-predict the flow through the screen, but this may be a facet of the extruder design (which are known to have limited extrusion throughputs under certain conditions) rather than a fault in the model. The screen pressure distribution over the length of a channel was presented in Figure 6.15 *(a)*, and is reproduced in Figure 8.7 overleaf.

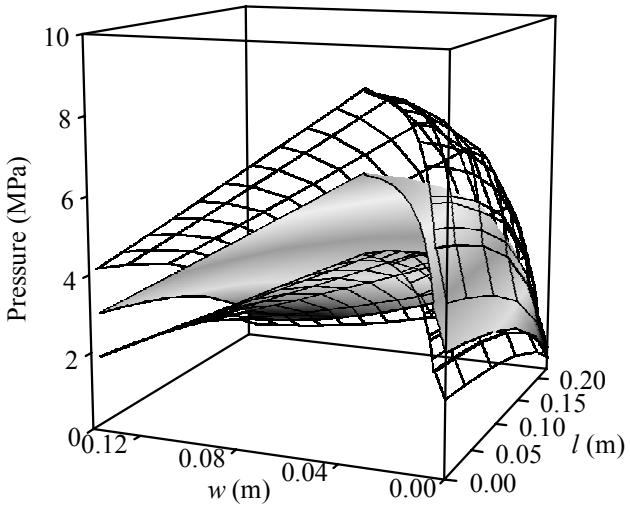

Figure 8.7 Screen pressure distribution over channel area
Shaded surface – best fit parameters. Open surface – boundary parameters

Experimental extruder modules were designed and commissioned in order to gain practical insight into paste flow within radial screen extruder, and also to provide experimental data against which to compare model predictions. It was found that the model predictions agreed reasonably well with measured experimental data when the paste flow pattern observed for the experiment matched that assumed in the flow model. Where this was not the case, the model severely over-predicted the stress distribution – which is what would be expected from an upper bound solution. It was unclear whether the usefulness of the model was fundamentally limited, or whether the experimental flow patterns were particular to the apparatus used and not generally found in radial screen extruders.

8.3.4 Practical application for industry

Modelling work

A model has been developed which predicts paste flow patterns and stress distributions within industrial radial screen extruders. From these fields the model can calculate useful parameters such as the torque on the extruder core, the distribution of extrusion rate through the screen, and the total extruder work rate. The model may be implemented using standard PC software and, once implemented, can be used with the minimum of effort. The current model possesses some significant limitations, but has been demonstrated to indicate the important trends observed from experimental extruders and

has the potential to be a valuable tool for the design and operation of industrial twin-screw radial screen extruders.

A sample investigation of an industrial extruder over a small range of parameters indicated some important trends. The most significant are listed here,

(i) The total extruder work rate and throughput increases approximately linearly with rotational speed.

(ii) Using more than one blade increases the fraction of paste extruded through the screen, at little extra work cost. This effect appears to level out at three blades.

(iii) Straightening out the extruder blade increases the fraction of paste extruded through the screen, at little extra work cost.

(iv) Significant leakage flow of paste over the blade occurred for all blade tip-screen gap widths.

(v) The angle of the nip between the screen and the blade does not have a significant impact on the flow.

(vi) The extrusion flow distribution of paste through the screen head always increased (from practically zero at the inlet) along the length of the extruder head.

Experimental work

Perhaps the most industrially useful insight which can be gained from experimental work was first presented by Rough and Saracevic (1997), in their preliminary study of screen extrusion from which this project developed. They found that pre-processing paste before it is fed to an extruder can greatly improve the extrusion performance. However, this is not always practised on industrial extruder lines. In the laboratory, this pre-processing was performed by pugging the paste through a mincer a number of times. This operation transforms the material from what appears as a damp powder, to a soft solid material with smooth consistency. Industrially, it might be more viable to use a rolling stage to achieve the same effect.

It is not clear whether the specific flow patterns encountered with the *rotating core module* with a single blade are generally applicable to all radial screen extruders. However, the ability of the two extruder modules which were developed as a part of this project has been demonstrated. The experimental equipment and procedures now exist upon which a wide ranging experimental investigation of radial screen extrusion could be based.

8.4 Future work

A paste flow model for radial screen extruders has successfully been developed based on established principles of flow. The accuracy of predictions made with this flow model has been limited. In this Section, three areas are identified which could be addressed to improve the model. This project has developed existing theories of paste flow into a novel technique for modelling paste flows in complex extruders. The final Section of this dissertation considers what potential this novel modelling technique has for improving the understanding and performance of other types of industrial extruder.

8.4.1 Better behaved pastes

The limited success of the flow model to predict the experimental stress distributions is thought to be largely a consequence of the disparity of flow patterns observed from experiments with those used in the model. Before any attempt to alter the model to account for the observed flow pattern, it would be worthwhile examining the experimental flows over a wider range of conditions. This would establish the extent of the disparity between the assumed flow pattern in the model and the flow patterns which occur in the extruders. Two approaches to this work could be taken; *(i)* extruding an alternative paste, and *(ii)* adjusting the experimental arrangement.

Extruding an alternative paste

It was noted in Chapter 3 that the talc-based model paste used in this project could be described as *badly-behaved*. The material relatively wet compared to many pastes, which contributed to a low yield stress and thus a propensity to shear in its bulk – rather than undergo the plug flow of a typical paste.

Conducting similar extruder module experiments as were described in Chapter 7 with better behaved pastes, and comparing the observed flow patterns and measured data with the flow model predictions, would indicate to what extent the experienced problems were specific to one particular type of paste. A suitable *well-behaved* paste could be based on the soap or alumina paste used by Amarasinghe (1998b). Alternatively, to maintain industrial relevance, a model paste which including harborlite as well as talc could be tried. However, this would introduce attrition issues which are not desirable in an experimental apparatus.

Adjusting the experimental arrangement

The unexpected flow pattern observed in the experiments may have just been specific to that experimental arrangement, and might not occur in a real extruder which has a frustum core ending in a dam. Introducing these features into the experimental work might generate flow patterns closer to those assumed in the model, and thus result in better agreement between the experimental data and the model predictions.

8.4.2 Improved modelling of pastes

If the proposed studies using different pastes in the extruder modules indicated that the assumed flow pattern used in the model needed modification, it would probably prove necessary to improve upon the theory and techniques used to characterize the materials.

If bulk shearing was a significant aspect of the flow, the Benbow-Bridgwater material model would not be sufficient. Ideally, something like the Herschel-Bulkley constitutive equation would need be implemented. However, despite a few attempts (*e.g.* Zheng *et al.* (1992)), no successful applications of this equation for a paste have been reported. Current work in this area is being undertaken by C. J. Lawrence and co-workers (Lawrence (2002)). It would take a concerted effort, with no guarantee of success, to try and establish robust constitutive equations for a paste. This work might involve developing new characterization devices, and particular attention would have to be made to changes in the microstructure of the material as it flows, and subsequent effects on the material properties.

8.4.3 Improved modelling of flows

Extending the current model

The main shortcoming of the current extruder flow model is the omission of an analysis of flow into the nip and either through the screen or over the blade tip. The beginnings of an analysis were included in the flow model, where the screen holes were considered as a *pseudo die land* always located immediate in front of the blade tip. From this starting point, the simplest approach might be to perform controlled experiments where the flow pattern through a screen is measured. The number of rows through which extrusion occurs could then be correlated to the nip and screen geometry, as well as the material parameters and flow rate. Such experiments could be performed using the *nip module*

with a side plate containing a screen, or a number of slots representing a screen, as illustrated in Figure 8.8 overleaf.

Alternatively, the flow could be modelled physically, again using the upper bound method. A general flow pattern could be assumed, and aspects of it varied to find the minimum work requirement and thus the predicted flow pattern. This approach would be worth attempting, but a similar attempt by Martin *et al.* (2001) for flows out the end and sides of a barrel did not predict the measured flow rates very successfully.

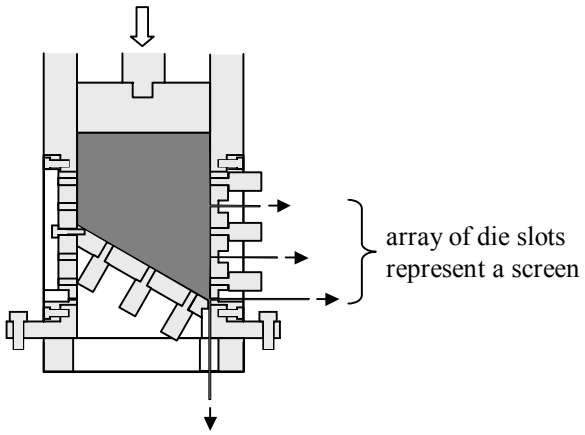

Figure 8.8 Nip module arrangement for the study screen flow near a nip

Improving the assumed flow pattern

Improved knowledge of the flow patterns within radial screen extruders could only help the model development. The flow patterns observed with the modules have been discussed, but only a general impression of the flow within the extruder head has been achieved. Two approaches which could possibly be employed to achieve detailed quantitative descriptions of the paste flow are Magnetic Resonance Imaging (*e.g.* Britton and Callaghan (1997)), and Positron Emission Particle Tracking (PEPT) (*e.g.* Wildman *et al.* (1999)).

Alternative techniques

If the improved constitutive equations discussed in the previous Section could be developed, a door would be opened to more rigorous modelling of paste flows. Rigorous flow models have been investigated in the past (*e.g.* Horrobin (1999)), but these tend to rely on assumed material flow properties. Developing a rigorous analysis can be difficult if the flow involves large area reductions, or very rate dependent materials.

Any attempt to develop the flow model presented in Chapter 6 would probably look to the Finite Element Method as a possible way forward. Major approximations were made in the model by decoupling the flow equations – thus separating the flow in the longitudinal direction from the flow in the cross-sectional direction, when obviously they are both aspects of one single flow. Also, approximate boundary conditions were used to simplify finding solutions. If these approximations were tightened, then the resulting flow equations would probably be too complex to solve by simple means.

8.4.4 Nip extrusion

A central theme of this dissertation has been the development of a novel approach for understanding and modelling the flow of paste materials through radial screen extruders. However, radial screen extrusion is just one, of many, type of granulation which employs the same basic principle – *the development of a nip between a surface and a screen*.

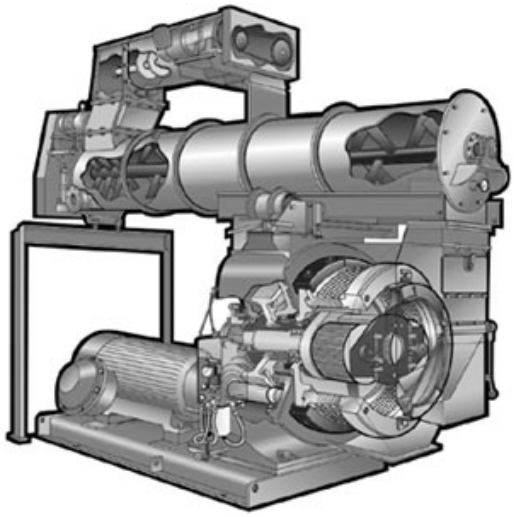

(a) Cut away view of a CPM pellet mill

Reproduced from promotional literature. (California Pellet Mill Co., Indiana, U.S.A.)

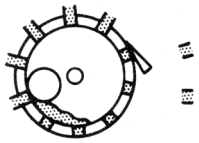

(b) Operating principle of pellet mill

Reproduced from Perry and Green (1997c).

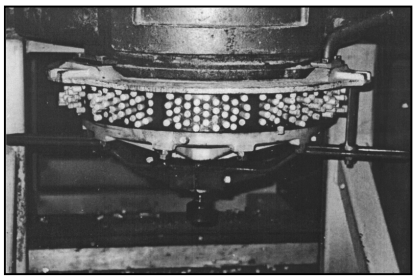

(c) Production of fuel pellets from a softwood sawdust

Reproduced from Cotton and Giffard (2001).

Figure 8.9 Features of a pellet mill

Extrusion-granulation is an important operation across a wide range of industries. One other granulation technique which employs the principle of nip extrusion is pellet milling, illustrated in Figure 8.9. In a pellet mill, a roller is in contact with the inside of a rotating, perforated drum. Material caught between the roller and the drum is forced through the perforations, and compacted into a pellet. Figure 8.9 *(c)* shows this technology being used to produce a novel fuel pellet from waste material.

Extrusion-granulation is generally not a very well understood process. The modelling approach developed in this dissertation for radial screen extruders, potentially offers a new way to improve the design and operation of many types of extrusion-granulator. An initial study at Cambridge (Barnes (2001)) has illustrated the new modelling approach for the pelletization of sugar beet waste to form animal feed. The full potential of the extended Benbow-Bridgwater model for nip extruders has yet to be assessed.

References

Adams, M. J., Aydin, İ, Briscoe, B. J. and Sinha, S. K. (1997) A finite element analysis of the squeeze flow of an elasto-viscoplastic paste material. *Journal of Non-Newtonian Fluid Mechanics*, **71**, 41-57.

Adams, M. J., Biswas, S. K., Briscoe, B. J. and Kamyab, M. (1991) The effects of interface constraints on the deformation of pastes. *Powder Technology*, **65**, 381-392.

Adams, M. J., Briscoe, B. J., Kothari, D. and Lawrence, C. J. (1998) Strain localisation during the axisymmetric squeeze flow of a paste. In *Dynamics of Complex Fluids*, pp. 399-404, eds. M. J. Adams, R. A. Mashelkar, J. R. A. Pearson and A. R. Rennie, Imperial College Press, London, U.K.

Adams, M. J., Briscoe, B. J. and Sinha, S. K. (1995) Interfacial and bulk rheological characterisations of paste materials in extrusion flow. *27th International SAMPE Technical Conference 9/12/95*.

Adams, M. J., Edmondson, B, Caughey, D. G. and Yahya, R. (1994) An experimental and theoretical study of the squeeze-film deformation and flow of elastoplastic fluids. *Journal of Non-Newtonian Fluid Mechanics*, **51**, 61-78.

Amarasinghe, A. D. U. S. (1998a) *Interpretation of Paste Extrusion Data*, pp. 36-39. PhD Thesis, University of Cambridge, U.K.

Amarasinghe, A. D. U. S. (1998b) *Interpretation of Paste Extrusion Data*, pp. 128-143. PhD Thesis, University of Cambridge, U.K.

Amarasinghe, A. D. U. S. and Wilson, D. I. (1997) Statistical analysis of pressure fluctuations in paste extrusion. In *The 1997 Jubilee Research Event,* Nottingham, U.K., Apr 8-9, vol. 1, pp. 529-532. Institution of Chemical Engineers, Rugby, U.K.

Atkinson, J. H. (1993) *An Introduction to the Mechanics of Soils and Foundations*, pp. 60-69. McGraw-Hill, Maidenhead, U.K.

Baert, L. and Down, G. R. B. (1994) A comparison of two methods of instrumenting a small-scale basket extruder. *International Journal of Pharmaceutics*, **107**, 219-222.

Baert, L., Remon, J. P., Elbers, J. A. C. and van Bommel, E. M. G. (1993) Comparison between a gravity feed extruder and a twin screw extruder. *International Journal of Pharmaceutics*, **99**, 7-12.

Bagley, E. B. (1957) End corrections in the capillary flow of polyethylene. *Journal of Applied Physics*, **28**, 624-627.

Barnes, E. (2001) *Pelletiser Fundamentals: A rheological study*. Part IIB Project Report, Department of Chemical Engineering, University of Cambridge, U.K.

Barnes, H. A. (1989) Shear-thickening ("dilatancy") in suspensions of nonaggregating solid particles dispersed in Newtonian liquids. *Journal of Rheology*, **33** (2), 329-366.

Barnes, H. A., Hutton, J. F. and Walters, K (1989) *An Introduction to Rheology*, pp. 115-139. Elsevier Science, Amsterdam, The Netherlands.

Barnes, H. A. and Walters, K. (1985) The yield stress myth? *Rheologica Acta*, **24**, 323-326.

Bayfield, M. (1997) *Liquid Phase Migration in Icing Sugar Pastes*. Part IIB Project Report, Department of Chemical Engineering, University of Cambridge, U.K.

Bell, G. A. (1989) Herbicide granules – review of processes and products. BCPC Brighton Crop Protection Conference - Weeds, Brighton, U.K., 1989.

Benbow, J. J. (1971) The dependence of output rate on die shape during catalyst extrusion. *Chemical Engineering Science*, **26**, 1467-1473.

Benbow, J. J., Blackburn, S., Lawson, T. A., Oxley, E. W. and Bridgwater, J. (1992) The causes and prevention of defects during ceramic forming. In *Special Ceramics 9* (*British Ceramic Proceedings*, No. 49 – Meeting of the Basic Science Section of the Institute of Ceramics at Imperial College, London, Dec 18-20 1990), eds. unknown, pp. 67-81. The Institute of Ceramics, Stoke-on-Trent, U.K.

Benbow, J. J. and Bridgwater, J. (1987a) The influence of formulation on extrudate structure and strength. *Chemical Engineering Science*, **42** (4), 753-766.

Benbow, J. J. and Bridgwater, J. (1987b) Measurement of paste yield by cone penetration. *Chemical Engineering Science*, **42** (4), 915-919.

Benbow, J. J. and Bridgwater, J. (1987c) The role of frictional forces in paste extrusion. Tribology in Particulate Technology, eds. B. J. Briscoe and M. J. Adams, pp. 80-90. IOP, Bristol, U.K.

Benbow, J. and Bridgwater, J. (1993a) *Paste Flow and Extrusion*, pp. 29-33. Clarendon Press, Oxford, U.K.

Benbow, J. and Bridgwater, J. (1993b) *Paste Flow and Extrusion*, pp. 37-38. Clarendon Press, Oxford, U.K.

Benbow, J. and Bridgwater, J. (1993c) *Paste Flow and Extrusion*, pp. 70. Clarendon Press, Oxford, U.K.

Benbow, J. and Bridgwater, J. (1993d) *Paste Flow and Extrusion*, pp. 83-92. Clarendon Press, Oxford, U.K.

Benbow, J. and Bridgwater, J. (1993e) *Paste Flow and Extrusion*, pp. 95-96. Clarendon Press, Oxford, U.K.

Benbow, J. J., Jazayeri, S. H. and Bridgwater, J. (1991) The flow of pastes through dies of complicated geometry. *Powder Technology*, **65**, 393-401.

Benbow, J. J., Oxley, E. W. and Bridgwater, J. (1987) The extrusion mechanics of pastes – the influence of paste formulation on extrusion parameters. *Chemical Engineering Science*, **42** (9), 2151-2162.

Berghaus, H. J. (1957) Rohr- und Blendendurchfluß plastischer Körper am Beispiel von Ton. *Forschung auf dem Gebiete des Ingenieurwesens*, **23** (4), 135-148.

Bingham, E. C. (1922) *Fluidity and Plasticity*, pp. 215-240. McGraw-Hill, New York, U.S.A.

Blackburn, S., Burbidge, A. S. and Mills, H. (2000) A critical assessment of the Benbow approach to describing the extrusion of highly concentrated particulate suspensions and pastes. *XIIIth International Congress on Rheology, Cambridge, U.K. 2000*, **4**-139-141.

Botten, A. J., Burbidge, A. S. and Blackburn, S. (2002) A model for a single screw paste extruder with non-constant channel depth. *Euro Ceramics VII, Pt 1-3 (Key Engineering Materials)*. Trans Tech Publications, Zurich, Switzerland.

Bridgman, P. W. (1946) *Dimensional Analysis*, pp. 36-47. Yale University Press, New Haven, U.S.A.

Britton, M. M. and Callaghan, P. T. (1997) Nuclear magnetic resonance visualization of anomalous flow in cone-and-plate rheometry. *Journal of Rheology*, **41** (6), 1365-1386.

Burbidge, A. S. and Bridgwater, J. (1992) Production of ceramics by extrusion: design of single screw extrusion equipment. In *The 1992 IChemE Research Event*, Manchester, U.K., Jan 1992, pp. 634-636. Institution of Chemical Engineers, Rugby, U.K.

Burbidge, A. S. and Bridgwater, J. (1995) The single screw extrusion of pastes. *Chemical Engineering Science*, **50** (16), 2531-2543.

Burbidge, A. S., Bridgwater, J. and Saracevic, Z. (1995) Liquid phase migration in paste extrusion. *Transactions of the Institution of Chemical Engineers, Part A (Chemical Engineering Research and Design),* **73**, 810-816.

Capper, P. L. and Cassie, W. F. (1969) *The Mechanics of Engineering Soils, 5th ed.*, pp. 29. Spon, London, U.K.

Capriz, G. (1963) A theoretical analysis of extrusion processes. *Transactions of the British Ceramic Society*, **62**, 339-361.

Capriz, G. and Laratta, A. (1965) Screw extrusion of Newtonian and Bingham bodies. *Transactions of the British Ceramic Society*, **64**, 19-31.

Carley, J. F., Mallouk, R. S. and Kelvey, J. M. (1953) Simplified flow theory for screw extruders. *Industrial and Engineering Chemistry*, **43** (5), 974-978.

Carley, J. F. and Strub, R. A. (1953) Basic concepts of extrusion. *Industrial and Engineering Chemistry*, **45** (5), 970-973.

Casson, N. (1959) A flow equation for pigment-oil suspensions of the printing ink type. In *Rheology of Disperse Systems,* ed. C. C. Mill, pp. 84-104. Permagon, London, U.K.

Cheyne, A., Wilson, D. I., Gedney, S., Barnes, O. J. and Scriven, F. (2001) Shear induced microstructural changes in starchy materials. *6th World Congress of Chemical Engineering, Melbourne, Australia, 2001*.

Cotton, R. A. and Giffard, A. (2001) *Introducing wood pellet fuel to the UK*. Report of the DTI Sustainable Energy Programme, Department of Trade and Industry, London, U.K.

Covey G. H. and Stanmore, B. R. (1981) Use of the parallel-plate plastometer for the characterisation of viscous fluids with a yield stress. *Journal of Non-Newtonian Fluid Mechanics*, **8**, 249-260.

Darnell, W. H. and Mol, E. A. J. (1956) Solids conveying in screw extruders. *Society of Physics Engineering (SPE) Journal*, **12**, 20-29.

Dupuis, J. F, Villemaire, J. P. and Felder, E. (1994) Capillary rheometer measurement of a plasticine used in order to simulate the hot extrusion of metals. *Journal of Materials Processing Technology* **43**, 237-257.

Engländer, A., Burbidge, A. and Blackburn, S. (2000) A preliminary evaluation of single screw paste extrusion. *Transactions of the Institution of Chemical Engineers, Part A (Chemical Engineering Research and Design),* **78**, 790-794.

Fielden, K. E., Newton, J. M. and Rowe, R. C. (1992) A comparison of the extrusion and spheronization behaviour of wet powder masses processed by a ram extruder and a cylinder extruder. *International Journal of Pharmaceutics* **81**, 225-233.

Formstone, C. A. (1995) SEM investigation effect of extruder design on flow properties of extrudable pastes. Zeneca Agrochemicals internal report TMY0747B.

Formstone, C. A. (1997) Pressure measurements on extruding pastes. Zeneca Agrochemicals internal report TMY0831B.

Fujimoto, T., Ohta, Y., Nakayama, M. and Uesugi, H. (1993) *Screw-type extrusion granulating apparatus, especially for producing very fine granules*. Patent number US5240400.

Furnas, C. C. (1933) Grading aggregates I: Mathematical relations for beds of broken solids of maximum density. *Industrial and Engineering Chemistry* **23** (9), 1052-1058.

Hagen, G. (1839) *Annals of Physical Chemistry*, **46**, 423-442.

Hamley, I. W. (2000a) *Introduction to Soft Matter*, pp. 133-189. John Wiley, Chichester, U.K.

Hamley, I. W. (2000b) *Introduction to Soft Matter*, pp. 193-263. John Wiley, Chichester, U.K.

Harris, J. M. (1998) The scale-up of ICIA5504 WG formulations (Part 10) – the establishment of azoxystrobin/cymoxanil WG on the Yalding I/F WG plant. Zeneca Agrochemicals internal report TMY0857B.

Hatzikiriakos, S. G. and Dealy, J. M. (1992) Wall slip of molten high density polyethylenes. II. Capillary rheometer studies. *Journal of Rheology*, **36** (4), 703-741.

Herschel, W. H. and Bulkley, R. (1926) Measurement of consistency as applied to rubber-benzene solutions. *Proceedings of the American Society for Testing Materials*, **26** (2), 621-633.

Hill R. (1950) *The Mathematical Theory of Plasticity*. Clarendon Press, Oxford, U.K.

Hill R. (1951) On the state of stress in a plastic-rigid body at the yield point. *Philosophical Magazine*, **42**, 865-875.

Horrobin D. J. (1999) *Theoretical Aspects of Paste Extrusion*. PhD Thesis, University of Cambridge, U.K.

Horrobin, D. J. and Nedderman, R. M. (1998) Die entry pressure drops in paste extrusion. *Chemical Engineering Science*, **53** (18), 3215-3225.

Husband, D. M., Aksel, N. and Gleissle, W. (1993) The existence of static yield stresses in suspensions containing noncolloidal particles. *Journal of Rheology*, **37** (2), 215-235.

Huzzard, R. J. and Blackburn, S. (1998) Slip flow in concentrated alumina suspensions. *Powder Technology*, **97**, 118-123.

Iwata, J. and Inoue, T. (2001) *Screen for extrusion granulating device*. Patent number US2001031290.

Janssen, H. A. (1895) Versuche über Getreidedruck in Silozellen. *Zeitschrift der Verein Deutsche Ingenieur*, **39** (35), 1045-1049.

Janssen, L. P. B. M. (1978a) *Twin Screw Extrusion,* pp. 1. Elsevier, Amsterdam, The Netherlands.

Janssen, L. P. B. M. (1978b) *Twin Screw Extrusion,* pp. 6-9. Elsevier, Amsterdam, The Netherlands.

Jastrzebski, Z. D. (1967) Entrance effects and wall effects in an extrusion rheometer during the flow of concentrated suspensions. *Industrial and Engineering Chemistry Fundamentals*, **6** (3), 445-454.

Kalyon, D. M. (1993) Review of factors affecting the continuous processing and manufacturability of highly filled suspensions. *Journal of Materials Processing and Manufacturing Science*, **2**, 159-187.

Kalyon, D. M., Yaras, P., Aral, B. and Yilmazer, U. (1993) Rheological behaviour of a concentrated suspension: a solid rocket fuel simulant. *Journal of Rheology*, **37** (1), 35-53.

Khan, A. U., Briscoe, B. J. and Luckman, P. F. (2001) Evaluation of slip in capillary extrusion of ceramic pastes. *Journal of the European Ceramic Society*, **21**, 483-491.

Kobayashi, S. and Thomsen, E. G. (1965) Upper- and lower-bound solutions to axisymmetric compression and extrusion problems. *International Journal of Mechanical Sciences*, **7**, 127-143.

Koga, T. (1994) *Dome-shaped die and its production and blank material for die to be used in this method*. Patent number JP6226076.

Krieger I. M. and Maron S. H. (1952) Direct determination of the flow curves of non-Newtonian fluids. *Journal of Applied Physics*, **23** (1), 147-149.

Kudo, H. (1960) Some analytical and experimental studies of axi-symmetric cold forging and extrusion–I. *International Journal of Mechanical Sciences*, **2**, 102-127.

Kytömaa, H. (1993) Liquefaction and solidification. In *Particulate Two-Phase Flow*, ed. M. C. Roco, pp. 861-883. Butterworth-Heinemann, Boston, U.S.A.

Lawal, A. and Kalyon, D. M. (1997) Viscous heating in nonisothermal die flows of viscoplastic fluids with wall slip. *Chemical Engineering Science*, **52** (8), 1323-1337.

Lawal, A. and Kalyon, D. M. (1999) Analysis of nonisothermal screw extrusion processing of viscoplastic fluids with significant backflow. *Chemical Engineering Science*, **54**, 999-1013.

Lawrence, C. J. (2002) Private communication.

Lawrence, C. J. and Corfield, G. M. (1998) Non-viscometric flow of viscoplastic materials: squeeze flow. In *Dynamics of Complex Fluids*, pp. 379-393, eds. M. J. Adams, R. A. Mashelkar, J. R. A. Pearson and A. R. Rennie, Imperial College Press, London, U.K.

Leighton D. and Acrivos, A. (1987) The shear-induced migration of particles in concentrated suspensions. *Journal of Fluid Mechanics*, **181**, 415-439.

Leuenberger, H. (1984) Monitoring granulation. *Manufacturing Chemist*, **55** (5), 67-71.

Liaw S. L. (2001) *Anionic Surfactant Pastes: The effect of additives during processing on paste structure and rheology*. CPGS Dissertation, University of Cambridge, U.K.

Lukner, R. B. and Bonnecaze, R. T. (1999) Piston-driven flow of highly concentrated suspensions. *Journal of Rheology*, **43** (3), 735-751.

Lyne, C. W. and Johnston, H. G. (1981) The selection of pelletisers. *Powder Technology*, **29**, 211-216.

Mackley, M. R. (1992) *The Extrusion of Chocolate*. U.K. patent number 9220477.5.

Martin, P. J., Wilson, D. I. and Challis, K. (2001) Extrusion of paste through non-axisymmetric systems. *6th World Congress of Chemical Engineering, Melbourne, Australia, 2001*.

Modigell, M., Hufschmidt, M., Koke, J., Heine, C., Han, S., Stapf, S. and Petera, J. (2000) Investigation of wall slippage in suspensions by NMR imaging. *XIIIth International Congress on Rheology, Cambridge, U.K., 2000*, **4**-175-177.

Mooney, M. (1931) Explicit formulas for slip and fluidity. *Journal of Rheology*, **30**, 210-222.

Nedderman, R. M. (1992) *Statics and Kinematics of Granular Materials*, pp. 84-116. Cambridge University Press, Cambridge, U.K.

Newitt, D. M. and Conway-Jones, J. M. (1958) A contribution to the theory and practice of granulation. *Transactions of the Institution of Chemical Engineers*, **36**, 422-442.

Newton, I. (1687) *Philosophiæ Naturalis Principia Mathematica*. Jussu Societatis Regiæ ac typis Josephi Streatii, London, U.K.

Oliver, D. R. and Whiskens, M. (1996) The effect of absolute pressure on the processing parameters of ceramic pastes. *British Ceramic Proceedings*, **55** (21st Century Ceramics, eds. D. P. Thompson and H. Mandal), 87-97.

Oveston, A. and Benbow, J. J. (1968) Effects of die geometry on the extrusion of clay-like material. *Transactions of the British Ceramic Society*, **67**, 543-567.

Pels Leusden, C. O. (1962) Plastische Eigenschaften der Tone und ihr Einfluß auf Elemente der Mundstücksgestaltung. *Berichte der Deutschen keramischen Gesellschaft*, **39** (8), 427-431.

Perry, R. H. and Green, D. W. (1997a) *Perry's Chemical Engineers' Handbook, 7th ed.*, pp. **18**-28. McGraw-Hill, .New York, U.S.A.

Perry, R. H. and Green, D. W. (1997b) *Perry's Chemical Engineers' Handbook, 7th ed.*, pp. **18**-72. McGraw-Hill, .New York, U.S.A.

Perry, R. H. and Green, D. W. (1997c) *Perry's Chemical Engineers' Handbook, 7th ed.*, pp. **20**-84. McGraw-Hill, .New York, U.S.A.

Press, W. H., Teukolsky, S. A., Vetterling, W. T. and Flannery, B. P. (1993) *Numerical Recipes in C: The Art of Scientific Computing*, pp. 661-681. Cambridge University Press, Cambridge, U. K.

Poiseuille, J. L. M. (1835) Recherches sur les causes du mouvement du sang dans les vaisseaux capillaires. *Comptes rendus hebdomadaires des séances de l'Académie des Sciences*, **1**, 554-560.

Poitou, A., Racineux, G. and Burlion, N. (1997) Identification and measurement of pastes rheological properties – effects of water dissociation. *Water Science and Technology,* **36** (11), 19-26.

Rabinowitsch, B. (1929) Über die Viskosität und Elastizität von Solen. *Zeitschrift für Physikalische Chemie – Abteilung A*, **145**, 1-26.

Richardson, J., Matchett, A. J., Coulthard, J. M., Gibbon, S., Wilson, C. and Watson, C. (2000) The characterization of pigment powders for titanium dioxide/polymer dispersions by the 'Masterbatch' process. *Transactions of the Institution of Chemical Engineers, Part A (Chemical Engineering Research and Design)*, **78**, 39-48.

Rough, S. L., Bridgwater, J. and Wilson, D. I. (2000) Effects of liquid phase migration on extrusion of microcrystalline cellulose pastes. *International Journal of Pharmaceutics*, **204**, 117-126.

Rough, S. L. and Saracevic, Z. (1997) *Final Report for Zeneca Agrochemicals*. Confidential report, Department of Chemical Engineering, University of Cambridge, U.K.

Rowell, H. S. and Finlayson, D. (1922) Screw viscosity pumps. *Engineering*, **114**, 606-607.

Scott, G. D. and Kilgour, D. M. (1969) The density of random close packing of spheres. *British Journal of Applied Physics*, **2** (2), 863-866.

Shah, R. D., Kabadi, M., Pope, D. G. and Augsburger, L. L. (1994) Physicomechanical characterization of the extrusion-spheronization process. I. Instrumentation of the extruder. *Pharmaceutical Research*, **11** (3), 355-360.

Steffe, J. F. (1996) *Rheological Methods in Food Process Engineering*, pp. 116-118. Freeman Press, East Lansing, MI, U.S.A.

Stieß-Konstanz, W. (1955) Über Auspreßversuche mit Ziegeleiton und ihre Auswertung zur Erlangung von weitgehend geräteunabhängigen Stoffkonstanten. *Kolloid Zeitschrift*, **142**, 168.

Stevenson, P. and Thorpe, R. B. (1999) Towards understanding sand transport in oil flowlines. *Multiphase '99, Cannes, France*, 583-594.

Stones, P. W. (1999) *Yield Properties of Solid-Liquid Pastes*. Part IIB Project Report, Department of Chemical Engineering, University of Cambridge, U.K.

Stronge, W. J. (1998) Private communication. Department of Engineering, University of Cambridge, U.K.

Tuchinda, P., Hartman Kok, P. J. A., Kazarian, S. G., Lawrence, C. J. and Briscoe, B. J. (2001) *Rheological Methods in Food Process Engineering*, pp. 116-118. Freeman Press, East Lansing, MI, U.S.A.

Van doorslaer Tom (1997) *Water dispersible granules by low pressure extrusion*. The Fitzpatrick Company Europe, Sint-Niklaas, Belgium.

Vervaet, C., Baert, L. and Remon, J. P. (1995) Extrusion-spheronisation; A literature review. *International Journal of Pharmaceutics*, **116**, 131-146.

Vervaet, C., Baert, L., Risha, P. A. and Remon, J. P. (1994) The influence of the extrusion screen on pellet quality using an instrumented basket extruder. *International Journal of Pharmaceutics*, **107**, 29-39.

Walker, D. M. (1966) An approximate theory for pressures and arching in hoppers. *Chemical Engineering Science*, **21**, 975-997.

Walters, J. K. (1973) A theoretical analysis of stresses in axially-symmetric hoppers and bunkers. *Chemical Engineering Science*, **28**, 779-789.

Wasp, E. J. (1977) *Solid-Liquid Flow: Slurry Pipeline Transportation*, pp. 67. Trans Tech Publications, Clausthal, Germany.

Weert, X., Lawrence, C. J., Adams, M. J. and Briscoe, B. J. (2001) Screw extrusion of food powders: prediction and performance. *Chemical Engineering Science*, **56**, 1933-1949.

Wildman, R. D., Blackburn, S., Benton, D. M., McNeil, P. A. and Parker, D. J. (1999) Investigation of paste flow using positron emission particle tracking. *Powder Technology*, **103**, 220-229.

Yaras, P., Kalyon, D. M. and Yilmazer, U. (1994) Flow instabilities in capillary flow of concentrated suspensions. *Rheologica Acta*, **33**, 48-59.

Yoshimura, A. and Prud'homme, R. K. (1988) Wall slip corrections for Couette and parallel disk viscometers. *Journal of Rheology*, **32** (1), 53-67.

Yilmazer, U. and Kalyon, D. M. (1989) Slip effects in capillary and parallel disk torsional flows of highly filled suspensions. *Journal of Rheology*, **33** (8), 1197-1212.

Yilmazer, U. and Kalyon, D. M. (1991) Dilatancy of concentrated suspensions with Newtonian matrices. *Polymer Composites*, **12** (4), 226-232.

Yuan, W. X., Burbidge, A. S., Blackburn, S., Fisher, K. A., Langston, P. A and Wilson, D. I. (2001) A micro scale model of paste flow in the ram extrusion process. *6th World Congress of Chemical Engineering, Melbourne, 2001.*

Zheng, J., Carlson, W. B. and Reed, J. S. (1992) Flow mechanics on extrusion through a square-entry die. *Journal of the American Ceramic Society*, **75** (11), 3011-3016.

Appendix A:
Industrial twin-screw radial screen extruder data

Design and operation data was received from the sponsoring company for two plants; the *Extruder WG Plant* (fungicides and insecticides), and the *Extruder Herbicide Plant*. Manufacturer's engineering drawings of the type of screws and frustums/blades used on the *Extruder Herbicide Plant* are showed in Figure A.2. Table A.1 lists the data received for the *Extruder WG Plant*. Table A.2 lists the data received for the *Extruder Herbicide Plant*, and also includes data read from Figure A.2 and some estimated parameters. The estimated parameters were based on; *(i)* the screen holes being arranged in an equilateral triangle pattern, with rows of holes aligned parallel to the blade (as shown in Figure A.1), *(ii)* the density of the material being 2000 kg/m^3 (see Section 3.4.1), *(iii)* the material being extruded only through the row of holes immediately in front of the blade, and *(iv)* an average of three blades extruding material at any one time.

Table A.1 Design and operation data for Extruder WG Plant

Throughput (product dependent), kg/h	600 - 1000
Speed range, rpm	20 - 58
Speed range (usual operational range), rpm	40 - 50
Screw diameter (new), mm	180
Gap size (unworn), mm	2.5
Gap size (most worn using harborlite formulations), mm	18.5*
Screen hole diameter (product dependent), mm	0.6 – 1.2

* *This value was supplied by the sponsoring company, but appears dubious.*

Table A.2 Design and operation data for Extruder Herbicide Plant

Throughput, kg/h	300
Speed, rpm	90
Screw diameter, mm	129
Blade-screen gap size, mm	1.35
Screen hole diameter, mm	0.6
Number of holes	71808
Frustum minimum diameter, mm	91
Frustum maximum diameter, mm	121
Frustum/screen length, mm	220
Frustum half angle, degrees	3.9
Screw helix angle, degrees	81
Extruder cross-section screw-screen nip angle, degrees	47
Extruder cross-section blade length, mm	4
Dam screen gap size, mm	1.35
Dam length, mm	5
Screen diameter, mm	131.7
Screen thickness, mm	0.6
Area of hole, mm^2	0.283
Screen area per hole, mm^2	1.27
Hole pitch, mm	1.21
Number of holes in row along length of extruder	182
Extrudate radial velocity (1 row of holes), m/s	0.27
Feed entrance axial velocity, m/s	0.0032
Feed screw diameter, mm	0.092
Feed screw length, mm	390
Feed screw helix angle, degrees	9.1
Feed barrel diameter, mm	129

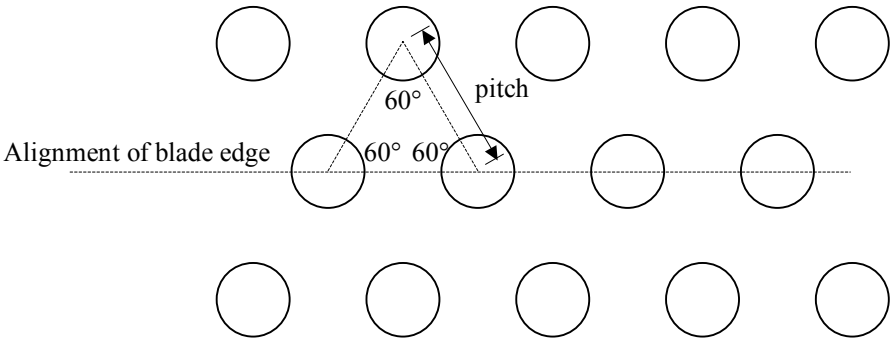

Figure A.1 Assumed screen hole pattern

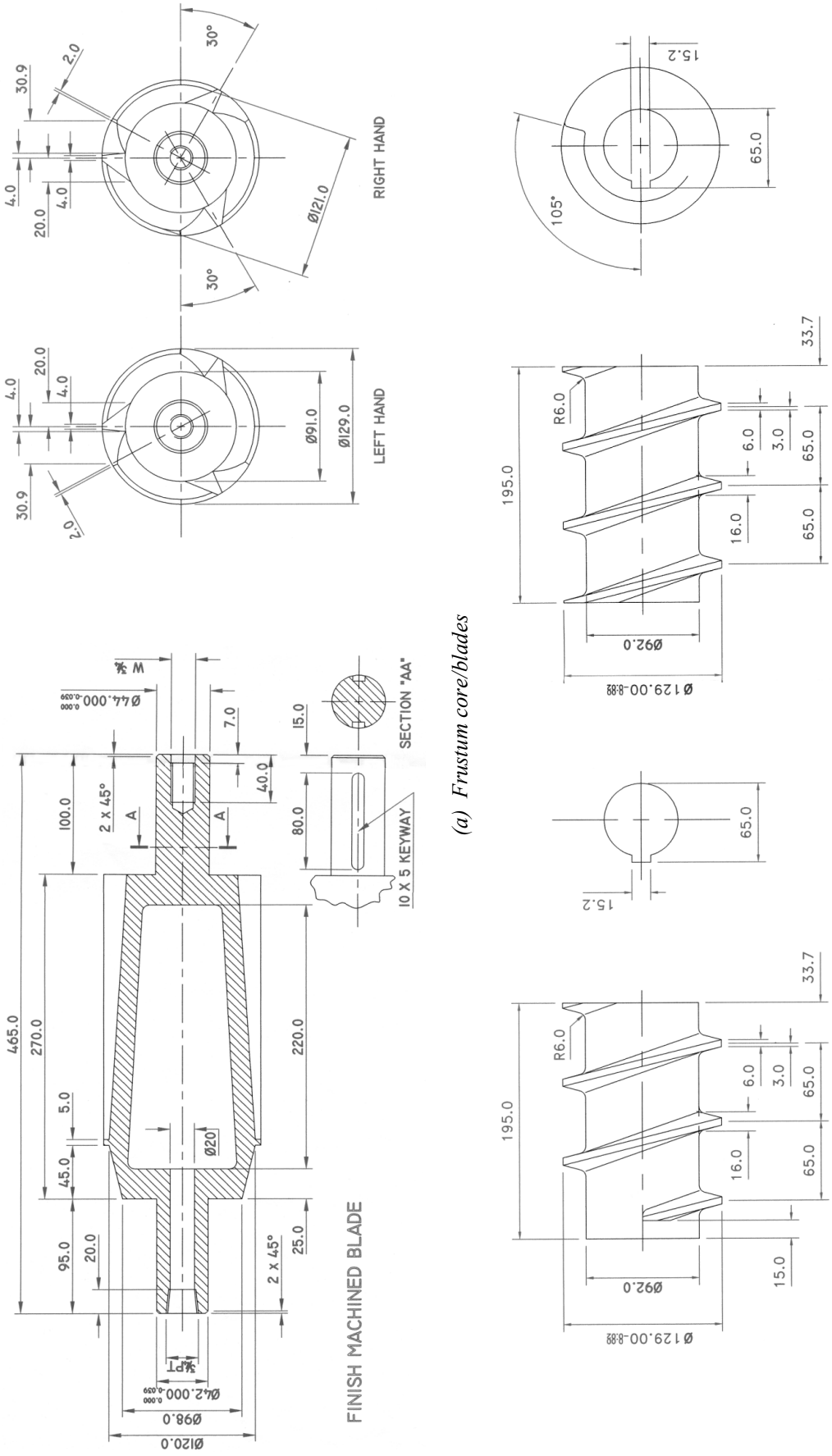

(a) Frustum core/blades *(b) Feed screw*

Figure A.2 Selected engineering drawings of a Fuji Paudal twin-screw radial screen extruder
Reproduced from drawings by Fuji Paudal Co. Ltd., Osaka, Japan. Dimensions in mm.